THE UNIVERSITY
of ADELAIDE

Self-noise of Airfoils Under Stalled Conditions

Alex Laratro

School of Mechanical Engineering
The University of Adelaide
South Australia 5005
Australia

A thesis submitted in fulfilment of
the requirements for the degree of
Doctor of Philosophy in July, 2017

Abstract

In recent years there have been reports of a transient impulsive noise signature being produced sporadically by wind turbines. Impulsive noise, where the noise level periodically increases and decreases at a rapid rate, is of concern to industry as turbines producing this noise restricts the growth potential of wind farms. By developing noise control techniques in order to mitigate the production of impulsive noise, it is easier for wind farm operators to comply with noise regulations, removing a significant barrier to growth and reducing the impact on the comfort of nearby residents.

One of the likely candidates for the source of impulsive wind turbine noise is stall of the turbine blade. While it is well understood that an increase in turbulence near a hard surface results in an increase sound production, the sound generated by airfoils under stall conditions is not well researched. The purpose of this thesis is to investigate the sound generated by simple airfoils under stall conditions in order to further the understanding of this noise.

In recent publications on the noise produced by stalling airfoils, the noise has been divided into two categories. For much of the stall regime the noise is referred to as “deep stall" noise, where the airfoil sheds large vortices at a specific frequency. This is then contrasted with a “light stall" noise regime, where the noise produced is more broadband and the source mechanism is less well understood.

The primary focus of this thesis is to understand of the effect of airfoil profile on this “light stall" noise. The data presented in this thesis show that as the airfoils enter a stalled state, a low frequency dipolar noise appears. The production of this noise corresponds to amplitude increases in the turbulent wake spectra seen in literature and this correlation between noise production and wake spectra was subsequently confirmed by studying the wake velocity spectra. It was found that there was significant coherence between the wake velocity and sound signals, indicating that the source of the noise produced at “light stall" is due to vorticity generated in the fully-separated boundary layer as the airfoil enters a stalled state.

The primary effect of the airfoil profile on the noise generated at stall is in the rate at which it increases with respect to angle of attack. A NACA 0021 airfoil was found to have

a much sharper increase in noise level with respect to angle of attack as it reaches the stall angle, compared with the thinner NACA 0012 profile and a flat plate. This can be related to the rate of change in lift force and the aforementioned changes in wake spectrum. A sharper increase in noise level with angle of attack is significant because it will lead to a more impulsive amplitude-modulation of the sound signal if the angle of attack of the airfoil is varying periodically with time. As wind turbines can experience stall due to unsteady inflow, this represents more evidence that stall is the source of the impulsive noise observed in the field.

Subsequently, an investigation was conducted on the effect of strong vortices, shed by airfoils undergoing dynamic stall, on the directivity of stall noise. A vortex generator was used to produce isolated vortices with a similar time-varying profile to a decaying dynamic stall vortex in order to study these effects in isolation. The effect of this changing vortex on the directivity of sound was measured and compared with a quasi-steady model derived from the literature, which indicated that there is no significant difference between quasi-steady modelling and the observed effects under the conditions that wind turbine airfoils can be expected to encounter. Using a quasi-steady approach the effect of refraction through shed dynamic stall vortices on airfoil noise can be modelled, and applied to wind turbines. Estimates indicate that large horizontal axis wind turbines are capable of producing dynamic vortices strong enough to induce significant scattering, however these vortices are produced on the inboard sections of the blade, and the dynamic stall is unlikely to occur on the outboard sections where the majority of the blade noise is generated.

Overall, the current research indicates that noise produced as an airfoil enters stall (the “light stall" regime) is a strong candidate for the source of impulsive wind turbine noise. In addition, the occurrence of dynamic stall may be causing short-term changes in noise directivity due to refraction of the sound and this is worth considering in future wind turbine noise modelling efforts.

Declaration

I certify that this work contains no material which has been accepted for the award of any other degree or diploma in any university or other tertiary institution and, to the best of my knowledge and belief, contains no material previously published or written by another person, except where due reference has been made in the text. In addition, I certify that no part of this work will, in the future, be used in a submission for any other degree or diploma in any university or other tertiary institution without the prior approval of the University of Adelaide and where applicable, any partner institution responsible for the joint-award of this degree.

I give consent to this copy of my thesis when deposited in the University Library, being made available for loan and photocopying, subject to the provisions of the Copyright Act 1968.

The author acknowledges that copyright of published works contained within this thesis resides with the copyright holder(s) of those works.

I also give permission for the digital version of my thesis to be made available on the web, via the University's digital research repository, the Library catalogue and also through web search engines, unless permission has been granted by the University to restrict access for a period of time.

I acknowledge the support I have received for my research through the provision of an Australian Government Research Training Program Scholarship.

Alex Laratro

Date

Acknowledgements

I would first like to thank my principal supervisor A/Prof Maziar Arjomandi for his unwavering support of my work. I am also incredibly grateful for the input and support of my co-supervisors, Prof Ben Cazzolato and A/Prof Richard Kelso. The completion of this thesis would not have been possible without you.

I would also like to thank the support and technical staff of the School of Mechanical Engineering. Garry Clarke for helping me with my experimental rig designs, and the Mechanical Workshop technicians for fabricating them. Philip Schmidt and Derek Franklin for fabricating my electronics and always being able to help me find the instrumentation I need, and Lydia Zhang for fixing countless broken hot-wire probes. Billy Constantine for maintaining my office and lab computers, and finding hardware that I needed for my instruments. I would also like to thank the office staff, who were always there to patch me up when I clumsily cut myself on something in the lab or kitchen.

To my colleagues, thank you for taking the time out to help me. Whether it was showing me how to use some equipment, helping me bounce ideas around, or just saying hi in the corridors, it helped make the building feel like home. I'm going to miss heading down to the lab and not knowing who I'm going to run into and which other projects I'm going to learn about.

To best friends both past and present: I am who I am today because of you, and you were there for me when I needed you. I will never forget our friendships, both the good times and the bad.

To my friends and family, thank you for your love and support throughout this period in my life, especially my mother and sister whose patience has been tested more than once. I know I was always hesitant to explain my work to you, but now that it's polished and finalised there's never been a better time.

Contents

Nomenclature

Acronyms

AM	Amplitude modulation
CAA	Computational aeroacoustics
CFD	Computational fluid dynamics
FWH	Ffowcs Williams-Hawking
GE	General Electric
GW	Gigawatt
LES	Large eddy simulation
LIDAR	Light detection and ranging
MW	Megawatt
NACA	National Advisory Committee for Aeronautics
NAM	Normal amplitude modulation
NREL	National Renewable Energy Laboratory
OAM	Other amplitude modulation
RANS	Reynolds-averaged Navier-Stokes
SODAR	Sound detection and ranging
TNO	Netherlands Organisation for Applied Scientific Research

Greek symbols

α	Angle of attack ($^\circ$)

α_{g} Geometric angle of attack (°)

α_{t} True angle of attack (°)

β Phase (radians)

γ Ratio of specific heats

Γ Circulation (m^2/s)

δ^* Displacement thickness (m)

Γ Normalised circulation: $\Gamma^* = \Gamma/(cU_\infty)$

ϵ Normalised circulation: $\epsilon = \Gamma/(a_\infty \lambda)$

θ Azimuthal observation angle (radians)

κ Reduced frequency

λ Acoustic wavelength (m)

$\tilde{\nu}$ Acoustic wavenumber: f/a_0 (1/m)

ν Kinematic viscosity (m^2/s)

ρ Density (kg/m^3)

ρ_{in} Density amplitude of the incident sound wave (kg/m^3)

ϕ Polar observation angle (radians)

Φ_{m} Moving axis spectrum

Φ_{22} Vertical velocity autospectrum ($\mathrm{m}^2/\mathrm{s}^2$)

Ψ Stability function

ω Angular frequency (rad/s)

ψ Sound scattering mode

Ω Oscillation frequency (rad/s)

Roman symbols

A_{in} Pressure mplitude of incident sound wave (Pa)

A_1, B_1 Shape function

a	Speed of sound (m/s)
c	Chord (m)
C_{L}	Coefficient of lift
D	Directivity function
$\mathbf{E}$, $\mathbf{H}$, $\mathbf{S}$	Euler equation terms
f_ω	Rotational frequency (rps)
f	Frequency (Hz)
h	Height (m)
h_0	Surface roughness height (m)
k_{in}	Wavenumber of incident sound wave (1/m)
K_1, K_2	Amplitude function
$\mathbf{k}$	Velocity wavenumber vector (1/m)
$\mathbf{l}$	Surface normal vector
L	Length scale (m)
$L_{\text{M}}\text{O}$	Monin-Obukhov length (m)
L_{sp}	Airfoil span (m)
M	Mach number: u_∞ / a_∞
m	Shear exponent
$\mathbf{n}$	Surface normal vector
p	Pressure (Pa)
$\mathbf{r}$	Distance between source and observer (m)
r_{c}	Vortex core radius (m)
r_{e}	Distance to observer (m)
Re_c	Reynolds number based on chord: cu_∞/ν
Re'_c	Stall equivalent Reynolds number: $3 \times Re_c$

S	Power spectral density
SPL	Sound pressure level
St	Strouhal number: fL/u_∞
TI	Turbulence intensity
u_c	Convection velocity (m/s)
$\mathbf{u}$	Velocity vector (m/s)
U	Magnitude of velocity vector (m/s)
$\mathbf{v}$	Surface velocity vector (m/s)
$\mathbf{x}$	Observer location (m)
$\mathbf{y}$	Source location (m)

Subscripts and other notation

α	Separation
∞	Freestream
$\overline{}$	Mean
$'$	Fluctuating component
p	Pressure side
ref	Reference
s	Suction side
TBL-TE	Turbulent boundary layer trailing edge noise

List of Figures

List of Tables

Chapter 1

Introduction

Growing demand for energy is one of the major challenges facing civilisation in the 21st century. It is currently projected that demand for energy will increase by 48% between 2012 and 2040, and much of that growth is to be driven by developing nations [1]. More generation capacity is required to meet rising demand, however traditional fossil fuel-based energy generation techniques necessitate large volumes of greenhouse gas emissions, thereby contributing to climate change. Current atmospheric greenhouse gas levels have contributed to a 1°C increase in global average temperature since the beginning of the industrial age, and it is predicted that this increase will rise to between 2°C and 4°C depending on the severity and speed at which mitigation strategies are employed [2]. The increase in total energy within the climate system is expected to result in more variable and extreme weather patterns, which in turn will result in a loss of biodiversity as well as human quality of life [3–6]. In light of this, there is a desire for a high proportion of global energy demand to be met by renewable sources of electricity in order to mitigate the effect on climate change of the increase in human energy consumption [7, 8].

1.1 Motivation

Wind energy is a small but rapidly-growing component of the renewable energy mix, with global installed capacity surpassing 432GW at the end of 2015 [9]. Wind resources large enough for economical power generation are often concentrated in small areas, which has led to a trend of installing larger turbines to capture a larger cross section of the incoming wind [10] [11].

As wind turbines grow in size their noise production increases due to the higher tip velocities and increased surface area of the blades. An analysis by Moller et al. [12] concluded that as turbines increase in size their noise production, especially in lower frequency bands, increases by a disproportionately large amount. These claims have

been disputed by Sondergaard [13] who found that more recent wind turbine models which produce more than 2MW of power have statistically significant shifts to more high-frequency noise. This may in part be due to Danish regulations on low-frequency noise production driving the design and development of turbines with a lower level of low frequency noise production. However, as both the installed capacity of wind turbines and the amount of nearby land used for housing continue to increase, the interests of residents and nearby wind turbines will inevitably conflict.

Small proportions of people living near wind turbines have reported increased annoyance due to auditory or visual factors [14–16]. While the evidence suggests that wind turbine noise is a direct detriment to the health of nearby residents [17], increases in discomfort and stress levels could lead to second order health effects and whether this is the case is a matter of some debate [18, 19]. Reports of discomfort can contribute to a negative perception of wind turbine technologies within the community [20, 21]. This can then lead to stronger noise regulations or increased scrutiny of new wind farm projects. Because of this, there is a large amount of ongoing research focused on designing quieter wind turbines and wind farms. A smaller turbine noise footprint would then allow turbine operators to develop wind resources that would otherwise be infeasible due to noise limits.

Advances in noise control therefore become more important as wind turbine technology proliferates, and is very important if wind turbines and wind farms are to continue to grow while still complying with noise regulations. However, because wind turbine blades operate under significantly different conditions to most other airfoils, some of the mechanisms through which wind turbines generate noise are poorly understood. In particular, the literature on airfoil noise production at high angles of attack is severely lacking. This represents a significant knowledge gap that will be the focus of the present work.

At high angles of attack the flow around an airfoil becomes separated and begins to shed large amounts of vorticity, a condition known as “stall". Beyond a certain angle this vorticityrolls up to form large, coherent vortices shed from the airfoil at a fixed frequency. Wind turbines are usually prevented from operating in this range by their control systems, as it results in a significant decrease in power output and increased vibration-induced fatigue loads. However, under certain conditions wind turbines can experience stall by periodically exceeding the stall angle. Vorticity shed from the airfoil near the stall angle and the associated noise are less well understood than the noise at very high angles of attack. This lack of understanding is further complicated by the fact that differently-shaped airfoils can give rise to very different flow patterns, and the literature is focused on airfoils that are not characteristic of those found on commercial wind turbines. The primary motivator of this research is this disparity between the literature and the information that is required to properly model the noise of wind turbine airfoils and the effect that stall conditions may have in contributing to impulsive turbine noise observed in the field.

1.2 Research aims and objectives

The primary aim of this research is to determine the mechanism that generates the sound produced by the flow over an airfoil that is near its stall angle. This is needed in order to inform future wind turbine noise control efforts. This is achieved by comparing the sound production mechanisms and directivities of thick and thin symmetric airfoil profiles under stall conditions using the results of two experimental campaigns:

- Measurement of the spectrum of self-noise produced by thick and thin airfoil models under two regimes of stall, and
- Measurement of the directivity of the frequency bands of self-noise associated with stall conditions.

Because using simple, symmetric airfoils is not entirely representative of the blades used on commercial wind turbines, this approach does not directly enable the prediction of wind turbine noise at stall. A recent numerical study by Lee [22] into the effects of airfoil camber on the generation of noise of wind turbine airfoils at low angles of attack indicates that as the airfoil camber increases, the production of low frequency noise increases on the suction side and decreases on the pressure side. In addition the production of high frequency noise on the suction side decreases with camber. However using simple profiles enables this research to provide a deeper understanding of the effects of thickness alone on noise production, without other complicating factors. In the future, other parameters can be changed and compared to the airfoils studied in this research, to further understand the parameters that may effect the noise production on a wind turbine airfoil.

In addition to limiting the number of airfoil features that may affect noise production, the use simple airfoils enables a better comparison with literature. Commercial wind turbine airfoils are specifically designed for wind turbine applications and are often proprietary. This restricts the amount of literature available on their flow fields which in turn limits the ability to compare the results of the current research with that of previous studies. By using simple airfoils a more thorough comparison of the results with existing literature is possible which enables a deeper insight into the how the flow around the airfoils affect noise production.

The secondary aim of this research is to investigate the effect of dynamic stall on airfoil noise production. The formation of a dynamic stall vortex will generate sound, however this event occurs over a short time scale and is thought to produce a pulse of sound [23] while briefly interrupting normal airfoil noise production. However once this vortex is shed into the wake of the airfoil the sound it generates will be due to turbulent shear stresses and is therefore expected to be signficiantly weaker than the airfoil noise under

subsonic conditions. The airfoil will then resume normal stall noise production and as the shed vortex can travel a significant distance before decaying, there will be some overlap between steady state noise production and the presence of the vortex. During this period the vortex in the airfoil wake will act to either refract or scatter the sound, depending on its frequency. As the dynamic stall vortex is not present under normal flow conditions it will have an effect on the directivity of the airfoil noise directly after a dynamic stall event. This aim was achieved by conducting an experimental campaign to determine the effect of an isolated, but decaying vortex on the propagation of sound through measurement of the changes in directivity of a known sound signal as it passes through a vortex representative of that shed during a dynamic stall event.

1.3 Thesis outline

The current chapter contains the research background and motivation, as well as an outline of research aims and objectives. Following this the subsequent chapters of the thesis are outlined, followed by a list of the publications arising from this research.

Chapter 2 contains a review of the literature relevant to wind turbine flow conditions, airfoil noise modelling, airfoil self-noise under stall conditions, and the production, refraction, and scattering of noise by vortices. This review draws attention to several gaps in the existing literature that this research aims to address.

Chapter 3 presents an outline and analysis of most of the commonly hypothesised sources of impulsive turbine noise currently referred to in the literature as “other amplitude modulation" (OAM). This chapter highlights why stall was considered to be a noise source that should be investigated in this thesis over several others. As mentioned in Chapter 2, OAM is characterised by a shift in the wind turbine sound spectrum to lower frequencies, the magnitude of which varies periodically. The discussion in Chapter 3 concludes that the most likely cause of OAM is unsteady inflow, resulting in either changes in turbulent-inflow noise or blade stall. While the discussion singles out dynamic stall as a potential cause of impulsive wind turbine noise, further research has indicated that quasi-steady stall on the wind turbine blades could also contribute to this phenomenon. This conclusion was also reached in a report commissioned by RenewableUK [24], which was publicly released soon after the article presented in this chapter was published. This resulted in a focus on the noise produced at stall instend of other potential sources of impulsive turbine noise in the present research.

Chapter 4 presents a preliminary investigation into the self-noise of two symmetric airfoil models, NACA 0012 and NACA 0021 profiles, at high angles of attack. An existing wall-mounted microphone array in the Anechoic Wind Tunnel at The University of Adelaide was used for this investigation, as well as airfoil profiles that had been previously researched

under similar conditions. This allowed confidence in the experimental methods to be established before moving onto directivity measurements with a polar microphone array. It was found that there was a noticeable increase in low-frequency noise at the onset of stall, corresponding to flow separation. While this information was generally known from the literature, this research gave insight into how these changes in spectra differ between the NACA 0012 and 0021 airfoil profiles, with noticeable differences in spectrum shape and the rates of change in sound level with angle of attack. Later experiments had a greater focus on the change in sound level with angle of attack, as seen in Chapter 5, due to this discovery.

Chapter 5 presents an investigation into the directivity of the self-noise of the NACA 0012 and NACA 0021 airfoil models, along with a new flat-plate model of equal chord and span. Directivity measurements were enabled through the use of a polar microphone array, which also enabled the determination of the sound coherence between opposite sides of the test chamber. The results confirmed that the noise generated at the onset of stall, as measured in Chapter 4, is highly dipolar as previously discussed in the literature. Other than the different angles of attack where the low-frequency noise source is formed, there was no discernible difference in directivity between the airfoils. Conversely, further investigation into the strength of the low frequency noise, first reported in the article in Chapter 4, showed that the NACA 0012, NACA 0021 and flat-plate airfoils all behave noticeably differently. All three airfoils produce differently shaped curves of sound level vs angle of attack, and the NACA 0021 transitions between a pre-stall and stalled states with no discernible angle of attack range where the flow is in an intermediate state.

Chapter 6 details an investigation into the effect of the shed dynamic stall vortex on the noise generation by an airfoil at stall. A vortex generator was used to investigate the effect of vortex decay on the scattering of sound in isolation from an airfoil. While the prescence and propagaton of a vortex being shed in the wake of an airfoil which subsequently resumes the production of steady-state stall noise are the primary factors in the scattering of the airfoil noise and are known quantities, whether the changing structure of the vortex can be treated as a quasi-steady event is unknown. The scattering amplitudes that can be expected on large wind turbines in the field and the implications for wind turbine noise propagation are then discussed.

Chapter 7 summarises the findings and conclusions of the research. Some possibilities for future work to expand and apply the current research are then detailed.

1.4 Publications arising from this thesis

This research has led to the creation of four journal manuscripts as well as one peer reviewed conference paper (which is presented in Appendix A). A fifth manuscript (presented in Appendix B) was primarily written by a co-author, but contrasted the experimental data from a similar experimental campaign to a computational flow model. The following is a list of manuscripts resulting from this research:

Journal articles

Laratro, A., Arjomandi, M., Kelso, R., and Cazzolato, B. A discussion of wind turbine interaction and stall contributions to wind farm noise. *Journal of Wind Engineering and Industrial Aerodynamics 127* (2014), 1–10

Laratro, A., Arjomandi, M., Cazzolato, B., and Kelso, R. An experimental comparison of the self-noise of NACA 0012 and NACA 0021 airfoils at stall. *International Journal of Aeroacoustics 16*, 3 (2017), 181–195

Laratro, A., Arjomandi, M., Kelso, R., and Cazzolato, B. Self-noise and directivity of simple airfoils during stall: An experimental comparison. *Applied Acoustics 127* (2017), 133–146

Laratro, A., Arjomandi, M., Kelso, R., and Cazzolato, B. An experimental investigation into the effect of vortex decay on the scattering of sound. Submitted to *International Journal of Acoustics and Vibration* (2017)

Conference papers

Laratro, A., Arjomandi, M., Cazzolato, B., and Kelso, R. A comparison of NACA 0012 and NACA 0021 self-noise at low Reynolds number. In *Fluid-Structure-Sound Interactions and Control* (2016), Springer, pp. 21–25

Co-authored publications

Sedaghatizadeh, N., Laratro, A., Arjomandi, M., Cazzolato, B., and Kelso, R. Aeroacoustic behaviour of a NACA 0012 airfoil

References for Chapter 1

[1] U.S. Energy Information Administration. *International energy outlook 2016.* (2016).

[2] IPCC. *Climate change 2013: The physical science basis. Contribution of Working Group I to the Fifth Assessment Report of the Intergovernmental Panel of Climate Change.* [Stocker, T.F., D. Quin, G.-K. Plattner, M. Tignor, S.K. Allen, J. Boschung, A. Nauels, Y. Xia, V. Bex and P.M. Midgley (eds.)]. Cambridge University Press Cambridge, UK, and New York, NY, USA, (2013).

[3] Deschenes, O., and Greenstone, M. The economic impacts of climate change: Evidence from agricultural output and random fluctuations in weather. *The American Economic Review 97*, 1 (2007), 354–385.

[4] Heller, N. E., and Zavaleta, E. S. Biodiversity management in the face of climate change: A review of 22 years of recommendations. *Biological Conservation 142*, 1 (2009), 14–32.

[5] Bellard, C., Bertelsmeier, C., Leadley, P., Thuiller, W., and Courchamp, F. Impacts of climate change on the future of biodiversity. *Ecology Letters 15*, 4 (2012), 365–377.

[6] Hajat, S., Vardoulakis, S., Heaviside, C., and Eggen, B. Climate change effects on human health: Projections of temperature-related mortality for the UK during the 2020s, 2050s and 2080s. *Journal of Epidemiology and Community Health* (2014), 641–648.

[7] IPCC. *Climate change 2014: Mitigation of climate change: Contribution of Working Group III to the Fifth Assessment Report of the Intergovernmental Panel on Climate Change*, vol. 3. [Edenhofer, O., R. Pichs-Madruga, Y. Sokona, E. Farahani, S. Kadner, K. Seyboth, A. Adler, I. Baum, S. Brunner, P. Eickemeier, B. Kriemann, J. Savolainen, S. SchlÃűmer, C. von Stechow, T. Zwickel and J.C. Minx (eds.)]. Cambridge University Press, Cambridge, United Kingdom and New York, NY, USA, (2014).

[8] Chandel, S., Shrivastva, R., Sharma, V., and Ramasamy, P. Overview of the initiatives in renewable energy sector under the national action plan on climate change in india. *Renewable and Sustainable Energy Reviews 54* (2016), 866–873.

[9] Global Wind Energy Council. Global wind statistics 2015, (2016).

[10] Burton, T., Sharpe, D., Jenkins, N., and Bossanyi, E. *Wind energy handbook.* John Wiley & Sons, New York, NY, USA, (2001).

[11] Islam, M., Mekhilef, S., and Saidur, R. Progress and recent trends of wind energy technology. *Renewable and Sustainable Energy Reviews 21* (2013), 456–468.

[12] Møller, H., and Pedersen, C. S. Low-frequency noise from large wind turbines. *The Journal of the Acoustical Society of America 129*, 6 (2011), 3727–3744.

[13] Søndergaard, B. Low frequency noise from wind turbines: do the danish regulations have any impact? An analysis of noise measurements. *International Journal of Aeroacoustics 14*, 5-6 (2015), 909–915.

[14] Pedersen, E., and Waye, K. P. Wind turbine noise, annoyance and self-reported health and well-being in different living environments. *Occupational and Environmental Medicine 64*, 7 (2007), 480–486.

[15] Pedersen, E., and Larsman, P. The impact of visual factors on noise annoyance among people living in the vicinity of wind turbines. *Journal of Environmental Psychology 28*, 4 (2008), 379–389.

[16] Kageyama, T., Yano, T., Kuwano, S., Sueoka, S., Tachibana, H., et al. Exposure-response relationship of wind turbine noise with self-reported symptoms of sleep and health problems: A nationwide socioacoustic survey in japan. *Noise and Health 18*, 81 (2016), 53.

[17] Schmidt, J. H., and Klokker, M. Health effects related to wind turbine noise exposure: A systematic review. *PLoS One 9*, 12 (2014), e114183.

[18] Baliatsas, C., van Kamp, I., van Poll, R., and Yzermans, J. Health effects from low-frequency noise and infrasound in the general population: Is it time to listen? A systematic review of observational studies. *Science of the Total Environment 557–558* (2016), 163–169.

[19] Michaud, D. S., Feder, K., Keith, S. E., Voicescu, S. A., Marro, L., Than, J., Guay, M., Denning, A., Bower, T., Villeneuve, P. J., et al. Self-reported and measured stress related responses associated with exposure to wind turbine noise. *The Journal of the Acoustical Society of America 139*, 3 (2016), 1467–1479.

[20] Knopper, L. D., Ollson, C. A., McCallum, L. C., Aslund, M. L. W., Berger, R. G., Souweine, K., and McDaniel, M. Wind turbines and human health. *Frontiers in Human Health 2*, 63 (2014), 1–20.

[21] Wilson, G. A., and Dyke, S. L. Pre-and post-installation community perceptions of wind farm projects: the case of Roskrow Barton (Cornwall, UK). *Land Use Policy 52* (2016), 287–296.

[22] Lee, S. Trailing edge noise source characteristics for wind turbine airfoils. In *23rd AIAA/CEAS Aeroacoustics Conference* (2017), p. 3168.

[23] Nagarajan, S., and Lele, S. Prediction of sound generated by a pitching airfoil: a comparison of RANS and LES. In *Twelfth AIAA/CEAS Aeroacoustics Conference, Cambridge, MA* (2006).

[24] Renewable UK. Wind turbine amplitude modulation: research to improve understanding as to its cause and effect, (2013).

[25] Laratro, A., Arjomandi, M., Kelso, R., and Cazzolato, B. A discussion of wind turbine interaction and stall contributions to wind farm noise. *Journal of Wind Engineering and Industrial Aerodynamics 127* (2014), 1–10.

[26] Laratro, A., Arjomandi, M., Cazzolato, B., and Kelso, R. An experimental comparison of the self-noise of NACA 0012 and NACA 0021 airfoils at stall. *International Journal of Aeroacoustics 16*, 3 (2017), 181–195.

[27] Laratro, A., Arjomandi, M., Kelso, R., and Cazzolato, B. Self-noise and directivity of simple airfoils during stall: An experimental comparison. *Applied Acoustics 127* (2017), 133–146.

[28] Laratro, A., Arjomandi, M., Kelso, R., and Cazzolato, B. An experimental investigation into the effect of vortex decay on the scattering of sound. Submitted to *International Journal of Acoustics and Vibration* (2017).

[29] Laratro, A., Arjomandi, M., Cazzolato, B., and Kelso, R. A comparison of NACA 0012 and NACA 0021 self-noise at low Reynolds number. In *Fluid-Structure-Sound Interactions and Control* (2016), Springer, pp. 21–25.

[30] Sedaghatizadeh, N., Laratro, A., Arjomandi, M., Cazzolato, B., and Kelso, R. Aeroacoustic behaviour of a NACA 0012 airfoil.

Chapter 2

Literature Review

As mentioned in Chapter 1 the motivation of this research is to develop a deeper understanding of the noise generated by wind turbines. In order to understand and model these noise mechanisms several core topics must be understood, the first of which is the flow conditions that wind turbines operate in, and the sound that is produced under these conditions. In turn this requires an understanding of the flow-induced sound produced by airfoils, and how this noise changes with angle of attack as the airfoil begins to experience stall. Furthermore, knowledge of the effect that transient phenomena such as dynamic stall and the associated local vortices will have on the production and propagation of sound is also required. This chapter provides an overview of the current state of the literature on each of these topics, and concludes by identifying some key gaps that that will be addressed in later chapters.

2.1 Wind turbines

When considering the sound production of wind turbines, the two main areas of investigation are the conditions under which the turbines operate and the sound generated under those conditions. This allows appropriate conditions to be reproduced in a laboratory experiment which is then used to produce data and inform noise models, both of which can be compared to the noise generated by turbines in the field.

2.1.1 Operating conditions

Due to their physical size, most wind turbines are restricted to operating within the atmospheric boundary layer. The atmospheric boundary layer on the Earht's surface has a thickness of anywhere between 100m and 3000m, although in the absence of any thickness data, an approximation of 1000m is typically used for analytical purposes [1, 2]. The atmospheric boundary layer is further composed of an Ekman layer that occupies the top 90% and a surface layer that occupies the bottom 10% (though these proportions may

vary significantly), which can be further decomposed into inertial and roughness sublayers. Most currently-installed commercial wind turbines are less than 200m high and therefore operate within the inertial sublayer of the surface layer and may partially penetrate the lower parts of the Ekman layer, depending on the conditions of the atmospheric boundary layer at the site [3]. The surface sublayer contains more small-scale turbulence than the high layers, although the amount of wind shear and turbulence vary depending on the thermal conditions of the terrestrial surface, which can also lead to stable, unstable or neutral stratification [4]. An air parcel near the surface will adiabatically cool as it rises into a region of lower air pressure. If the surface is already cool, then the high density of the air parcels near the surface may prevent them from rising, resulting in stable stratification. A stably-stratified region of the atmospheric boundary layer has high wind shear, and turbulence generation within it is mostly due to the effect of surface roughness. Conversely, a warm surface will result in low wind shear as air parcels are free to rise further, leading to large-scale vertical mixing and turbulent structures. In between these regimes is neutral stratification, where an air parcel is able to maintain thermal equilibrium with the surrounding air as it rises. All of these cases are important to consider when designing wind turbines, as large amounts of incoming turbulence, wind shear, or changes in wind direction, are detrimental to wind turbine operation and this can be further compounded when considering the role that atmospheric turbulence plays in the turbine's wake recovery.

Quantifying these effects when situating a wind turbine or wind farm can be done either by gathering meteorological data at the potential sites, simulation of the proposed farm layout, or with simpler approximations. The surface layer profile is best described by a logarithmic expression

$$\frac{\overline{u}(h)}{\overline{u}(h_{ref})} = \frac{\ln(h/h_0) + \Psi(h/L_{MO})}{\ln(h_{ref}/h_0) + \Psi(h/L_{MO})}, \tag{2.1}$$

where $\overline{u}$ is the mean wind speed, h is the height, h_0 is the surface roughness height and $\Psi(h/L_{MO})$ is a stability function that depends on the ratio between the height and the Monin-Obukhov length [5, 6]. When the atmosphere is neutral, $\Psi(0) \ll 1$, and Equation (2.1) reduces to

$$\frac{\overline{u}(h)}{\overline{u}(h_{ref})} \approx \frac{\ln(h/h_0)}{\ln(h_{ref}/h_0)}. \tag{2.2}$$

However, it is more common for wind engineering standards to use the simpler power law approximation

$$\frac{\overline{u}(h)}{\overline{u}(h_{ref})} = \left(\frac{h}{h_{ref}}\right)^m, \tag{2.3}$$

where m represents a shear exponent. The logarithmic profile depends on surface roughness and atmospheric stability, which are condensed into an empirical exponent in the power law approximation. For the regions of the boundary layer where current wind turbines are situated, the power law is valid, but only for neutral atmospheric conditions [7, 8]. Values of m can be taken from wind engineering standards but as the value is terrain- and weather-dependent, it is considered more useful to measure the exponents for a specific site. Shear exponents and turbulent intensities from two example wind farms are shown in Figures 2.1 & 2.2 respectively.

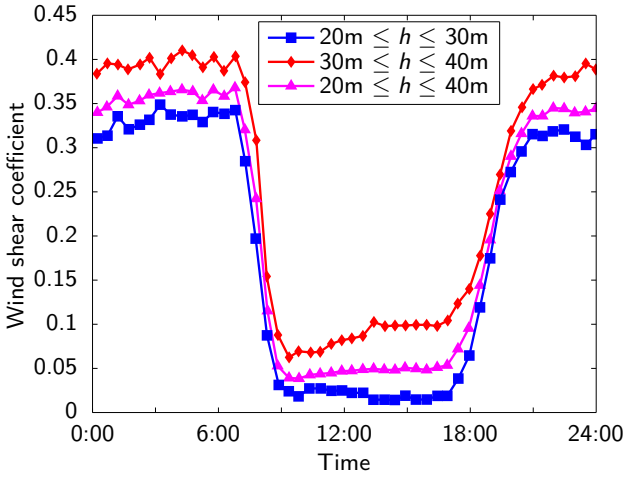

Figure 2.1: Diurnal variation of wind shear exponent at a potential wind farm site in Dhulom. Adapted from Rehman & Al-Abbadi [9]

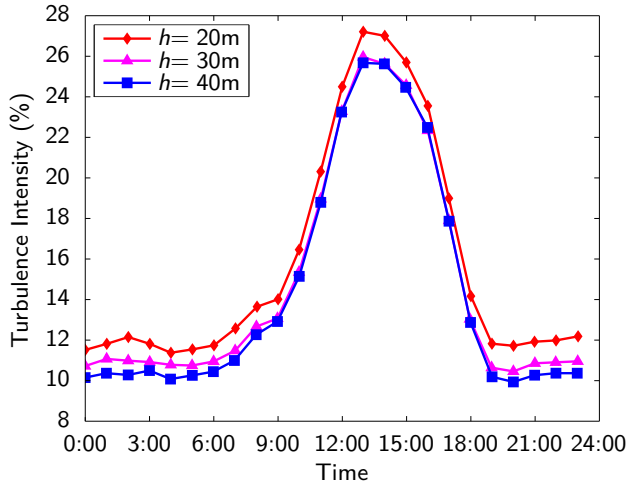

Figure 2.2: Diurnal variation of turbulence intensity at a potential wind farm site in Dhulom. Adapted from Rehman & Al-Abbadi [9]

A large proportion of the air velocity at the blade tip is due to the turbine rotation, so wind turbine blades are twisted along their length to ensure an optimal angle-of-attack is maintained along their length. Commercial wind turbines in operation today employ control systems to change the pitch of each blade as the wind conditions change to maintain the desired angle of attack, regulating speed and power generation. Blade twist can only be designed for one tip-speed ratio, so deviations from the design condition will result in sub-optimal angles-of-attack somewhere on the blade as the angle of attack distribution along the blade changes, which cannot entirely be accounted for by changes in pitch [10]. An example of this was provided by Burton et al. [4], where for the blade twist profile studied, the greatest difference in the angle of attack experienced at two points along the blade ($\Delta\alpha$) is about 5° at the design tip-speed ratio of 6, but increases dramatically as the turbine slows down. This leads to maximum differences in angle of attack experienced along the blade that make the occurrence of stall at some location on the blade unavoidable, which must then be taken into account by the control system. Usually the region that is allowed to stall is near the root of the blade, which rotates more slowly and contributes the least to power and noise production [11]. This effect is further compounded by manufacturing limitations preventing the optimal twist along the blade from being achieved, as the required twist increases quickly closer to the root, and structural considerations require the blade root to carry the highest loads [11, 12].

A standard method of monitoring the flow into a wind turbine rotor is an anemometer which is typically mounted onto either the turbine nacelle or a nearby meteorological mast [13]. Long-term averages of the data from the anemometer, extrapolated into velocity profiles using the power law and statistical turbulence models, are fed into the control system. This approach allows the blades to be pitched at angles that optimise power generation and noise production, but often fails to take into account the effects of non-uniformity and turbulence in the incoming flow such as wind gusts and the wakes of other wind turbines. Non-uniformities in both space and time can result in unsteady loading leading to a decrease in fatigue life and power generation of the turbine [13]. Some wind turbines used for research purposes have a more complex sensor suite. For example, a study by Madsen et al. [14] used blade-mounted pitot tubes to gather information at multiple stations along the blades to improve the knowledge of the incoming flow. In this study the inflow data was used to correlate observed increases in low-frequency noise production with an angle-of-attack range of about 12-13°, showing that with more development, inflow data may be useful as a predictor of generated noise.

More recently, LIDAR-based systems have been emerging as an effective alternative to the current measurement approaches, as they allow the capture of multi-dimensional velocity data at locations in-front of the blade. Currently these systems are mounted onto the nacelle, like anemometers previously, however there is at least one research turbine

that features a rotating LIDAR mounted in the hub [15, 16]. Whether this approach yields more effective measurements has not yet been determined. By capturing changes in wind velocity before the air reaches the turbine, a more effective control system can be implemented using feed-forward techniques and a much more detailed map of the flow field can be achieved than is possible with older techniques [15]. This approach still does not provide a complete picture of the wind profile experienced by the blades, due to both the evolution of the wind between the measurement plane and the rotor and the deformation of the flow as it encounters the rotor [16]. These measurement techniques also suffer from some drawbacks; for example they are restricted to lower frequencies than pressure sensors and are less effective at measuring turbulence [17]. A LIDAR system is unable to simultaneously sample every point of interest, necessitating an appropriate scanning strategy to optimally approximate the flow field [18]. However, as research into LIDAR flow monitoring continues it is very likely that it will become a common component in wind turbine control. A real-time measurement of the incoming flow field is also a very powerful tool for noise prediction, provided that aeroacoustic models employed are able to take advantage of it. While currently wind turbine control systems are focused on optimising power generation and minimising fatigue, control approaches that take the noise emissions of the turbine into account are also possible if passive noise control methods are not viable. In order to control the turbine in this way a model of the noise generated by the turbine airfoils is required that is capable of accurate prediction at all of the angles of attack, flow speeds and turbulence levels anticipated during operation.

Computational fluid dynamics simulations have been used to predict the turbulence and non-uniformities near a wind farm, which can potentially be used to compute noise levels [19, 20]. This method, if further developed for noise computation, would prove computationally expensive, takes a large amount of time to solve, and is unable to be applied to real-time noise control applications. It would, however, give an insight into the noise levels that can be expected at a site, and can therefore be useful when designing a turbine or wind farm layout to reduce the potential for conditions that promote noise generation. The effectiveness of this method, like real-time control in the field, is ultimately restricted by the quality of turbine noise models and noise control methods.

2.1.2 Noise

As the prediction and control of wind turbine noise is often restricted by the capabilities of the noise models employed, research into improving these models is one way to improve the accuracy of the overall results. Improving the understanding of noise generation mechanisms, as well as the comprehensiveness and accuracy of noise models, then enables control efforts, both active and passive, to be more accurately targeted at noise sources

where they will be the most effective.

The changing angle of attack of turbine blades due to wind shear leads to a noise phenomenon known as amplitude modulation, where the broadband noise level varies periodically [21]. In recent years this phenomenon has been referred to as “normal" amplitude modulation or NAM in order to differentiate it from a separate phenomenon referred to as “other" amplitude modulation or OAM. The exact source of OAM has not yet been determined and is discussed further in Chapter 3, but it is currently thought to be due to stall occurring periodically on the blade during certain conditions [22]. OAM is of more interest to researchers than NAM due to its greater low-frequency content, which makes it a candidate for the undetermined source of noise complaints in some communities near wind farms [22].

An annoyance study by Ioannidou et al. [23] indicated that the intermittence of OAM is not inherently more annoying that NAM, with the primary determining factor in annoyance being the modulation depth. This indicates that the primary reason for OAM being the focus of reports is the large amount low frequency content resulting in a persistence of audibility over long distances. This is compounded by other propagation effects that can result in an increase in audibility over long distances, such as cylindrical spreading due to refraction through the atmospheric boundary layer [24].

Attempts to relate the occurrence of OAM to transient stall by Fischer et al. [25] showed that the surface pressure is a good indicator of the far field noise. A modulation in surface pressure of 16dB was observed in the 100Hz to 200Hz range when the wind turbine was operating at a suboptimal pitch such that the blades crossed into the stall regime (see Figure 2.3). Several strategies were employed to try to mitigate this modulation and it was found that stall avoidance using individual pitch control of the blades achieves the best compromise with losses in power generation [25].

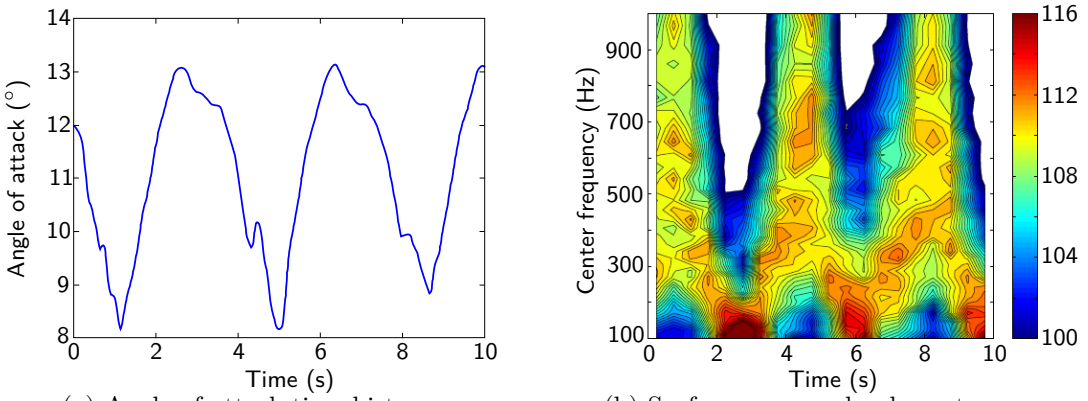

(a) Angle of attack time history (b) Surface pressure level spectrogram

Figure 2.3: Angle of attack and surface pressure measured from a wind turbine blade during operation with intermittent stall. Surface pressure levels in dB with 1/12th octave bands. Stall occurs at approximately 12.9°. Adapted from Fischer et al. [25]

Measurements of the sound pressure level spectrum of a wind turbine were also taken during the experimental campaign reported by Fischer et al. [25], and reported by Madsen et al. [14]. The wind turbine sound spectrum shows that low-frequency noise levels increased at angles of attack beyond the stall angle. This behaviour (shown in Figure 2.4) shows the effect that stall can have on a wind turbine noise during operation.

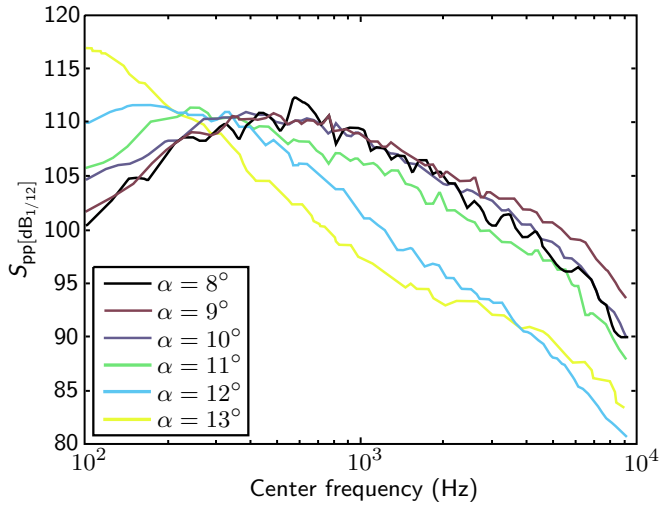

Figure 2.4: Noise spectra from a wind turbine during operation with intermittent stall (1/12th octave bands). Adapted from Madsen et al. [14]

The work of Stigwood et al. [26] suggests that high levels of NAM caused by convective amplification may be the primary cause of far-field noise impact, with OAM caused by stall only being a contributing factor. Research by Bradley [27] demonstrates that time-

dependent interference between the three direct and three indirect paths from the turbine blades can result in amplitude modulation as shown in Figure 2.5. Generally OAM is reported as occurring at the blade-pass frequency. However, in this case the further the observer is from the turbine, the smaller the path differences, leading to a reduction in modulation frequency. It is conceivable that this effect may occur in the field, but as there has been no experimental observation of a position-dependent modulation frequency, there is no evidence that it is responsible for OAM.

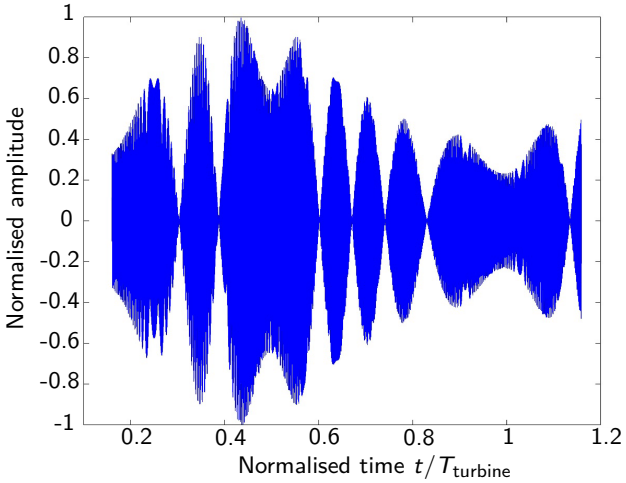

Figure 2.5: Simulation of tone modulation due to interference between direct and indirect paths. Adapted from Bradley [27]

Convective amplification is also responsible for several higher than expected noise-level observations downstream of wind turbines. It has been observed that cylindrical spreading occurs beyond a critical distance, which has estimated to be approximately 1.3km and 2.5km depending on the shape of the velocity profile for a typical wind turbine configuration [28]. This results in a reduction in noise level of 3dB per doubling of distance beyond the critical distance, instead of the 6dB reduction in the spherical spreading regime closer to the turbine.

In the literature, wind turbine noise prediction is often modelled using a combination of Paterson & Amiet's [29] model for turbulent inflow noise and Brooks et al.'s [30] model for trailing-edge noise, the latter of which will be detailed in Section 2.2 [31–33]. Angles of attack for these models are calculated by assuming that inflow is governed by a power law velocity profile as shown in Figure 2.6, and if the blade twist is unknown then it can be assumed to be the value that gives a uniform angle of attack for a flat inflow velocity profile.

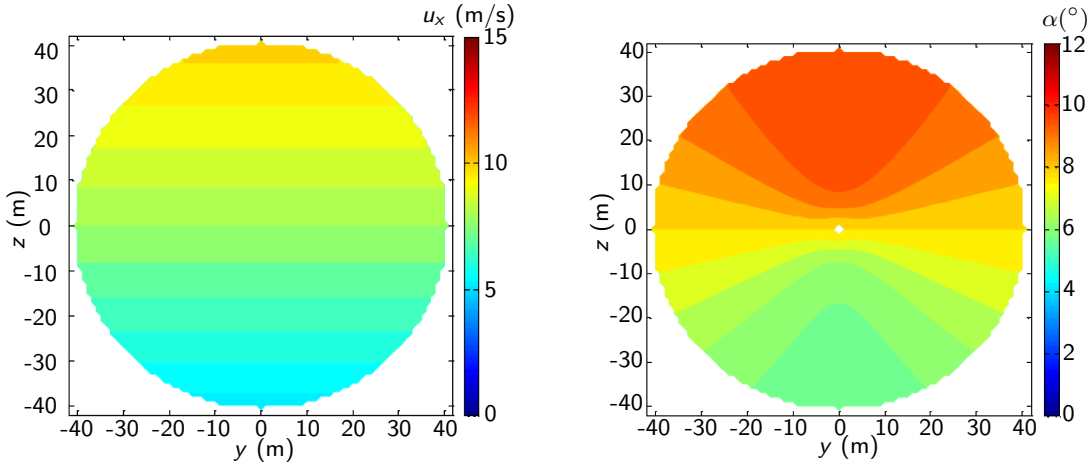

(a) Axial velocity profile

(b) Angle of attack profile

Figure 2.6: Predicted velocity profile and resulting angle of attack pattern for an 80m diameter wind turbine rotor. $U_{\text{ref}} = 8\text{m/s}$, $U_{\text{hub}} = 8\text{m/s}$, $m = 0.6$, and 0° yaw. Unit vector $\hat{\mathbf{x}}$ is the flow direction, $\hat{\mathbf{z}}$ is the vertical, and $\hat{\mathbf{y}}$ is transverse to the rotor. Adapted from Smith [34]

Under most conditions these models give good agreement with experiment, as shown by Oerlemans & Schepers [33] and Zhu et al. [35]. In the work of Oerlemans & Schepers, source localisation was carried out on a GE 2.3MW wind turbine using a phased array located on the ground in front of the turbine. This array was used to generate source maps of the apparent sound power level (Figure 2.7), which is the sound power of an equivalent monopole source. The apparent sound power distribution measured on the wind turbine indicated that the main noise source is located on the outer parts of the blades, where the relative airspeed is greatest, but not at the tip where the generation of tip vortices is the dominant flow feature [36]. The sound source at a given frequency was found to be strongest closer to the tip at higher frequencies, from 72% of tip radius at 315Hz to 90% of tip radius at 5kHz.

As also shown in Figure 2.7, Oerlemans & Schepers' prediction for the sound produced by a GE 2.3MW turbine agreed with the experimental data, with the real turbine's source map of apparent sound power level showing more axisymmetry. It was also found that significantly more noise is observed from ground level during the downstroke, which is because the trailing edge noise of the blade is radiated most strongly diagonally forward of the blade. This leads to a large portion of the noise generated during the upstroke being radiated skywards, an observation which was corroborated by Lee et al. [37]. The model does however accurately predict the source location's movement outwards towards the tip of the blade as the frequency increases.

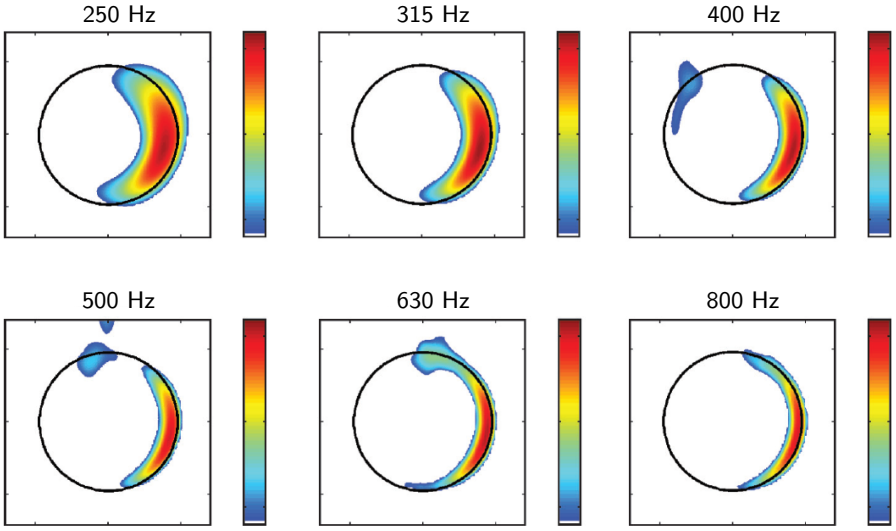

(a) Prediction

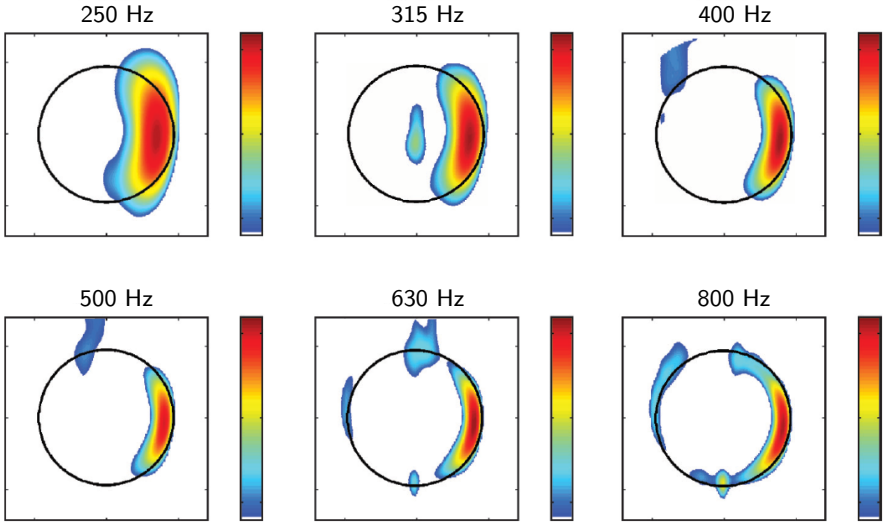

(b) Experiment

Figure 2.7: Comparison of theoretical and experimental source maps of apparent sound power level for a GE 2.3MW wind turbine. The displayed range always spans 12dB but the maxima and minima differ. Adapted from Oerelmans & Schepers [33]

Ryi et al. [38] attempted to relate the noise generated during wind tunnel tests on a scale wind turbine model with a diameter of 1.4m, and a scale airfoil model of chord 0.35m, to the noise produced by a full-scale wind turbine with a diameter of 8m. In these experiments, the sound in the wind tunnel tests was measured using microphones aligned normal to the flow direction at radii of 2.1m and 2.18m for the scale wind turbine, and 1.75m and 1.83m for the airfoil. The full-scale measurements were taken with a microphone

located on the ground, 22m behind the rotor and 18m below its axis of rotation. It was found that, with the appropriate frequency and magnitude scaling, the noise measurements from the small-scale wind turbine could predict the noise generated by the full-scale turbine up to a frequency of about 3kHz. However the predictions for the 2D scale airfoil model were not well matched to the other results, as shown in Figure 2.8.

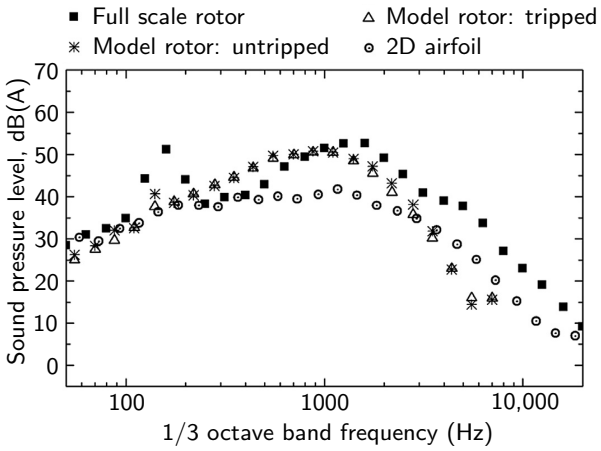

Figure 2.8: Comparison between wind tunnel data based noise estimates and noise measurements from a full scale wind turbine. Adapted from Ryi et al. [38]

Ryi et al. [38] did not discuss the reasons for their models failing to predict the correct spectrum, but some potential causes are immediately apparent. The flow fields around wind turbines are highly complex and their far-field sound spectra often vary with time. So, if an attempt is made to produce an equivalent noise source by varying the inflow parameters to a 2D airfoil, they must be well matched to the scale turbine model. Ryi et al. report that this matching took place, but provided no data to justify that it was the case. As such, it is difficult to assess the reasons why their 2D airfoil results do not agree with the scale-turbine data. In addition, the airfoil section used was characteristic of an outboard location at 75% of span and, as mentioned previously, the noise source is strongest in this location only at low frequencies, which is what is observed in the data in Figure 2.8. This shows that great care must be taken when attempting to relate the noise generated by 2D airfoil sections to the noise produced on wind turbine blades during operation.

Blade flexibility should also be taken into account when trying to relate the noise of airfoils to the noise produced by an operating wind turbine. The pitching moment generated by flow over the blades induces a blade twist that decreases the angle of attack, and this overprediction of angle of attack can lead to an overprediction in noise level [39].

Overall, the current models used in the literature are sufficient to predict wind turbine noise under standard operating conditions where stall does not occur. However these

models do not capture the impulsive noise phenomenon, as evidenced by continuing reports of its occurrence. This indicates that the source of this noise escapes capture by current modelling techniques, which aligns with the observations of the noise being short-lived and unpredictable. The current modelling techniques fail to predict this noise because they simulate conditions under which the noise was not observed. In addition, these models do not take into account the effects of transient flow non-uniformities, such as gusts or the wakes of other wind turbines, which are likely to be the cause of the observed impulsive wind turbine noise. The models also rely on airfoil noise modelling techniques which may not be adequate to properly predict the noise under stall conditions as discussed in Sections 2.2 & 2.3.

2.2 Airfoil noise

As mentioned in the previous section, one of the facets of accurate wind turbine noise prediction is the underlying method of predicting airfoil noise. Accurate airfoil noise models can be applied to the inflow conditions of the wind turbine blades and used to predict the total noise level and directivity radiated from each blade segment.

Aeroacoustic noise is often modelled as a distribution of multipole sources that are generated by the flow, each with its own mechanism and directivity function ($D(\theta)$). Monopole sources are conceptualised as the expansion and contraction of a sphere, or as a periodic inflow and outflow of fluid from a central point. In terms of aeroacoustics, monopole source distributions are created by the movement of surfaces, and their acoustic power scales according to the fourth-power of Mach number [40]. Conceptually, dipole sources are a pair of monopoles of opposite phase, or a small body undergoing oscillatory translation. Aeroacoustic dipole source distributions are created by fluctuating surface pressures, and are therefore generally the most relevant to airfoil noise. For a dipole source, acoustic power scales to the sixth-power of Mach number [40]. Conceptually, quadrupole sources are two pairs of dipoles of opposite phase and are classified into two types, lateral quadrupoles and longitudinal quadrupoles. Lateral quadrupoles take the form of a grid of four monopoles separated by a small distance, out of phase with their nearest neighbours by 180°, whereas longitudianl quadrupoles are a line of monopole sources of alternating phase. Aeroacoustically, quadrupole source distributions form due to the shear stresses in a fluid, and their acoustic power scales with the eighth-power of Mach number [40]. The directivity functions, aeroacoustic sources and scaling functions are summarised in Table 2.1 and plots of each source directivity are shown in Figure 2.9.

Table 2.1: Multipole source directivities and Mach number scaling [40]

	Monopole	**Dipole**	**Lateral quadrupole**	**Longitudinal quadrupole**
Generated by	Surface movement	Surface pressure	Shear stresses	
Directivity function $D(\theta)$	1	$\cos(\theta)$	$\cos(\theta)\sin(\theta)$	$\cos(\theta)^2$
Acoustic power scales as	M^4	M^6	M^8	

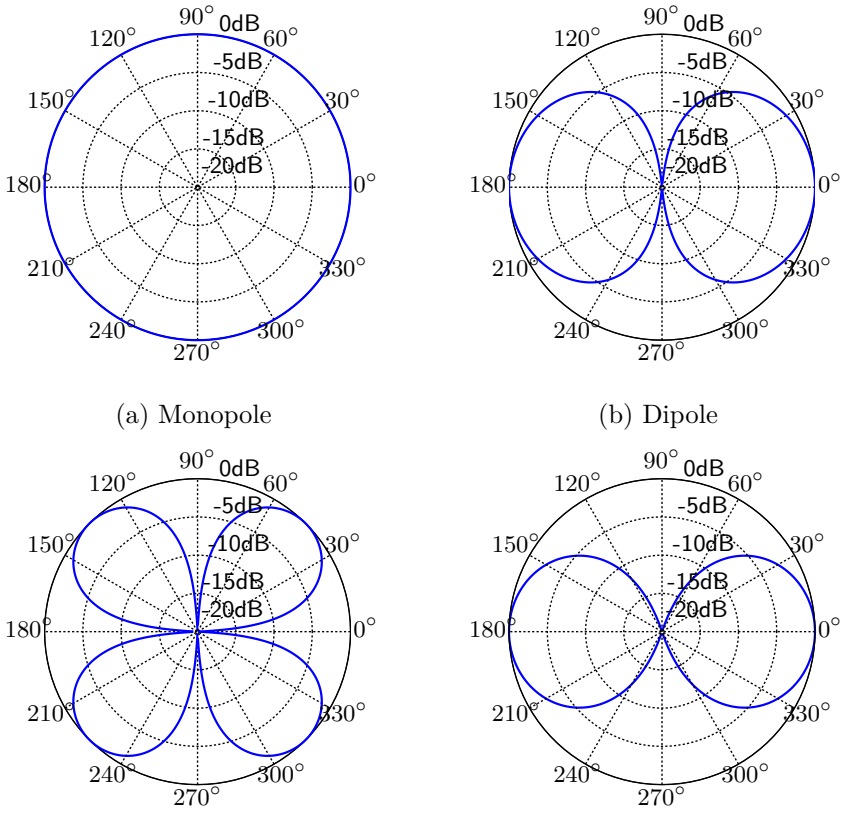

(a) Monopole

(b) Dipole

(c) Lateral quadrupole

(d) Longitudinal quadrupole

Figure 2.9: Multipole directivity functions

2.2.1 Noise prediction

Historically the prediction of airfoil noise has been based on the work of Brooks et al. [30], where the experimental data is used to derive functions that describe the shape of the airfoil noise spectrum. These shape functions can then be scaled using analytical relationships to predict the noise at a receiver. This model, known as Brooks, Pope and Marcolini (BPM)

provides a framework for modelling five major sources of airfoil self-noise:

Turbulent boundary-layer trailing edge noise: Noise generated as turbulence in the boundary layers as it is convected past the trailing edge

Laminar boundary-layer trailing edge noise: Tonal noise generated as boundary layer instabilities are convected past the trailing edge, amplified by flow-sound coupling

Separation-stall noise: Noise generated from shear and fluid-structure interaction in unsteady separated flow at high angles of attack

Trailing edge bluntness noise: Noise generated as vortices are shed from a trailing edge of non-negligible thickness

Tip vortex formation noise: Noise generated as turbulence is generated at and shed from the airfoil tip.

The experimental data detailed in the same report shows that as an airfoil stalls there is a shift in the noise spectrum towards lower frequencies. This is due to separation-stall noise begining to dominate the spectrum as the airfoil enters stall. In the model [30], the turbulent boundary layer trailing-edge and separation-stall noise are represented by

$$SPL_{\text{TBE–TE}} = 10\log_{10}\left(10^{SPL_{\text{p}}/10} + 10^{SPL_{\text{s}}/10} + 10^{SPL_{\alpha}/10}\right) \tag{2.4}$$

where SPL_{p}, SPL_{s} and SPL_{α} are the contributions from the pressure-side boundary layer, suction-side boundary layer, and separated flow, respectively. The boundary layer terms are given by [30]

$$SPL_{\text{i}} = 10\log_{10}\left(\frac{\delta_{\text{i}}^{*} M^{5} L_{\text{sp}}}{r_{\text{e}}^{2}}\right) + A\left(\frac{St_{\text{i}}}{St_{1}}\right) + (K_1 - 3),\ \text{i} = \text{p}, \text{s} \tag{2.5}$$

where δ_{i} is the boundary layer displacement thickness, L_{sp} is the airfoil span, M is the Mach number, r_{e} is the distance from the trailing edge to the observer, $St_{\text{i}} = \frac{f\delta_{\text{i}}^{*}}{U_{\infty}}$ and St_1, A and K_1 are empirically derived functions that estimate the peak frequency, shape and amplitude of the spectrum respectively. As the experiment was conducted in an open jet wind tunnel the value α_{t} is used for the angle of attack, which is a true angle of attack corrected for jet deflection. The stall angle, $\alpha_{\text{t}})_{\text{stall}}$, is the minimum value between 12.5°and the angle at which the peak of the shape function K_2 (which is an equivalent function to K_1) occurs.

The separated flow term in Equation 2.4 is given by

$$SPL_\alpha = 10\log_{10}\left(\frac{\delta_s^* M^5 L_{sp}}{r_e^2}\right) + B\left(\frac{St_s}{St_2}\right) + K_2 \tag{2.6}$$

for $\alpha_t < (\alpha_t)_{stall}$, where B is an equivalent function to A; and

$$SPL_\alpha = 10\log_{10}\left(\frac{\delta_s^* M^5 L_{sp}}{r_e^2}\right) + A'\left(\frac{St_s}{St_2}\right) + K_2 \tag{2.7}$$

for $\alpha_t \geq (\alpha_t)_{stall}$, where A' is the equivalent A for the stall equivalent Reynolds number based on chord $Re'_c = 3 \times Re_c$. This approach is still used in many trailing-edge noise predictions, despite appearing to have a few short-comings. The data in Brooks et al. [30] was presented in 1/3rd octave bands which, in the 200Hz to 1000Hz range being investigated, have a bandwidth of 40Hz to 230Hz. Presenting the data in this manner reduces the relative amplitude of any narrow spectral peaks to the surrounding data, making them difficult or impossible to discern compared to an analysis using smaller frequency bins. The equations used to generate the shape of the spectrum are based on this low resolution data, and therefore any predictive curve that they produce will be similarly limited, having a poor frequency resolution due to using a general spectrum shape based on 1/3rd octave data.

Another model, known as the TNO-Blake model, developed by Parchen [41] based on the work of Blake [42], predicts the far-field noise using the data from the turbulent boundary layer. The far-field pressure spectrum is given by [41] as

$$S(\omega) = \frac{L_{sp}}{4\pi r_e^2}\int_{-\infty}^{\infty}\frac{\omega}{a_\infty \mathrm{k}_1}\Phi_p(\mathbf{k},\omega)\Big|_{k_3=0}\mathrm{dk}_1 \tag{2.8}$$

where $\mathbf{k}$ is the vector of surface pressure wavenumbers and a_∞ is the freestream speed of sound. Here the wavenumber-frequency surface-pressure spectrum is given by

$$\Phi_p(\mathbf{k},\omega) = 4\rho_0^2\frac{k_1^2}{k_1^2+k_3^2}\int_0^\infty L_2(y_2)\overline{u_2'^2}\left(\frac{\mathrm{d}\overline{u}_1}{\mathrm{d}y_2}\right)^2\Phi_{22}(\mathbf{k},\omega)\Phi_m\left[\omega - u_c k_1\right]\mathrm{e}^{-2|\mathbf{k}|y_2}\mathrm{d}y_2 \tag{2.9}$$

where y_2 is the spanwise coordinate of the source location $\mathbf{y}$, L_2 is the vertical integral length scale, $\overline{u_2'^2}$ is a Reynolds stress component, $\overline{u}_1$ is the chordwise component of the mean velocity $\overline{\mathbf{u}}$, u_c is the convection velocity, Φ_m is a moving axis spectrum, and Φ_{22} is the spectrum of vertical velocity fluctuations. The use of the fluctuations in velocity and surface pressure as the main input to trailing-edge noise predictions gives the TNO-Blake model versatility. The data can be obtained from detailed LES computational simulations, simpler computational methods such as RANS, or prediction codes such as XFOIL coupled

with empirical relationships [43–47].

Prediction of airfoil noise can also be done by applying computational aeroacoustics (CAA) methods to computational fluid dynamics models, and this takes two main forms. Direct computational aeroacoustics solves the flow field and acoustic pressure field simultaneously, and therefore gives high-fidelity predictions provided that the simulation mesh is fine enough to both capture all of the noise sources and propagate the sound. This is very computationally intensive, especially for far-field predictions where a fine mesh capable of propagating short wavelength perturbations may have to extend tens of characteristic lengths. It also requires a sufficiently-large dynamic range to capture both the fluid and sound pressures, as sound-pressure fluctuations are usually many orders of magnitude smaller than fluid pressure fluctuations. However in some cases, such as when there is a large amount of flow-sound coupling, this approach may be necessary to produce accurate results. Alternatively, the flow field can be solved at high fidelity only in the sound source regions, and then the acoustic pressure can be propagated from these sound sources separately. This is the approach used by the aeroacoustic analogies, the TNO-Blake model, as well as the acoustic/viscous splitting and linearised Euler methods and the acoustic perturbation and non-linear disturbance equations.

In the acoustic/viscous splitting method [48], and approaches that use the non-linear disturbance equations [49] or acoustic perturbation equations [50], the problem is broken into seperately solved hydrodynamic and acoustic terms solved on separate computational grids. In the acoustic/viscous splitting method the hydrodynamic terms are incompressible and the acoustic terms account for compressibility effects, making the approach suitable only for low Mach numbers where mean compressibility is negligible. Like many computational aeroacoustic schemes these methods cannot account for acoustic feedback effects affecting the flow-field, as the hydrodynamic field is solved first and the results of the simulation are used to force the acoustic simulation.

Similar to the numerical methods mentioned above, linearised Euler methods involve propagating the sound sources by numerically solving a set of linearised partial differential equations for invisicid flow [51, 52]. The two-dimensional linearised Euler equations are given by

$$\frac{\partial \mathbf{U}}{\partial t} + \frac{\partial \mathbf{E}_{\mathrm{i}}}{\partial x_{\mathrm{i}}} + \mathbf{H} = \mathbf{S}, \ \mathrm{i} = 1, 2, 3 \tag{2.10}$$

where x_{i} is the ith component of the observer location $\mathbf{x}$ and the $\mathbf{U}$ and $\mathbf{E_i}$ vectors are

given by

$$\mathbf{U} = \begin{pmatrix} \rho' \\ \overline{\rho} u_1' \\ \overline{\rho} u_2' \\ p' \end{pmatrix} \tag{2.11}$$

and

$$\mathbf{E}_\mathrm{i} = \begin{pmatrix} \rho' \overline{u}_\mathrm{i} + \overline{\rho} u_\mathrm{i}' \\ \overline{u}_\mathrm{i} \overline{\rho} u_1' + \delta_{1\mathrm{i}} p' \\ \overline{u}_\mathrm{i} \overline{\rho} u_2' + \delta_{2\mathrm{i}} p' \\ \overline{u}_\mathrm{i} p' + \gamma \overline{p} u_\mathrm{i}' \end{pmatrix}. \tag{2.12}$$

Here $\overline{u_\mathrm{i}}$ and u_i' are the ith components of the mean and fluctuating components of the fluid velocity, $\overline{\mathbf{u}}$ and $\mathbf{u}'$, respectively. The term γ is the ratio of specific heats, $\mathbf{H}$ describes the gradient of the mean flow and is zero if it is uniform, and $\mathbf{S}$ contains the source terms. The main advantage of these methods that solve for the acoustic field numerically is that, since the propagation of the sound is solved numerically, it is able to take scattering and other propagation effects into account [53]. Integral methods, or aeroacoustic analogies assume free-field propagation and cannot account for these effects.

The most commonly used aeroacoustic analogies stem from the work of Lighthill regarding the sound generation by a free flow, modelling the distribution of quadrupole sources generated by turbulent stresses [54, 55]. This work was then extended by Curle who took surfaces into account, modelling the surface dipole distribution generated by unsteady surface pressures [56]. Ffowcs Williams and Hawkings extended this analogy further to moving surfaces, adding a monopolar thickness term. The Ffowcs Williams-Hawking (FWH) equations have become a commonly-used method for indirect computational aeroacoustics in areas such as helicopter rotors and airframes as well as being implemented in some commericial CFD packages such as ANSYS Fluent [57–62].

One major advantage of the FWH method is greater freedom in the selection of the control surface. Ordinarily the control surface is the physical surface within the simulation domain, for example the surface of an airfoil. It is this hard surface that the surface pressures and thickness effects are calculated from, before the quadrupolar term is calculated for the rest of the domain. Using a permeable control surface that does not coincide with the airfoil surface, captures all of the sound sources within its boundaries in its thickness and loading terms. An example control surface is shown in Figure 2.10, where the control surface S, which has a velocity given by $\mathbf{v}$, is the boundary between regions 1 and 2 of the total volume V, which is bounded by the surface Σ. The vectors $\mathbf{l}$ and $\mathbf{n}$ are

the surface normals to the surfaces Σ and S respectively.

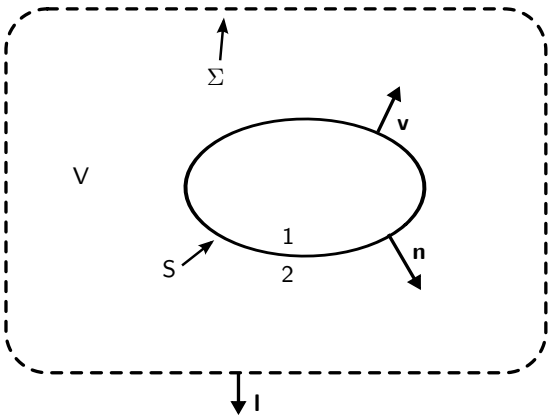

Figure 2.10: Schematic of a Ffowcs Williams-Hawking control surface. Adapted from Zinoviev [63]

Therefore if the control surface is placed outside of the region where the quadrupole source is strongest, the effects of this noise source can be more easily taken into account, provided that the simulation retains sufficient fidelity at the control surface boundary. If quadrupolar effects are negligible outside of the boundary, then the volume integral term can be dropped from the equations, which reduces the computational cost of the calculation. However in many situations quadrupolar effects are already small, as they scale most strongly with Mach number, so consequently the monopole and dipole sources generally dominate the total noise in subsonic cases. A widely-used solution of the FWH equations is Farassat's Formulation 1A, which neglects the quadrupole term and is detailed in Equations (2.13) to (2.15) [64, 65]. In Farassat's 1A formulation the total pressure fluctuation at an observation point $\mathbf{x}$ and time t is given by [64]

$$p'(\mathbf{x},t) = p'_{\mathrm{T}}(\mathbf{x},t) + p'_{\mathrm{L}}(\mathbf{x},t), \tag{2.13}$$

where p' is the fluctuating component of the far-field pressure and the subscripts T and L indicate the thickness (monopole) and loading (dipole) terms respectively. The thickness and loading terms are given by

$$4\pi p'_{\mathrm{T}}(\mathbf{x},t) = \int_{\mathrm{S}} \left[\frac{\rho_0(\dot{v}_n + v_{\dot{n}})}{\|\mathbf{r}\||1-M_r|^2}\right]_{\mathrm{ret}} \mathrm{dS} + \int_{\mathrm{S}} \left[\frac{\rho_0 v_n(\|\mathbf{r}\|\dot{M}_r + a_\infty M_r - a_\infty M^2}{\|\mathbf{r}\|^2|1-M_r|^3}\right]_{\mathrm{ret}} \mathrm{dS}, \tag{2.14}$$

and

$$4\pi p'_{\mathrm{L}}(\mathbf{x},t) = \frac{1}{a_\infty}\int_{\mathrm{S}}\left[\frac{\dot{l}_r}{\|\mathbf{r}\||1-M_r|^2}\right]_{\mathrm{ret}}\mathrm{dS} + \int_{\mathrm{S}}\left[\frac{l_r - l_M}{\|\mathbf{r}\||1-M_r|^2}\right]_{\mathrm{ret}}\mathrm{dS} + \int_{\mathrm{S}}\left[\frac{l_r(\|\mathbf{r}\|\dot{M}_r + a_\infty M_r - a_\infty M^2}{\|\mathbf{r}\|^2|1-M_r|^3}\right]_{\mathrm{ret}}\mathrm{dS}, \quad (2.15)$$

where $\mathbf{r}$ is the vector connecting the observation ($\mathbf{x}$) and source ($\mathbf{y}$) points, and ρ_0 is the density of the fluid at rest. The subscripts r and n denote a dot product with the vectors $\mathbf{r}$ and $\mathbf{n}$ respectively, and the integral is performed over the control surface S. The subscript "ret" indicates that for a given time at the observation point, the sound received will have been generated at some retarded time $\tau = t - \mathbf{r}/a_\infty$.

While the FWH technique can very accurately model aeroacoustic noise, it is not without its disadvantages. High-fidelity computational models are required to produce the flow field data, which can result in a very large computational cost. In order to properly resolve the acoustic field inside the control surface the mesh must be fine enough for acoustic waves to propagate, which necessitates a grid with multiple nodes per wavelength. The simulation time step must also be very small to allow the acoustic field in this region to be properly resolved which also contributes to the size of the computational cost.

2.3 Static stall

As the angle of attack of an airfoil is increased, the adverse pressure gradient along the chord eventually grows too large for the flow to overcome and the boundary layer begins to separate. As the proportion of the airfoil affected increases there is a substantial loss of lift, which is the main indicator of the condition known as stall. Stall results in a large amount of vorticity impinging on the airfoil surface and therefore leads to increased noise production. The length scale of this vorticity is larger than when not under stall conditions leading to a shift in the airfoil's noise to lower frequencies.

2.3.1 Noise

As with most airfoil self-noise, the unsteady fluctuations in the flow field interacting with the surface of the airfoil is the main source of noise during stall [30]. While there is some contribution to the overall noise from the turbulence in the separated flow, this term scales with M^8 compared to the M^6 scaling of the surface pressure contributions [66]. Under conditions where the noise due to stall (i.e., wind farm noise) the quadrupole term is usually neglected as the Mach number is low enough such that the dipole term dominates.

However, care should be taken as, in some systems, the quadrupole term of a flow can begin to dominate at Mach numbers as low as $M = 0.5$ [67].

As discussed in Sections 2.1 & 2.2, most modern wind turbine noise prediction methods use a semi-empirical noise model developed by Brooks et al. [30] for the prediction of both trailing-edge and separation-stall noise. This model is often suitable for the level of accuracy required by the wind turbine industry, however, the 1/3rd-octave band spectra it generates are unsuitable for identifying any tones or other narrow-band spectral features that may be present. In addition, it focuses on the 12% thick NACA 0012 airfoil profile, which is not representative of the thickness of a modern wind turbine airfoil section, which tends to be closer to 20% thick. As mentioned in Section 2.2, separation noise is taken into account by the turbulent boundary-layer trailing-edge noise model shown in Equation (2.4). However in the model of Brooks et al., as the airfoil moves further past the stall angle and the airfoil enters the deep stall state, the model underpredicts the noise level by approximately 10dB, as shown in Figure 2.11e & 2.11f.

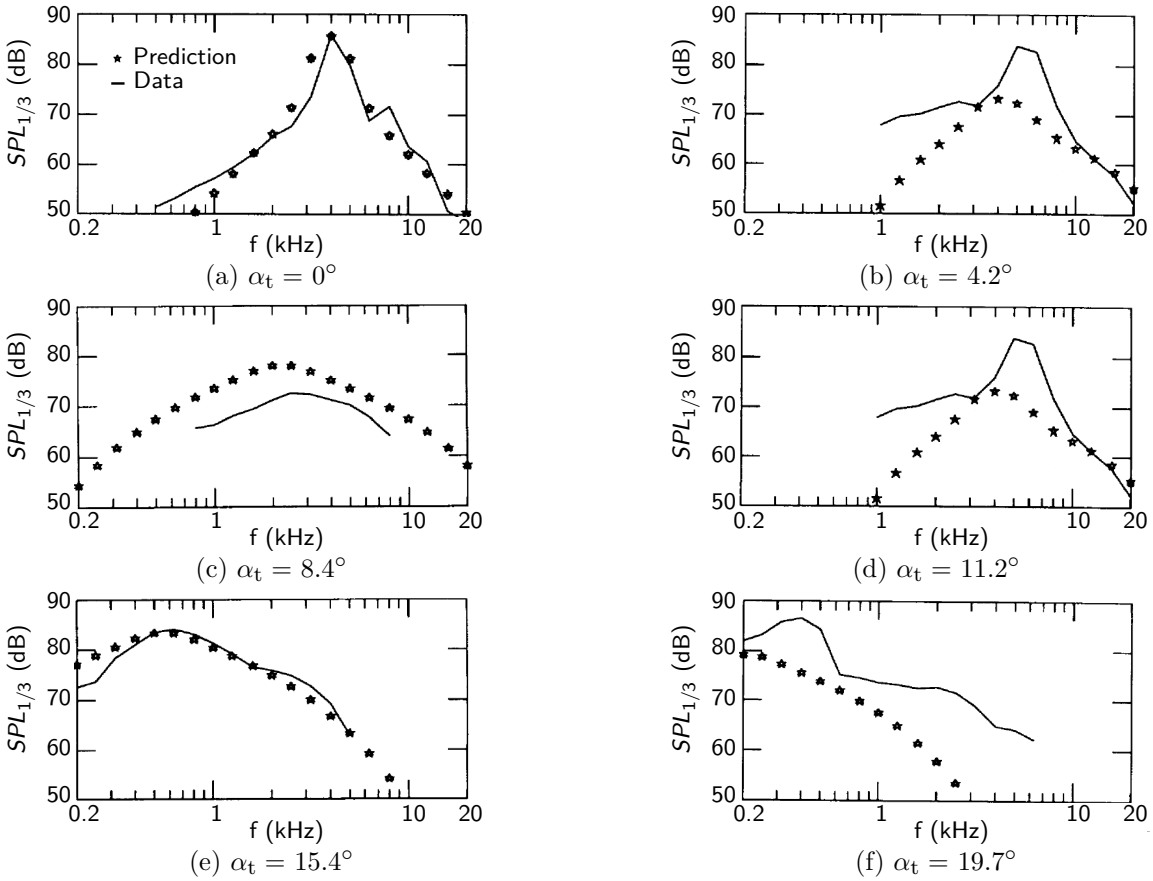

(a) $\alpha_t = 0°$ (b) $\alpha_t = 4.2°$

(c) $\alpha_t = 8.4°$ (d) $\alpha_t = 11.2°$

(e) $\alpha_t = 15.4°$ (f) $\alpha_t = 19.7°$

Figure 2.11: Measured self-noise spectrum of an untripped NACA 0012 airfoil (line) compared with predicted sound levels for each source, as well as the overall predicted sound level. Adapted from Brooks et al. [30]

More recently another stall-noise model has been developed by Moreau et al. [68] based on an experimental campaign focusing on the NACA 0012 and a flat plate. The experimental results of Moreau et al., shown in Figure 2.12, show a noise regime refered to as “light stall" which occurs at the onset of stall before the large, narrow peaks associated with bluff body-like vortex shedding behaviour (referred to in that work as “deep stall") have formed. The light-stall regime is characterised by the formation of several low frequency peaks that are wider and smaller in amplitude than those observed during deep stall. The source of this noise was not conclusively determined in that work.

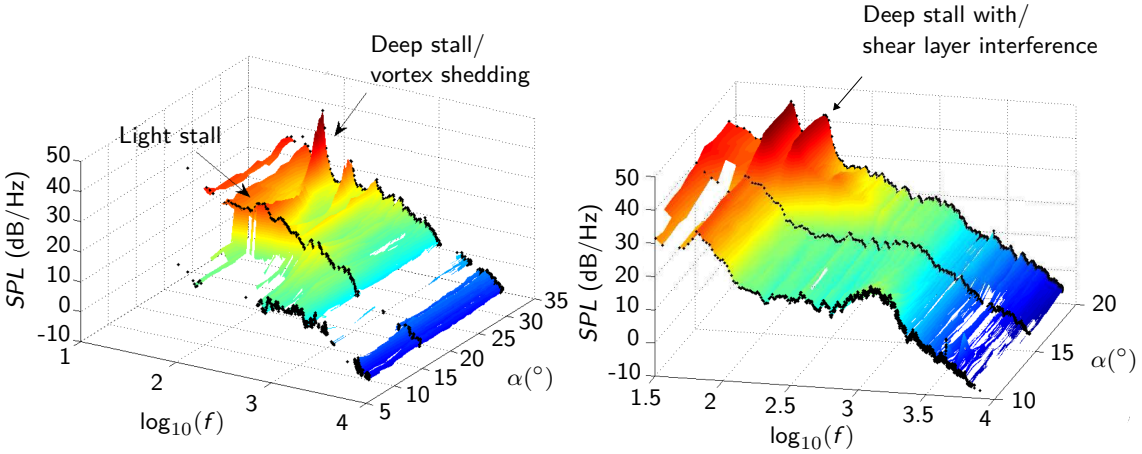

(a) Small span, wide jet setup

(b) High span, narrow jet setup

Figure 2.12: NACA 0012 experimental self-noise measurements.
Adapted from Moreau et al. [68]

The model used by Moreau et al. [68] can produce more narrowband spectra, and is capable of reproducing peaks in the data that the model of Brooks et al. [30] cannot. The Moreau et al. model uses the wall pressure spectra taken at the airfoil surface to predict the generated noise, as shown in Equation (2.16), thereby increasing the model fidelity but requiring the acquisition of more experimental data. The spectra are calculated by the equation

$$S_{\mathrm{pp}}(\mathbf{x},\omega) = \left(\frac{k_1 L\cos(\phi)\sin(\theta)}{4\pi r_{\mathrm{e}}}\right)^2 \int_{-\infty}^{\infty} \mathrm{sinc}^2\left[(k_2 - k_1\sin(\phi)\sin(\theta))\frac{L}{2}\right] \Phi_{\mathrm{FF}}(k_2)\mathrm{d}k_2, \quad (2.16)$$

where where L is the airfoil span, $k_1 = f/c_0$ is the acoustic wavenumber, and ϕ and θ are the angles between the source and observation points. The Φ_{FF} term is the spanwise wavenumber spectrum given by

$$\Phi_{\mathrm{FF}}(k_2) = \frac{1}{2\pi}\int_{-\infty}^{\infty} R_{\mathrm{FF}}(\eta)\mathrm{e}^{\mathrm{i}k_2\eta}\mathrm{d}\eta, \quad (2.17)$$

where η is the spanwise distance between sources, k_2 is the spanwise wavenumber and the spanwise unsteady lift correlation is given by

$$R_{\mathrm{FF}}(\eta) = \langle F(\omega, y_2), F(\omega, y_2 + \eta) \rangle \,, \tag{2.18}$$

where $F(\omega, y_2)$ is the chord-wise fluctuating lift spectrum per unit span.

Much like the work of Brooks et al. [30], the research by Moreau et al. [68] was focused on the common NACA 0012 airfoil profile and no data has been collected on the noise of thicker airfoils under stall conditions. The experimental results were also heavily affected by interaction between the airfoil and the shear layer of the jet. This led to the production of a single large spectral peak through the entire pre-stall regime and none of the more numerous peaks observed at any point (Figure 2.12b). As the angle was increased into the deep-stall regime this peak bifurcated and the spectrum began to take on a shape more like that seen in the deep stall regime. Because the stall noise model of Moreau et al. [68] has only been validated in the deep-stall regime, it is currently not known whether it is valid under light stall conditions.

It is also unknown how the airfoil section affects the characteristics of the noise generated at stall. Differences in surface pressure distributions based on airfoil section have been well documented, and these imply that the noise produced will also differ. Thinner airfoils (low thickness-to-chord ratio) are expected to stall more abruptly, with thick airfoils (large thickness-to-chord ratio) undergoing a more gradual flow separation [69]. However this is not always the case as the stall behaviour of an airfoil profile can vary dramatically with Reynolds number and turbulence intensity. The NACA 0021 airfoil, for example, exhibits a very abrupt stall behaviour at low Reynolds numbers and turbulence intensity but can exhibit a gradual reduction in lift at higher turbulence intensities as shown in Figure 2.13 [70]. Sheldahl et al. [71] observed a shift in the stall behaviour of a NACA 0012 airfoil with Reynolds number, from a more gradual loss of lift for $Re_c = 36,000$ to a sharper drop at $Re_c = 176,000$. It was also observed that for a range of airfoil sections tested at a Reynolds number of 70,000, the post-stall behaviour showed greater slopes as the thickness increases (Figure 2.14).

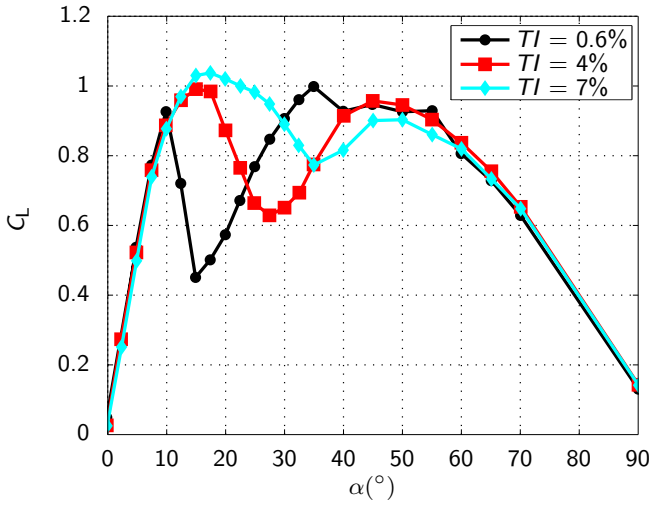

Figure 2.13: Measured lift coefficients for a NACA 0021 at several turbulence intensities and a Reynolds number of 70,000. Adapted from Swalwell et al. [70]

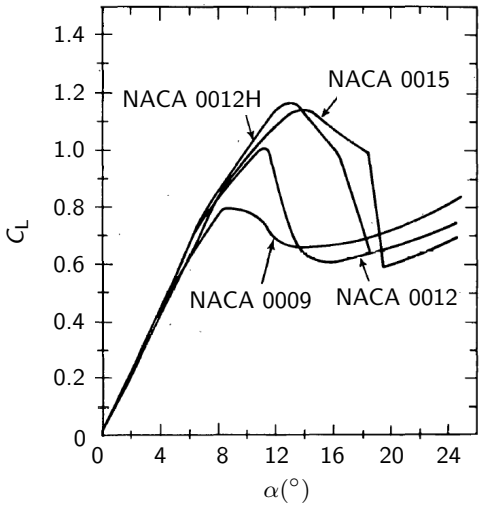

Figure 2.14: Lift coefficients for several airfoil profiles at a Reynolds number of 70,000. Adapted from Sheldahl et al. [71]. Used courtesy of Sandia National Laboratories

2.4 Dynamic stall

While Section 2.3 focused on stall under steady-state conditions, it is not the only process through which stall occurs. If an airfoil experiences a rapid enough change in angle of attack the flow around it will instead undergo dynamic stall, which is characterised by the shedding of several large vortices, as shown in Figure 2.15, before the flow settles into a vortex-shedding behaviour similar to that of steady-state stall.

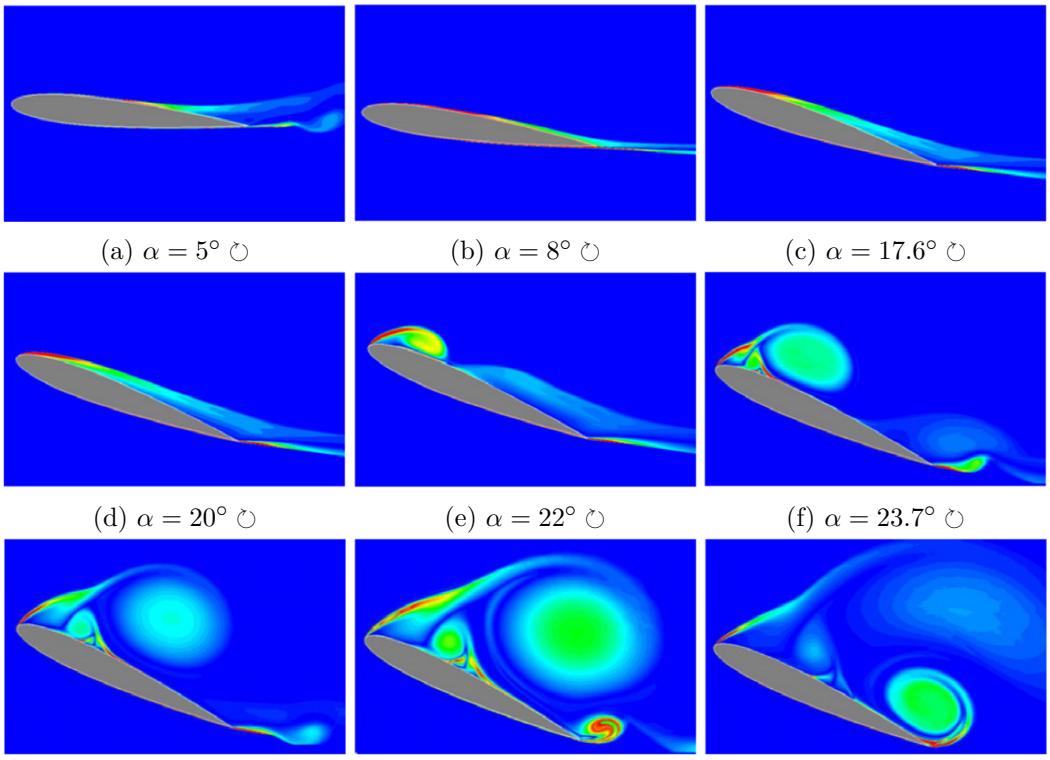

(a) $\alpha = 5°$ ↻ (b) $\alpha = 8°$ ↻ (c) $\alpha = 17.6°$ ↻

(d) $\alpha = 20°$ ↻ (e) $\alpha = 22°$ ↻ (f) $\alpha = 23.7°$ ↻

(g) $\alpha = 24.7°$ ↻ (h) $\alpha = 25°$ (i) $\alpha = 24.7°$ ↺

Figure 2.15: Turbulent intensity field of a NACA 0012 airfoil undergoing dynamic stall, $Re \approx 10^5$, $\kappa = 0.15$. Adapted from Wang et al. [72]

The characteristics of dynamic stall primarily depend on the Reynolds number and the reduced frequency (κ)

$$\kappa = \frac{\dot{\alpha} c}{2 U_\infty}, \tag{2.19}$$

where $\dot{\alpha}$ is the rate of change of angle of attack in radians/second, c is the airfoil chord and U_∞ is the free-stream velocity. A reduced frequency of $\kappa = 0.02$ is generally considered to be the boundary between quasi-steady and unsteady stall behaviour, however it has been shown that an increase in lift and delayed stall are present even at these low reduced frequencies [73, 74]. In general, as shown in Figure 2.16, increasing the reduced frequency will increase the delay in stall angle as well as increasing the maximum lift coefficient of the airfoil. Due to their large chord and higher velocity, the outboard segments of a horizontal-axis wind turbine blade are more likely to experience steady-state or quasi-steady stall. However, on inboard segments where the chord is larger and the velocity is lower, dynamic stall is more likely to occur [75, 76]. It has been found that the negative slope of the lift curve during dynamic stall is greater at higher reduced frequencies, and while thicker airfoils produce a more rapid loss of lift, this effect decreases with reduced frequency [77].

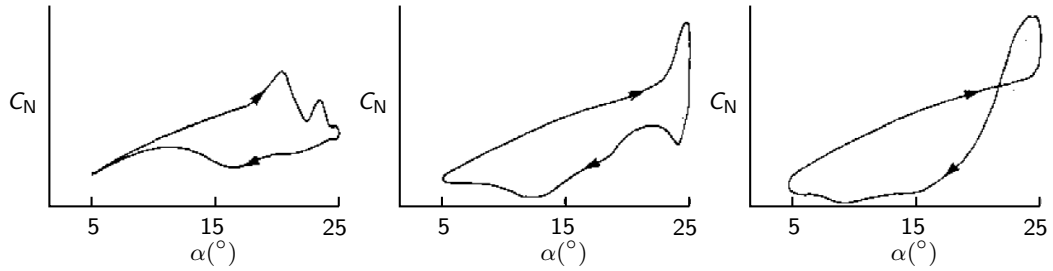

(a) $\kappa = 0.05$ (b) $\kappa = 0.15$ (c) $\kappa = 0.25$

Figure 2.16: Effect of reduced frequency, κ, on the change in normal force coefficient, C_N, of a NACA 0012 airfoil undergoing dynamic stall at a Reynolds number of 2.5×10^6. Adapted from McCroskey et al. [78]

2.4.1 Noise during dynamic stall

A computational study by Nagarajan & Lele [79] and an analytical study by Manela [80] of the noise generated by a rapidly-pitching airfoil predicted a noise signature dominated by harmonic tones at the pitching frequency. These tones are due to the periodic change in angle of attack leading to a periodic change in noise and not due to the noise produced by the formation of the dynamic stall vortex. In both cases the time series of acoustic pressure was reported, with the CFD modelling of Nagarajan & Lele showing a single dominating pulse in the noise signature and the analytical approach of Manela predicting a pulse followed by some ringing. To date, neither of these studies have been verified experimentally, nor is there is any experimental data about the noise generated by a pitching airfoil in the literature. This may be because the time scales of the events under laboratory conditions are generally very small, and this makes observation difficult. For example, in the $\kappa = 0.25$ case from Figure 2.16, a 1.22m chord is used and this results in a required frequency of 1.94Hz or a period of 0.52 seconds. The time for the dynamic stall vortex to be generated and shed is a fraction of this time, which makes attempting to analyse any noise generated problematic. In smaller experimental facilities, where a smaller chord must be used, the required time-scales to achieve a given reduced frequency will decrease even further.

2.4.2 Vortex generation during dynamic stall

Another factor in the airfoil noise during a dynamic stall event is the effect of the generation and shedding of a large amount of vorticity on propagation. PIV visualisation of dynamic stall on NACA 0015 airfoils was reported by Gharali & Johnson [81] and Yu et al. [82], which showed that the circulation of the leading-edge vortex increased approximately linearly until after the angle of maximum lift (shown in Figure 2.17). Beyond this point the

circulation of the vortex decreases as the vortex detaches, and measurements by Ferreira et al. [83] showed that after detachment the vortex circulation continues to decrease linearly as it is convected by the wake (Figure 2.18).

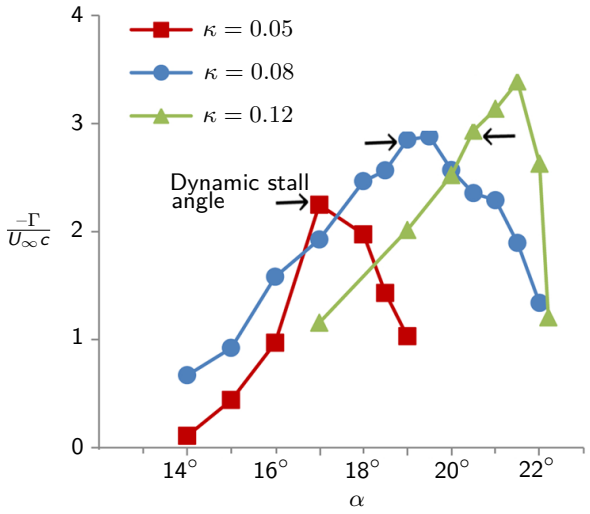

Figure 2.17: Circulation, normalised by chord and freestream velocity, of leading dynamic stall vortices during formation for several reduced frequencies, κ, as a function of angle of attack. Adapted from Gharali & Johnson [81]

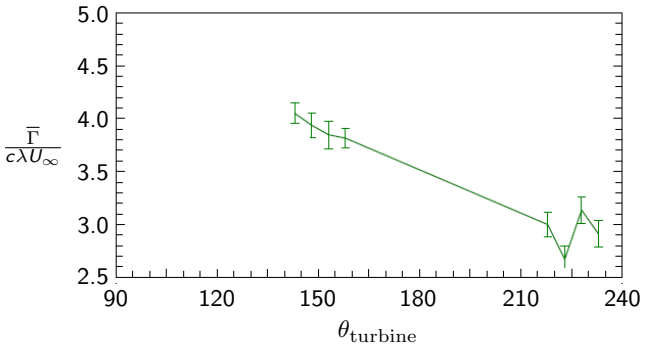

Figure 2.18: Change of mean circulation of dynamic stall vortices shed from a vertical axis wind turbine with rotor angle θ_{turbine}. Mean circulation is normalised by chord, c, tip-speed ratio, λ, and freestream velocity, U_∞. Adapted from Ferreira et al. [83]

Formation of a dynamic stall vortex will produce its own noise signature, which is difficult to quantify as previously discussed. However once a dynamic stall vortex is shed into the wake a deep-stall noise regime will establish and the airfoil will return to steady-state noise production. The presence of the vortex in the wake will scatter and refract this noise, leading to time-varying changes in the overall directivity as the vortex convects downstream and dissipates. This differentiates the noise due to the shedding of the dynamic

stall vortex from the effect that the vortex has on noise propagation, which is discussed in Section 2.5.

2.5 Vorticies

As well as shed vorticity contributing to the self-noise of airfoils, the vortices themselves also have an effect. Free vortices both generate sound and affect the propagation of sound from other sources such as the trailing edge. Sound with a short wavelength compared to the turbulence length scale is refracted due to variations in the speed of sound, but if the wavelength is long, interaction with turbulence will result in a secondary scattered sound field instead [84].

2.5.1 Structure

Most free vortices are characterised by a viscous, low pressure core surrounded by an approximately irrotational flow. This results in a tangential velocity profile that increases with radius within the core to some peak, then decays outside of the core. There are a number of different models in the literature to describe the tangential velocity profile, the simplest of which is the Rankine model given by [85]

$$\overline{u}_\theta = \begin{cases} \overline{r}, \overline{r} \leq 1 \\ \frac{1}{\overline{r}}, \overline{r} > 1 \end{cases}, \tag{2.20}$$

where $\overline{u}_\theta = (u_\theta 2\pi r_\mathrm{v})/\Gamma_\infty$, $\overline{r} = r/r_\mathrm{c}$, u_θ is the tangential velocity, Γ_∞ is the circulation outside the vortex core and r_c is the core radius. However the Lamb-Oseen vortex [86]

$$\overline{V}_\theta = \frac{1 - \mathrm{e}^{-1.2526\overline{r}^2}}{\overline{r}} \tag{2.21}$$

and Vatistas vortex [87]

$$\overline{V}_\theta = \frac{\overline{r}}{\left(\overline{r}^{2n} + 1\right)^{1/n}} \tag{2.22}$$

models (shown in Figure 2.19) are often used as they provide a better model of real vortices, while remaining relatively simple. The Vatistas model uses the tuning parameter, n, in order to achieve a more accurate fit to an experimental vortex and collapses to the Rankine model as $n \to \infty$.

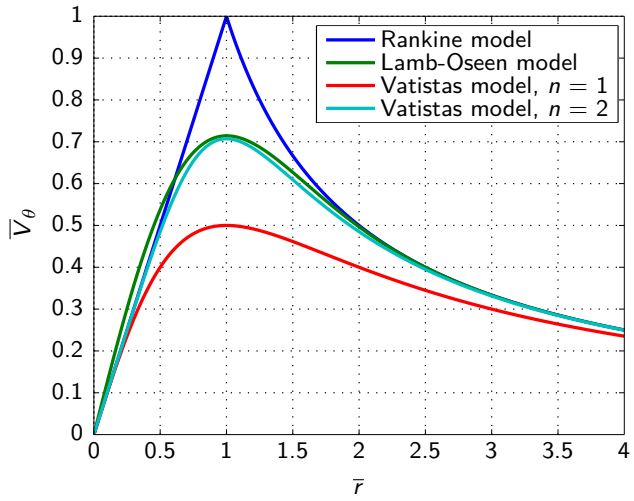

Figure 2.19: Tangential velocity profiles for the Rankine, Lamb-Oseen and Vatistas vortex models

The Proctor-Winckelmans model can more accurately model the wingtip vortex of an aircraft, but requires three tuning parameters to be set correctly in order to do so [85]. However, in another study by Bhagwat & Leishman [88], the Lamb-Oseen model was found to accurately model the tip vortices of a helicopter rotor, which corroborates a study by Vatistas et al. [87] that indicates that the Vatistas model with $n = 2$ accurately models the vortices from multiple experiments in the literature. This indicates that the appropriate vortex model can depend on the context of the vortex being modelled.

When the flow is isentropic is the pressure and density inside the vortex are related by

$$\frac{p}{p_\infty} = \left(\frac{\rho}{\rho_\infty}\right)^\gamma, \tag{2.23}$$

where γ is the ratio of specific heats, and the p_∞ and ρ_∞ are the ambient fluid pressure and density respectively. The density and velocity fields can then be related by

$$\int \frac{u_\theta^2}{r} \mathrm{d}r = \frac{\gamma p_\infty}{(\gamma - 1)\rho_\infty^\gamma} \rho^{\gamma - 1} + \text{constant}, \tag{2.24}$$

but, as shown in Bagai & Leishman [89], the Rankine vortex model underpredicts the density in the core.

2.5.2 Noise production

The primary method of noise production from vorticity is by inducing pressure fluctuations at a solid surface, which then radiate as sound as discussed in Section 2.2. However free vortical flows also generate noise due to shear stresses. This noise, described by Lighthill's

acoustic analogy, is the quadrupolar sound neglected in the equations in Section 2.2 [54]. The density perturbation observed at a location $\mathbf{x}$ due to flow in a volume V is given by

$$\rho(\mathbf{x}) - \rho_\infty = \frac{1}{4\pi a_\infty^2} \frac{\partial^2}{\partial x_\mathrm{i} \partial x_\mathrm{j}} \int_\mathrm{V} \frac{\mathrm{T_{ij}}\left(\mathbf{y}, t - \frac{|\mathbf{x}-\mathbf{y}|}{a_\infty}\right)}{|\mathbf{x}-\mathbf{y}|} \mathrm{d}\mathbf{y}, \tag{2.25}$$

where $\mathbf{y}$ is the source location, a_∞ is the speed of sound, and the Lighthill stress tensor components T_ij are given by

$$T_\mathrm{ij} = \rho v_\mathrm{i} v_\mathrm{j} + p_\mathrm{ij} - a_0^2 \rho \delta_\mathrm{ij}, \tag{2.26}$$

where v_i and v_j are the ith and jth components respectively of the fluid velocity $\mathbf{v}$. The tensor components p_ij are given by,

$$p_\mathrm{ij} = p\delta_\mathrm{ij} + \mu \left\{ -\frac{\partial v_\mathrm{i}}{\partial x_\mathrm{j}} - \frac{\partial v_\mathrm{j}}{\partial x_\mathrm{i}} + \frac{2}{3}\left(\frac{\partial v_\mathrm{k}}{\partial x_\mathrm{k}}\right) \right\}, \tag{2.27}$$

where μ is the viscosity and p is the static pressure. As mentioned in Section 2.2 this noise is generally small compared to noise generated at surfaces for low Mach numbers, and so Lighthill's analogy is mostly used to describe the sound generated by high-speed jets [90, 91].

2.5.3 Sound scattering

As the noise production is low under subsonic conditions, the main effect on sound due to the presence of free vorticity is scattering by turbulence, convective and refraction effects. Refraction occurs when local variations in the speed of sound result in a change of the angle of propagation of a sound wave. Refraction is only considered when in the high-frequency limit, where the sound waves can be approximated as rays compared to the size of the vortices. Using numerical ray tracing techniques, these acoustic rays can then be propagated through the vortex to show the new directivity pattern, as shown in Figure 2.20 [84, 92–94].

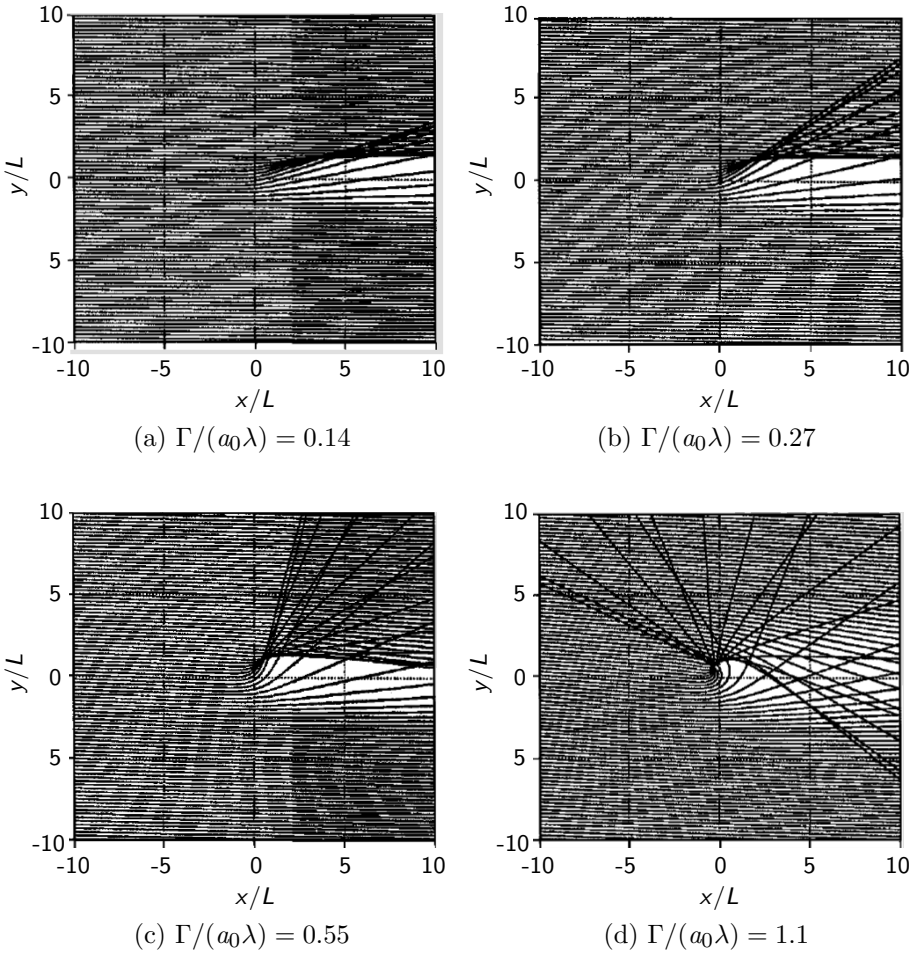

(a) $\Gamma/(a_0\lambda) = 0.14$ (b) $\Gamma/(a_0\lambda) = 0.27$

(c) $\Gamma/(a_0\lambda) = 0.55$ (d) $\Gamma/(a_0\lambda) = 1.1$

Figure 2.20: Acoustic rays propagated through a vortex centered on $x = 0$, $y = 0$. Adapted from Colonius [84]

Experiments have also been performed on the scattering of sound by a vortex using various means of producing the vortex. Horne [95] formed a vortex between two discs using tangential air jets around the perimeter to induce vorticity, and suction in the centre to form a low pressure core. Labbe & Pinton [96] also used a two-disc setup with suction to form the low pressure core, but induced vorticity by rotating the discs, as did Maneville et al. [97].

For an incident plane wave of amplitude A_{in} and wavenumber k_{in}, Berry et al. [98] determined that the pressure field is given by

$$p(\mathbf{r},\theta) = A_{\text{in}}\mathrm{e}^{-\mathrm{i}k_{\text{in}}\|\mathbf{r}\|\cos(\theta)+\mathrm{i}\Delta\beta\theta/2\pi} + A_{\text{in}}F(\theta)\sin(\Delta\beta/2)\frac{\mathrm{e}^{\mathrm{i}k_{\text{in}}\|\mathbf{r}\|}}{\sqrt{2\mathrm{i}\pi k_{\text{in}}\|\mathbf{r}\|}}, \tag{2.28}$$

where $F(\theta) = \mathrm{e}^{\mathrm{i}\theta/2}/\mathrm{icos}(\theta/2)$, θ is the angle between the observation point and the propagation direction of the incident wave, and the term $\Delta\beta = 2\pi f\Gamma/a_\infty^2$ represents the phase distortion in the low-Mach-number approximation. The two terms of the expression represent the incident plane wave, and a scattered cylindrical wave respectively. This expression is valid in the region $\sqrt{2\pi k_{\mathrm{in}}\|\mathbf{r}\|} \gg 1$ and $\sqrt{k_{\mathrm{in}}\|\mathbf{r}\|}(\pi - \theta) \gg 1$.

Maneville et al. [97] adapted the analytical expression described by Berry et al. [98] and found that for a cylindrical incident wave in the low Mach number approximation the pressure field would given by

$$p(\mathbf{r},\theta) = A_{\mathrm{in}}\frac{\mathrm{e}^{-\mathrm{i}k_{\mathrm{in}}\|\mathbf{r}\|\cos(\theta)+\mathrm{i}\Delta\beta\theta/2\pi}}{\sqrt{2\mathrm{i}\pi k_{\mathrm{in}}\|\mathbf{r}'\|}} + A_{\mathrm{in}}F(\theta)\sin(\Delta\beta/2)\frac{\mathrm{e}^{\mathrm{i}k_{\mathrm{in}}\|\mathbf{r}\|}}{2\mathrm{i}\pi k_{\mathrm{in}}\sqrt{\|\mathbf{r}\|L_{\mathrm{em}}}}, \tag{2.29}$$

where $\mathbf{r}'$ is the distance between the centre of the incident cylindrical wave and the observation point, and $\mathrm{L_{em}}$ is the distance between the centre of the incident cylindrical wave and the vortex axis. This expression is the same as the expression in Equation 2.28, comprised of an incident cylindrical wave and a scattered cylindrical wave. The extra scaling factor in the second term is due to the difference in wave amplitude caused by the spreading of the incident wave. Comparison with experiments showed that neglecting the curvature of the wave and the core radius of the vortex resulted in a slight difference in the predicted and measured phases of the amplitude oscillations due to the precession of the vortex.

When the size of the vortex is much smaller than the wavelength of the sound, the Born approximation can be used to predict the change in directivity instead [84, 99]. Several analytical solutions have been posed for this problem including one by Colonius [84] for an incident plane wave, which is detailed in Equations (2.30) to (2.34) [99, 100]. The density pertubation is then given by

$$\rho_{\mathrm{rms}} = \rho_{\mathrm{in}}\epsilon\frac{1}{\sqrt{2}}\left|2\mathrm{i}\sum_{m-1}^{\infty}\psi^m\sin(\mathrm{i}\theta m)\right|, \tag{2.30}$$

where ρ_{in} is the amplitude of the incident density wave, $\epsilon = \Gamma/(\alpha_\infty\lambda)$ is a dimensionless circulation, and θ is the observation angle. Here ψ^m is given by

$$\psi^m(\tilde{r}) = \begin{cases} C_{1m}^{-}J_m + C_{2m}^{-}Y_m - m\mathrm{i}^m\left(\frac{\tilde{r}}{\tilde{r}_0}\right)^2\frac{J_m{}'}{\tilde{r}}, \tilde{r} < \tilde{r}_0 \\ C_{1m}^{-}J_m + C_{2m}^{-}Y_m - m\mathrm{i}^m\frac{J_m}{\tilde{r}^2}{}' + \\ \pi\mathrm{i}^m\left[Y_m\sum_{n=m}^{\infty}{J_n}^2 + J_m\left(\sum_{n=1}^{m-1}J_nY_n + \frac{1}{2}J_0Y_0\right)\right], \tilde{r} > \tilde{r}_0 \end{cases}, \tag{2.31}$$

where J_n and Y_n are Bessel functions of the first and second kind respectively, and nth

order. The term $\tilde{r} = 2\pi\|\mathbf{r}\|/\lambda$ is a dimensionless radius, and the constants C are given by

$$C_{2m}^{-} = 0, \tag{2.32}$$

$$C_{2m}^{+} = \mathrm{i}\, C_{1m}^{+} - \frac{1}{2}\pi \mathrm{i} m, \tag{2.33}$$

and

$$C_{1m}^{-} = C_{1m}^{+} = \frac{1}{2}\pi \mathrm{i}^{(m-1)} - m\mathrm{i}^{m}\frac{J_m{}'(\tilde{r}_0)}{\tilde{r}_0} + m\mathrm{i}^{m}\frac{J_m(\tilde{r}_0)}{\tilde{r}_0^2}$$
$$- \pi \mathrm{i}^{m}\left[Y_m(\tilde{r}_0)\sum_{n-m}^{\infty} {J_n}^2(\tilde{r}_0) + J_m(\tilde{r}_0)\left(\sum_{n-1}^{m-1} J_n(\tilde{r}_0)\, Y_n(\tilde{r}_0) + \frac{1}{2}J_0(\tilde{r}_0)\, Y_0(\tilde{r}_0)\right)\right]. \tag{2.34}$$

A comparison of the Navier-Stokes-based computational analysis and the high-frequency-approximation ray tracing showed good agreement for the scattering of sound from a finite-circulation vortex (Figure 2.21) [84]. Another comparison bewtween the low-frequency-approximation analysis and an experiment by Howe (Figure 2.22) also showed a good qualitative agreement, although the experimental results were underpredicted [84]. It was observed by Colonius that the scattered field, which is the component of the acoustic field that is not due to the incident wave, has a local minimum near 0°, and local maxima at approximately ±30°.

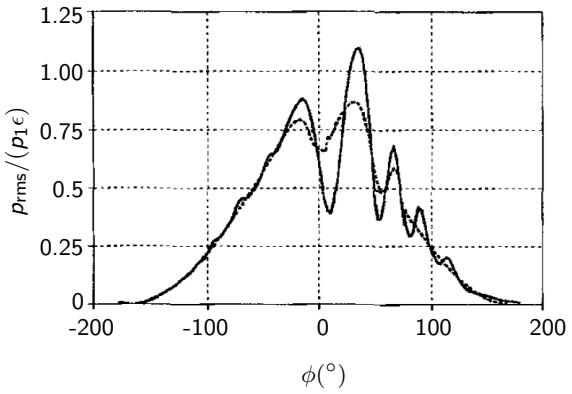

Figure 2.21: Comparison of the Navier-Stokes solution and high-frequency approximation solution for the scattered field due to sound refraction through a vortex with $\epsilon = 0.55$. Adapted from Colonius [84]

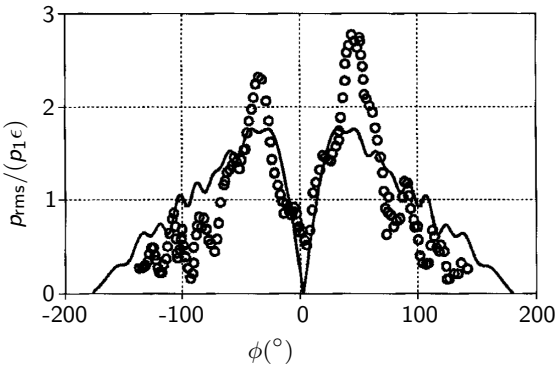

Figure 2.22: Comparison of the low-frequency approximation solution (solid line) and the experimental results (circles) of Horne [95] for the scattered field due to sound scattering from a vortex with $\epsilon = 0.12$. Adapted from Colonius [84]

All of the approaches in the literature have thus been restricted to steady-state cases. For vortices that vary on a large time scale a quasi-steady approach, where the scattering is assumed to be steady-state at each time step, can be expected to will suffice. Whether there is a significant difference between quasi-steady predictions and a rapidly-changing vortex is currently unknown, which means that the applicability of analytical prediction to the problem of the effect of dynamic stall vortices on stall noise is also unknown.

2.6 Chapter summary and discussion

The theoretical models developed to predict wind turbine noise are only as good as the components of which they are comprised. For the most part, improvements in the measurement or simulation of the incoming flow, and modelling the generation of noise by airfoils are more necessary than advances in understanding the propagation of the noise which is already relatively well understood. However, by using more detailed treatments of propagation than are typically used, more accurate predictions can be made. Recent efforts using computational fluid dynamics have resulted in more detailed models of the flow field in a wind farm, and advances in remote sensing have enabled collection of real-time data about the flow. However the flow-field data are only useful for noise predictions if there are accurate aeroacoustic models in which they can be used, and more research is required to refine these models. While current wind turbine noise modelling techniques are more than adequate for the task of modelling noise under standard operating conditions, the low-frequency noise generated during other amplitude modulation events is not predicted by these models. More advanced modelling incorporating stall and a more detailed treatment of propagation is required in order to properly model these events.

Airfoil noise modelling in industry is primarily performed using the Brooks-Pope-

Marcollini (BPM) noise model [30]. This model allows the production of 1/3rd octave spectra of trailing-edge noise at low angles of attack, with some corrections to account for stall behaviour. However, due to limitations in both the angle of attack and frequency resolution of the BPM model, computational approaches are often used to predict more specific phenomena. Of these models the most commonly used is the Ffowcs Williams-Hawking aeroacoustic analogy [57, 63], which enables the prediction of far-field sound using high fidelity flow field data. However the FWH model can only be applied to computational data, which requires a lot of time and expertise to produce.

Modelling of the noise produced at stall is also based on the semi-empirical BPM model, but in recent years some modelling has been performed based on experimental or computation data. These newer models allow the production of higher-fidelity spectra but have only been verified in very limited cases, like the BPM model. This problem is compounded by a lack of experimental noise data for static stall for airfoil profiles other than the NACA 0021 airfoil, and a lack of information about the noise produced at the onset of stall. In order to improve current noise models, these deficiencies in the current literature must be addressed.

Dynamic stall, a flow event characterised by a transient and large loss of lift and the generation of a large leading-edge (and smaller trailing-edge) vortex, commonly occurs on wind turbines during operation. However, the effect that these events have on wind turbine noise is currently unknown. Some preliminary computational studies suggest that the noise generated by the leading-edge vortex itself may take the form of a periodic pulse, however, they do not take the effect that the dynamic stall event has on regular noise generation into account. When a dynamic-stall event occurs, it disrupts the normal flow around the airfoil, and therefore the normal noise sources. Then, once the normal noise sources have been reestablished, the presence of the dynamic stall vortex in the airfoil wake will have a currently unknown effect on the propagation of the regular noise signature of the airfoil.

The problem of sound refraction through a vortex and sound scattering from a vortex is well documented in the literature, both experimentally and through analytical solutions. The scattered field of the plane or cylindrical incident wave scattered by a vortex has a local minimum in the incident direction, and the amplitude of the scattered sound field peaks at $\pm 30^\circ$ to each side. However these solutions have only been verified experimentally for steady-state conditions, and while a quasi-steady approach to the problem of dynamic-stall-vortex scattering is possible without experimental verification, the validity of this approach is currently unknown.

This chapter identifies several key deficiencies in the literature that must be addressed before the phenomenon of impulsive wind-turbine noise can be properly understood and predicted. The gaps that are the focus of this research are as follows:

- There are several flow conditions experienced by wind turbines that may produce impulsive noise, and the amount that they contribute to the overall impulsive wind turbine noise phenomenon is poorly understood
- Most existing data regarding the noise produced by airfoils changes as it enters a stalled state is available at a coarsely-spaced angles of attack and/or has low frequency resolution
- The effects that the airfoil profile have on the noise spectrum, noise levels, and noise directivity produced by an airfoil as it enters a stalled state are unknown
- The source of light-stall noise is not well understood
- The effect that of the decaying dynamic-stall vortex has on the propagation of airfoil noise is unknown.

These gaps will be addressed in the following chapters. Firstly, in order to understand how each potential source of impulsive wind turbine noise may be contributing to the overall phenomenon, deeper review and analysis of the research into each of the potential sources is required.

References for Chapter 2

[1] Garratt, J. R. Review: the atmospheric boundary layer. *Earth-Science Reviews 37*, 1-2 (1994), 89–134.

[2] Stull, R. B. *An introduction to boundary layer meteorology*, vol. 13. Springer, Dordrecht, Netherlands, (1988).

[3] Landberg, L. *Meteorology for Wind Energy: An Introduction*. Wiley, Chichester, West Sussex, UK, (2015).

[4] Burton, T., Sharpe, D., Jenkins, N., and Bossanyi, E. *Wind energy handbook*. John Wiley & Sons, New York, NY, USA, (2001).

[5] Obukhov, A. Turbulence in an atmosphere with a non-uniform temperature. *Boundary-layer Meteorology 2*, 1 (1971), 7–29.

[6] Van den Berg, G. Effects of the wind profile at night on wind turbine sound. *Journal of Sound and Vibration 277*, 4–5 (2004), 955–970.

[7] Touma, J. S. Dependence of the wind profile power law on stability for various locations. *Journal of the Air Pollution Control Association 27*, 9 (1977), 863–866.

[8] Zoumakis, N. Dependence of the wind profile power law exponent on the Pasquill stability classes and height interval in a stably stratified surface boundary layer. *Il Nuovo Cimento C 16*, 1 (1993), 79–81.

[9] Rehman, S., and Al-Abbadi, N. M. Wind shear coefficient, turbulence intensity and wind power potential assessment for Dhulom, Saudi Arabia. *Renewable Energy 33*, 12 (2008), 2653–2660.

[10] Hau, E. *Wind turbines: fundamentals, technologies, application, economics*. Springer, New York, NY, US, (2000).

[11] Guntur, S., SÃŸrensen, N. N., Schreck, S., and Bergami, L. Modeling dynamic stall on wind turbine blades under rotationally augmented flow fields. *Wind Energy 19*, 3 (2016), 383–397.

[12] Pechlivanoglou, G., Nayeri, C., and Paschereit, C. Fixed leading edge auxiliary wing as a performance increasing device for HAWT blades. In *DEWEK, Bremen, Germany* (2010).

[13] Barthelmie, R. J., Frandsen, S. T., Nielsen, M., Pryor, S., Rethore, P.-E., and Jørgensen, H. E. Modelling and measurements of power losses and

turbulence intensity in wind turbine wakes at Middelgrunden offshore wind farm. *Wind Energy 10*, 6 (2007), 517–528.

[14] Madsen, H. A., Bertagnolio, F., Fischer, A., and Bak, C. Correlation of amplitude modulation to inflow characteristics. In *43rd International Congress on Noise Control Engineering* (2014).

[15] Mikkelsen, T., Angelou, N., Hansen, K., Sjöholm, M., Harris, M., Slinger, C., Hadley, P., Scullion, R., Ellis, G., and Vives, G. A spinner-integrated wind lidar for enhanced wind turbine control. *Wind Energy 16*, 4 (2013), 625–643.

[16] Simley, E., Pao, L. Y., Frehlich, R., Jonkman, B., and Kelley, N. Analysis of light detection and ranging wind speed measurements for wind turbine control. *Wind Energy 17*, 3 (2014), 413–433.

[17] Sathe, A., Mann, J., Gottschall, J., and Courtney, M. Can wind lidars measure turbulence? *Journal of Atmospheric and Oceanic Technology 28*, 7 (2011), 853–868.

[18] Banta, R. M., Pichugina, Y. L., Brewer, W. A., Lundquist, J. K., Kelley, N. D., Sandberg, S. P., Alvarez II, R. J., Hardesty, R. M., and Weickmann, A. M. 3D volumetric analysis of wind turbine wake properties in the atmosphere using high-resolution doppler lidar. *Journal of Atmospheric and Oceanic Technology 32*, 5 (2015), 904–914.

[19] Perivolaris, Y. G., Vougiouka, A. N., Alafouzos, V. V., Mourikis, D. G., Zagorakis, V. P., Rados, K. G., Barkouta, D. S., Zervos, A., and Wang, Q. Coupling of a mesoscale atmospheric prediction system with a CFD microclimatic model for production forecasting of wind farms in complex terrain: Test case in the Island of Evia. In *Proceedings of the European Wind Energy Conference, Athens, Greece* (2006).

[20] Porté-Agel, F., Wu, Y.-T., Lu, H., and Conzemius, R. J. Large-eddy simulation of atmospheric boundary layer flow through wind turbines and wind farms. *Journal of Wind Engineering and Industrial Aerodynamics 99*, 4 (2011), 154–168.

[21] Bowdler, D. Amplitude modulation of wind turbine noise: a review of the evidence. *Institute of Acoustics Bulletin 33*, 4 (2008), 31–41.

[22] Oerlemans, S. Effect of wind shear on amplitude modulation of wind turbine noise. *International Journal of Aeroacoustics 14*, 5–6 (2015), 715–728.

[23] Ioannidou, C., Santurette, S., and Jeong, C.-H. Effect of modulation depth, frequency, and intermittence on wind turbine noise annoyance. *The Journal of the Acoustical Society of America 139*, 3 (2016), 1241–1251.

[24] Hansen, K., Hessler, G., Hansen, C., and Zajamsek, B. Prediction of infrasound and low frequency noise propagation for modern turbines. In *Proceedings of the Six International Meeting on Wind Turbine Noise, Glasgow* (2015).

[25] Fischer, A., Aagaard Madsen, H., Kragh, K. A., and Bertagnolio, F. Analyses of the mechanisms of amplitude modulation of aero-acoustic wind turbine sound. In *Proceedings of EWEA 2014* (2014).

[26] Stigwood, M., Stigwood, D., and Large, S. Initial findings of the UK Cotton Farm wind farm long term community noise monitoring project. In *43rd International Congress on Noise Control Engineering* (2014).

[27] Bradley, S. Wind turbine amplitude modulation noise due to time-dependent interference. In *Acoustics 2015 Hunter Valley* (2015).

[28] Makarewicz, R. Cylindrical spreading of noise from a wind turbine. *Journal of Wind Engineering and Industrial Aerodynamics 148* (2016), 1 – 5.

[29] Paterson, R. W., and Amiet, R. K. Noise and surface pressure response of an airfoil to incident turbulence. *Journal of Aircraft 14*, 8 (1977), 729–736.

[30] Brooks, T. F., Pope, D. S., and Marcolini, M. A. *Airfoil self-noise and prediction*. National Aeronautics and Space Administration, Office of Management, Scientific and Technical Information Division, (1989).

[31] Grosveld, F. W. Prediction of broadband noise from horizontal axis wind turbines. *Journal of Propulsion and Power 1*, 4 (1985), 292–299.

[32] Moriarty, P., and Migliore, P. G. Semi-empirical aeroacoustic noise prediction code for wind turbines. Tech. rep., National Renewable Energy Laboratory Golden, CO, USA, 2003.

[33] Oerlemans, S., and Schepers, J. Prediction of wind turbine noise and validation against experiment. *Noise Notes 9*, 2 (2010), 3–28.

[34] Smith, M. Fundamental research into possible causes of amplitude modulation. Tech. rep., University of Southampton, ISVR, 2013.

[35] Leloudas, G., Zhu, W. J., Sørensen, J. N., Shen, W. Z., and Hjort, S. Prediction and reduction of noise from a 2.3 MW wind turbine. In *Journal of Physics: Conference Series* (2007), vol. 75, IOP Publishing.

[36] Oerlemans, S., Sijtsma, P., and López, B. M. Location and quantification of noise sources on a wind turbine. *Journal of Sound and Vibration 299*, 4–5 (2007), 869–883.

[37] Lee, G.-S., Cheong, C., Shin, S.-H., and Jung, S.-S. A case study of localization and identification of noise sources from a pitch and a stall regulated wind turbine. *Applied Acoustics 73*, 8 (2012), 817–827.

[38] Ryi, J., Choi, J.-S., Lee, S., and Lee, S. A full-scale prediction method for wind turbine rotor noise by using wind tunnel test data. *Renewable Energy 65* (2014), 257–264.

[39] Kim, H., Lee, S., Son, E., Lee, S., and Lee, S. Aerodynamic noise analysis of large horizontal axis wind turbines considering fluid–structure interaction. *Renewable Energy 42* (2012), 46–53.

[40] Russell, D. A., Titlow, J. P., and Bemmen, Y.-J. Acoustic monopoles, dipoles, and quadrupoles: An experiment revisited. *American Journal of Physics 67*, 8 (1999), 660–664.

[41] Parchen, R. R. *Progress report DRAW: A prediction scheme for trailing edge noise based on detailed boundary layer characteristics.* TNO Institute of Applied Physics, (1998).

[42] Blake, W. K. *Mechanics of flow-induced sound and vibration*, vol. 2. Academic Press, San Diego, CA, USA, (1986).

[43] Lutz, T., Herrig, A., Würz, W., Kamruzzaman, M., and Krämer, E. Design and wind-tunnel verification of low-noise airfoils for wind turbines. *AIAA journal 45*, 4 (2007), 779–785.

[44] Kamruzzaman, M., Herrig, A., Lutz, T., Würz, W., Krämer, E., and Wagner, S. Comprehensive evaluation and assessment of trailing edge noise prediction based on dedicated measurements. *Noise Control Engineering Journal 59*, 1 (2011), 54–67.

[45] Kamruzzaman, M., Lutz, T., Würz, W., Shen, W. Z., Zhu, W. J., Hansen, M. O. L., Bertagnolio, F., and Madsen, H. A. Validations and improvements of

airfoil trailing-edge noise prediction models using detailed experimental data. *Wind Energy 15*, 1 (2012), 45–61.

[46] Bertagnolio, F., Madsen, H. A., Bak, C., Troldborg, N., and Fischer, A. Aerodynamic noise characterization of a full-scale wind turbine through high-frequency surface pressure measurements. *International Journal of Aeroacoustics 14*, 5-6 (2015), 729–766.

[47] Stalnov, O., Paruchuri, C., and Joseph, P. Prediction of broadband trailing-edge noise based on Blake model and Amiet theory. In *21st AIAA/CEAS Aeroacoustics Conference, AIAA AVIATION Forum* (2015).

[48] Hardin, J., and Pope, D. An acoustic/viscous splitting technique for computational aeroacoustics. *Theoretical and Computational Fluid Dynamics 6*, 5 (1994), 323–340.

[49] Morris, P. J., Long, L. N., Bangalore, A., and Wang, Q. A parallel three-dimensional computational aeroacoustics method using nonlinear disturbance equations. *Journal of Computational Physics 133*, 1 (1997), 56–74.

[50] Ewert, R., and SchrÃűder, W. Acoustic perturbation equations based on flow decomposition via source filtering. *Journal of Computational Physics 188*, 2 (2003), 365 – 398.

[51] Bailly, C., and Juve, D. Numerical solution of acoustic propagation problems using linearized Euler equations. *AIAA journal 38*, 1 (2000), 22–29.

[52] Bogey, C., Bailly, C., and Juvé, D. Computation of flow noise using source terms in linearized Euler's equations. *AIAA journal 40*, 2 (2002), 235–243.

[53] Van Renterghem, T. Efficient outdoor sound propagation modeling with the finite-difference time-domain (FDTD) method: a review. *International Journal of Aeroacoustics 13*, 5–6 (2014), 385–404.

[54] Lighthill, M. J. On sound generated aerodynamically. I. General theory. *Proceedings of the Royal Society of London A: Mathematical, Physical and Engineering Sciences 211*, 1107 (1952), 564–587.

[55] Lighthill, M. J. On sound generated aerodynamically. II. Turbulence as a source of sound. *Proceedings of the Royal Society of London A: Mathematical, Physical and Engineering Sciences 222*, 1148 (1954), 1–32.

[56] Curle, N. The influence of solid boundaries upon aerodynamic sound. *Proceedings of the Royal Society of London A: Mathematical, Physical and Engineering Sciences 231*, 1187 (1955), 505–514.

[57] Williams, J. F., and Hawkings, D. L. Sound generation by turbulence and surfaces in arbitrary motion. *Philosophical Transactions of the Royal Society of London A: Mathematical, Physical and Engineering Sciences 264*, 1151 (1969), 321–342.

[58] Casalino, D., Jacob, M., and Roger, M. Prediction of rod-airfoil interaction noise using the Ffowcs-Williams-Hawkings analogy. *AIAA journal 41*, 2 (2003), 182–191.

[59] Iida, A., Mizuno, A., and Kamemoto, K. Prediction of aerodynamic noise radiated from a vertical-axis wind turbine. In *ASME/JSME 2003 4th Joint Fluids Summer Engineering Conference* (2003), American Society of Mechanical Engineers, pp. 63–69.

[60] Fleig, O., Iida, M., and Arakawa, C. Wind turbine blade tip flow and noise prediction by large-eddy simulation. *Journal of solar energy engineering 126*, 4 (2004), 1017–1024.

[61] Khorrami, M. R., and Mineck, R. E. Towards full aircraft airframe noise prediction: Detached eddy simulations. In *20th AIAA/CEAS Aeroacoustics Conference, AIAA AVIATION Forum* (2014).

[62] Weber, J., Becker, S., Scheit, C., Grabinger, J., and Kaltenbacher, M. Aeroacoustics of Darrieus wind turbine. *International Journal of Aeroacoustics 14*, 5-6 (2015), 883–902.

[63] Zinoviev, A. On the equivalence of the Ffowcs Williams-Hawkings and the non-uniform Kirchhoff equations of aeroacoustics. In *Acoustics 2011: Breaking New Ground Proceedings of the Annual Conference of the Australian Acoustical Society* (2011), The Australian Acoustical Society Queensland Division.

[64] Farassat, F., and Succi, G. P. The prediction of helicopter rotor discrete frequency noise. In *American Helicopter Society, Annual Forum, 38th, Anaheim, CA* (1982), vol. 1, American Helicopter Society, pp. 497–507.

[65] Brentner, K. S., and Farassat, F. Modeling aerodynamically generated sound of helicopter rotors. *Progress in Aerospace Sciences 39*, 2–3 (2003), 83–120.

[66] Hanson, D., and Fink, M. The importance of quadrupole sources in prediction of transonic tip speed propeller noise. *Journal of Sound and Vibration 62*, 1 (1979), 19–38.

[67] Goldstein, M. E., Dittmar, J. H., and Gelder, T. F. *Combined Quadrupole-Dipole Model for Inlet Flow Distortion Noise from a Subsonic Fan.* (1974).

[68] Moreau, S., Roger, M., and Christophe, J. Flow features and self-noise of airfoils near stall or in stall. In *15th AIAA/CEAS Aeroacoustics Conference* (2009).

[69] Roskam, J., and Lan, C.-T. E. *Airplane aerodynamics and performance.* DARcorporation, Lawrence, KA, US, (1997).

[70] Swalwell, K., Sheridan, J., Melbourne, W., et al. The effect of turbulence intensity on stall of the NACA 0021 aerofoil. In *Proceedings of the14th Australasian Fluid Mechanics Conference* (2001), pp. 10–14.

[71] Sheldahl, R. E., and Klimas, P. C. Aerodynamic characteristics of seven symmetrical airfoil sections through 180-degree angle of attack for use in aerodynamic analysis of vertical axis wind turbines. Tech. rep., Sandia National Labs, Albuquerque, NM, US, 1981.

[72] Wang, S., Ingham, D. B., Ma, L., Pourkashanian, M., and Tao, Z. Numerical investigations on dynamic stall of low Reynolds number flow around oscillating airfoils. *Computers & Fluids 39*, 9 (2010), 1529–1541.

[73] Lorber, P. F., and CARTA, F. O. Airfoil dynamic stall at constant pitch rate and high Reynolds number. *Journal of Aircraft 25*, 6 (1988), 548–556.

[74] Tsang, K., So, R., Leung, R., and Wang, X. Dynamic stall behavior from unsteady force measurements. *Journal of Fluids and Structures 24*, 1 (2008), 129–150.

[75] Shipley, D. E., Miller, M. S., and Robinson, M. C. Dynamic stall occurrence on a horizontal axis wind turbine blade. Tech. rep., National Renewable Energy Lab, Golden, CO, US, 1995.

[76] Choudhry, A., Arjomandi, M., and Kelso, R. Horizontal axis wind turbine dynamic stall predictions based on wind speed and direction variability. *Proceedings of the Institution of Mechanical Engineers, Part A: Journal of Power and Energy 227*, 3 (2013), 338–351.

[77] Choudhry, A., Leknys, R., Arjomandi, M., and Kelso, R. An insight into the dynamic stall lift characteristics. *Experimental Thermal and Fluid Science 58* (2014), 188–208.

[78] McCroskey, W., Carr, L., and McAlister, K. Dynamic stall experiments on oscillating airfoils. *AIAA Journal 14*, 1 (1976), 57–63.

[79] Nagarajan, S., and Lele, S. Prediction of sound generated by a pitching airfoil: a comparison of RANS and LES. In *12th AIAA/CEAS aeroacoustics conference* (2006).

[80] Manela, A. On the acoustic radiation of a pitching airfoil. *Physics of Fluids 25* (2013).

[81] Gharali, K., and Johnson, D. A. PIV-based load investigation in dynamic stall for different reduced frequencies. *Experiments in Fluids 55* (2014), 1–12.

[82] Yu, J., Leu, T., and Miau, J. Investigation of reduced frequency and freestream turbulence effects on dynamic stall of a pitching airfoil. *Journal of Visualization 20* (2016), 1–14.

[83] Ferreira, C. S., van Kuik, G., van Bussel, G., and Scarano, F. Visualization by PIV of dynamic stall on a vertical axis wind turbine. *Experiments in Fluids 46*, 1 (2009), 97–108.

[84] Colonius, T., Lele, S. K., and Moin, P. The scattering of sound waves by a vortex: numerical simulations and analytical solutions. *Journal of Fluid Mechanics 260* (1994), 271–298.

[85] Hommes, T., Bosschers, J., and Hoeijmakers, H. Evaluation of the radial pressure distribution of vortex models and comparison with experimental data. In *Journal of Physics: Conference Series* (2015), vol. 656.

[86] Lamb, H. *Hydrodynamics*. Cambridge University Press, (1932).

[87] Vatistas, G. H., Kozel, V., and Mih, W. A simpler model for concentrated vortices. *Experiments in Fluids 11*, 1 (1991), 73–76.

[88] Bhagwat, M. J., and Leishman, J. G. Correlation of helicopter rotor tip vortex measurements. *AIAA journal 38*, 2 (2000), 301–308.

[89] Bagai, A., and Leishman, J. G. Flow visualization of compressible vortex structures using density gradient techniques. *Experiments in Fluids 15*, 6 (1993), 431–442.

[90] Morris, P. J., and Farassat, F. Acoustic analogy and alternative theories for jet noise prediction. *AIAA journal 40*, 4 (2002), 671–680.

[91] Liu, G., Zhang, T., Zhang, Y., and Li, X. Underwater jet noise simulation based on a Large-Eddy Simulation/Lighthill hybrid method. *The Journal of the Acoustical Society of America 136*, 4 (2015), 2318.

[92] Salant, R. F. Acoustic rays in two-dimensional rotating flows. *The Journal of the Acoustical Society of America 46*, 5b (1969), 1153–1157.

[93] Georges, T. Acoustic ray paths through a model vortex with a viscous core. *The Journal of the Acoustical Society of America 51*, 1b (1972), 206–209.

[94] Freund, and Fleischman. Ray traces through unsteady jet turbulence. *International Journal of Aeroacoustics 1*, 1 (2002), 83–96.

[95] Horne, W. Measurements of the scattering of sound by a line vortex. In *Proceedings of the AIAA 8th Aeroacoustics Conference* (1983).

[96] Labbé, R., and Pinton, J.-F. Propagation of sound through a turbulent vortex. *Physical Review Letters 81*, 7–17 (1998), 1413–1416.

[97] Manneville, S., Roux, P., Tanter, M., Maurel, A., Fink, M., Bottausci, F., and Petitjeans, P. Scattering of sound by a vorticity filament: An experimental and numerical investigation. *Physical Review E 63*, 3 (2001).

[98] Berry, M., Chambers, R., Large, M., Upstill, C., and Walmsley, J. Wavefront dislocations in the Aharonov-Bohm effect and its water wave analogue. *European Journal of Physics 1*, 3 (1980), 154–162.

[99] Howe, M. On the scattering of sound by a rectilinear vortex. *Journal of Sound and Vibration 227*, 5 (1999), 1003–1017.

[100] Ford, R., and Smith, S. G. L. Scattering of acoustic waves by a vortex. *Journal of Fluid Mechanics 386* (1999), 305–328.

Chapter 3

Review of Other Wind Turbine Noise Generation Mechanisms

3.1 Chapter overview

While this research project focuses on stall as a potential source of impulsive wind turbine noise, it is not the only possibility. In order to understand the phenonomenon it is necessary to analyse each of the proposed noise mechanisms to obtain a clear picture of how each one may or may not be contributing to the overall sound heard by far-field observers. Researching these proposed mechanisms led to the publication of a paper in the Journal of Wind Engineering and Industrial Aerodynamics (doi:10.1016/j.jweia.2014.01.007), which is presented in this chapter. As mentioned in Chapter 2, it was determined that stall was a likely candidate that merited further investigation.

Blade-tower interaction is not considered to be significant in upwind horizontal-axis wind turbines and so it is unlikely to be the source of the impulsive noise. Candidates such as interference between wind turbines and atmospheric refraction may result in louder noise for an observer but cannot increase modulation depth. There is evidence to suggest that blade-vortex interaction could contribute to the noise phenomenon, but the vortices that are produced by upstream turbines are unfavourable for strong noise production. Dynamic stall noise is a potential candidate but as the time scale of a dynamic stall event is very small, the production of the vortex is unlikely to produce the modulation patterns observed on wind turbines. Occurence of dynamic stall could however contribute due to scattering the airfoil noise, a concept which is further discussed in Chapter 6. Stall is not only likely to be the primary contributor to impulsive wind turbine noise, but it also is one of the most poorly-captured by current models. Improving these models requires higher fidelity noise data and a better understanding of the noise sources during stall, both of which are discussed in Chapters 4 & 5.

3.2 Supplementary discussion of potential other amplitude modulation mechanisms

Statement of Authorship

Title of Paper	A discussion of wind turbine interaction and stall contributions to wind farm noise
Publication Status	☑ Published ☐ Accepted for Publication ☐ Submitted for Publication ☐ Unpublished and Unsubmitted w ork w ritten in manuscript style
Publication Details	Laratro, A., Arjomandi, M., Kelso, R., and Cazzolato, B. A discussion of wind turbine interaction and stall contributions to wind farm noise. Journal of Wind Engineering and Industrial Aerodynamics 127 (2014), 1-10

Principal Author

Name of Principal Author (Candidate)	Alex Laratro		
Contribution to the Paper	- Research - Writing of the manuscript and production of original figures - Correspondence with editor and reviewers including the production of all cover letters and rejoinders		
Overall percentage (%)	80%		
Certification:	This paper reports on original research I conducted during the period of my Higher Degree by Research candidature and is not subject to any obligations or contractual agreements with a third party that would constrain its inclusion in this thesis. I am the primary author of this paper.		
Signature		Date	

Co-Author Contributions

By signing the Statement of Authorship, each author certifies that:

i. the candidate's stated contribution to the publication is accurate (as detailed above);

ii. permission is granted for the candidate to include the publication in the thesis; and

iii. the sum of all co-author contributions is equal to 100% less the candidate's stated contribution.

Name of Co-Author	Maziar Arjomandi		
Contribution to the Paper	- Supervision of the work, including the production of the manuscript - Participation in the development of the concepts and ideas presented in the manuscript - Evaluation and editing of the manuscript prior to submission		
Signature		Date	

Name of Co-Author	Richard Kelso		
Contribution to the Paper	- Supervision of the work, including the production of the manuscript - Participation in the development of the concepts and ideas presented in the manuscript - Evaluation and editing of the manuscript prior to submission		
Signature		Date	

Name of Co-Author	Benjamin Cazzolato		
Contribution to the Paper	- Supervision of the work, including the production of the manuscript - Participation in the development of the concepts and ideas presented in the manuscript - Evaluation and editing of the manuscript prior to submission		
Signature		Date	

J. Wind Eng. Ind. Aerodyn. 127 (2014) 1–10

Contents lists available at ScienceDirect

Journal of Wind Engineering and Industrial Aerodynamics

journal homepage: www.elsevier.com/locate/jweia

A discussion of wind turbine interaction and stall contributions to wind farm noise

Alex Laratro *, Maziar Arjomandi, Richard Kelso, Benjamin Cazzolato

School of Mechanical Engineering, The University of Adelaide, South Australia 5005, Australia

ARTICLE INFO

Article history:
Received 13 August 2013
Received in revised form
6 January 2014
Accepted 19 January 2014
Available online 21 February 2014

Keywords:
Wind energy
Wind farm noise
Thumping
Turbulent inflow
Dynamic stall

ABSTRACT

Wind farms have recently been reported to produce a noise signature that is described as possessing a "thumping" quality. Measurements of these signatures are limited and their effects are debated but their effect on public opinion and complaints make them a concern for researchers in this field. Proposed reasons for these noise signatures include amplitude modulation, interference patterns and wake–rotor interaction. This paper discusses these effects and concludes that wake–rotor interaction plays a role by causing variations in turbulent-inflow noise and dynamic stall. The current state of research into stall noise and wind turbine wake structure is also reviewed and it is concluded that the available information and collected data on wind turbine wake are insufficient to determine how strong this role is. More information on the velocity and turbulence fields in the wake of horizontal-axis wind turbines as well as a characterisation of the noise produced by an airfoil experiencing dynamic stall is required in order to make a full assessment of rotor–wake contributions to wind farm noise.

1. Introduction

In the past few years there has been substantial growth in the non-hydroelectric areas of the renewable energy sector, with production capacity globally increasing by 21.5% between 2011 and 2012 (Sawin, 2013). Some elements of these technologies result in reduced economic viability or public acceptance which limits growth. Advancements that address these concerns, such as improvements to efficiency and better noise control, are necessary in order for rapid growth to continue.

Wind power was the fastest growing renewable in 2012, accounting for 39% of global added capacity (Sawin, 2013). Given that wind speed increases with distance from the ground, larger wind turbines are constantly being developed in order to take advantage of this. A greater swept area enables more wind energy to be captured and the increase in height gives them more reliable access to high wind-speeds. Being able to access higher wind speeds more reliably increases the capacity factor of large turbines resulting in a lower levelised cost of energy compared to smaller models (Bolinger and Wiser, 2012). However this increase in size can have adverse effects on the turbine's noise spectrum and its efficiency in an array configuration.

Wind turbine noise control is becoming increasingly problematic as wind turbines grow larger, as they individually emit more noise and the low frequency component of their spectrum grows (Møller and Pedersen, 2011). Low frequency sound is attenuated less by the atmosphere than high frequency sound which makes large wind turbines audible from further away (ISO, 1993). There is a significant amount of negative public opinion with regards to wind turbine sound emissions due to the reported "annoying qualities" they possess. These are qualities of the sound that would increase the annoyance of wind turbine noise above that of equivalent A-weighted broadband noise level (Persson Waye and Öhrström, 2002). Low-frequency sound with these qualities will therefore have a greater effect on a wider area than high-frequency noise sources. Many regulations require that an extra 5 dB is added to the noise level to compensate for increased annoyance if these qualities are present (EPA South Australia, 2009; NSW Department of Planning & Infrastructure (NSW DPI), 2011). These legal restrictions on sound pressure level/exclusion zones near residential areas encourage shorter distances between turbines in a wind farm. However close spacing creates the possibility that the wind turbines in a farm will adversely interact with each other, which can lead to unsteady blade loading, reducing power output and increasing noise level and blade fatigue (Högström et al., 1988; Thomsen and Sørensen, 1999). An understanding of the mechanisms of wind farm noise production is required in order to continue to comply with noise limits and understand adverse interactions between turbines in a wind farm.

Unsteady blade loads stem from variations in velocity and turbulence. Incoming wind will always possess these qualities, so wind turbines will always experience unsteady loading to some extent. Understanding how higher levels of unsteady inflow resulting from operating in the wake of another turbine affect this loading is important.

* Corresponding author. Tel.: +61 411 039 805.
E-mail address: alex.laratro@adelaide.edu.au (A. Laratro).

0167-6105/$ - see front matter © 2014 Elsevier Ltd. All rights reserved.
http://dx.doi.org/10.1016/j.jweia.2014.01.007

The authors posit that inflow turbulence due to wake-interaction is a significant source of noise with these reported qualities. This can manifest as periodic increases in noise level due to changes in angle-of-attack and separation effects, dynamic stall and blade–vortex interaction. Several questions need to be answered before a conclusion can be reached on this matter.

- Are large-scale turbulent structures present in the far wake of a wind turbine?
- How are the wake and its parameters affected by wind gusts?
- Will the blades of downstream turbine(s) be adversely affected by these structures?
- Will this interaction generate noise and what qualities will that noise have?

Once the answers to these questions are known whether wake–rotor interaction is contributing significantly to wind turbine noise can be determined.

Determining the loading due to unsteady flow requires definition of the flow-field, but wake structure is complicated. Due to this complexity most studies only analytically model parameters in a one-dimensional or axisymmetric fashion (Vermeer et al., 2003). These simplified models are suitable for typical power prediction and layout optimisation but are too simple to properly predict unsteady loading and noise. Understanding of how the wake affects downstream turbine is greatly hindered unless computational or experimental data is used. Computational simulations often implement actuator line, actuator disc or blade element momentum models, which approximate the blades as lines or discs that apply a force to the fluid. This approach is much faster than full modelling of the blades, and suitable for most applications but occasionally insufficient. Recently large-eddy simulations (LES) of the wakes of horizontal-axis wind turbines have been conducted (Bazilevs et al., 2011, Jimenez et al., 2007, Hsu et al., 2014, Porté-Agel et al., 2011, Sezer-Uzol and Long, 2006). This is a turbulence model that directly resolves large-scale eddies and models smaller ones, eliminating the extra computational cost of simulating very small scale turbulence. There is often cross-over in these approaches, with LES studies using actuator line or disc methods (Jimenez et al., 2007; Porté-Agel et al., 2011). Using simplified approaches instead of modelling the blades directly may lead to missed details in the wake flow-field and airfoil noise. Differences in the approaches are largest in the near-wake, but may result in other changes in wake structure further downstream (Réthoré et al., 2011). Investigations of far-wake turbulence line actuator methods are currently appropriate because such downstream differences are not known to occur in wind turbine wake simulations (Shen et al., 2012). If any discrepancies are found between the full rotor and actuator line or actuator disc models the new information can be added to these models in the form of corrections.

LES enables high fidelity simulations on a range of scales without prohibitive computational cost. Resolving structure in the velocity field in the downstream region where other turbines operate requires high fidelity models such as LES. If there is a large amount of large scale structure in the wake in this region then angle-of-attack and blade–vortex interaction effects will become significant. Changes in airfoil spectra due to these effects are understood well enough to suggest that they will increase the low frequency component of wind turbine noise. However characterisation of the noise due to dynamic stall is still required, which presents a significant challenge to determining the contribution of wake–rotor interaction.

2. Adverse wind farm noise characteristics

Most wind farm noise is broadband—that is its spectrum contains a wide range of frequencies with no large spectral peaks. While some tonal noise is produced in the mechanical components of the turbine it is drowned out by the stronger aerodynamic noise sources.

Studies into how this noise affects humans show that under certain conditions the annoyance rating by test subjects will increase. In addition the closer the subject is to the source the greater this effect becomes and a greater decrease in the ability to perform cognitive tasks occurs. Qualities of the noise such as frequency content have also been found to have an effect, with low-frequency noise being reported as more annoying (Nobbs et al., 2012).

Other factors also need to be considered as visual stimuli have been found to mitigate these effects, and parameters such as turbine colour have also been weakly linked to the reported annoyance (Iachini et al., 2012; Maffei et al., 2013; Ruotolo et al., 2012). This is of concern as many studies report that exposure to high enough levels of noise can disturb sleep leading to increases in stress (Pedersen et al., 2009). When trying to sleep there is a lack of visual stimuli which may result in disturbance from noise that is not disturbing at other times of day.

Despite these factors many residents near wind turbines report no ill-effects. In addition to this some aspects of wind turbine noise complaints suggest psychosomatic elements (Farboud et al., 2013). It is not currently known whether this is the case, but as the noise signatures can vary with location it is possible that only some households are affected.

Other studies of the characteristics of wind turbine noise report complaints of subjective or descriptive measures. These studies report complaints due to qualities referred to as “swishing”, “thumping” or “throbbing” (among others), which often occur at the blade pass frequency (Oerlemans and Schepers, 2009; Pedersen et al., 2009; Pedersen and Persson Waye, 2004; Persson Waye and Öhrström, 2002; Van den Berg, 2004). Characterisation of these noise qualities is hindered by the subjective and interchangeable use of the terms “throbbing”, “swishing” and “thumping” in the literature. This is due to the terms being used by residents near wind turbines to describe their experiences. Amplitude modulation, which is a periodic variation in sound level is defined by a modulation frequency (the distance between peaks) and a modulation depth (the size of the amplitude change), is considered the cause of these effects. These qualities are hard to categorise as few studies report on both the descriptors used by residents and the properties found in the noise recordings. It is likely that some, if not all, of the aforementioned characteristics stem from amplitude modulation of different noise sources but to the authors' knowledge there is no standard quantitative definition of each descriptor.

These descriptors are useful for targeting further research into some of the poorly understood intermittent phenomena that may go unnoticed in large-scale experiments. Measurements have found that short periods of amplitude modulated noise sometimes occur at night in the signature of the Rhedes Park wind farm, as shown in Fig. 1, but this variation has not been observed to this degree in a single turbine (Van den Berg, 2004). Mechanisms for the production of this noise have been suggested; including velocity gradients, turbulent inflow, interference patterns and blade–tower interaction but the cause is still disputed and will be discussed further in the next section.

It is possible that the use of different descriptors in qualitative studies is due to the changes in the characteristics of amplitude modulated noise over time. Fig. 2 shows a turbine spectrogram that transitions from modulated low-frequency to modulated high-frequency noise (Smith et al., 2012).

To summarise, there are a large number of descriptors that have been used when people living near wind farms report their experiences listening to turbine noise. As they have stemmed from subjective surveys they are not yet well quantified which both hinders and assists attempts to classify the noise that people in

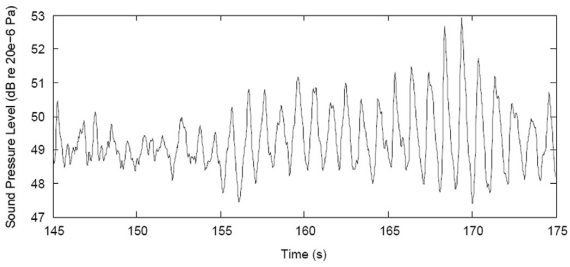

Fig. 1. Sound pressure level per 50 ms due to Rhedes Park wind farm, measured at 750 m from nearest turbine (adapted from Van den Berg, 2004).

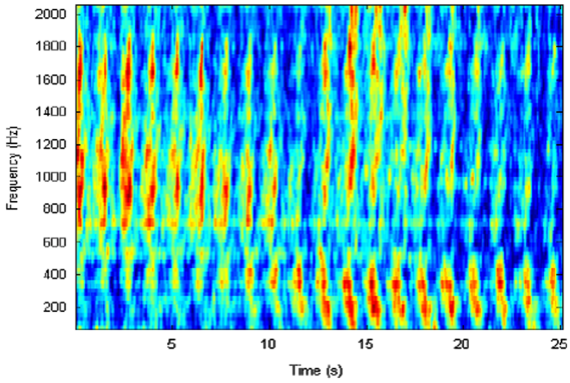

Fig. 2. Wind turbine spectrogram from 80 m (Smith et al., 2012).

nearby communities report as annoying. The noise cannot be properly classified from these descriptions alone but by comparing the use of these descriptors to the noise signals and atmospheric conditions at the time patterns may begin to emerge. It is likely that noise modulated by wind variability and directivity changes will result in sounds that could be described differently depending on the spectrum of the modulated noise, which can only be determined using recordings.

3. Possible noise mechanisms

There have been many reports of a "thumping" noise intermittently being produced by wind farms, but its cause is not understood (Bowdler, 2008; Thorne, 2011; Van den Berg, 2004). It has been argued that this is due to amplitude modulation, unsteady turbulent-inflow, interference patterns, and blade–tower interaction. Due to its intermittency and similarity to the "thumping" noise emitted by helicopters unsteady turbulent-inflow is likely to be a key contributor but all of these effects are present and will play a role in forming the overall acoustic signature of the wind farm.

Turbulent-inflow noise occurs when an airfoil encounters an unsteady inflow which changes the pressure distribution across the airfoil resulting in sound (Brooks et al., 1989). The sound spectrum produced by this pressure can be predicted analytically if the energy spectrum of the incoming turbulence is known. Turbulent-inflow noise is a problem in helicopters, where the blade tip vortices interact with subsequent blades causing impulsive noise (Schlinker and Amiet, 1983). This effect is called blade vortex interaction or rotor–vortex interaction noise and is responsible for giving helicopters their distinctive "blade-slap" sound during flight, which is easily discernible above the trailing-edge noise (Widnall, 1971). While there are major differences in airspeed and separation distance in the case of helicopter blade–vortex interactions, the possibility of blade–vortex interaction occurring in wind farms is not discussed in the literature. This is likely due to the lack of evidence of large-scale eddies in the far wake, as research in this is area is ongoing. The authors hypothesise that this is a significant contributor to "thumping", and a later section will focus on this source.

It has also been proposed that blade–tower interaction is responsible for "thumping" as it is in downwind turbine configurations where the rotor is situated behind the tower. Once a popular design, downwind turbines have fallen out of favour as they produce large amounts of impulsive noise during operation. As the blades pass the tower they interact with the wake vortices shed by the tower and this leads to a "thumping" noise (Kelley et al., 1985). As upwind type wind turbine blades do not pass through the tower wake they do not interact with these vortices, however the tower still causes a deformation of the flow immediately upstream, which the blade does pass through and it has been proposed that this is significant enough to result in impulsive noise (Doolan et al., 2012a). A study investigating the effect of the tower on unsteady blade loads found them to be insignificant compared to stochastic load variations from turbulence under most conditions (Kim et al., 2011). In addition, increasing mean wind speed and yaw error leads to a larger variation in wind speed around a wind turbine rotor, which increases modulation depth. Conversely the relative levels of load fluctuations due to the tower decrease with increasing wind speed and yaw error (Kim et al., 2011). This indicates that blade–tower interaction noise is lower in conditions favourable to high noise levels from other sources.

Another proposed explanation is that turbines in a wind farm are causing areas of large constructive interference (Cand et al., 2011). It was thought that if the depth of amplitude modulation is large enough, amplitude-modulated noise would approach an impulsive signal which could be described as "thumping" and several studies report that "thumping" noise in horizontal axis wind turbines is most likely due to extreme instances of amplitude modulation (Bowdler, 2008; Lee et al., 2011). Local variations in mean wind speed results in each turbine operating at a different rotational speed, which was thought to produce variations in far-field sound pressure as they move in and out of phase, amplifying the effects of amplitude modulation (Van den Berg, 2004). But this is not the case as the sound pressure level variations of two turbines being in phase will not increase modulation depth (Bowdler, 2008). However being in phase will raise the average sound level, which can make qualities of the turbine noise temporarily audible at distances where they otherwise would not be (Bowdler, 2008). Because of this the role of interference should not be completely dismissed.

Similarly the role of sound propagation cannot be overlooked. Lower frequency sound, which as stated previously may be perceived as annoying, travels further than higher frequencies and will increase in dominance over distance. In addition velocity or temperature gradients result in refraction of noise which can lead to changes in audible distance (Cummings, 2013). When downwind of a turbine the sound refracts downwards and reflects off of the ground. This refraction is pronounced at low frequencies, with 8 Hz sound levels at 5000 m reaching up to 20 dB higher than expected for spherical spreading (Willshire, 1985). A temperature inversion, where the temperature at ground level is lower that the temperature higher in the atmosphere, also causes downward refraction of sound and will lead to similar effects. This indicates that wind turbine noise will in general propagate further at night, when temperature inversion is a common occurrence. The properties of the ground also affect the sound propagation, as acoustic impedance changes both the reflection coefficient and phase change at reflection. As such noise will propagate further over acoustically harder ground, where more of the noise is reflected.

ISO 9613 suggests that farmland and similar terrain, where wind turbines are most often situated should be considered acoustically soft, however field measurements have found that this under-predicts noise levels at 500 m (ISO, 1993; Plovsing and Søndergaard, 2011). Additionally in Australia the grass around farmland is dry in summer and often short due to grazing, which will increase its acoustic hardness.

Smaller scale effects will also result in changes in the sound. This difficulty in predicting noise propagation is amplified by the presence of complex terrain, as it will obstruct and reflect sound, as well as introducing changes to the local flow and temperature field which further affect how the sound will propagate (Kaliski et al., 2011). This may be contributing to the audibility of adverse noise qualities but it is unlikely that variations in propagation are coherent enough to cause the "thumping" signatures themselves.

In summary while the cause of these characteristics is disputed some potential causes are more probable explanations. Interference patterns and other propagation effects may make low frequency amplitude modulation patterns more audible, but this requires an existing signature, the cause of which is still unknown. Helicopters produce similar noise signatures due to the interaction between the rotor and the blade tip vortices and this sound is audible over the trailing edge noise. Determining whether this could occur in horizontal-axis wind turbines requires knowledge of the structure of the wake downstream turbines are operating in and the amount of noise produced by these events. This discussion focuses on effects due to rotor–wake interaction, which included amplitude modulation of turbulent inflow noise, blade–vortex interaction and dynamic stall.

4. Wake structure and propagation

In order to best predict loading and noise on wind turbine blades the following parameters are required in the plane of the rotor

- Velocity
- x, y and z turbulence intensities
- Turbulence energy spectrum
- Turbulence length scale

This is problematic when investigating wake operation as existing studies of horizontal axis wind turbine wakes have a different focuses or use simplifications that can disrupt the wake structure. For example most wind turbine wake research focuses on the magnitude of the axial velocity deficit and the magnitude of turbulent intensity as these are the parameters that most influence power output (Chamorro and Porté-Agel, 2009). Additionally, wake parameters are often reported as one-dimensional averages or axisymmetric distributions, which render them useless for determining how blade loading changes during a revolution.

The study of wind turbine wake structure has been focused on experimental and numerical investigations. Wind tunnel testing is more controlled than field experiments, giving a faster turnaround and better resolution and characterisation of inflow. Field experiments are preferable however, as it is not known how much of an effect flow confinement has on wind turbine wake structure. Computational models are also valuable as they produce finer data sets, but they are difficult to produce and the other methods are still required for validation.

Experimental measurements of the structure of the flow field are mostly concentrated on the near wake, which only extends a few rotor diameters downstream due to the costs associated with large scale experiments. Typically wind farms have a turbine spacing of approximately 7–10 rotor diameters and so the wake structure at this distance is of interest (Ahmed, 2011; Hirth and Schroeder, 2013; Meyers and Meneveau, 2012). One of the most comprehensive wind tunnel tests of a horizontal-axis wind turbine was performed by the National Research Energy Laboratory (NREL) and gathered very little far wake data (Simms et al., 2001). Concentrating on the near wake enables the helical vortices shed from the blade tips to be resolved with smoke probes and studied as shown in Fig. 3. In the far wake these vortices break down, and the smoke trails do not yield much useful data. Some experiments have been conducted using particle image velocimetry but these are also currently focused on near-wake measurements (Vermeer et al., 2003). Wind tunnel tests have also been performed to show the effects of the tower on wake development, but measurements across the whole turbine were not taken (Nygard, 2011).

Field experiments have similarly not been conducive to determining the significance of wake–rotor interaction. A turbulence cross-section in the near wake (at 2 rotor diameters) of a full-scale turbine has been captured using SODAR, but further work was hampered by variability in the wind direction (Högström et al., 1988). Most studies focus on the distribution of parameters in vertical lines at various stations behind the tower, which is a limitation currently shared by many reports detailing computational models.

Computational models to investigate the structure of wind turbine wakes are also lacking in number and detail. Many large-eddy simulation (LES) simulations do not model the area of the wake in which other turbines operate (Bazilevs et al., 2011, Hsu et al., 2014, Sezer-Uzol and Long, 2006). Actuator disc models which model the rotor as a porous disc are often used but these simplifications can result in the loss of the desired accuracy (Norris et al., 2010). When investigating wake structure, actuator line, actuator surface or full-rotor models should be used where possible, as they capture some details of the flow that actuator disc models may not. Some models have used larger domains but the region of interest is still close to the exit (at approximately 10 rotor diameters) which may affect the results (Troldborg et al., 2010). These studies can still provide other useful information about the formation of the far wake. Vorticity isosurfaces reveal

Fig. 3. NREL Phase IV experiment with smoke trail (Hand, 2001).

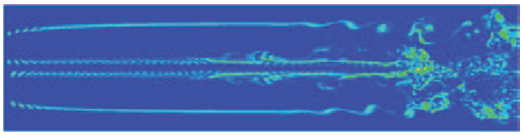

Fig. 4. Vorticity isosurfaces in horizontal plane (Troldborg et al., 2010).

that as wind speed increases the helical tip vortices break down at larger downstream distances. At a free-stream speed of 10 m/s the tip vortices have only just broken down at 7 rotor diameters (7D) as shown in Fig. 4. Other simulations used sufficiently large domains but reported data in a longitudinal plane, which does not give much information about wake structure (Jimenez et al., 2007; Porté-Agel et al., 2011; Zahle and Sørensen, 2007). However when using longitudinal data the turbulence intensity can be still be seen to change at least 3% across the rotor at 7 rotor diameters in wind tunnel measurements, indicating some level of increased unsteady loading (Porté-Agel et al., 2011).

A recent large-eddy simulation of the NREL experiment observed that after the collapse of the helical tip vortices, large stream-wise vortices were formed, as shown in Fig. 5 (Mo et al., 2013). The regions containing these vortices also contained most of the vorticity and turbulence intensity in the region indicating they are the main source of unsteady loading.

How the wakes of turbines in a wind farm interact must also be considered. Full rotor simulations of wind farms are not common due to the size of the domain that must be considered resulting in an impractical computational cost for little benefit. Actuator-disc/line or analytical methods are more common as are wind tunnel experiments with the choice of method depending on application (Christiansen and Hasager, 2005; Frandsen et al., 2006). For systems larger than two turbines, analytical models are often used, and while these are adequate for optimising a wind farm layout for power output, they cannot give insight into how the flow structure is affected as each turbine interacts with the combined wakes of the upstream turbines. Experiments performed on scale wind farms yield some useful information about the flow but are limited by the data that can be collected (Lebrón et al., 2009). Some studies have been conducted using line-actuators and periodic boundary conditions and these show the velocity deficit and turbulence increasing due to each row of turbines (Sørensen et al., 2007). Most of these are focused on the velocity deficit behind the turbines and report little or one-dimensional information about the turbulence or vorticity in the wake.

In a simulation of a tandem wind turbine system, it has been found that the turbulence in the incoming wind has a large effect on the system's wake structure, with high incoming turbulence resulting in the downstream rotor ingesting still higher levels of turbulence, and its wake in turn breaking down closer to the turbine (Troldborg et al., 2010). This results in smaller scale turbulent structures for downstream turbines, which may reduce the generated turbulent inflow noise (Troldborg et al., 2010). However if two turbines are laterally offset and turbulence is low then ingesting the upstream turbine wake results in an asymmetric near-wake with high levels of turbulence on the side of the upstream turbine and a flow still dominated by tip vortex structures on the other, which may contribute to variation in noise level over time (Chamorro and Arndt, 2011; Troldborg et al., 2010).

Upon comparing several studies it is apparent that simulations of the wakes of horizontal-axis wind turbines vary with modelling, conditions and turbine design. Common elements are present however, the most notable of which is a series of helical tip vortices which break down further downstream. A recent simulation suggests the existence of large stream-wise vortices downstream but more simulations and experiments are needed in order to confirm the existence of large-scale coherent vortices in the far wake. In addition to this, the large effects that placing wind turbines in an array can have on their respective wakes means that structures found in the wake of a single turbine may only be applicable to some turbines in an array or none at all. Once the properties of horizontal-axis wind turbine wakes are more defined the effect that operating in the wake has on turbine noise can be assessed.

5. Turbulent-inflow noise

Turbulent-inflow noise is a form of aerodynamic noise that arises when an airfoil encounters an unsteady flow. It is characterised by its low-frequency dominant spectra and dipole-like

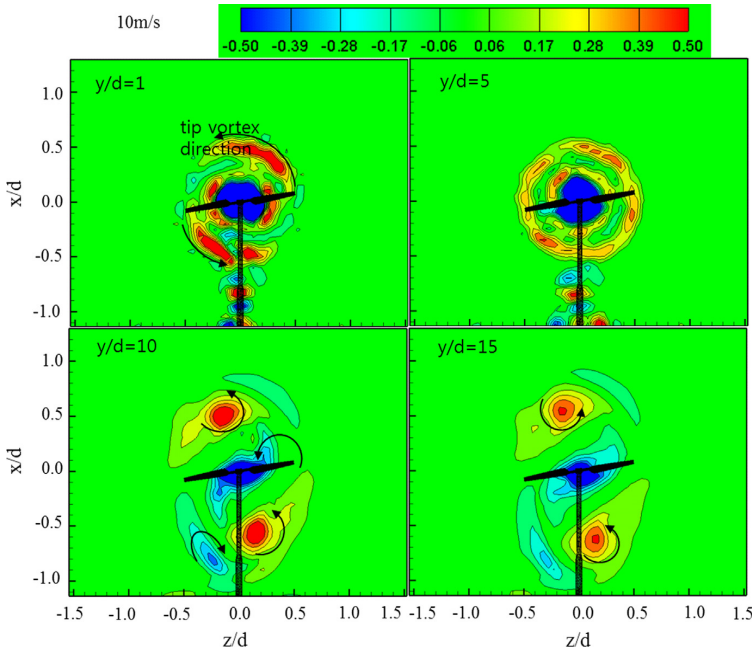

Fig. 5. Simulated wake vortices in NREL experiment (adapted from Mo et al., 2013).

directivity pattern. The production of large amounts of turbulent-inflow noise will contribute to wind turbine noise at large distances as it is dominated by low frequencies. Blade–vortex interaction is a related effect that is of some concern. However it seems likely that if it occurs it will not do so under ideal conditions and is likely to be insignificant compared to more general turbulent-inflow effects.

When an airfoil encounters unsteady flow there is a transient disruption to its surface pressure, resulting in a change in lift and noise signature. This noise is known as turbulent-inflow noise and it is responsible for giving helicopters their distinctive sound (Widnall, 1971). It is usually predicted using analytical models since simulations of aerofoil noise require extremely fine spatial and temporal resolution along the sound's path in order to resolve the spectrum. Analytically predicting the spectrum due to turbulent inflow requires, at a minimum, the distributions of turbulent length scale and intensity, but is most accurate if the turbulent energy spectrum is used.

Analytical work describing how vortices and turbulence affect airfoil noise was pioneered by Amiet using a model that was originally applied to rotor–vortex interaction in helicopters but still sees widespread use for more general applications (Amiet, 1975, 1978, 1986). The model determines the surface pressure fluctuations using the airfoil's lift response and the turbulent energy spectrum normal to the blade and these fluctuations are then propagated to the far-field as sound. It uses a large aspect-ratio, thin airfoil approximation, and while corrections for airfoil shape, thickness and backscattering have been developed they are not yet widely implemented (Moriarty et al., 2005, Roger and Moreau, 2005; Zhu et al., 2005). Predicted and experimental spectrum differ by less than 6 dB for frequencies below 1.5 kHz, above this however the accuracy of the model appears to decline rapidly (Amiet, 1975; Schlinker and Amiet, 1983).

Using Amiet's model and an appropriate turbulent energy spectrum, equations can be produced that relate turbulence intensity, turbulence length scale and airfoil geometry to third-octave spectrum. This is mostly performed using the Von Karman turbulent energy spectrum, as this is a good approximation to atmospheric turbulence. It has been shown that if the turbulence is non-uniform then the turbulence field can be discretised to yield results that also agree with experiment to within about 3 dB until 1500 Hz (Doolan et al., 2012b). Results are further expected to improve if the actual energy spectrum of the turbulence can be measured—especially if the assumption of Von Karman turbulence is not valid. Amiet's model is also used predict to the spectrum of blade–vortex interaction (Schlinker and Amiet, 1983). Using this technique the turbulent-inflow noise due to operating in a wind turbine wake can be determined if the turbulence spectrum or intensity and length scale are known.

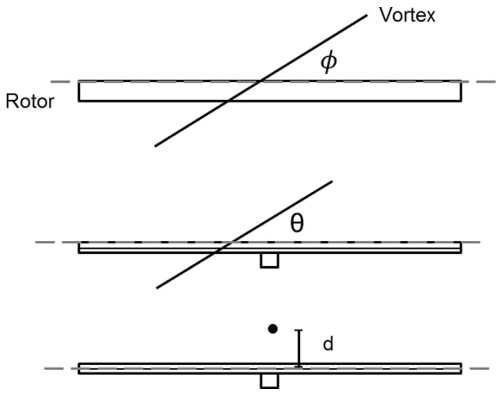

Fig. 6. Vortex orientation parameters. ϕ: rotor-plane angle, θ: shaft-plane angle, and d: miss distance.

Blade–vortex interactions are a subset of inflow turbulence noise that are of some concern due to the possibility of vortices in the wake. These interactions are divided into parallel, oblique and perpendicular configurations, describing the angle of the vortex line in the chordal plane of the airfoil. Parallel and perpendicular configurations are when this angle (referred to as the rotor-plane angle in the context of helicopters) is 0° and 90° respectively. The other main orientation parameters are the shaft-plane angle and the miss distance which are shown in Fig. 6.

Beyond the initial studies little experimental parameterisation of blade–vortex interaction noise has been performed. Sensitivity analyses of blade–vortex interaction noise have instead been performed by calculating spectra using the existing model (Gallman, 1994; Malovrh and Gandhi, 2005). Increases in circulation strength, which is proportional to both the tangential velocity and radius, increase noise levels, but when radius is increased noise levels decrease (Gallman, 1994). This suggests that changing the peak tangential velocity has a greater effect on the noise than the radius. Increases in local Mach number also found increase in generated noise levels (Malovrh and Gandhi, 2005). Parallel interactions are the loudest due to maximising the affected area, and perpendicular interactions are the quietest (Malovrh and Gandhi, 2005). Increasing the angle between the chord plane and the vortex line also reduces noise level, as does increasing the perpendicular distance between vortex line and chord plane (Gallman, 1994; Malovrh and Gandhi, 2005). The effects of changing these parameters is summarised in Table 1. Loud interactions therefore occur when a small, strong vortex undergoes a parallel interaction with an airfoil in high Mach number flow. This indicates that large, stream-wise vortices are unlikely to contribute much to wind turbine sound level through blade–vortex interaction.

In summary it is possible to predict the noise due to blade–vortex interaction if the spectrum of the incoming turbulence is known. If the spectrum is not known then the turbulence can be assumed isotropic and a grid of turbulence intensities can be used to estimate the noise level. Interaction with wake vortices also generates noise, but current wake structure research indicates that if vortices are formed they will interact in a way that is unfavourable for loud noise generation. However interaction with vortices can result in local variations in angle-of-attack, which is another avenue that must be explored to determine the extent to which wake interaction affects wind farms.

6. Changes in angle-of-attack and directivity

In addition to inflow turbulence noise, non-uniform flow can affect noise due to changes in the angle-of-attack and directivity. Changes in the angle-of-attack modify the overall sound level, whereas changes in directivity result in the largest portion of sound power radiating to different locations at different points during a cycle. Large angle of attack variations can also result in the blades experiencing stall, which is likely to further increase sound levels through boundary layer growth and vortex shedding.

Table 1
Summary of blade–vortex interaction parameters.

	Change in parameter	Noise level
Circulation strength	Increasing	Increasing
Core radius	Increasing	Decreasing
Rotor-plane angle	Towards 0°	Increasing
Shaft-plane angle	Towards 0°	Increasing
Miss distance	Increasing	Decreasing
Mach number	Increasing	Increasing

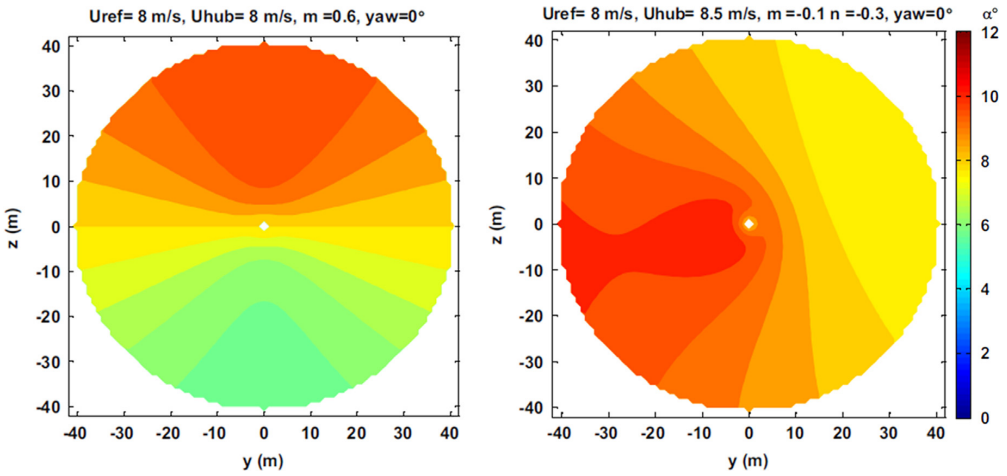

Fig. 7. Estimated variation in angle of attack due to wind shear; vertical (left) and combined horizontal and vertical (right) (Smith et al., 2012).

Non-uniform velocity and turbulence intensity across a wind turbine rotor result in the blades experiencing a different angle of attack at different points of the cycle. The distribution of angles of attack will indicate how each section of the airfoil will behave during a cycle. Fig. 7 shows that it is possible to predict the changes in angle-of-attack due to wind shear; factors *m* and *n* are the vertical and lateral wind shear exponents respectively. As the flow field in the wake of a horizontal-axis wind turbine is not currently well defined, true angle-of-attack distributions have not been produced.

It is evident that operating an airfoil at different angles of attack results in variation in boundary layer thickness at the trailing edge which in turn produces a variation in noise level. As the thickness of the boundary layer and the trailing edge increases with angle-of-attack so does the overall noise level of the airfoil (Brooks et al., 1989). Dynamic stall will also result if the angle-of-attack variation is large and frequent enough and this is likely to cause further increases in noise level as large eddies are formed and subsequently collapse which will be discussed in the next section.

Changes in directivity have been proposed as an additional factor in far-field low-frequency noise (Smith et al., 2012). Noise due to separation or turbulent-inflow has dipole directivity which makes it strongest normal to the airfoil. In contrast, trailing edge noise directivity is cardioid-like—strongest diagonally forward of the leading edge as shown in Fig. 8 (Oerlemans and Schepers, 2009). A change from low-frequency dominant to high-frequency dominant noise will result in a change in directivity of the overall blade turbine noise as shown in Fig. 9. It has been suggested that this results in turbulent-inflow and separation noise being more prominent normal to the rotor plane (Lee et al., 2011).

As previously mentioned, much of the trailing edge noise is then directed into the atmosphere on the upstroke and the ground on the downstroke. Sound in the atmosphere is also refracted depending on the temperature and wind speed gradient. The speed of sound decreases with temperature and thus distance from the ground (on a warm day), upwind sound is refracted upwards and downwind sound may be refracted upwards or downwards (Bies and Hansen, 2003). It has been suggested that these effects result in a decreased contribution from trailing-edge noise to far-field measurements (Smith et al., 2012). It is difficult to correlate these predicted directivities of wind turbine noise with complaints due to a lack of data regarding the observer's locations

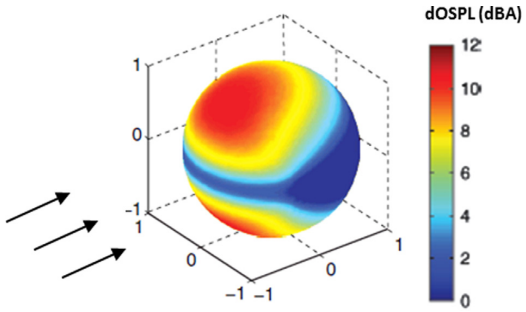

Fig. 8. Trailing-edge noise directivity (adapted from Oerlemans and Schepers, 2009).

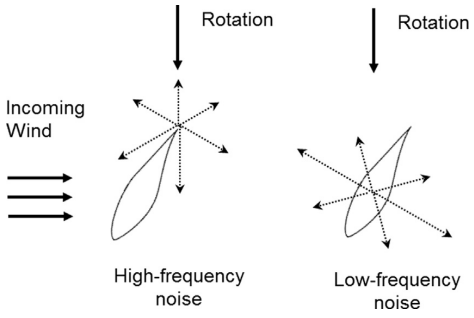

Fig. 9. Change in directivity with noise frequency.

and the wind direction at the time of complaint. This data should be more often reported in future to assist in determining if these effects are responsible for complaints.

In summary, as a wind turbine blade undergoes each revolution it is subjected to a cyclic variation in angle of attack. High angles of attack result in increased noise levels due to louder trailing-edge noise and subsequently the occurrence of stall. In addition, as the spectrum transitions from trailing-edge noise dominated to stall and turbulent-inflow noise dominated there is a change in directivity. When trailing-edge noise dominates, the noise is directed approximately in the direction of blade movement. When

Table 2
Influence of parameters on dynamic stall (adapted from McCroskey et al., 1976).

	Reynolds Number	Oscillation amplitude	Reduced frequency	Leading edge geometry
Effect on vortex **shedding**	Negligible	Major in isolated cases	Small	Moderate
Effect on lift	Small	Major in isolated cases	Major	Major
Boundary layer **separation**	Small	Moderate	Major	Major

stall and turbulent-inflow noise dominate, the noise is directed orthogonal to the rotor plane. Correlating this with noise complaints is difficult due to lack of data. Combinations of amplitude and directivity variations can lead to amplitude modulation, depending on the level of non-uniform flow and ground temperature.

7. Dynamic stall noise

Airfoils experience dynamic stall when they are subjected to a large and rapid variation in angle of attack. This results in the formation of large vortices which increase the unsteady loads on the airfoil followed by a drop into deep stall (McCroskey., 1981). It is thought that these vortices may also result in increased noise generation but while current dynamic stall models can predict their size they are insufficient to predict finer details.

Dynamic stall is a major source of unsteady loading on horizontal-axis wind turbines. Under normal operational conditions dynamic stall can occur on up to half the cycles of a turbine (Shipley et al., 1995). The occurrence of dynamic stall is dependent on span-wise location, free-stream velocity, yaw error, as well as tilting and coning of the rotor. Of these, highly yawed flow is the major contributor to the occurrence of dynamic stall (Shipley et al., 1995). Increases in unsteady inflow due to operation in the wake of another turbine are thought to increase the probability of dynamic stall (Choudhry et al. 2012). This increase in dynamic stall occurrence will change the noise signature of the turbine and may contribute to complaints.

The properties of dynamic stall are affected by the Reynolds number and the reduced frequency ($k=c\Omega/2U$)—where c is the airfoil chord (m), Ω is the oscillation frequency (rad/s) and U is the fluid velocity (m/s). These parameters affect the strength of vortex shedding and lift hysteresis as shown in Table 2.

Fig. 10 shows a comparison of the reduced frequency along the blade between the NREL turbine and some large scale turbines. As many commercial turbines use a simplified version of the optimal chord vs span-wise location curve these can be taken as representative of large-scale turbines. The curve shows that for the large turbines approximately half the blade is in the unsteady flow regime ($k > 0.05$), above which unsteady flow effects cannot be neglected. This indicates that these regions of the blade are susceptible to dynamic stall if angle of attack variations are large enough. This reduced frequency will increase further if the blade is experiencing unsteady inflow from other sources.

Detailed analysis of the flow field when dynamic stall occurs is restricted to experimental data and computational models. Existing semi-empirical models are limited to predicting the variation in aerodynamic coefficients with angle of attack (Holierhoek et al., 2013, Leishman, 2002). Some models—such as the Leishman–Beddoes model—explicitly account for the formation and shedding of the dynamic stall vortex but cannot be used to predict the structure of the vortex. Semi-empirical models of dynamic stall are therefore currently unsuitable for acoustic predictions.

To the authors' knowledge noise measurements have not been made on an airfoil experiencing dynamic stall. Some papers reporting on computational simulations suggest that their models could be adapted to predict the spectrum, but this has not been

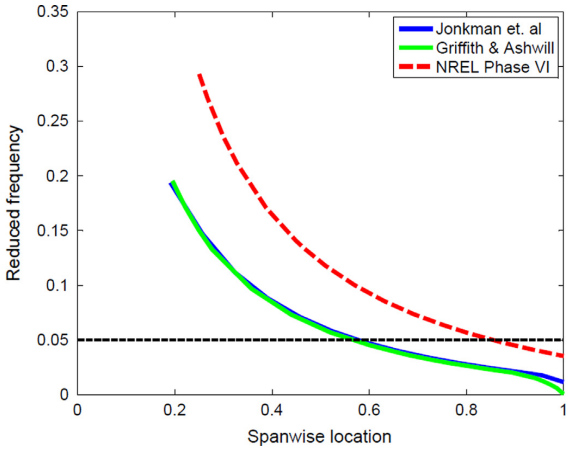

Fig. 10. Reduced frequency k vs span-wise location for several turbine blades.

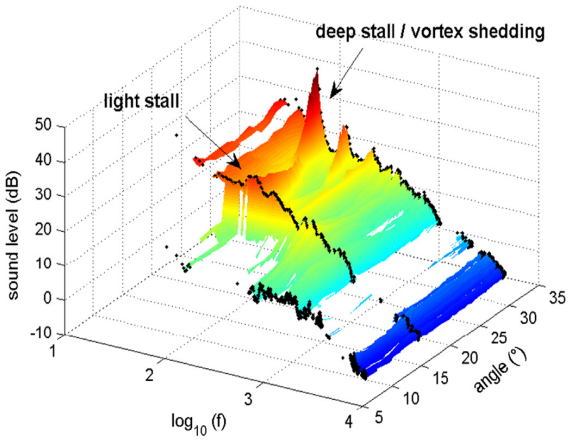

Fig. 11. Noise due to stall on a NACA 0012 airfoil at Re$\sim 1.5\times10^5$ (Moreau et al., 2009).

performed. Despite this there is sufficient information about similar phenomenon to make some predictions about the nature of noise produced during dynamic stall.

From experiments on stall it is known that the onset of vortex shedding will increase the amplitude of the main spectral peak as shown in Fig. 11 (Moreau et al., 2009). As the angle-of-attack grows the main peak also shifts to slightly lower frequencies as vortex shedding begins to occur (Moreau et al., 2009). Experiments on flat-plates and axial fans have shown similar spectral peaks at the during vortex shedding (Longhouse, 1977; Roger et al., 2006).

Noise is also produced when counter-rotating vortices interact. Direct numerical simulation of interacting vortex pairs has shown that a large pulse of acoustic pressure is produced when two vortices interact, followed by a period of less intense noise (Zhang

et al., 2013).This indicates that dynamic stall noise may have a periodic impulsive component due to interaction between vortices shed from the leading and trailing edge.

Dynamic stall flow features are dominated by large vortices which are shed from the leading and trailing edge and interact as the move downstream. Vortex shedding and interaction are both sources of low frequency noise and so dynamic stall events are likely to have similar spectra. More research into dynamic stall is required in order to determine the extent to which wind farms may be affected by this noise, but the authors hypothesise that large amounts of turbulent inflow noise and dynamic stall due to wake operation are the primary source of "thumping" noise.

8. Discussion and conclusion

Wind turbines in wind farms have been seen to produce rapidly varying noise levels, which are not well understood. Reasons that have been proposed to explain this include:

- Amplitude modulation of trailing-edge noise due to wind gradients and changes in directivity
- Amplitude modulation of turbulent-inflow noise due to the wake of upstream turbines
- Turbulent inflow noise changes due to wind gusts
- Dynamic stall noise due to unsteady inflow
- Blade–vortex interaction noise
- Interference patterns from multiple turbines
- Atmospheric refraction and frequency-dependent attenuation
- Interaction between the blades and upstream deformation from the tower

These effects are all present in wind farms but it is currently unclear to what extent they contribute to the overall noise signatures. Interference patterns may increase the overall noise level but not the depth of modulation and atmospheric effects will filter out some frequencies. This may amplify existing noise signatures but it does not provide an explanation for their root cause. Blade–tower interaction can also occur in single turbines where these noise patterns are not observed and so it is likely not the cause of the "thumping" patterns. Due to lack of consistency in measurements even the existence of disturbances due to wind turbine noise is disputed. Measurement and simulation of horizontal-axis wind turbine wakes is currently underdeveloped with regard to this application and cannot provide enough insight into flow structure to determine the strength of these effects. Turbulent-inflow noise depends on the size, strength and orientation of wake vortices. Large changes in angle of attack due to non-uniformities in the flow field result in dynamic stall which increases noise level due to vortex shedding and collapse. High fidelity simulations of wind turbine wake development are required in order to determine the extent to which these phenomena contribute to noise level. More experimental measurements of wind turbine wake flow fields are also needed to compare with simulations.

Records of the noise produced during dynamic stall have not been published, but it can be inferred from prior research into noise due to vortex shedding and stall that the noise during dynamic stall will likely be louder than during normal operation. Due to the large surface pressure fluctuations and vortex shedding during dynamic stall it is likely that there will be an increase in noise level over normal operation. Unsteady flow affects the noise signature in horizontal-axis wind turbines and with more research, the significance of these noise sources can be determined.

Acknowledgements

The authors would like to thank Sophie Hollitt and Amelia Thomas for their contributions to editing.

References

Ahmed, S., 2011. Wind Energy: Theory and Practice. PHI Learning Pvt. Ltd., New Dehli, India.
Amiet, R.K., 1975. Acoustic radiation from an airfoil in a turbulent stream. J. Sound Vib. 41, 407–420.
Amiet, R.K., 1978. Noise due to rotor-turbulence interaction. NASA Conference Publication 2052, pp. 109–126.
Amiet, R.K., 1986. Airfoil gust response and the sound produced by airfoil-vortex interaction. J. Sound Vib. 107, 487–506.
Bazilevs, Y., Hsu, M.-C., Akkerman, I., Wright, S., Takizawa, K., Henicke, B., Spielman, T., Tezduyar, T.E., 2011. 3D simulation of wind turbine rotors at full scale. Part I: Geometry modeling and aerodynamics. Int. J. Numer. Methods Fluids 65, 207–235.
Bies, D., Hansen, C., 2003. Engineering Noise Control: Theory and practice, 3rd ed. Taylor & Francis, New York, United States.
Bolinger, M., Wiser, R., 2012. Understanding wind turbine price trends in the US over the past decade. Energy Policy 42, 628–641.
Bowdler, D., 2008. Amplitude modulation of wind turbine noise: a review of the evidence. Inst. Acoust. Bull. 33, 31–41.
Brooks, T.F., Pope, D.S., Marcolini, M.A., 1989. Airfoil self-noise and prediction. National Aeronautics and Space Administration, Scientific and Technical Information, Hampton, United States.
Cand, M., Bullmore, A., Smith, M., Von-Hunerbein, S., Davis, R., 2011. Wind turbine amplitude modulation: research to improve understanding as to its cause and effect. In: Proceedings of Wind Turbine Noise.
Chamorro, L.P., Porté-Agel, F., 2009. A wind-tunnel investigation of wind-turbine wakes: boundary-layer turbulence effects. Boundary-Layer Meteorol. 132, 129–149.
Chamorro, L.P., Arndt, R.E.A., 2011. Turbulent flow properties around a staggered wind farm. Boundary-Layer Meteorol. 141, 349–367.
Choudhry, A., Mo, J.-O., Arjomandi, M., Kelso, R., 2012. Effects of spacing between wind turbines on blade dynamic stall. Australasian Fluid Mech. Conf. 2012.
Christiansen, M.B., Hasager, C.B., 2005. Wake effects of large offshore wind farms identified from satellite SAR. Remote Sensing Environ. 98, 251–268.
Cummings, J., 2013. The variability factor in wind turbine noise. In: Proceedings of the 5th International Conference on Wind Turbine Noise.
Doolan, C., Moreau, D.J., Brooks, L.A., 2012a. Wind turbine noise mechanisms and some concepts for its control. Acoust. Australia 40, 7–13.
Doolan, C.J., Coombs, J.L., Moreau, D.J., Zander, A.C., Brooks, L.A., 2012b. Prediction of noise from a wing-in-junction flow using computational fluid dynamics. Proceedings of Acoustics 2012 – Fremantle.
EPA South Australia, 2009. Wind farms environmental noise guidelines. EPA South Australia, Adelaide, Australia.
Gallman, J.M., 1994. Parametric computational study of isolated blade-vortex interaction noise. AIAA J. 32, 232–238.
Farboud, A., Crunkhorn, R., Trinidade, A., 2013. 'Wind turbine syndrome': fact or fiction? J. Laryngol. Otol. 127, 222–226.
Frandsen, S., Barthelmie, R., Pryor, S., Rathmann, O., Larsen, S., Højstrup, J., Thøgersen, M., 2006. Analytical modelling of wind speed deficit in large offshore wind farms. Wind Energy 9, 39–53.
Hand, M., 2001. Unsteady Aerodynamics Experiment Phase VI: Wind Tunnel Test Configurations And Available Data Campaigns. National Renewable Energy Laboratory, Golden, United States.
Hirth, B.D., Schroeder, J.L., 2013. Documenting wind speed and power deficits behind a utility-scale wind turbine. J. Appl. Meteorol. Climatol. 52, 39–46.
Högström, U., Asimakopoulos, D.N., Kambezidis, H., Helmis, C.G., Smedman, A., 1988. A field study of the wake behind a 2 MW wind turbine. Atmospher. Environ. (1967) 22, 803–820.
Holierhoek, J.G., De Vaal, J.B., Van Zuijlen, A.H., Bijl, H., 2013. Comparing different dynamic stall models. Wind Energy 16, 139–158.
Hsu, M.-C., Akkerman, I., Bazilevs, Y., 2014. Finite element simulation of wind turbine aerodynamics: validation study using NREL phase VI experiment. Wind Energy 17 (3), 461–481.
Iachini, T., Maffei, L., Ruotolo, F., Senese, V.P., Ruggiero, G., Masullo, M., Alekseeva, N., 2012. Multisensory assessment of acoustic comfort aboard metros: a virtual reality study. Appl. Cogn. Psychol. 26, 757–767.
ISO 9613-1, 1993. Acoustics – Attenuation of sound during propagation outdoors. Part 1: Calculation of the absorption of sound by the atmosphere. ISO, Geneva, Switzerland.
Jimenez, A., Crespo, A., Migoya, E., Garcia, J., 2007. Advances in large-eddy simulation of a wind turbine wake. J. Phys.: Conf. Ser. 75.
Kaliski, K., Duncan, E., Wilson, D.K., Vecherin, S., 2011. Improving predictions of wind turbine noise using PE modeling. In: INTER-NOISE and NOISE-CON Congress and Conference Proceedings 2011, pp. 371–383.
Kelley, N.D., McKenna, H.E., Hemphill, R.R., Etter, C.L., Garrelts, R.L., Linn N.C., 1985. Acoustic noise associated with the MOD-1 wind turbine: its source, impact, and control. Solar Energy Research Institute, Golden, United States.

Kim, H., Lee, S., Lee, S., 2011. Influence of blade-tower interaction in upwind-type horizontal axis wind turbines on aerodynamics. J. Mech. Sci. Technol. 25, 1351–1360.
Lebrón, J., Cal, R.B., Kang, H., Castillo, L., Meneveau, C., 2009. Interaction between a wind turbine array and a turbulent boundary layer. In: Proceedings of the 11th Americas Conference on Wind Engineering.
Lee, S., Kim, K., Choi, W., Lee, S., 2011. Annoyance caused by amplitude modulation of wind turbine noise. Noise Control Eng. J. 59, 38–46.
Leishman, J.G., 2002. Challenges in modelling the unsteady aerodynamics of wind turbines. Wind Energy 5, 85–132.
Longhouse, R.E., 1977. Vortex shedding noise of low tip speed, axial flow fans. J. Sound Vib. 53, 25–46.
Malovrh, B., Gandhi, F., 2005. Sensitivity of helicopter blade-vortex-interaction noise and vibration to interaction parameters. J. Aircr. 42, 685–697.
Maffei, L., Iachini, T., Masullo, M., Aletta., F., Sorrentino, F., Senese, V.P., Ruotolo, F., 2013. The effects of vision-related aspects on noise perception of wind turbines in quiet areas. Int. J. Environ. Res. Publ. Health 10, 1681–1697.
McCroskey, W.J., Carr, L.W., McAlister, K.W., 1976. Dynamic stall experiments on oscillating airfoils. AIAA J. 14, 57–63.
McCroskey W.J., 1981. The phenomenon of dynamic stall. NASA Ames Research Center, Moffett Field, United States.
Meyers, J., Meneveau, C., 2012. Optimal turbine spacing in fully developed wind farm boundary layers. Wind Energy 15, 305–317.
Møller, H., Pedersen, C.S., 2011. Low-frequency noise from large wind turbines, 2011. J. Acoust. Soc. Am. 129, 3727–3744.
Mo, J.-O., Choudhry, A., Arjomandi, M., Lee, Y.-H., 2013. Large eddy simulation of the wind turbine wake characteristics in the numerical wind tunnel model. J. Wind Eng. Ind. Aerodyn. 112, 11–24.
Moreau, S., Roger, M., Christophe, J., 2009. Flow features and self-noise of airfoils near stall or in stall. In: Proceedings of the 15th AIAA/CEAS Aeroacoustics Conference.
Moriarty, P., Guidati, G., Migliore, P., 2005. Prediction of turbulent inflow and trailing-edge noise for wind turbines. In: Proceedings of the 11th AIAA/CEAS Aeroacoustics Conference.
Nobbs, B., Doolan, C.J., Moreau, D.J., 2012. Characterisation of noise in homes affected by wind turbine noise. In: Proceedings of Acoustics 2012 – Fremantle.
Norris, S.E., Cater, J.E., Stol, K.A., Unsworth, C.P., 2010. Wind turbine wake modelling using large eddy simulation. In: Proceedings of the 17th Australasian Fluid Mechanics Conference.
NSW Department of Planning & Infrastructure (NSW DPI), 2011. NSW planning guidelines: Wind farms. NSW DPI, Sydney, Australia.
Nygard, Ø.V., 2011. Wake behind a horizontal-axis wind turbine. Masters thesis, Norwegian University of Science and Technology, Trondheim, Norway.
Oerlemans, S., Schepers, J.G., 2009. Prediction of wind turbine noise and validation against experiment. Int. J. Aeroacoust. 8, 555–584.
Pedersen, E., Persson Waye, K., 2004. Perception and annoyance due to wind turbine noise—a dose–response relationship. J. Acoust. Soc. Am., 3460–3470.
Pedersen, E., Van den Berg, F., Bakker, R., Bouma, J., 2009. Response to noise from modern wind farms in the Netherlands. J. Acoust. Soc. Am. 126, 634–643.
Persson Waye, K., Öhrström, E., 2002. Psycho-acoustic characters of relevance for annoyance of wind turbine noise. J. Sound Vib. 250, 65–73.
Plovsing, B., Søndergaard, B., 2011. Wind turbine noise propagation: Comparison of measurement and predictions by a method based on geometrical ray theory. Noise Control Eng. J. 59 (1), 10–22.
Porté-Agel, F., Wu, Y.-T., Lu, H., Conzemius, R.J., 2011. Large-eddy simulation of atmospheric boundary layer flow through wind turbines and wind farms. J.Wind Eng. Ind. Aerodyn. 99, 154–168.
Réthoré, P.-E., Troldborg, N., Zahle, F., Sørensen, N.N., 2011. Comparison of the near wake of different kinds of wind turbine CFD models. Wake Conference Book of Abstracts, pp. 33–38.
Roger, M., Moreau, S., 2005. Back-scattering correction and further extensions of Amiet's trailing-edge noise model. Part 1: Theory. J. Sound Vib. 286, 477–506.
Roger, M., Moreau, S., Guédel, A., 2006. Vortex-shedding noise and potential-interaction noise modeling by a reversed Sears' problem. In: Proceedings of the 12th AIAA/CEAS Aeroacoustics Conference and Exhibit, pp. 8–10.
Ruotolo, F., Senese, V.P., Ruggiero, G., Maffei, L., Masullo, M., Iachini, T., 2012. Individual reactions to a multisensory immersive virtual environment: the impact of a wind farm on individuals. Cogn. Process. 13, 319–323.
Sawin, J., 2013. Renewables 2013: Global Status Report. REN21, Paris, France.
Schlinker, R.H., Amiet, R.K., 1983. Rotor-vortex interaction noise. National Aeronautics and Space Administration, Scientific and Technical Information, Hampton, United States.
Sezer-Uzol, N., Long, L.N., 2006. 3-D time-accurate CFD simulations of wind turbine rotor flow fields. AIAA Paper no. 2006-0394.
Shen, W.Z., Zhu, W.J., Sørensen, J.N., 2012. Actuator line/Navier–Stokes computations for the MEXICO rotor: comparison with detailed measurements. Wind Energy 2012 (15), 811–825.
Shipley, D.E., Miller, M.S., Robinson, M.C., 1995. Dynamic Stall Occurrence on a Horizontal Axis Wind Turbine Blade. National Renewable Energy Lab, Golden, United States.
Simms, D.A., Schreck, S., Hand, M., Fingersh., L.J., 2001. NREL Unsteady Aerodynamics Experiment in the NASA-Ames Wind Tunnel: A Comparison of Predictions to Measurements. National Renewable Energy Laboratory, Colorado, USA
Smith, M., Bullmore, A.J., Cand, M.M., Davis, R., 2012. Mechanisms of amplitude modulation in wind turbine noise. In: Proceedings of the Acoustics 2012 Nantes Conference, pp. 823–828.
Sørensen, J.N., Mikkelsen, R., Troldborg, N., 2007. Simulation and modelling of turbulence in wind farms. In: Proceedings of the European Wind Energy Conference & Exhibition 2007.
Thomsen, K., Sørensen, P., 1999. Fatigue loads for wind turbines operating in wakes. J. Wind Eng. Ind. Aerodyn. 80, 121–136.
Thorne, B., 2011. The problems with "noise numbers" for wind farm noise assessment. Bull. Sci. Technol. Soc. 31, 262–290.
Troldborg, N., Sorensen, J.N., Mikkelsen., R., 2010. Numerical simulations of wake characteristics of a wind turbine in uniform inflow. Wind Energy 13, 86–99.
Van den Berg, G.P., 2004. Effects of the wind profile at night on wind turbine sound. J. Sound Vib. 277, 955–970.
Vermeer, L.J., Sørensen, J.N., Crespo, A., 2003. Wind turbine wake aerodynamics. Prog. Aerosp. Sci. 39, 467–510.
Widnall, S., 1971. Helicopter noise due to blade–vortex interaction. J. Acoust. Soc. Am. 50, 354–365.
Willshire, W.L., 1985. Long-range downwind propagation of low-frequency noise. NASA Technical Report.
Zahle, F., Sørensen, N.N., 2007. On the influence of far-wake resolution on wind turbine flow simulations. J. Phys.: Conf. Ser. 75 (012042).
Zhang, S., Li, H., Liu, X., Zhang, H., Shu, C.-W., 2013. Classification and sound generation of two-dimensional interaction of two Taylor vortices. Phys. Fluids 25.
Zhu, W.J., Heilskov, N.H., Shen, W.Z., Sørensen, J.N., 2005. Modeling of aerodynamically generated noise from wind turbines. J. Sol. Energy Eng. 127 (4), 517–528.

Chapter 4

Preliminary Measurements of Airfoil Self-Noise

4.1 Section overview

This chapter discusses an experiment that was conducted in order to investigate the noise generated under static stall conditions by two simple airfoil models; A NACA 0012 and NACA 0021 airfoil. These airfoils were used since their simple profiles enabled the development of fundamental understanding about the noise source. The aerodynamics of both of these airfoils have been extensively studied in the literature, and detailed flow-field and wake data are also available for the NACA 0012.

The work is presented in this chapter in the form of a manuscript that was submitted to the International Journal of Aeroacoustics, and subsequently accepted in a revised form (which can be found at DOI: doi:10.1177/1475472X17709929). In this investigation the acoustic spectra of the two airfoils were measured at Reynolds numbers of 64,000 and 96,000 and at angles of attack from –5° to 40° in 1°increments or less. It was determined that, while there are only minor differences in noise spectrum between the airfoil models, the range of angles of attack over which this noise develops is significantly different.

A faster rate of change in low-frequency noise level with angle of attack indicated that the rate of change in noise level with time is greater for the NACA 0021 than for the NACA 0012 airfoil experiencing a given rate of change of angle of attack under these conditions. Comparison with the lift curves of the airfoils at the relevant Reynolds numbers indicate that the change in noise level may be inferred from the rate of change in lift with respect to angle of attack as the airfoil stalls. This also shows that some airfoils can produce sharp increases in noise level at stall, which would result in a highly unsteady noise signature if a wind turbine airfoil exhibited this behaviour. However, with only two airfoil profiles a trend could not be established.

Furthermore the source of the noise could not be determined from the flow field data from the literature and the acoustic measurements alone. This neccessitated a more comphrehensive investigation, with a higher angle of attack resolution near the stall angle and the addition of a flat plate model. The results of this second investigation are presented in Chapter 5.

4.2 Measurements of airfoil self-noise under stall conditions

Statement of Authorship

Title of Paper	An experimental comparison of the self-noise of NACA 0012 and NACA 0021 airfoils at stall
Publication Status	☑ Published ☐ Accepted for Publication ☐ Submitted for Publication ☐ Unpublished and Unsubmitted w ork w ritten in manuscript style
Publication Details	Laratro, A., Arjomandi, M., Cazzolato, B., and Kelso, R. An experimental comparison of the self-noise of NACA 0012 and NACA 0021 airfoils at stall. International Journal of Aeroacoustics 16, 3 (2017), 181-195

Principal Author

Name of Principal Author (Candidate)	Alex Laratro		
Contribution to the Paper	- Data collection, analysis, visualisation, and interpretation - Writing of the manuscript and production of original figures - Correspondence with editor and reviewers including the production of all cover letters and rejoinders		
Overall percentage (%)	80%		
Certification:	This paper reports on original research I conducted during the period of my Higher Degree by Research candidature and is not subject to any obligations or contractual agreements with a third party that would constrain its inclusion in this thesis. I am the primary author of this paper.		
Signature		Date	

Co-Author Contributions

By signing the Statement of Authorship, each author certifies that:

i. the candidate's stated contribution to the publication is accurate (as detailed above);

ii. permission is granted for the candidate to include the publication in the thesis; and

iii. the sum of all co-author contributions is equal to 100% less the candidate's stated contribution.

Name of Co-Author	Maziar Arjomandi		
Contribution to the Paper	- Supervision of the work, including the production of the manuscript - Participation in the development of the concepts and ideas presented in the manuscript - Evaluation and editing of the manuscript prior to submission		
Signature		Date	

Name of Co-Author	Benjamin Cazzolato		
Contribution to the Paper	- Supervision of the work, including the production of the manuscript - Participation in the development of the concepts and ideas presented in the manuscript - Evaluation and editing of the manuscript prior to submission		
Signature		Date	

Name of Co-Author	Richard Kelso		
Contribution to the Paper	- Supervision of the work, including the production of the manuscript - Participation in the development of the concepts and ideas presented in the manuscript - Evaluation and editing of the manuscript prior to submission		
Signature		Date	

Self-noise of NACA 0012 and NACA 0021 airfoils at the onset of stall

Alex Laratro[a], Maziar Arjomandi[a], Benjamin Cazzolato[a], Richard Kelso[a]

[a]*School of Mechanical Engineering, The University of Adelaide, South Australia 5005, Australia*

Abstract

The aerodynamic noise of a NACA 0012 and NACA 0021 airfoil are measured and compared in order to determine whether there are differences in their noise signatures with a focus on the onset of stall. Measurements of the self-noise of each airfoil are measured in an open-jet anechoic wind tunnel at Reynolds numbers of 64,000 and 96,000, at geometric angles-of-attack from -5° through 40°at a resolution of 1°. Further measurements are taken at Re = 96,000 at geometric angles-of-attack from -5 through 16°at a resolution of 0.5°. Results show that while the noise generated far into the stall regime is quite similar for both airfoils the change in noise level at the onset of stall is significantly different between the two airfoils with the NACA 0021 exhibiting a much sharper increase in noise levels below a chord-based Strouhal number of $St_c = 1.1$. This behaviour is consistent with the changes in lift of these airfoils as well as the rate of collapse of the suction peak of a NACA 0012 airfoil under these flow conditions.

Keywords:
Stall noise, Aerodynamic noise, Airfoil noise

1. Introduction

Stall noise has not traditionally been a concern for aeronautical applications such as aircraft as the system is not intended to operate under stall conditions. This has lead to past research being largely focused on trailing-edge noise sources. However for turbomachinery the rotational motion of the blade contributes a large portion of the relative wind speed. Because the speed of the rotating blade changes along its span the angle-of-attack seen by each section of the blade can be quite different. To account for this many rotating blade designs incorporate twist, in order to achieve a more optimal angle-of-attack for a greater portion of the blades span at the expected operating condition. Away from this operating condition the combination of relative flow velocity and twist angle may lead to stall and in many cases deviating from the optimal conditions

Email address: alex.laratro@adelaide.edu.au (Alex Laratro)

is unavoidable. In the case of wind turbines this can be due to suboptimal wind speeds, the effect of which can be mitigated somewhat by pitch control, or unexpected non-uniformity or turbulence in the oncoming flow which is more transient and unpredictable. This has resulted in a need for more research into the nature of the noise generated at stall in order to devise new noise control methods.

A lot of research has gone into the measurement and analysis of trailing-edge noise, and continual improvements are being made to prediction methods [1, 2, 3, 4, 5, 6, 7]. Conversely the prediction of stall noise is still lacking, with most performed using the semi-empirical model of Brooks et al. [8, 9, 10] or through computational aeroacoustics methods [11]. The model of Brooks et al. produces third–octave spectra which are suitable for many applications but cannot well predict tonality if it is present. Further experimental measurements can be found in the literature but share the same low resolution in frequency and/or angle of attack [12]. More recently there has been an increase in interest in airfoil noise generated under stall and pre-stall conditions. This is driven by a desire for advances in noise control of wind turbines and other turbomachinery as noise production is a major restriction on where and when these systems can be operated.

A study by Moreau et al. in 2009 [13] is an substantial advancement in the measurement of airfoil noise under stall conditions, as it shows a detailed acoustic signature of an untripped NACA 0012 airfoil from 5° to 35° at a Reynolds number of 150,000. Figure 1 shows the results for two perpendicular airfoil mountings with Figure 1a showing the airfoil mounted with a low aspect ratio and high flow width (the ratio of airfoil chord to nozzle height) and Figure 1b showing the airfoil mounted with a high aspect ratio and low flow width. The main drawback of this setup is that the small amount of separation between the airfoil and the jet shear layer results in an interaction that results in substantial changes to the observed noise characteristics. By using a high resolution for the angle-of-attack and a lower frequency interval new detail was observed in the low aspect ratio setup, showing distinct peaks in the spectrum forming at stall, with their levels falling as the angle-of-attack is further increased until they give way to large-scale vortex shedding. Discovery of low-frequency peaks in the spectrum at stall indicates that existing stall models for applications such as wind turbine design may under-predict the noise generated and its effect on the surrounding environment.

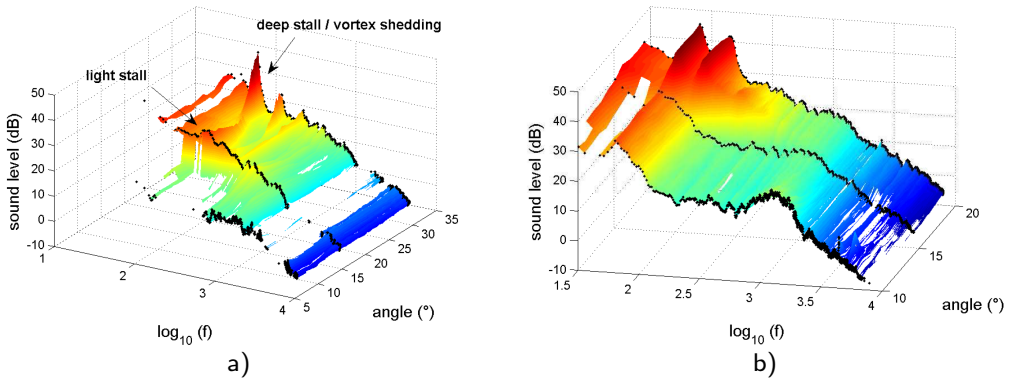

Figure 1: Frequency spectra of a NACA 0012 airfoil in high flow-width (left) and high flow-width (right) configurations [13]

Moreau et al.'s work also involved a large-eddy simulation of the airfoil flow-field around the airfoil mounted in the high aspect ratio configuration (Figure 1). The simulations indicated that the aforementioned shear-layer interaction was likely contaminating the results. The simulation results also indicated that there is vortex shedding near the leading edge due to boundary layer instabilities formed near separation. A frequency spectrum of these instabilities showed that they correspond to the large peaks observed after the onset of stall. A subsequent direct numerical simulation by Rodriguez et al.[14] on the NACA 0012 airfoil under stall conditions at a Reynolds number of 50,000 observed similar instabilities at much lower angles-of-attack. As shown in Figure 2 as the angle-of-attack is increased from 9.25° to 12° the leading edge instabilities become weaker and shift vertically further from the airfoil. Meanwhile, vorticity shed from the rear section of the airfoil becomes stronger and begins to engulf a wider area.

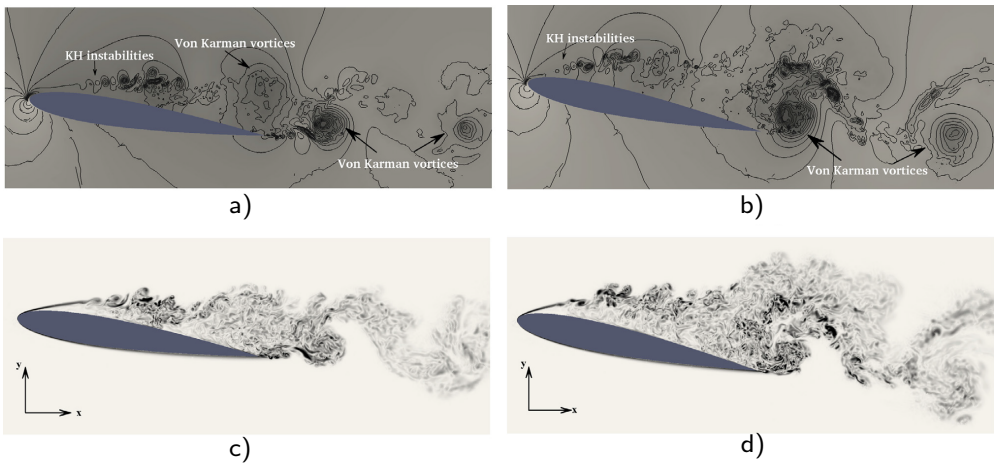

Figure 2: (a,b) Pressure contours for NACA 0012 at $\alpha = 9.25°$ and 12° respectively. (c,d) Vorticity contours for NACA 0012 at $\alpha = 9.25°$ and 12° respectively [14]

Understanding the characteristics of noise produced by airfoils under stall

conditions is therefore important if wind farms are to continue to grow while maintaining an acceptable acoustic footprint. Many people are unable to tolerate noise with spectral peaks or transience as well as broadband noise of the same level and this is often reflected in legislated noise limits [15, 16]. Large wind turbine designs employ thick cambered airfoils in contrast to the thin uncambered airfoils used for most research and it is unknown whether the different flow characteristics these profiles produce affect the noise produced at stall. To that end this research focuses on investigating potential differences in the characteristics of the stall noise of NACA 0012 and NACA 0021 airfoil, expanding on work presented at the Symposium of Fluid-Sound-Structure Interactions and Control [17]. The NACA 0021 profile has a thickness of 21% of chord which is more representative of current wind turbine airfoils (compared to a thickness of 12% of chord for the NACA 0012) while maintaining a simple uncambered shape. This airfoil's aerodynamic characteristics have also been well researched, though not to the extent of the NACA 0012, which makes it a logical step between the current knowledge base and real wind turbine airfoils.

2. Method

The experiment was conducted in the Anechoic Wind Tunnel at The University of Adelaide. This is a low speed wind tunnel with a 1.4m x 1.4m x 1.6m test chamber and foam wedge treated walls that are anechoic down to approximately 250Hz. The flow is driven by an upstream fan and passes through a silencer which mitigates upstream noise from the fan, and a settling chamber which conditions the flow before it reaches the nozzle. A bell mouth located on the other side of the anechoic chamber allows the flow to be discharged back into the still air in the wider laboratory. The open return design makes the flow susceptible to changes in environmental conditions and external gusts, but as the wind tunnel is located indoors and a large number of data is averaged to give the final results these effects were expected to be insignificant.

The wind tunnel nozzle has a height of 75mm and width of 275mm, which is too thin to conduct high angle-of-attack experiments when mounted horizontally, so the airfoil was mounted vertically. Compared to a normal horizontal setup this mitigates interaction between the airfoil and jet shear layer at high angles-of-attack.

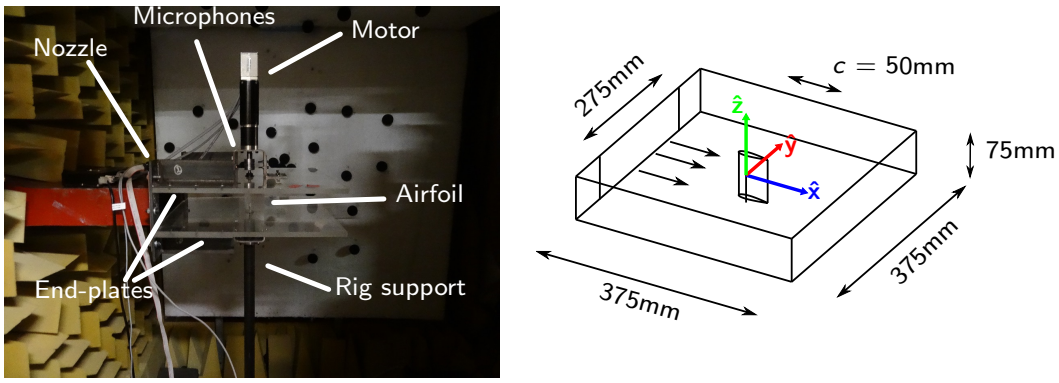

(a) Test setup diagram (b) Test setup dimensions

Figure 3: Experimental setup in the Anechoic Wind Tunnel

2.1. Test model

The chords of both the NACA 0012 and NACA 0021 airfoil models were chosen to be $c = 50$mm, which results in a chord-normalised nozzle size comparable to the experiments conducted by Moreau et al [13] as shown in Table 1. Furthermore a correction from geometric (α) to true angle-of-attack (α_t) is required to account for the finite height of the jet and a smaller chord decreases this reduction in angle [8]. For a chord of 50mm and a jet height of 275mm this correction takes the form $\alpha_t = 0.76\alpha$. The airfoils were also mounted between two perspex end-plates to constrain the flow into a more 2D flow regime, with spans of 73mm to give clearance for rotation.

Each end-plate extended 3.5 chord lengths upstream to give a wider potential microphone arc for future experiments and 3 chord lengths downstream to enable proper wake development. The use of hard-walled end-plates was however expected to increase the background noise level due to both the fluid-structure interaction noise and reflection of the airfoil noise leading to higher levels of noise at the microphones. These effects can be seen in the results shown in the next section and their effect on the results are briefly discussed. The plates were bolted to both the nozzle flange and a monopod to reduce deflection and support the weight of the rig. A servo-motor was attached to the airfoil shaft and used to remotely modify the angle-of-attack. Although the motor generated some noise while idle it could not be detected above the jet noise under the test conditions. The experimental setup is shown in Figure 3a along with a dimensioned diagram and coordinate system.

Table 1: Comparison of airfoil parameters with those from literature

	Current work		**Moreau et al.** [13]	
Nozzle size	75mm x 275mm		130mm x 300mm	300mm x 130mm
Airfoil profile	NACA 0012	NACA 0021	NACA 0012	
Chord	50mm		80mm	100mm
Span	73mm		130mm	300mm
Thickness	6mm	10.5mm	9.6mm	12mm
Aspect ratio	1.46		1.6	3
Relative flow width	5.5		3.8	1.3
Reynolds number	64,000 96,000		150,000	
Turbulent intensity	0.5		Not reported	

2.2. Side-plate boundary layer

Hot-wire measurements were conducted at the airfoil location to characterise the flow with the end-plates installed, the results of which are shown in Figure 4. These measurements show that the free-stream velocity is reached along approximately 70% of the airfoil span and that the turbulent intensity is below 0.5% in this region.

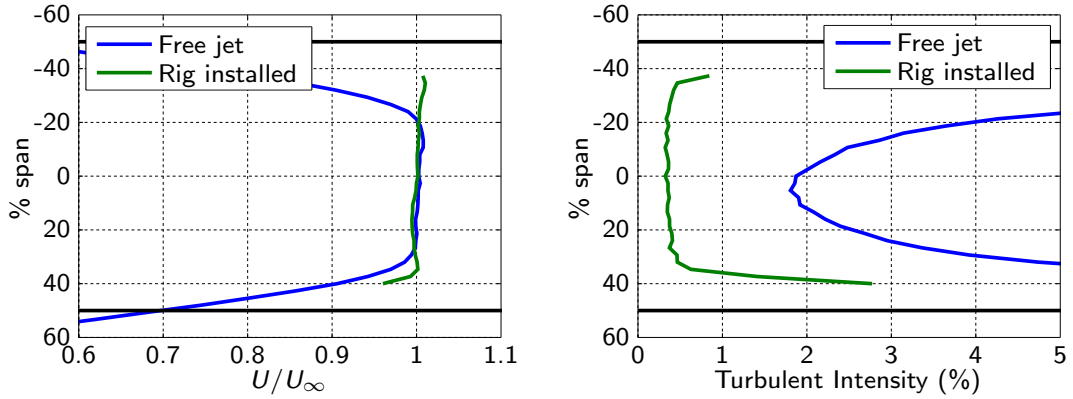

(a) Velocity profile (b) Turbulence profile

Figure 4: Flow profiles at $x = 0$, $y = 0$, $U_\infty = 30$m/s

2.3. Data collection & processing

The acoustic data were recorded using several of the GRAS 40PH 1/4" microphones in the side-wall microphone array in the Anechoic Wind Tunnel. Of the 31 microphones in the array, 13 did not have their line of sight to the airfoil blocked by the end-plates and so these were the microphones used in the experiment. Due to the low frequency of the noise being investigated compared to the spacing between the experimental setup and the array, and the small amount of separation between the microphones with line of sight beamforming was not available. The primary microphone (microphone 9) was located 0.61m at 91° from the rotation axis of the airfoil as shown in Figure 5 and was covered with a wind shield during testing. The acoustic data were collected in 10 consecutive 15s samples at a sampling frequency of 2^{15}Hz. Multiple consecutive samples

were used in lieu of one continuous sample to increase the ease of data storage and replacing samples contaminated by external noise or experimental error. Acoustic spectra were then calculated for each sample using Welch's method with a Hamming window of length 2^{13}Hz and an overlap of 50%. The spectra resulting from this were then averaged in the frequency domain to obtain the final spectrum for each case which has the parameters shown in Table 3.

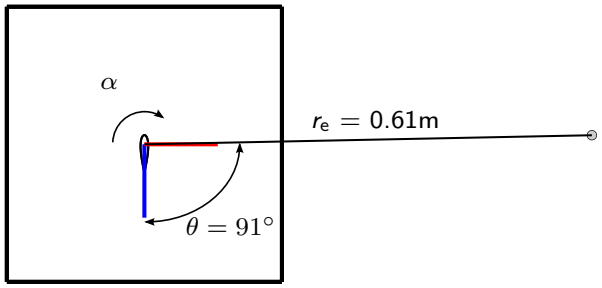

Figure 5: Primary microphone (microphone 9) location with respect to rotation axis of airfoil, microphones have line-of-sight to the suction side of the airfoil for positive angle-of-attack

Table 2: Microphone locations

	R(m)	$\theta(°)$	$\phi(°)$
Microphone 1	0.63	77	-0.9
Microphone 2	0.64	74	-0.9
Microphone 3	0.63	76	2.6
Microphone 4	0.62	80	1.3
Microphone 5	0.62	80	-3.1
Microphone 6	0.63	76	-4.4
Microphone 7	0.67	67	6.3
Microphone 9	0.61	91	-0.4
Microphone 11	0.67	67	-8.9
Microphone 16	0.73	57	-3.1
Microphone 19	0.64	108	-3.8
Microphone 22	0.81	49	-0.0
Microphone 29	0.69	117	6.2

Table 3: Parameters of data used to plot spectra

Sample rate	32768Hz
FFT length	8192
Resolution bandwidth	4Hz
Number of averages	1190

Acoustic data were collected for the NACA 0012 and NACA 0021 airfoils at 20ms^{-1} and 30ms^{-1} corresponding to Reynolds Numbers based on chord of 64,000 and 96,000 respectively. The airfoils were set to a geometric angle-of-attack of -5° and then the angle was increased in 1° increments until reaching 40°, the negative starting angle was chosen to enable correction of misalignment

when post-processing the data. Data with the higher angular resolution of 0.5° were also collected between -5° and 16° in subsequent tests for the 30ms^{-1} case. 16°was chosen as the upper limit for this test case as it is located past the stall point of the airfoils. Due to the possibility of error when performing initial alignment at the beginning of each session corrections are made during post-processing to correct for the starting misalignment by determining the point of symmetry in the noise levels around 0°. The amount of correction required changes between each case and the accuracy of the angle is limited by the resolution of the data. Due to the likelihood of the angle of misalignment differing slightly between them, the data sets for the 0.5° resolution and 1° resolution cases are kept separate.

3. Results

3.1. Acoustic spectra

Results for the 20ms^{-1} and 30ms^{-1} cases with 1° angular resolution are shown in Figures 6 and 7 respectively. Two features of the airfoil spectra are immediately evident. Above 25° in each case the airfoils display a series of distinct diagonal peaks. These peaks are due to large-scale vortex shedding as the airfoil begins to behave more like bluff body (deep stall) as described by Moreau et al. [13]. The Strouhal number with respect to frontal height ($St_h = f \cdot c \cdot \sin(\alpha)/U$) of these peaks begin to converge as the angle-of-attack increases, reaching a value of 0.18 at 40°. This value is typical of the bluff body vortex shedding regime for an airfoil, and the value is expected to converge to approximately 0.11 at 90° [18].

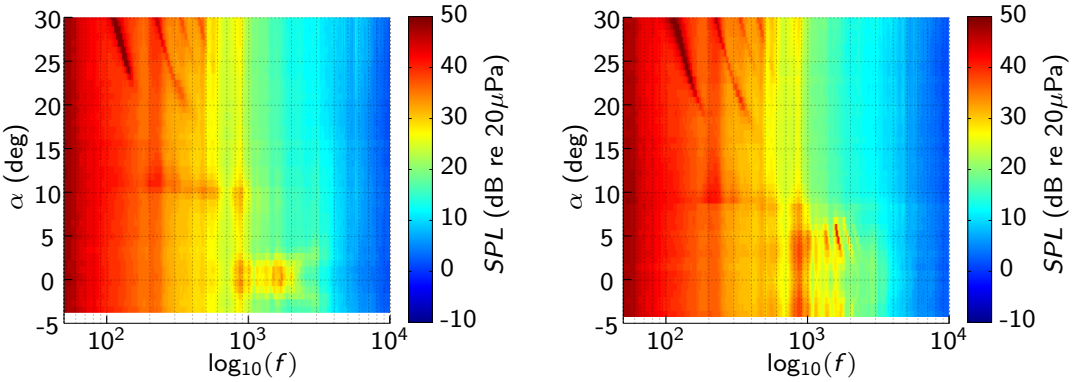

(a) NACA 0012 (b) NACA 0021

Figure 6: Spectra of airfoils at $U_\infty = 20\text{ms}^{-1}$, $Re = 64{,}000$, $\Delta\alpha = 1°$, $\Delta f = 4\text{Hz}$

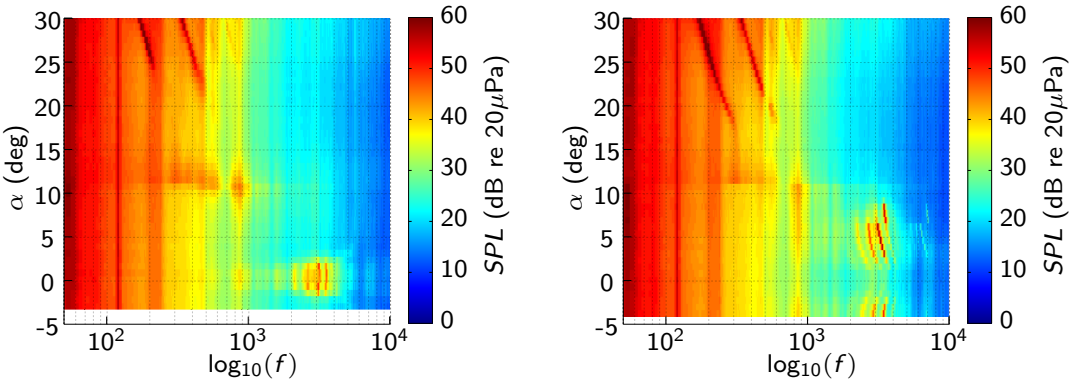

(a) NACA 0012 (b) NACA 0021

Figure 7: Spectra of airfoils at $U_\infty = 30\text{ms}^{-1}$, $Re = 96{,}000$, $\Delta\alpha = 1°$, $\Delta f = 4\text{Hz}$

From 0° to 3° for the NACA 0012 and 3° to 10° for the NACA 0021 high frequency tonal noise is observed. This is a well-documented behaviour of airfoils in this Reynolds number range which is thought to be due to an aeroacoustic feedback loop where the Tollmien-Schlichting waves in the boundary layer are excited by noise radiated by the convection of instabilities past the trailing edge [19]. NACA 0021 airfoils not producing tonal noise at 0° was previously documented by Hansen et al. [20] which may indicate that this profile consistently exhibits tonal noise that begins and ends at higher angles-of-attack than the NACA 0012 airfoil at these Reynolds numbers. Trailing edge tonal noise was also not observed at 0°in a simulation of an untripped NACA 0018 airfoil at a Reynolds number of 160,000 by Nakano et al. [21]. Trailing edge tonal noise is also known to not form in the prescence of a large adverse pressure gradient on both airfoil surfaces and some data indicates this condition may exist on the NACA 0021 at low angles of attack [22, 23]. However without a focused investigation it is difficult to determine conclusively as tonal noise patterns are extremely sensitive to experimental conditions [19, 20].

At 13° for the NACA 0012 airfoil and 15° for the NACA 0021 airfoil there is an increase in noise below 680Hz and a (smaller) decrease of noise above 680Hz, indicating that the airfoil has entered stall. The noise is concentrated into several peaks that are several dB above the broadband noise of the airfoil as previously documented [13]. Four features are labelled in Figure 8, which shows the changes of the frequency spectra of the airfoils in this range as the angles-of-attack are increased from a pre-stall regime through the onset of stall to the point where the noise signatures labelled *b)* and *c)* are greatest. From this point the noise in those regions decreases before giving way to the large peaks mentioned previously as the airfoil enters deep stall. In region *c)* the peaks share their frequency with peaks in the background noise. This indicates that the frequency of the peaks in this region may be influenced to a degree by the frequencies of instabilities in the jet.

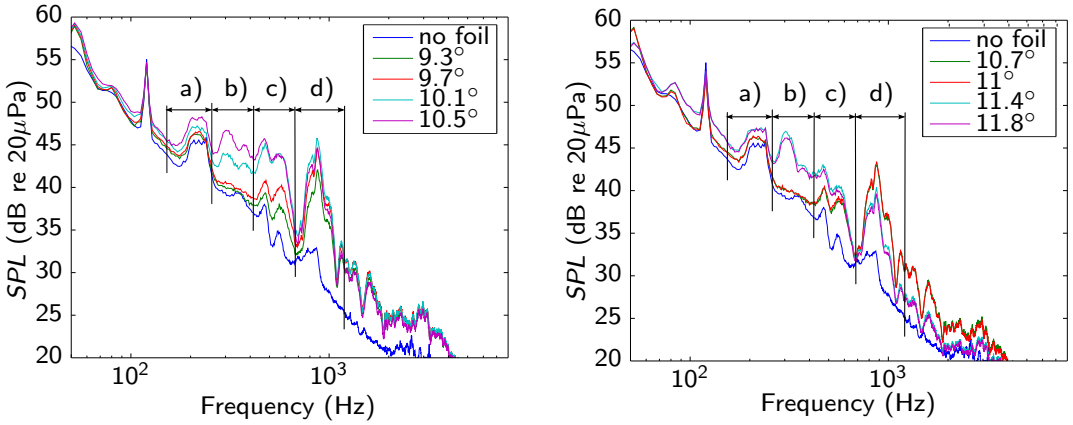

(a) NACA 0012 (b) NACA 0021

Figure 8: Spectra at $U_\infty = 30\text{ms}^{-1}$ in light stall regime with bands for a) f = 152–256Hz, b) f = 260–416Hz, c) f = 420–676Hz, d) f = 680–1196Hz marked

At 850Hz in all cases a wide peak labelled (region *d)*) can be observed, which is strongest at angles where the tonal and stall noise signatures occur. As this noise occurs at constant frequency and is only co-present with other noise sources it is thought to be enhanced or created by an aeroacoustic feedback effect within the wind tunnel. The peaks' rapid growth compared to other noise, as shown in Figure 8 lends weight to this hypothesis, however this feature of the spectrum also appears in the high flow-width data of Moreau et al. [13], though with a comparatively lower magnitude. Although attempts were made to eliminate this noise by changing the length of the end-plates to 145mm, with the airfoil axis located at 75mm from the nozzle. Large reductions were achieved along with a clearer signal for the peaks at stall, shown in Figure 9, unfortunately the high angle-of-attack vortex shedding peaks were also eliminated. This indicated that the aeroacoustic effect generating this noise could not be mitigated in this experimental setup without restricting the proper formation of the airfoil wake. After the flow exited the end-plates a large increase in turbulence was observed, and it was thought that by reducing the distance between the airfoil and the end of the plates that this sudden change in the flow was preventing the proper formation of the deep stall flow regime. While the signature of interest appeared clearer under these conditions it was decided that there was a risk of contamination due to the malformed wake and the results were not used.

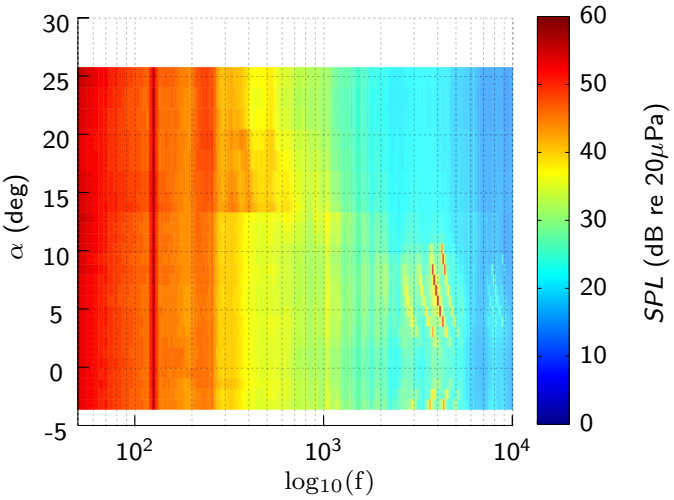

Figure 9: Spectra of NACA 0021 airfoil with shortened end plates at U_∞ =30ms^{-1}, Re = 96,000, $\Delta\alpha = 1°$, Δf = 4Hz

Two large peaks can be observed at 120Hz and 220Hz, which are roughly constant with angle-of-attack and remain when the airfoil is removed. The sharp peak at 120Hz is due to fan noise and the broader peak at 220Hz is produced by the end plates. However as shown in Section 3.3 the level of low-frequency noise in this region (labelled *a)*) still noticeably increases when the airfoil begins to stall. Also shown in Section 3.3 is that the peak values of the two peaks in regions c) and d) as well as the secondary peak in region b) have a lower maximum sound pressure level for the NACA 0021 than the NACA 0012, though this appears to be related to the difference in stall angles. The spectra of the airfoils for the 30ms^{-1} case are shown once again in Figure 10b with the features discussed in this section labelled.

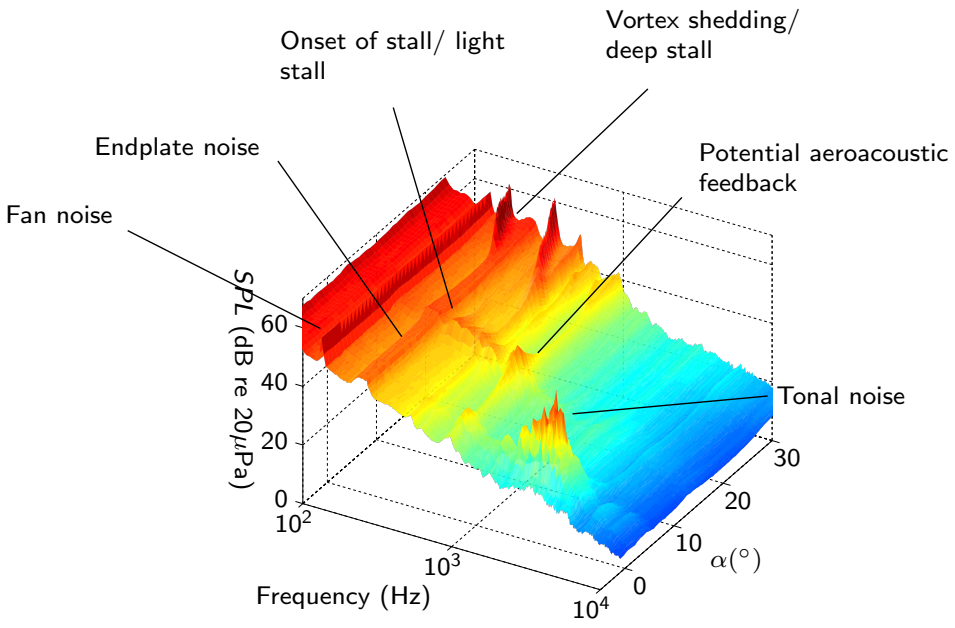

(a) NACA 0012

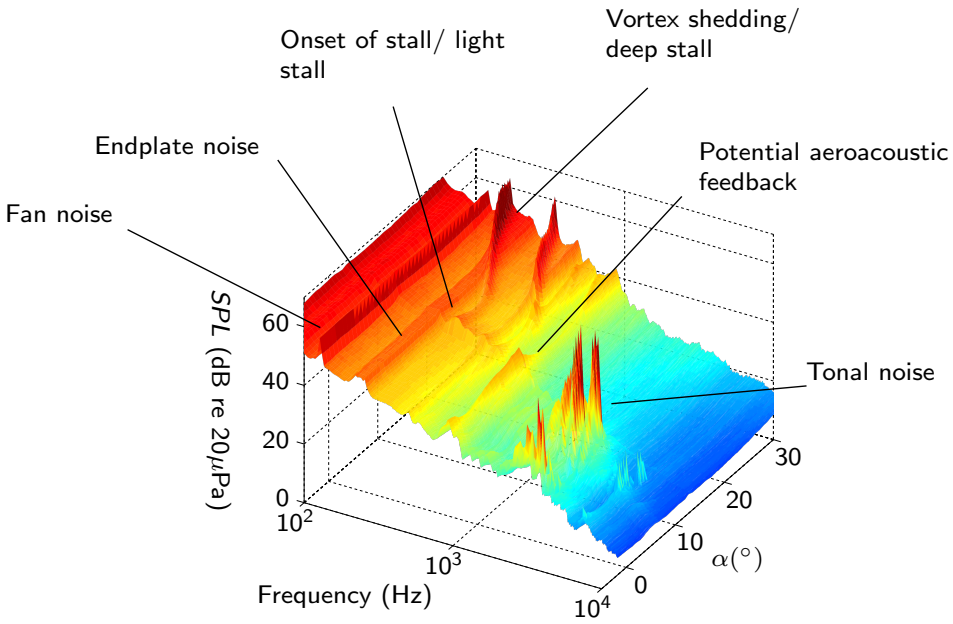

(b) NACA 0021

Figure 10: Spectra of airfoils at U_∞ =30ms^{-1}, Re = 96,000, $\Delta\alpha = 1°$, Δf = 4Hz

3.2. Comparison with literature

A DNS simulation by Rodriguez et al. [14], with a domain width of 20 chord lengths, showed that for a NACA 0012 airfoil wake vortices are shed at a frontal height-based Strouhal number ($St_h = f \cdot c \cdot \sin(\alpha)/U_\infty$) of 0.183 at 9.25°

when stall begins, and increases to 0.127 as the angle increases to 12°. When converted to a Strouhal number based on chord ($St_c = f \cdot c/U_\infty$) the values become 1.1 and 0.61 respectively. The four main peaks for the NACA 0012 in this case are located at chord-based Strouhal numbers of 0.52, 0.63, 0.8 and 0.94 and constant with frequency indicating that they are likely due to this vortex shedding phenomenon. There is no comparable flow-visualisation or simulation data for the NACA 0021 airfoil at these angles-of-attack and Reynolds numbers available in literature. However the formation of similar peaks in the noise spectrum indicates a similar vortex shedding phenomenon is likely the cause.

Rodriguez et al's simulation also shows a broadband peak in fluctuating pressure at frontal height-based Strouhal numbers of $St_h = 1.109$ and $St_h = 2.025$ for the 9.25° and 12° cases due to instabilities in the separated shear layer near the leading edge, and another peak at frontal height-based Strouhal numbers of 0.02, which corresponds to the low frequency oscillation of the separated shear layer. The high frequency signal does not appear in this work's data, however the low frequency peak at $St_h \approx 0.02$ is observed, most prominently around 10.5° as shown in Figure 11. Large-eddy simulation by Moreau et al. [13] indicated that instabilities in the separated boundary layer near the leading-edge similar to that observed by Rodriguez et al. were responsible for one of the low frequency peaks ($St_c = 0.34$) at high angles-of-attack in their low relative flow width case.

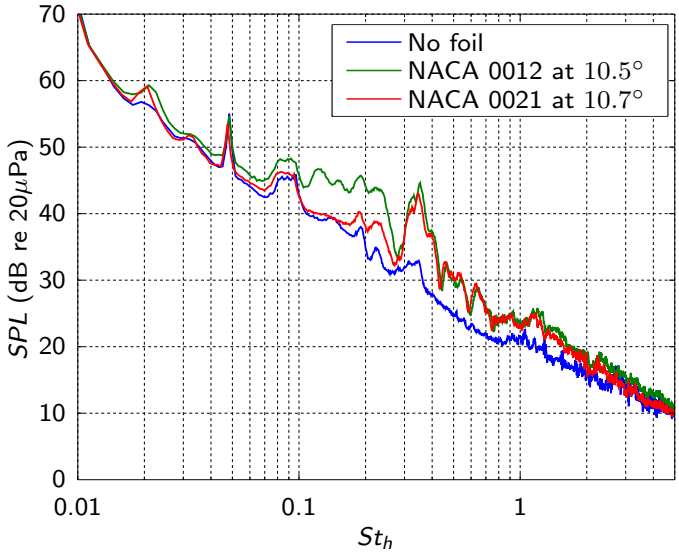

Figure 11: Spectra of NACA 0012 and NACA 0021 airfoils at $U_\infty = 30\text{ms}^{-1}$

3.3. Noise level profiles

Using the 0.5° (geometric) resolution data to calculate and plot the total noise levels across the bands *a)* to *d)* shown in Figure 8, it is easier to see the changes in noise during stall and the differences between the airfoils. Figure 12 shows there is a much clearer difference in both high and low frequency noise levels for the NACA 0021 airfoil when presented in this manner. Under these

conditions the NACA 0012 airfoil stall noise signature forms over a noticeably larger range of angles-of-attack than the NACA 0021, and it can be seen that the NACA 0012 stalls approximately 2°earlier. The stall noise formation of the NACA 0021 airfoil occurs over less than 0.4° (true), as opposed to a ramp up of noise level seen over a period of at least 0.8° (true) for the NACA 0012.

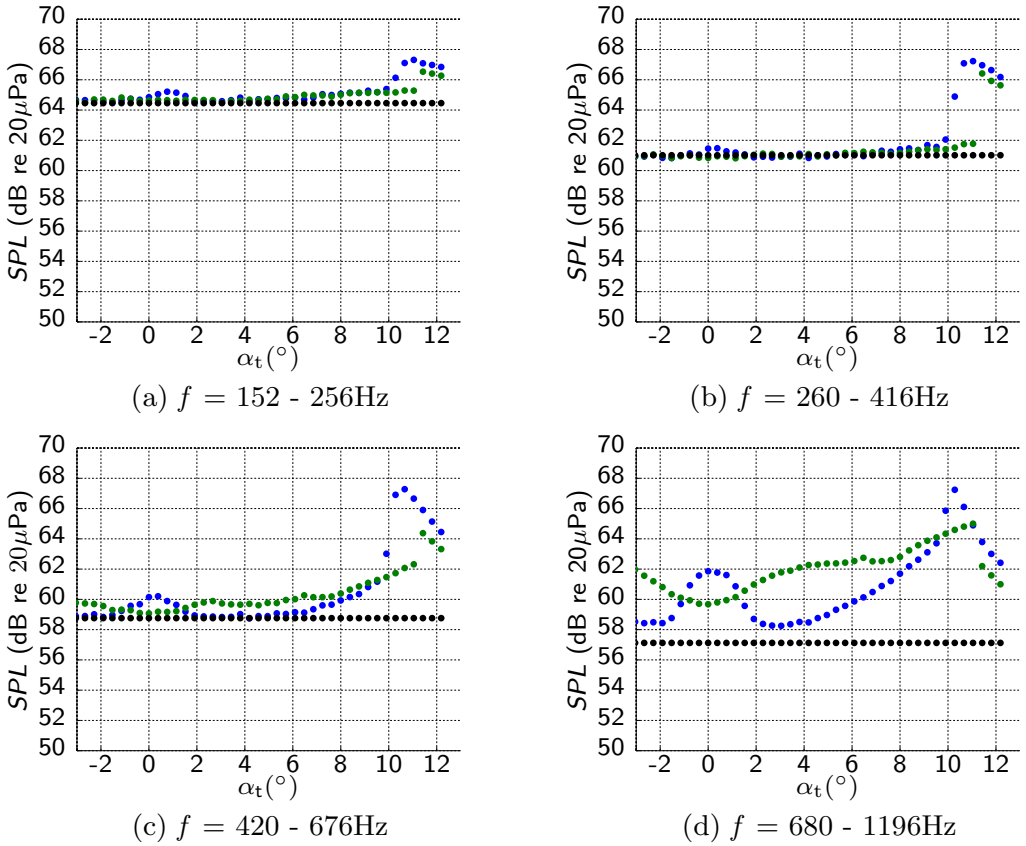

Figure 12: Sound pressure levels of each spectrum feature versus angle-of-attack. Blue - NACA 0012, Green - NACA 0021, Black - no airfoil

It is hypothesised that this is due to the differences in the rate at which stall occurs for the airfoils under these conditions. By comparing the lift curves near stall for the airfoils in this Reynolds number range it appears that the rate of change in noise level is indicated somewhat by the differences in the lift behaviour, with the NACA 0021 experiencing a much sharper decrease in lift at the onset of stall [24, 25, 26]. A slow change in flow-field and surface pressures of the NACA 0012 airfoil between pre-stall and stall flow regimes has been noted previously by Rodriguez et al. [14] at a Reynolds number of 50,000 , with a separation process that occurs over a range of angles-of-attack. This similarity may seem self-evident, but as far as the authors are aware this possibility has not been discussed in the literature. It should also be noted that this difference in the rate of stall noise formation may not hold at higher Reynolds numbers where the stall of the NACA 0012 can become more sudden like that observed for the NACA 0021 under these experimental conditions.

Figure 13 shows the sound pressure level of the primary light stall band at 260-416Hz for 8 of the 13 microphones used in the experiment. Microphones 1 through 6 are located in a small cluster and so produce very similar data. It can be seen that there is an increase in SPL in this band of approximately 6dB for the NACA 0012 and 5dB for the 0021 at stall for Microphones 6, 7, 9 and 11. For the microphones that are further away and at a greater angle to the airfoil the noise level drops slightly as expected. The smallest increase is seen at microphones 22 and 29, which are located upstream of the airfoil and close to the chordline where the noise from stall is expected to be lowest given a dipolar directivity.

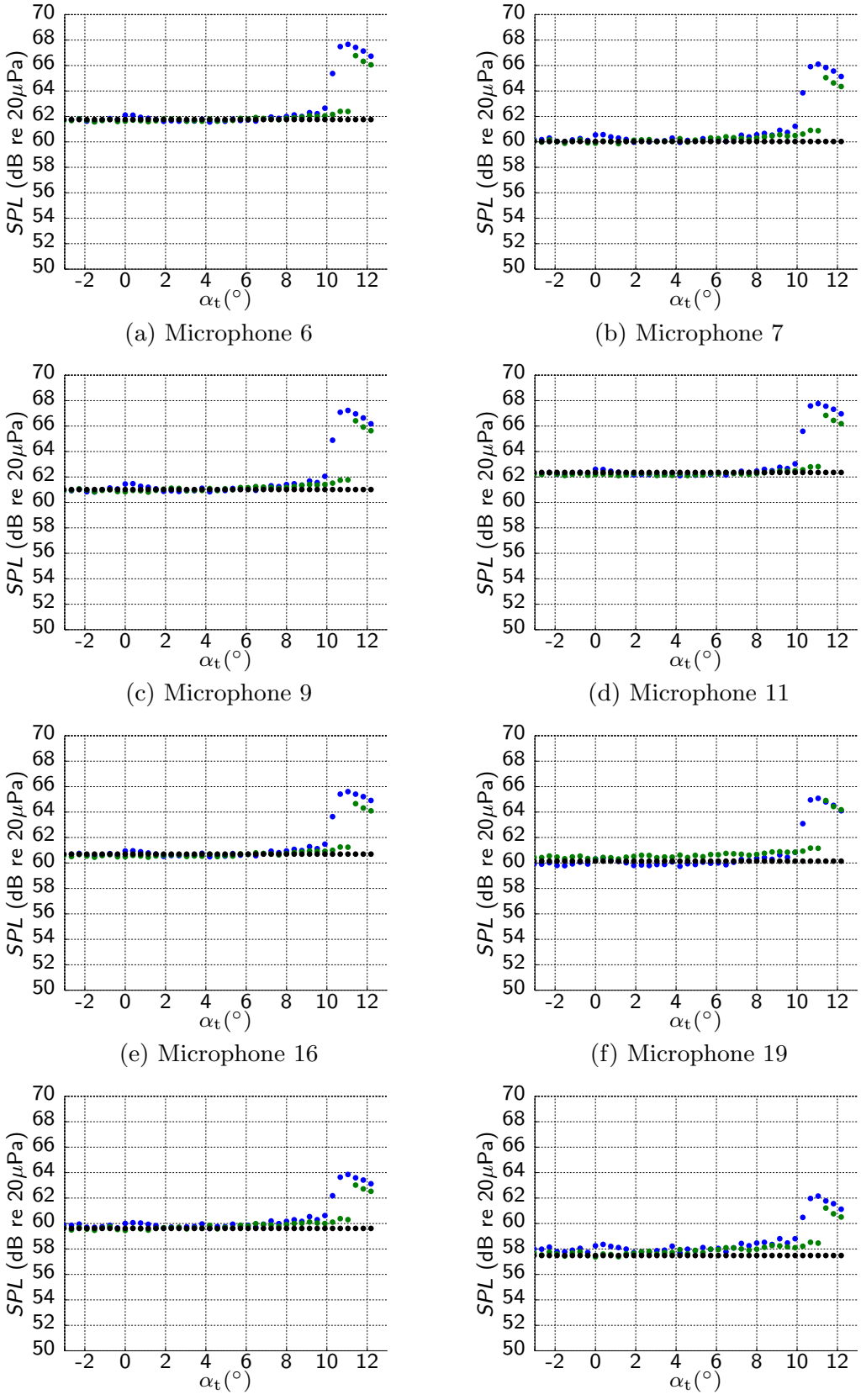

(a) Microphone 6

(b) Microphone 7

(c) Microphone 9

(d) Microphone 11

(e) Microphone 16

(f) Microphone 19

(g) Microphone 22

(h) Microphone 29

Figure 13: Sound pressure levels of the f = 260-416Hz band at each microphone. Blue - NACA 0012, Green - NACA 0021, Black - no airfoil

4. Conclusion

The noise signatures of a NACA 0012 and NACA 0021 airfoil with chord lengths of 0.05m were measured experimentally at Reynolds Numbers of 64,000 and 96,000 in an open-jet wind tunnel with a flow-width of 5.5. Measurements were taken at angles-of-attack from -5° to 40° at a resolution of 1° and from -5° to 16° at a resolution of 0.5°. At the onset of stall an broadband increase in noise level was observed below $St_c = 1.1$ and a broadband decrease in noise level was observed above $St_c = 1.1$. There was a greater increase in low frequency noise level between $St_c = 0.4$ and $St_c = 1.1$ than lower frequencies, which is in line with the range of leading-edge and wake vortex shedding of the NACA 0012 airfoil at stall from simulations in the literature. In this range the noise is concentrated into several peaks at chord-based Strouhal numbers of $St_c = 0.52$, 0.63, 0.8 and 0.94. Of these, the frequency of the peaks at $St_c = 0.8$ and $St_c = 0.94$ are may be due to coupling with existing flow instabilities in the wind tunnel. Overall the noise level produced at stall was slightly higher for the NACA 0012 airfoil, and the secondary peak was more pronounced. This indicates that the thicker NACA 0021 profile has a more desirable noise signature when operating under stall conditions.

The data also show that under these conditions the formation of these peaks is significantly more rapid for the NACA 0012 airfoil. The transition of the low frequency noise into peaks at stall occurs over a range of at least 0.8°(true) for the NACA 0012 and less than 0.4°(true) for the NACA 0021. This is in agreement with both the rate of change of lift for both airfoil profiles at these Reynolds Numbers as well as the collapse of the suction peak of the NACA 0012. This indicates that some information about the rate of formation of stall noise peaks can be inferred from the aerodynamics of the airfoil which is useful information for modelling moderate Reynolds number airfoils that must operate under stall conditons, such as on small wind turbines.

[1] Paterson, R. W., Vogt, P. G., Fink, M. R., and Munch, C. L. Vortex noise of isolated airfoils. *Journal of Aircraft 10*, 5 (1973), 296–302.

[2] Amiet, R. Noise due to turbulent flow past a trailing edge. *Journal of sound and vibration 47*, 3 (1976), 387–393.

[3] Brooks, T. F., and Hodgson, T. Trailing edge noise prediction from measured surface pressures. *Journal of sound and vibration 78*, 1 (1981), 69–117.

[4] Parchen, R. R. *Progress report DRAW: A prediction scheme for trailing edge noise based on detailed boundary layer characteristics*. TNO Institute of Applied Physics, (1998).

[5] Kamruzzaman, M., Lutz, T., Würz, W., Shen, W. Z., Zhu, W. J., Hansen, M. O. L., Bertagnolio, F., and Madsen, H. A. Validations and improvements of airfoil trailing-edge noise prediction models using detailed experimental data. *Wind Energy 15*, 1 (2012), 45–61.

[6] Kamruzzaman, M., Bekiropoulos, D., Wolf, A., Lutz, T., and Kraemer, E. Rnoise: A RANS based airfoil trailing-edge noise prediction model. In *20th AIAA/CEAS Aeroacoustics Conference, AIAA AVIATION Forum* (2014).

[7] Pröbsting, S., Scarano, F., and Morris, S. Regimes of tonal noise on an airfoil at moderate Reynolds number. *Journal of Fluid Mechanics 780* (2015), 407–438.

[8] Brooks, T. F., Pope, D. S., and Marcolini, M. A. *Airfoil self-noise and prediction*. National Aeronautics and Space Administration, Office of Management, Scientific and Technical Information Division, (1989).

[9] Lee, G.-S., Cheong, C., Shin, S.-H., and Jung, S.-S. A case study of localization and identification of noise sources from a pitch and a stall regulated wind turbine. *Applied Acoustics 73*, 8 (2012), 817–827.

[10] Oerlemans, S. Effect of wind shear on amplitude modulation of wind turbine noise. *International Journal of Aeroacoustics 14*, 5–6 (2015), 715–728.

[11] Kamruzzaman, M., Lutz, T., Arnold, B., Bekiropoulos, D., Illg, J., Krämer, E., Wolf, A., Hann, R., and Kamruzzaman, M. Prediction of flow-induced noise sources of wind turbines and application examples. *International Journal of Aeroacoustics 14*, 5–6 (2015), 675–714.

[12] Wasala, S. H., Storey, R. C., Norris, S. E., and Cater, J. E. Aeroacoustic noise prediction for wind turbines using Large Eddy Simulation. *Journal of Wind Engineering and Industrial Aerodynamics 145* (2015), 17–29.

[13] Moreau, S., Roger, M., and Christophe, J. Flow features and self-noise of airfoils near stall or in stall. In *15th AIAA/CEAS Aeroacoustics Conference* (2009).

[14] Rodríguez, I., Lehmkuhl, O., Borrell, R., and Oliva, A. Direct numerical simulation of a NACA 0012 in full stall. *International Journal of Heat and Fluid Flow 43* (2013), 194–203.

[15] Berger, R. G., Ashtiani, P., Ollson, C. A., Aslund, M. W., McCallum, L. C., Leventhall, G., and Knopper, L. D. Health-based audible noise guidelines account for infrasound and low-frequency noise produced by wind turbines. *Frontiers in Public Health 3*, 31 (2015).

[16] Lee, J., and Wang, L. Assessment of noise-induced annoyance by tones in noise from building mechanical systems. In *43rd International Congress on Noise Control Engineering* (2014).

[17] Laratro, A., Arjomandi, M., Cazzolato, B., and Kelso, R. A comparison of NACA 0012 and NACA 0021 self-noise at low Reynolds number. In *Fluid-Structure-Sound Interactions and Control* (2016), Springer, pp. 21–25.

[18] Huang, R. F., and Lin, C. L. Vortex shedding and shear-layer instability of wing at low-Reynolds numbers. *AIAA Journal 33*, 8 (1995), 1398–1403.

[19] Arcondoulis, E., Doolan, C., and Zander, A. C. Airfoil noise measurements at various angles of attack and low Reynolds number. In *Proceedings of Acoustics 2009: Research to Consulting* (2009), pp. 23–25.

[20] Hansen, K., Kelso, R., and Doolan, C. Reduction of flow induced tonal noise through leading edge tubercle modifications. In *16th AIAA/CEAS Aeroacoustics Conference* (2010).

[21] Nakano, T., Fujisawa, N., and Lee, S. Measurement of tonal-noise characteristics and periodic flow structure around NACA 0018 airfoil. *Experiments in Fluids 40*, 3 (2006), 482–490.

[22] Nash, E. C., Lowson, M. V., and McAlpine, A. Boundary-layer instability noise on aerofoils. *Journal of Fluid Mechanics 382* (1999), 27–61.

[23] Choudhry, A., Arjomandi, M., and Kelso, R. A study of long separation bubble on thick airfoils and its consequent effects. *International Journal of Heat and Fluid Flow 52* (2015), 84–96.

[24] Greenblatt, D., and Wygnanski, I. Effect of leading-edge curvature and slot geometry on dynamic stall control. In *1st Flow Control Conference, Fluid Dynamics and Co-located Conferences* (2002).

[25] Marchman, F., Gunther, C., and Gundlach, J. Semi-span testing at low Reynolds number. In *36th AIAA Aerospace Sciences Meeting and Exhibit* (1998).

[26] Rostmzadeh, N., Kelso, R.M.and Dally, B., and Hansen, K. The effect of wavy leading edge modifications on NACA 0021 airfoil characteristics. In *Proceedings of the 18th Australasian Fluid Mechanics Conference* (2012).

Chapter 5

Symmetric Airfoil Self-Noise and Directivity

5.1 Chapter overview

New data regarding the noise generated by NACA 0012 and NACA 0021 airfoils experiencing stall (Chapter 4) highlighted a previously unreported phenomenon. As the airfoils begin to stall, the increase in the low-frequency noise generated correlates with the loss of lift, and the rate of change of the formation of this noise source with respect to angle of attack is significantly different for each airfoil. However, with only two airfoil models, a trend between the low-frequency noise generation and the airfoil profile thickness could not be established. In addition to this, the source of the noise was still undetermined.

The primary objective of the experiments presented in this chapter was to gather data on the directivity of the airfoil models from the preliminary experiments detailed in Chapter 4. In addition, it was intended to relate this data the existing flow-field measurements and wake spectra from the literature. A third airfoil model, a flat plate, was added to the experimental campaign for which there was a large amount of existing flow-field knowledge to draw from in the analysis.

The experiments presented in this chapter produced three main results. Firstly, the data showed that the observed low-frequency noise of all three airfoils was well matched to a convected dipole oriented normal to the airfoil, whereas before stall the noise did not show such highly directional behaviour. This result was expected from theory and previous experiments on the sound generated by a NACA 0012 airfoil, but the applicability to other airfoil profiles had not been experimentally confirmed.

Secondly, by obtaining measurements of the low-frequency sound pressure level at the onset of stall with a high angle-of-attack resolution, more insight was gained into the formation of the noise source. A smoother curve was produced by the NACA 0012 airfoil

but the transition of the NACA 0021 airfoil remained sharp. Even with a 0.1°angle of attack spacing, the only transitional behaviour observed was a single angle of attack where the airfoil oscillated between its stalled and unstalled states before settling into the stalled state when the angle was further increased. These observations were corroborated by wake measurements which showed that the NACA 0021 airfoil suddenly began shedding low-frequency turbulence into the wake at stall, whereas the NACA 0012 displayed a smoother transition behaviour. The flat plate demonstrated behaviour that was disimilar to the NACA profiles, forming a low frequency noise source over a much wider angle of attack range.

Thirdly, by comparing the observed changes in sound and wake velocity spectra with flow-field data from the literature, conclusions could be drawn about the source of the noise produced under light-stall conditions. The primary low-frequency noise source during light stall was found to be vortex shedding due to boundary layer separation on the airfoil. While the flow is mostly fully separated at this stage, the shear layer remains close enough to the surface of the airfoil that it does not display the coherent vortex shedding characteristic of a bluff body. Once the angle increases further, the shear layer moves further from the surface and the large-scale coherent vortex shedding mode appears.

A pre-print manuscript based on this experiment was submitted to Applied Acoustics and is presented in the next section, with the published version of the article available at doi:10.1016/j.apacoust.2017.05.027. It presents the noise and wake velocity spectra of the airfoils as well as the changes in low-frequency noise with angle of attack. A computational simulation of the flow field around the NACA 0012 airfoil under similar conditions was conducted by another researcher at The University of Adelaide, further illustrating the separation pattern under the light stall condition. The results of this simulation (the manuscript is provided in Appendix B) show that at a geometric angle of attack of $18°(\alpha_t = 13.7°)$ the flow is fully separated but the airfoil is not yet acting as a bluff body. In addition to this, the airfoil is seen to shed pressure dipoles in the direction of the chord line. These pressure dipoles are seperated by a region of more turbulent wake without coherent structure, which may explain why coherence between wake velocity and far-field sound was not observed in the experiments.

5.2 Measurements of airfoil self-noise, directivity, and wake velocity at stall

Statement of Authorship

Title of Paper	Self-noise and directivity of simple airfoils during stall: An experimental comparison
Publication Status	☑ Published ☐ Accepted for Publication ☐ Submitted for Publication ☐ Unpublished and Unsubmitted w ork w ritten in manuscript style
Publication Details	Laratro, A., Arjomandi, M., Kelso, R., and Cazzolato, B. Self-noise and directivity of simple airfoils during stall: An experimental comparison. Applied Acoustics 127 (2017), 133-146

Principal Author

Name of Principal Author (Candidate)	Alex Laratro		
Contribution to the Paper	- Data collection, analysis, visualisation, and interpretation - Writing of the manuscript and production of original figures - Correspondence with editor and reviewers including the production of all cover letters and rejoinders		
Overall percentage (%)	80%		
Certification:	This paper reports on original research I conducted during the period of my Higher Degree by Research candidature and is not subject to any obligations or contractual agreements with a third party that would constrain its inclusion in this thesis. I am the primary author of this paper.		
Signature		Date	

Co-Author Contributions

By signing the Statement of Authorship, each author certifies that:

i. the candidate's stated contribution to the publication is accurate (as detailed above);

ii. permission is granted for the candidate to include the publication in the thesis; and

iii. the sum of all co-author contributions is equal to 100% less the candidate's stated contribution.

Name of Co-Author	Maziar Arjomandi		
Contribution to the Paper	- Supervision of the work, including the production of the manuscript - Participation in the development of the concepts and ideas presented in the manuscript - Evaluation and editing of the manuscript prior to submission		
Signature		Date	

Name of Co-Author	Benjamin Cazzolato		
Contribution to the Paper	- Supervision of the work, including the production of the manuscript - Participation in the development of the concepts and ideas presented in the manuscript - Evaluation and editing of the manuscript prior to submission		
Signature		Date	

Name of Co-Author	Richard Kelso		
Contribution to the Paper	- Supervision of the work, including the production of the manuscript - Participation in the development of the concepts and ideas presented in the manuscript - Evaluation and editing of the manuscript prior to submission		
Signature		Date	

Self-noise and directivity of simple airfoils during stall: An experimental comparison

Alex Laratro[a], Maziar Arjomandi[a], Benjamin Cazzolato[a], Richard Kelso[a]

[a]*School of Mechanical Engineering, The University of Adelaide, South Australia 5005, Australia*

Abstract

Noise measurements of NACA 0012, NACA 0021 and flat plate airfoils are obtained at a Reynolds number of 96,000, at angles of attack ranging from -30°to 30°. As the airfoils enter a separated flow regime a dipolar low-frequency noise source was observed which the literature indicates is the result of incoherent vorticity formed in the separated flow. As the angle of attack is increased a dipolar low frequency noise source forms. This noise source grows in strength over a much smaller range of angles as the thickness of the airfoils is increased, causing the sound pressure level of the NACA 0021 airfoil in this frequency range to increase sharply. This is consistent with the observed impulsive noise signatures sometimes obversed in wind turbine noise measurements, indicating that they may be generated by a similar noise source.

Keywords:
Stall noise, Aerodynamic noise, Airfoil noise

1. Introduction

Self-noise of airfoils immersed in a moving fluid is one of the foremost topics of aeroacoustics and is of great interest to both the aeronautical and maritime industries. Much of the work in this area is still based on the pioneering work of Brooks et al. [1] who measured the noise generated by several airfoils at various Reynolds numbers and angles of attack and provided a semi-empirical framework for modelling the noise. Their work was primarily focused on the noise generated by the laminar and turbulent boundary layers at low angles of attack as these are the components of airfoil noise most often encountered by and therefore of most interest to industry. The work of Brooks et al. followed from that of Paterson et al. [2] on airfoil-tip vortex interaction, where a large increase in far-field noise and surface pressure fluctuations was observed between 250Hz and 1000Hz at stall. This phenonemon was subsequently noted by Fink & Bailey [3] when investigating airframe noise control methods, with increases

Email address: alex.laratro@adelaide.edu.au (Alex Laratro)

of up to 10dB in the noise level at stall. These publications agreed that the source of the noise near stall angles was eddies in the separated boundary layer radiating from the trailing-edge. However there has been little interest in the spectrum and directivity of noise generated by stalling airfoils since, as airfoils usually operate outside of the stall regime.

However, recently the wind industry has shown some interest in this noise as when a turbine airfoil stalls its noise spectrum shifts to lower frequencies and its directivity changes, meaning that the noise will travel further in the upstream and downstream directions [4, 5]. Stall can occur on wind turbine or fan blades due to a variety of unpredictable factors such as unsteady inflow operation in the wake of upstream disturbances [6]. In the case of industrial fans, stall can also be caused by too large a pressure change across the fan and is generally avoided using passive stall control systems [7]. In the case of a pitch-regulated wind turbine, the pitch of the blades is constantly modified to maintain a target angle of attack and optimise power generation. In this case a large spatial or temporal variation in inflow velocity that occurs in either a small area or over a small period of time can be difficult for the pitch-control system to account for and therefore leads to part of the blade stalling for some portion of each revolution. Accounting for this can be done with either active or passive stall-control mechanisms, or modifications to the pitch control system [4, 5]. This is of concern to the wind power industry as it could reduce the power that can be generated in a given area in order to comply with noise limits. Furthermore, a lack of information about the noise generated by airfoils near their stall angle makes optimisation of these factors challenging. As seen in recent noise predictions by Oerlemans & Schepers [8], wind turbine noise prediction uses the model of Brooks et al. [1] in order to predict the noise after stall. This approach models the onset of stall as a sudden change in the governing equations when the airfoil stalls, which can fail to capture nuances of the transition.

In recent years Moreau et al. [9] have collected data on the noise generated near stall that indicates that further investigation into the change in noise during the transition to a stalled state may be warranted. It was found that the noise generated by a NACA 0012 airfoil at the onset of stall exhibits broad low-frequency peaks before decaying and giving way to the better-known tones from large-scale separation (shown in Figure 1a). This regime, referred to as "light stall", is of great interest because it is characterised by a non-trivial rise and decay. As wind turbine blades are more likely to unexpectedly encounter small variations in angle of attack, leading to this flow regime, properly modelling this transition is important for accurately modelling the sound generated by wind turbines in operation. However Moreau et al. [9] also noted that the experimental conditions greatly affected the noise production. While the results described above are from an experiment with an airfoil with a 130mm span in a 300mm high jet, results from an airfoil of a 300mm span in a 130mm high jet were also presented (shown in Figure 1b). When the self-noise of the airfoil in the narrower jet was measured, the light stall regime was not observed and the peaks from large scale vortex shedding were formed at a much lower angle of

attack. While a computational analysis of the flow-field was performed, it was undertaken on the narrow jet airfoil setup. Analysis of the computational results indicated that there was some coupling between the flow around the airfoil and the shear layer of the jet which may have been responsible for the change in stall pattern. Investigation of the narrow jet stall noise at moderate angles of attack indicated that the main noise source was vorticies produced due to instabilities in the airfoil shear-layer near the leading edge. This is not representative of the usual "deep stall" regime which is characterised by large-scale vortex shedding similar to that of a bluff body.

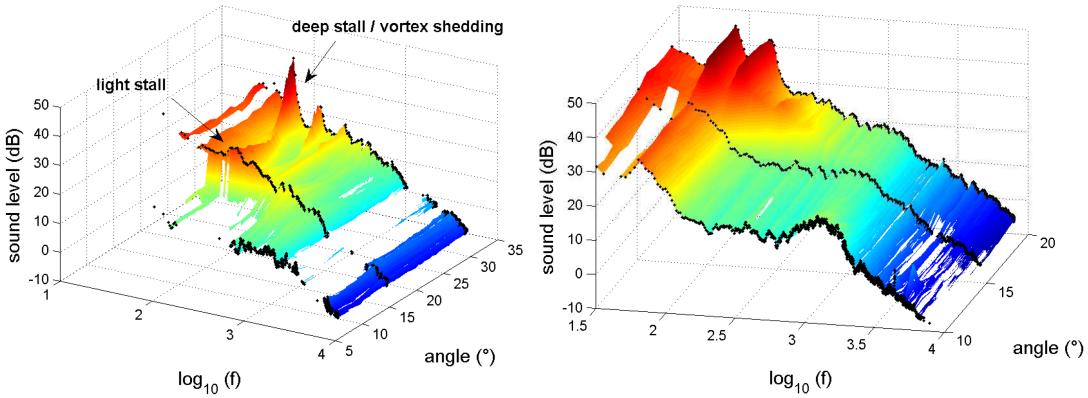

(a) Wide jet setup (b) Narrow jet setup

Figure 1: NACA 0021 self-noise map [9]

Due to the limited information about the noise generated near the stall angle, more experiments are required to characterise the noise produced in this regime. This will both help to direct future research and begin to strengthen the literature available to industry when tackling this issue. To that end the present research aims to gain an understanding of the spectrum and directivity of the self-noise of some common airfoils at low Reynolds numbers, which when combined with previous results, will provide a stronger framework for future research in this area. This is achieved by gathering data with a higher resolution in both frequency and angle of attack from multiple locations, and then analysing the directivity of the noise generated under stall conditions. Whilst the results are not directily applicable to wind turbines, the insight gained can be used to guide future experiments under more representative conditions.

2. Method

In modern wind turbines several airfoils profiles are typically employed along the length of the blade due to the different inflow conditions experienced at different radii. Aerodynamic research reported in the literature often approximates the complex, often proprietary airfoil designs found on these turbines as simpler designs such as the NREL S809, the NACA 44xx and the NACA 6 series

[10, 11, 12]. In previous work, simple 4-digit NACA airfoils such as the NACA 0015 through NACA 0021 were often used for aerodynamics research intended to be further developed for wind turbine applications [13, 14]. For this study the NACA 0021 was chosen as this the thick airfoil profile. For comparison, data from two more test models were collected. Firstly, the NACA 0012, as a large amount of aerodynamic research has been performed with it, as well as much of the existing research into self-noise near stall. The final test model used was a flat plate, which like the NACA 0012 has been the subject of a large amount of aerodynamic research. Furthermore common aeroacoustic models use a thin plate as their basis [1, 9, 15].

Data were collected in the open-jet Anechoic Wind Tunnel at the University of Adelaide. The wind tunnel consists of a 75mm high by 275mm wide rectangular nozzle in a 1.4m by 1.4 by 1.6m chamber which is acoustically treated with foam wedges, making it anechoic down to 250Hz. Due to the low nozzle height, attempting high angle of attack airfoil experiments in this wind tunnel using a horizontally hinged airfoil would result in a large amount of shear-layer-airfoil interaction which will heavily affect the results [9]. Because of this the airfoil was mounted vertically, which significantly increases the distance between the airfoil model and the jet's shear layer but decreases the airfoil surface area and therefore the noise produced. The data were collected at a free-stream velocity of 30ms^{-1} which corresponds to a Reynolds number of 96,000. This Reynolds number was chosen as aerodynamic data for the NACA 0021 at $Re = 100{,}000$ had been previously recorded at the University of Adelaide, and more $Re = 100{,}000$ data is present in the literature for the other test models. Using $Re = 96{,}000$ also enables comparison with the noise data of Moreau et al.[9] which were recorded at a Reynolds number of 150,000.

2.1. Test models

Due to the restrictions of the nozzle, the span of the test model was limited to a maximum of 73mm, providing a 1mm clearance from the end-plates. A 50mm chord was chosen as a compromise between aspect ratio, planform area and blockage. A larger chord would result in a lower aspect ratio and more interference with the jet which was undesirable, and a smaller chord would further reduce the surface area and adversely impact the signal-to-noise ratio. In addition to this the true angle of attack, which is the angle of attack experienced by the airfoil after accounting for jet deflection, is given by $\alpha_{\text{t}} = \alpha_{\text{g}}/\zeta$, where α_{g} is the geometric angle of attack and ζ increases non-linearly with the ratio between chord and jet height. In the case of this experiment $\zeta \approx 1.3$ in a vertical configuration used compared to a value of 2.45 in a hypothetical horizontal configuration, which is overly restrictive for high angle of attack measurements. The airfoil parameters and those from the work of Moreau et al. [9] are compared in Table 1. The relative flow width is the ratio of jet width to airfoil chord. Low values of this parameter result in interaction between the airfoil wake and the jet shear layer, leading to corruption of the noise measurements [9].

Table 1: Comparison of airfoil parameters with those from literature

	Present work			**Moreau et al.** [9]	
Nozzle size	75 x 275mm			130 x 300mm	300 x 130mm
Airfoil profile	NACA 0012	NACA 0021	Flat plate	NACA 0012	
Chord	50mm			80mm	100mm
Span	73mm			130mm	300mm
Thickness	6mm	10.5mm	4mm	9.6mm	12mm
Aspect ratio	1.46			1.6	3
Relative flow width	5.5			3.8	1.3

The airfoil test setup, shown in Figure 3, consists of the test airfoil coupled to a brushless DC motor and held between two acrylic end-plates. These end-plates constrain the flow and reduce the rate at which the shear layer forms as shown in Secton 2.2. The inward-facing surfaces of the end-plates were smooth except for the holes for the airfoil shaft, with all of the mounting components located on the opposite side.

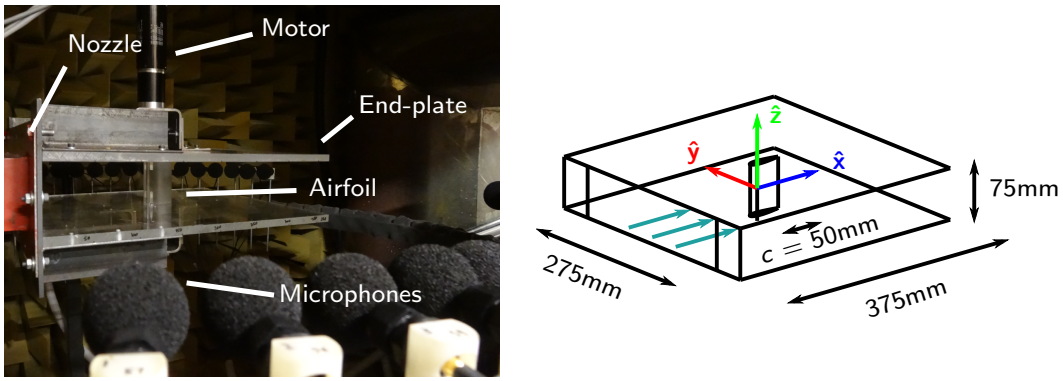

(a) Test setup diagram (b) Nozzle and end-plate dimensions

Figure 2: Experimental setup in the Anechoic Wind Tunnel

One potential downside to using large end-plates is the introduction of hard surfaces that can scatter and reflect the sound produced by the airfoils. Any specular reflection from the plates may increase the amplitude of sound received from $\pm 25\%$to$\pm 50\%$ span, which will increase the contribution to the measured sound from the boundary layer. This will introduce some uncertainty to the results with regards to the top of the boundary layer where the velocity is still close to the free stream, but as the noise sources being investigated scale with U^5 the noise generated by the segment of the airfoil inside the boundary layer will quickly become negligible regardless. Scattering of the sound will generate a diffuse secondary sound field which may obscure the directivity somewhat. But as the focus of the current work is on changes in the sound field the effect on the results due to the use of end-plates was not considered a high priority versus the advantages of their use. These advantages were to introduce space between the nozzle and the airfoil to increase the available arc for directivity data collection and space behind to allow development of the wake. It was observed during the

experiment that there is an increase in turbulence as the flow exits from the end-plates, and when a shorter plate setup was trialled to improve the signal-to-noise ratio the large-scale vortex shedding noise expected at high angles of attack was not observed. This indicated improper development of the airfoil wake under these conditions, so testing was resumed with the extended plates. Another secondary trailing edge source is expected to form where the flow leaves the end-plates, as shown in Figure 3a but since the elevation angle between these locations and the microphones is small (Figure 3b) and the directivity scales with the squared sine of this angle the contribution from this source at the microphones will be small, with a directivity factor of -45dB for sound generated at the airfoil junction and -39dB for sound generated at the edge of the plate.

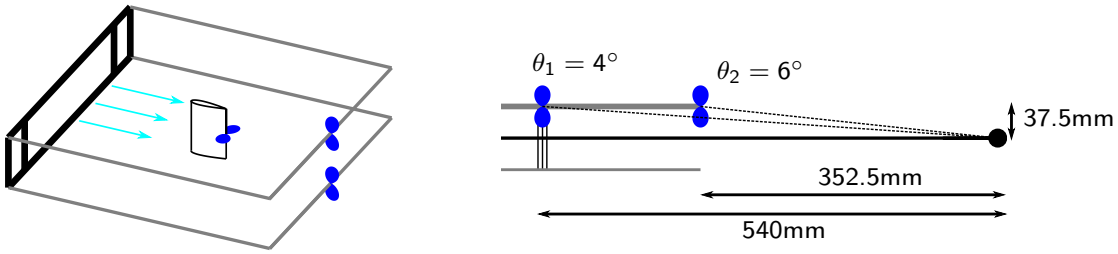

(a) Primary and potential secondary noise sources

(b) Angles between end-plate surface and microphones

Figure 3: Illustration of low directivity between end-plates and microphone array

2.2. Side-plate boundary layer

In order to investigate the effect that the end-plates had on the flow field the velocity and turbulent intensity were measured using a normal hot-wire probe. Measurements taken in the y-z plane (Figure 2b) at the rotation axis of the airfoil show that the shear layer of the free jet has expanded to almost 50% of the airfoil span by this location and the turbulence intensity is greater than 2% for over 90% of the airfoil as shown in Figure 4. However with the plates installed to constrain the flow the shear layer spans less than 30% of the channel and the turbulence intensity is also greatly reduced, maintaining a value less than 0.5% for much of the span.

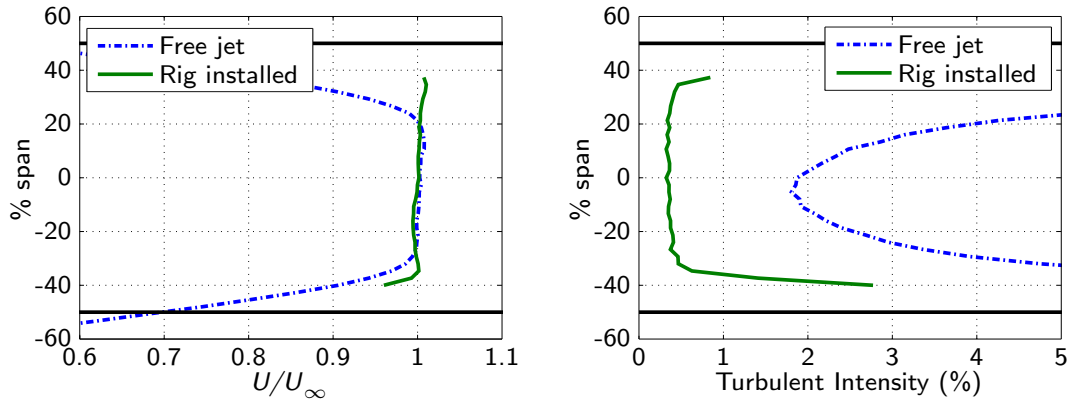

(a) Velocity profile (b) Turbulence profile

Figure 4: Flow profiles at $x = 0$, y = 0, $U_\infty = 30$m/s

As the airfoil angle-of-attack is increased the boundary layer changes, which must also be taken into account. Hot-wire measurements of the flow in a plane behind the NACA 0021 test model at geometric angles of attack of 14° and 15° (Figures 5 & 6) show that when the airfoil experiences stall the proportion of the span affected by the boundary layer increases from approximately 30% to approximately 50%. However as will be shown in Section 3.4 it is possible to determine that the source of the observed sound is not within the boundary layer.

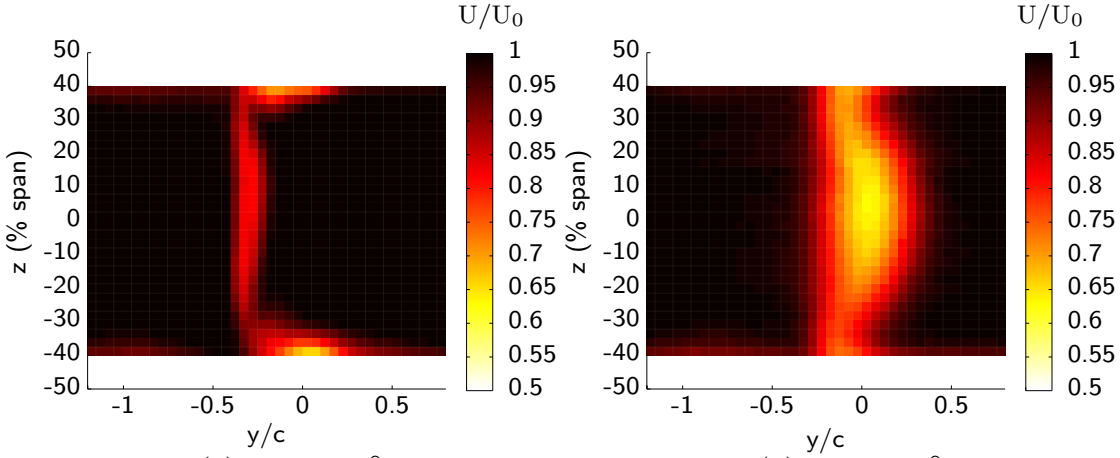

(a) $\alpha_t = 10.7°$ (b) $\alpha_t = 11.4°$

Figure 5: Velocity profiles at $x = 1.75c$, $U_\infty = 30$m/s with the NACA 0021 before and after stall

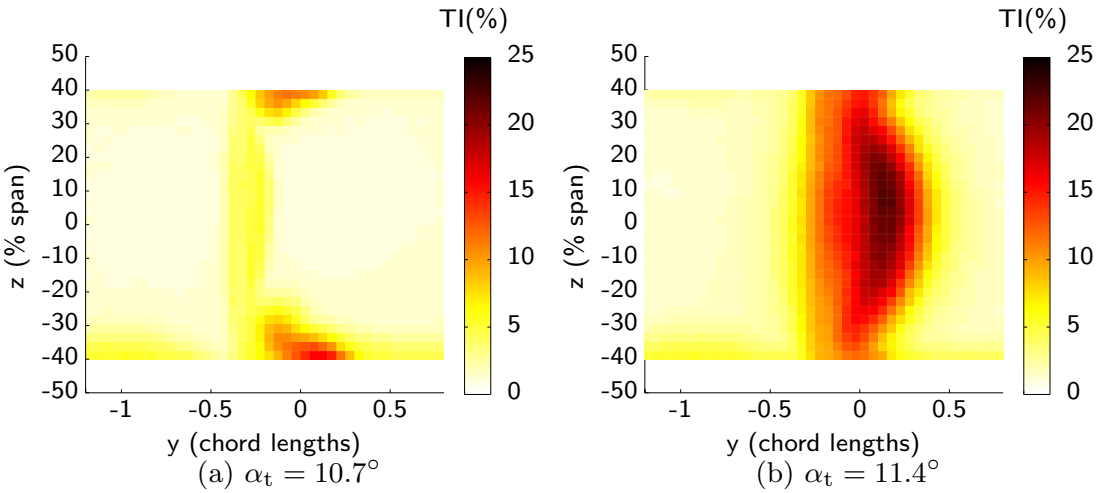

(a) $\alpha_t = 10.7°$ (b) $\alpha_t = 11.4°$

Figure 6: Turbulent intensity profiles at $x = 1.75c$, $U_\infty = 30$m/s with the NACA 0021 before and after stall

2.3. Data collection & processing

Acoustic data were gathered using a polar microphone array consisting of two arcs of 16 GRAS 40PH microphones from -110° to -35° and 35° to 110° with an angular spacing of 5°. GRAS 40PH microphones are free-field array microphones with a frequency response of ±1 dB from 250Hz between 50Hz and 5kHz. The array was positioned such that the microphones were located in the midplane of the airfoil and centred on the rotation axis, as shown in Figure 7.

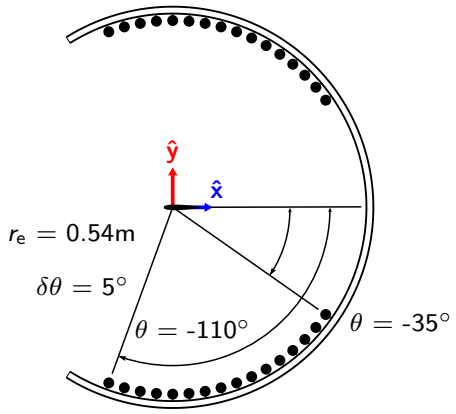

Figure 7: Microphone locations in the x-y plane

Acoustic data were gathered in ten time series of fifteen second duration at a the sampling frequency of 32kHz. When processing the data each of the ten time series were converted to a power spectral density using Welch's method with a Hann window, a sample length of 8192 points, and an overlap of 50%. Initially the data were processed using a Hamming window, however it was found that the spectral leakage from the very low frequency pressure fluctuations in the wind tunnel was too great. The data were then reprocessed using a Hanning window which exhibits a much faster side-lobe roll-off, reducing spectral leakage

as shown in Figure 8. While not shown in Figure 8 the global maximum of the spectrum is 98dB at 4Hz which is considerably higher than the rest of the data. Using these parameters gives a resolution bandwidth of 4Hz which sacrifices some of the definition of the narrow peaks but makes the spectra clearer. Taking the root-mean-square amplitude of the ten resulting spectra resulted in the final spectra shown in this article which represent a total of 1190 averages. These parameters are also collated in Table 2.

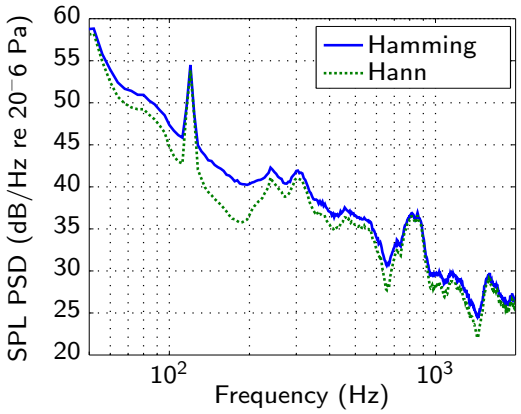

Figure 8: Sound pressure level PSD showing a comparison between the temporal window functions

Table 2: Parameters of data used to plot spectra

Sample rate	32,768Hz
FFT length	8192
Resolution bandwidth	4Hz
Number of averages	1190

The data were collected by rotating the airfoil clockwise into positions from -5° to 40°, holding stationary every 1° for recording and then counter-clockwise from 5° to -40° in -1°increments, again holding stationary in 1° increments for recording. Once this was done for both of the airfoils, the process was performed a second time to show repeatability and check for any effect removal and replacement the airfoils may have had on the results.

Each time one of the airfoils was installed there was a tolerance of ±1° in location of the 0°datum. This is a source of error but not a cause for concern as determining the absolute angle tack at certain phenomena occur is not a focus of this research, and in cases where the error is greater than 1° it was identified and corrected for when examining the results, as they are expected to be symmetrical between ±5°.

In addition to the main dataset, a second dataset was obtained at the end of the experimental campaign in order to further investigate the rate of change of noise levels as the airfoils enter stall. This has been previously investigated at an angular resolution of $\delta\alpha_g = 0.5°$[16] but in the current work it is revisited

with an angular resolution of $\delta\alpha_g = 0.1°$. Nominally the geometric angles of attack range from 11° to 16° for the NACA 0012 and 13° to 17° for the NACA 0021, but as the angular resolution is far higher than the error in the location of the 0° datum, only differences in angle of attack between two points in a set of contiguous data are meaningful. This could have been mitigated by gathering data about 0° before moving to the angles of attack of interest, but due to experimental constraints this would have required a reduction in the range of angles investigated.

Velocity data were acquired using a 2.5mm long, 5μm diameter, tungsten single-wire hot-wire anemometer at a sampling freqeuency of 32kHz. This frequency is higher than the cutoff frequency of the probe use, but because the data were acquired simultaneously with data from a reference microphone in order to cross-reference the sound and velocity measurements, and obtain magnitude-squared coherence, the frequencies could not differ. The hot-wire was positioned using a three-axis traverse with 6.25μm positional accuracy. While sample times and positional resolutions varied depending on the data (as detailed in Section 3.4), all measurements were taken in a single plane behind the airfoil at x = 1.75c as shown in Figure 9b. The measurements presented below were primarily taken in the y-direction at z = 0, and in the z-direction at y = –0.5c. y = –0.5c was chosen because it was the location where the signal from the Von Karman vortices shed from the trailing edge was expected to be the strongest based on the results of Rodriguez et al. [17], as shown in Figure 9a.

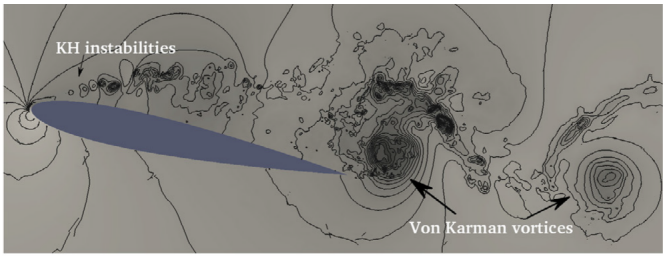

(a) Pressure contours from a DNS of a NACA 0012 airfoil at 12°, Re = 50,000 [17]

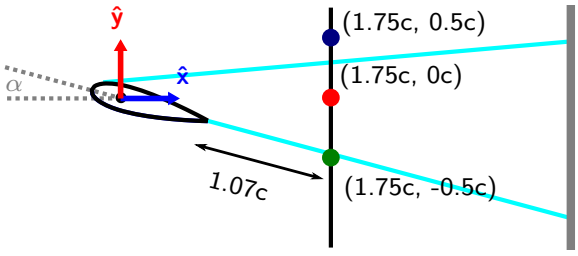

(b) Measurement plane for wake velocity data

Figure 9: Comparison of expected wake vortex locations and wake measurement locations

3. Results

In order to fully understand the differences between the noise generated by each of the three airfoils, four different visualisation methods are used. Firstly a series of pseudocolour plots shows the relationship between frequency, angle of attack and the power spectral density of the sound pressure level. Then standard 2D spectra are used to focus on some of the changes in the spectrum with angle of attack as the airfoils enter the "light stall" regime and the changes in the frequency-integrated sound pressure level with angle of attack integrated of some of the spectral features of the spectra are displayed for the $\delta\alpha_g = 0.1°$ case. Finally, some of the frequency-integrated sound pressure level of some the aforementioned spectral features are displayed for $\delta\alpha_g = 1°$ in directivity plots. Unless otherwise specified, the data presented in this section are from the first of the two experimental sessions with a clockwise rotation direction.

3.1. Pseudocolour plots

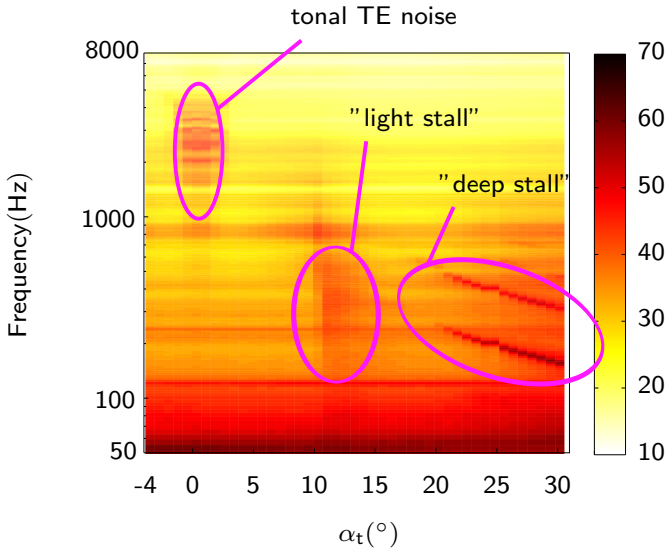

Figure 10: Example SPL PSD (dB/Hz re 20^{-6}Pa) of the NACA 0012 airfoil with noise regimes labelled

Three noise regimes can be immediately identified from the plots of airfoil spectra versus angle of attack, shown labelled in Figure 10 for the NACA 0012 airfoil. These regimes are low angle of attack tonal trailing edge noise, high angle of attack "deep stall" tonal noise and a third regime between the two where the noise is concentrated into a low frequency band but exhibits less tonality. This third regime represents the onset of the "light stall" described by Moreau et al. [9], appearing quickly when the airfoils reach their respective stall angles and then slowly fading before the high angle of attack tonal noise peaks begin to form. As the high angle of attack peaks represent the large-scale "deep stall" vortex shedding from the fully-seperated boundary layer, it is thought that this transitional regime represents an intermediate seperated state with a different vortex shedding pattern.

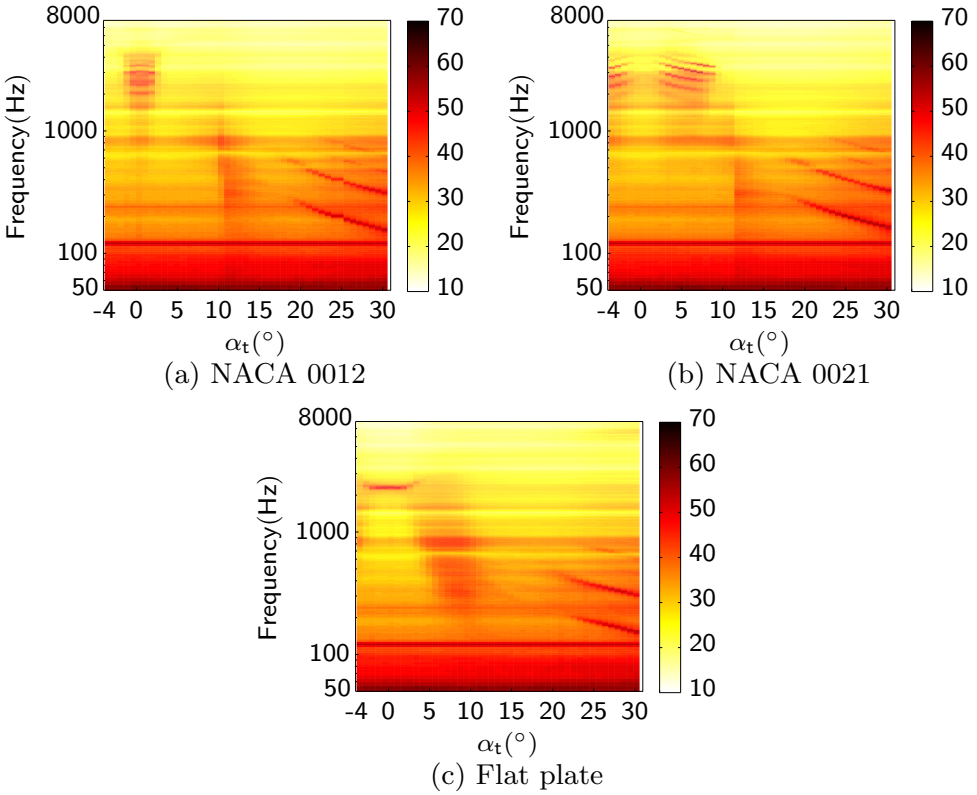

(a) NACA 0012 (b) NACA 0021

(c) Flat plate

Figure 11: SPL PSD (dB/Hz re 20^{-6}Pa) at $\theta = 90°$

The formation of peaks at the onset of stall occurs over a smaller range of angles of attack for the NACA 0021 than the NACA 0012, as previously discussed [16]. As there are recordings from either side of the airfoil in this data set the magnitude-squared coherence between the signals on either side of the chamber can be determined (Figures 12a, 12b & 12c). In this case a higher value of coherence at a given frequency indicates that the signals received on either side of the tunnel are generated by the same source. Coherence can be lowered by the presence of measurement noise, but will also be lower if there are multiple sources or if the sources are spatially distributed over a large enough area [18].

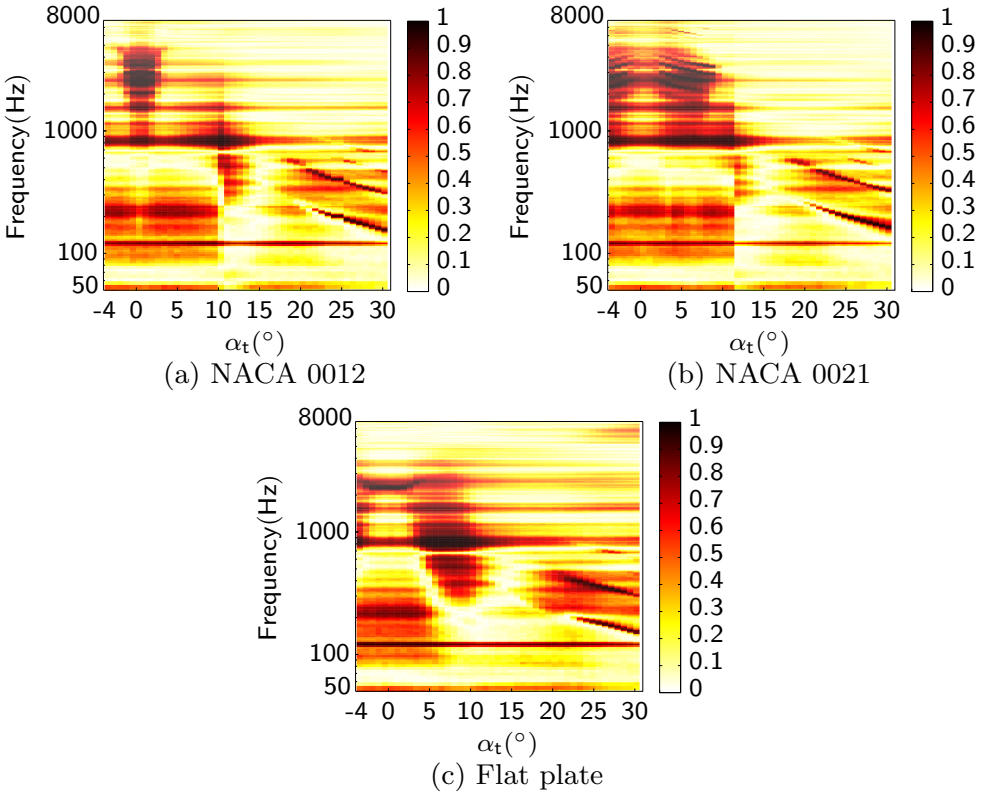

(a) NACA 0012 (b) NACA 0021

(c) Flat plate

Figure 12: Coherence between signals at $\theta = \pm 90°$

3.2. Spectrum plots

In this section the measured sound pressure level power spectral density from the experiment is presented. Figure 13,show the noise measured from the NACA 0012, NACA 0021 and flat plate models respectively at angles of attack from when they begin to exhibit the "light stall" noise described by Moreau et al.[9] until the it reaches its peak strength. The primary difference between the noise generated by the NACA 0012 and NACA 0021 airfoils at light stall is a slight difference in the strength of the noise between 400Hz and 700Hz, making the stall noise portion of the NACA 0012's spectra in this range appear flatter. Overall this means that the total noise generated at light stall by the NACA 0012 is a few dB higher, as further discussed in Section 3.3.

It is also immediately apparent that the rates of onset of the light stall noise signatures for these airfoils differ from one another, with the NACA 0012 entering an intermediate state where the noise generated between 400Hz and 700Hz has increased far more rapidly than that from 200Hz to 400Hz. This feature does not appear in the NACA 0021 data which appears to immediately transition to the light stall noise signature when moving from 10.7° to 11.4°.

The flat plate spectrum in Figure 13c show a much slower formation of the light stall peaks as the angle of attack increases. The light stall spectrum for the flat plate is more similar to that of the NACA 0012 than the NACA 0021, with a relatively flat distribution and the formation of a broad peak between 400Hz and 700Hz before the portion of the noise between 200Hz and 400Hz forms.

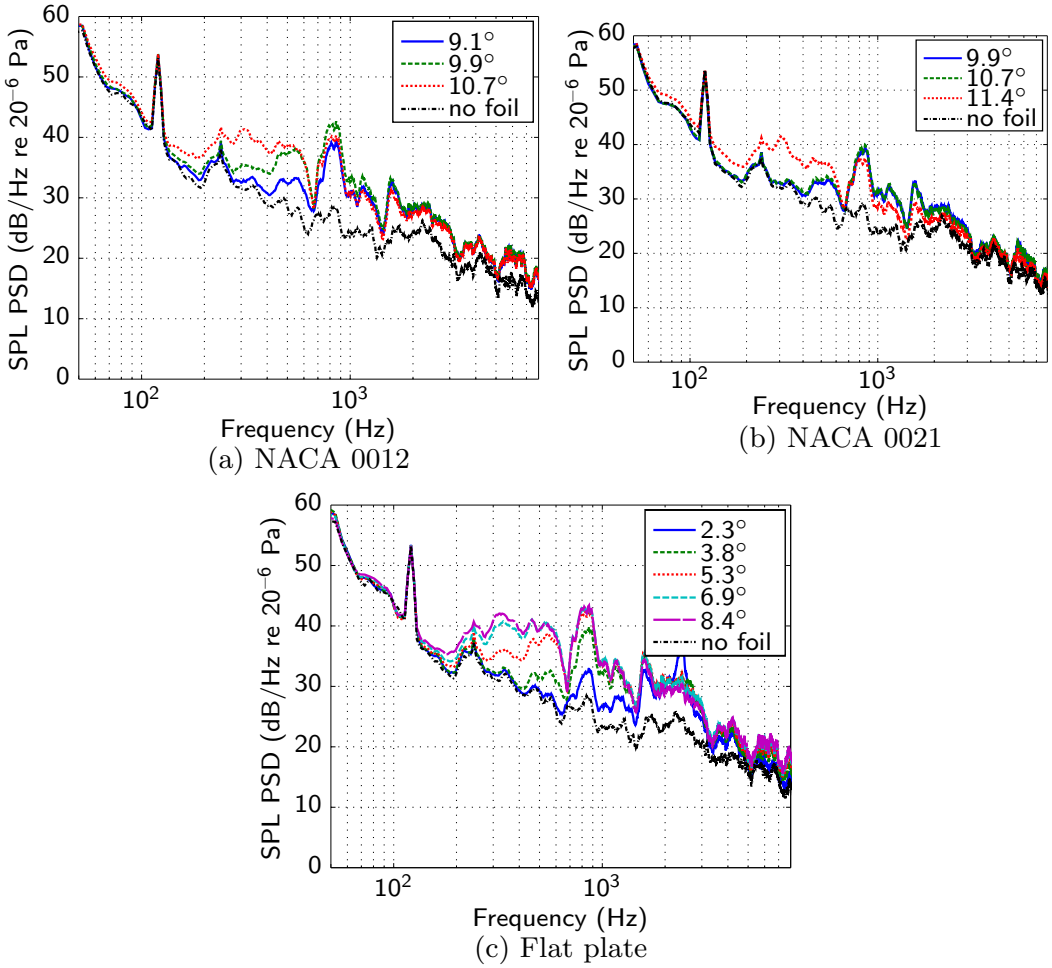

(a) NACA 0012 (b) NACA 0021

(c) Flat plate

Figure 13: SPL PSD at onset of light stall noise at $\theta = 90°$

3.3. Noise levels

Integrating across the stall peaks and plotting the sound pressure level for the high-resolution data reveals more information about the rate at which the stall signatures form. As shown in Figure 14 the trends from the $\delta\alpha_g = 1°$ data continue in the $\delta\alpha_g = 0.1°$ data. There remains a smooth transition between the NACA 0012's pre-stall and "light stall" states, whereas the transition appears even more abrupt and rapid for the NACA 0021 as it still occurs over very few data points. For the NACA 0021 there is a decrease in noise level during light stall between 676Hz 1044Hz, and the noise level in this frequency range also behaves differently to the noise at lower frequencies. Conversely the flat plate noise levels maintain a similar shape for the three frequency ranges inspected, and transitions over a much larger range of angles of attack.

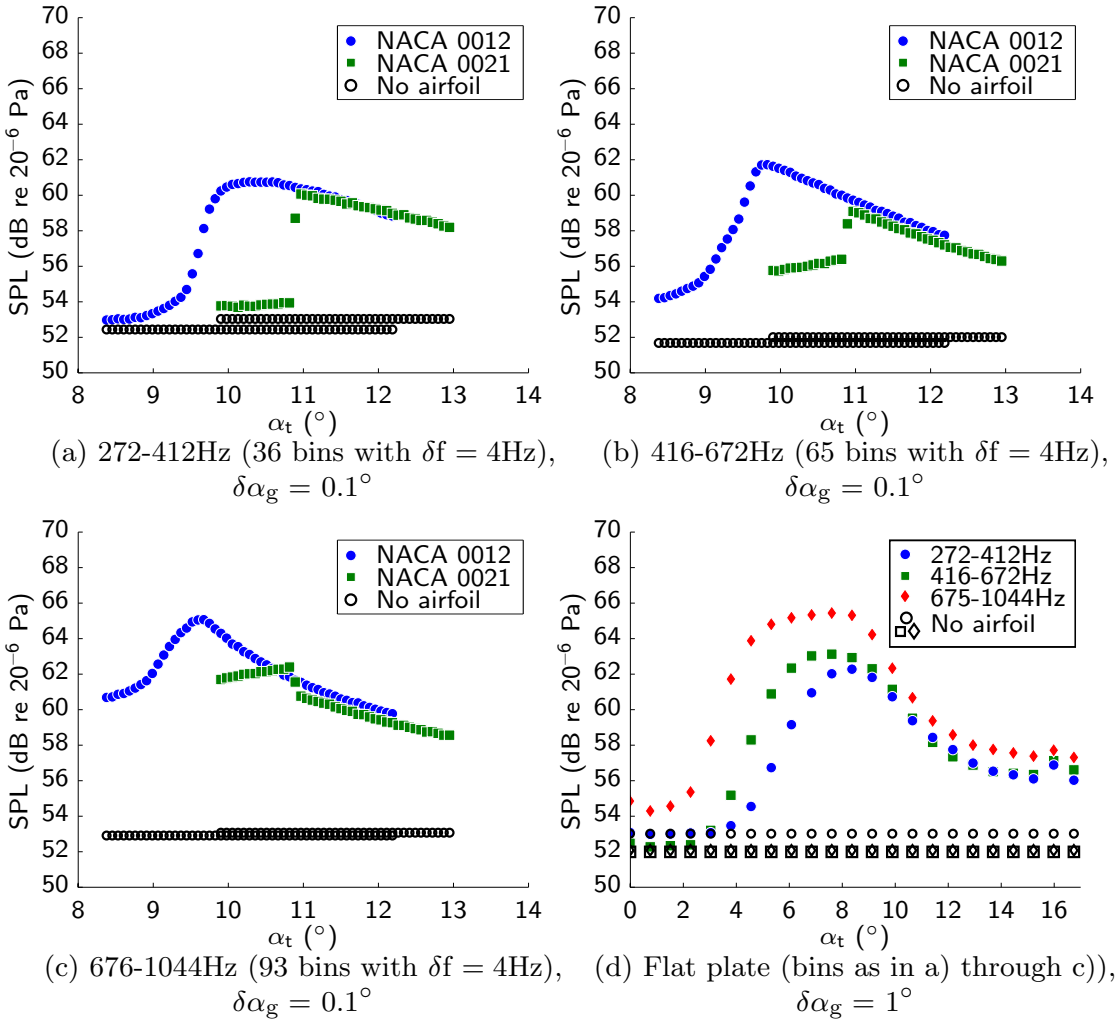

(a) 272-412Hz (36 bins with $\delta f = 4$Hz), $\delta\alpha_g = 0.1°$

(b) 416-672Hz (65 bins with $\delta f = 4$Hz), $\delta\alpha_g = 0.1°$

(c) 676-1044Hz (93 bins with $\delta f = 4$Hz), $\delta\alpha_g = 0.1°$

(d) Flat plate (bins as in a) through c)), $\delta\alpha_g = 1°$

Figure 14: SPL measured in "light stall" bins. The bandwidth of each summation is shown in the subcaption.

It is interesting to note that while the noise data for the NACA 0021 shown in Figure 14 appears to show a transitional state between pre-stall and light stall at 10.9°, this is not actually the case. In Figure 15, which shows the data from each of the ten recordings that comprise the final spectrum at this angle, it can be seen that the pre-stall and light stall states are being alternately observed. The NACA 0021 flow field only exhibits either the stalled or pre-stall behaviour in each sample indicating that what appears to be a transitional state, like those observed for the NACA 0012 and flat plate, are actually the result of flow instability. Once the angle of attack is further increased the noise observed settles into a steady light stall behaviour.

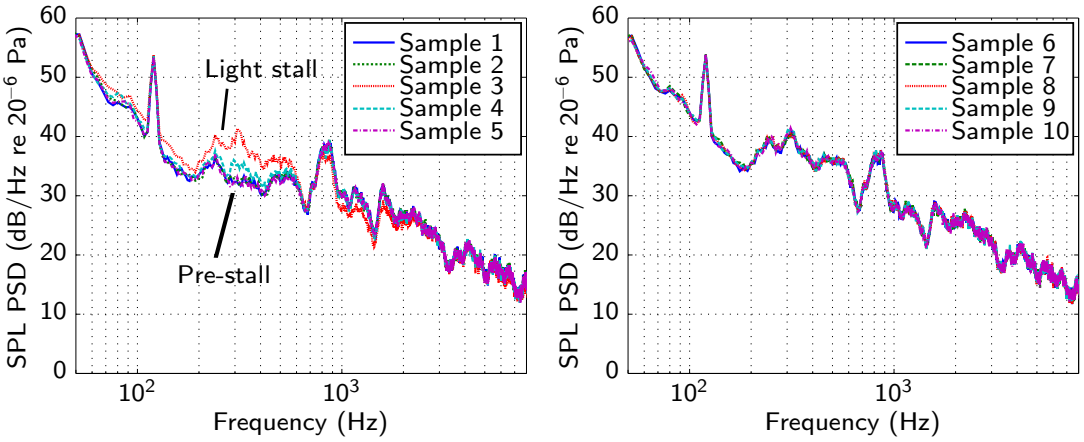

Figure 15: Spectra of the individual NACA 0021 recordings from Figure 14 at $\alpha_t = 10.9°$

3.4. Wake measurements

The results from Section 3.3 were used in order to target a study of velocity spectra downstream of the airfoil. Initially 10 second samples were collected without the airfoil in order to determine if any of the observed noise was being generated by the flow upstream. As shown in Figure 16 there is a peak in the velocity spectrum near 50Hz which corresponds to a peak in the sound spectra. This indicates that this noise is being generated by a flow oscillation stemming from an upstream source. There is no matching signal for the peak in the background noise around 100Hz indicating that this stems from a mechanical source, most likely the wind tunnel fan.

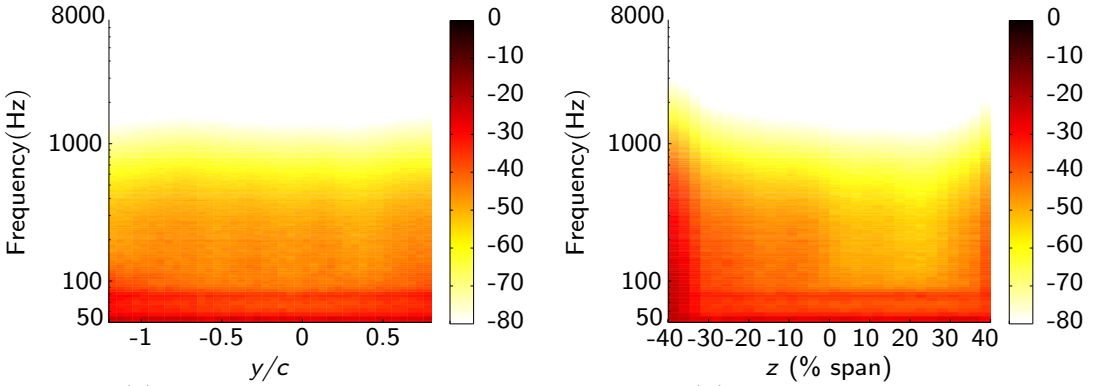

(a) $z = 0$mm, $\delta y = 2.5$mm (b) $y = 0$mm, $\delta z = 2$mm

Figure 16: Velocity PSD with no airfoil at $x = 1.75c$

Subsequently investigation of the NACA 0021 airfoil, again using 10 second samples, at true angles of attack of 10.7°and 11.4°(shown in Figure 17) shows that when the light stall signature in the spectrum forms a corresponding broad peak appears in the velocity spectrum. The coherence between the velocity and sound measurements also greatly increases when this happens, indicating the the sound is generated upstream of the observation plane. This peak in the

velocity spectrum is observed on both sides of the airfoil for approximately one chord length, but not in the immediate wake where the spectrum is dominated by a much larger broadband signal.

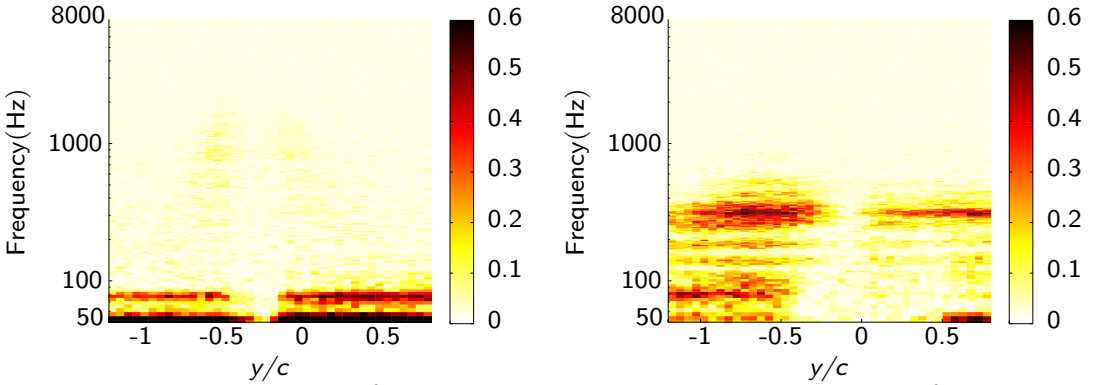

(a) $\alpha_t = 10.7°$ (b) $\alpha_t = 11.4°$

Figure 17: Velocity-sound pressure coherence of the NACA 0021 airfoil at $z = 0$mm, $x = 1.75c$, $\delta y = 2.5$mm, $\delta z = 2$mm

It can be seen that apart from the signals that are found in the flow without the airfoil installed there is little coherence in the velocity and sound spectra. However once the angle of the airfoil is increased and stall occurs peaks appear in the coherence that correspond to the light stall noise. The coherence disappears inside the wake, which is attributed to the large broadband velocity fluctuations in this region. The data shown in Figure 17 were then used to determine the location where the velocity and sound spectra are the most coherent for further study.

When investigating the spanwise distribution of velocity-sound pressure coherence, 30-second-long data samples were collected at locations from z = -40% to 40% span with $\delta z = 2$mm. An investigation of the spanwise coherence of the sound and velocity (Figure 18) indicates that the source of the light stall noise is concentrated in the mid-span, outside the plate-foil boundary layer. This indicates that the primary sound source is located near the $z = 0$ plane of the airfoil.

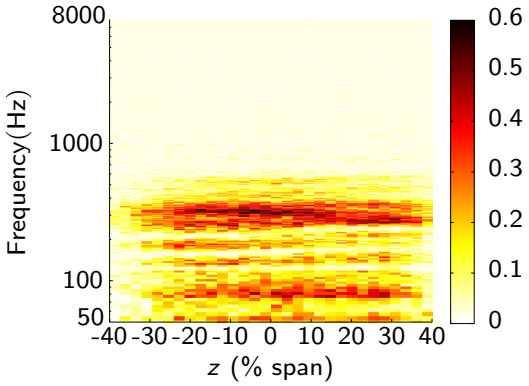

Figure 18: Velocity-sound presure coherence of the NACA 0021 airfoil at $y = 0.5$c, $x = 1.75c$, $\alpha_t = 11.4°$, $\delta z = 2$mm with $\delta f = 4$Hz

Reprocessing the data with frequency bands of $\delta f = 64$Hz instead of $\delta f = 4$Hz we can obtain a better idea of the coherence between the observed sound and wake velocity spectral peaks in their entirety. As seen in Figure 19, between 25% and 32% of the acoustic energy in the 288-352Hz frequency band is coherent in the central ±20% span, and this value falls away as the measurement location moves towards the edges of the test section. While 32% coherence appears low, it should be noted that this is expected due to the distance between the airfoil and the measurement location. Figure 20 shows an estimate of coherence loss between two points with chordwise separation, developed by Bertagnolio et al. [19]. This figure indicates that, for the current experimental setup, the expected coherence between surface pressures separated by a distance of $1.07c$ is between 0.3 and 0.4, depending on the choice of flow separation point. While the experimental results presented in Figure 19 are separated from the trailing edge and not measured along a hard surface, the model gives an indication that the expected coherence and the measured coherence are similar.

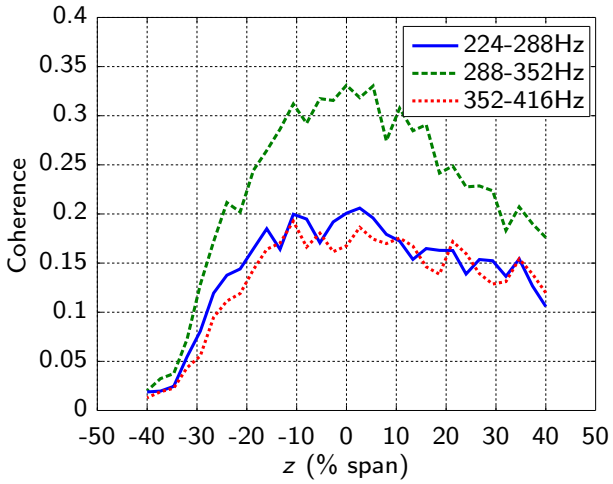

Figure 19: Velocity-sound presure coherence of frequency bands of interest for the NACA 0021 airfoil at $y = 0.5c$, $x = 1.75c$, $\alpha_t = 11.4°$, $\delta z = 2$mm with $\delta f = 64$Hz

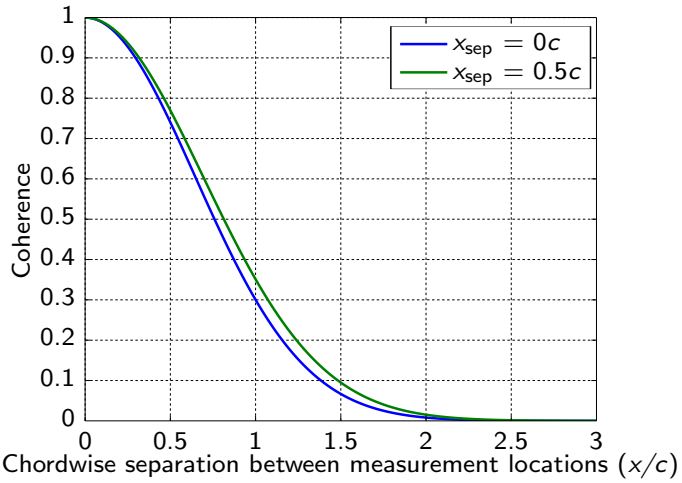

Figure 20: Velocity-sound presure coherence of frequency bands of interest for the NACA 0021 airfoil at $y = 0.5c$, $x = 1.75c$, $\alpha_t = 11.4°$, $\delta z = 2$mm with $\delta f = 4$Hz

Figure 21 presents the velocity spectra from the $z = 0$mm measurements as the airfoils stall. The data show that the velocity spectrum peaks at a frequency of approximately 300Hz, which corresponds to the light stall noise observed in the sound spectra (Figure 13). The formation of this peak and increase of the velocity power spectral density in this frequency range correspond to the change in noise level between given angles of attack. Because of these correlated observations and the coherence between the velocity and sound measurements it is likely that these velocity fluctuations are generated by the source of light stall noise.

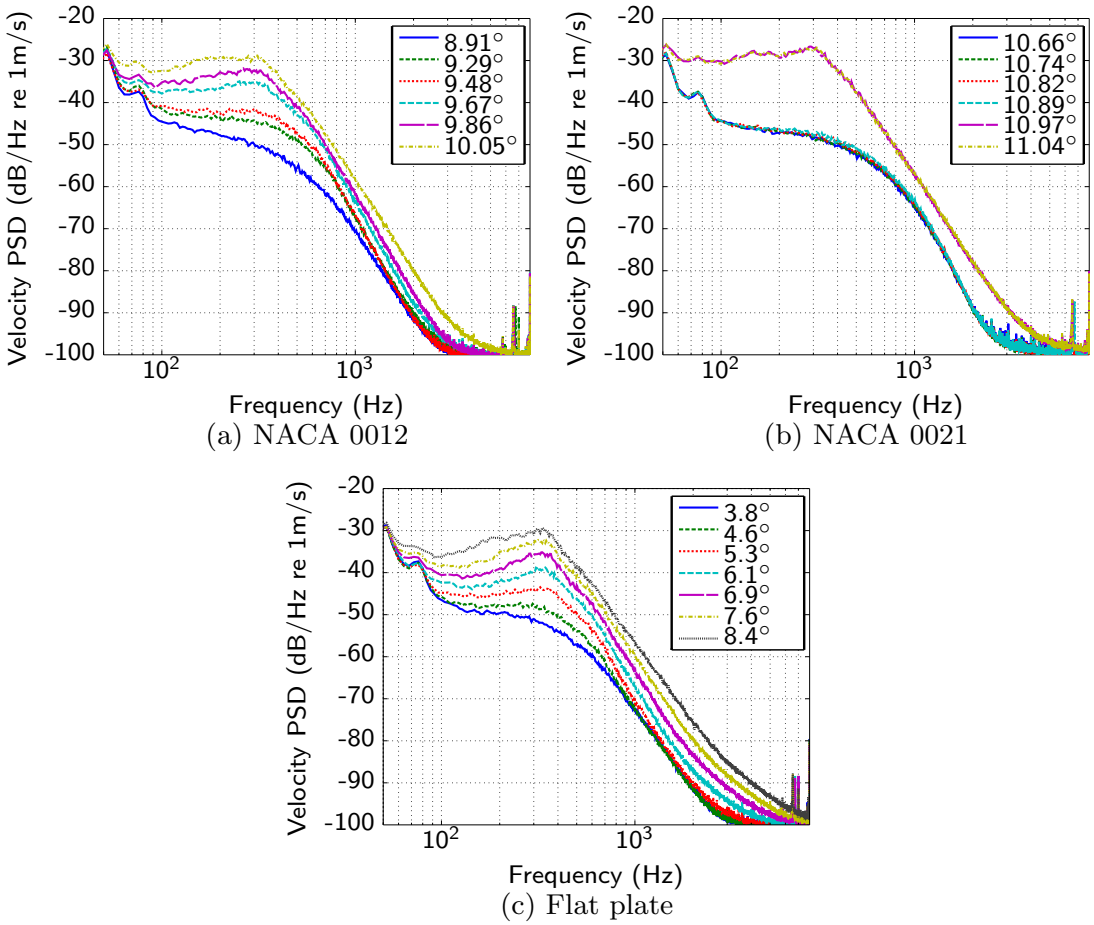

(a) NACA 0012 (b) NACA 0021

(c) Flat plate

Figure 21: Velocity PSD at onset of light stall noise for the airfoil models, $y = 0.5c$, $x = 1.75c$, $z = 0$mm

3.5. Directivity plots

Figures 22 to 24 show how the directivity of the mean-squared pressure varies as the angle of attack increases. The directivity is presented as the integral of the spectra across the frequency range where light stall noise is observed (270-670Hz). This sound pressure level is then normalised so that the directivity value observed at $\theta = 90°$ is equal to the expected convected dipole. When calculating the theoretical dipole, $\theta + \alpha$ is used as the observation angle as the theory assumes that this value is the angle relative to both the chord line and the convection velocity. In the case where the airfoil is at a non-zero angle of attack, the observer-convection velocity angle and observer-airfoil chord angle are often not parallel, and correcting for this effect can lead to the introduction of larger errors [1].

It can be seen that as the airfoils enter the light stall regime the directivity changes to a shape that is in good agreement with the theoretical dipole before shifting back to its original shape as the contribution to the noise level from the dipolar source falls. Outside of the range of angles of attack where the light stall noise is present the noise takes on a roughly rectangular directivity pattern. This is thought to be due to contributions to the measured noise by

the jet noise dominating the measurements. As the jet is trapezoidal in shape and the microphone array is circular and centred on the airfoil, the microphones further away from 90° are closer to the jet, thereby increasing the background noise level at those locations.

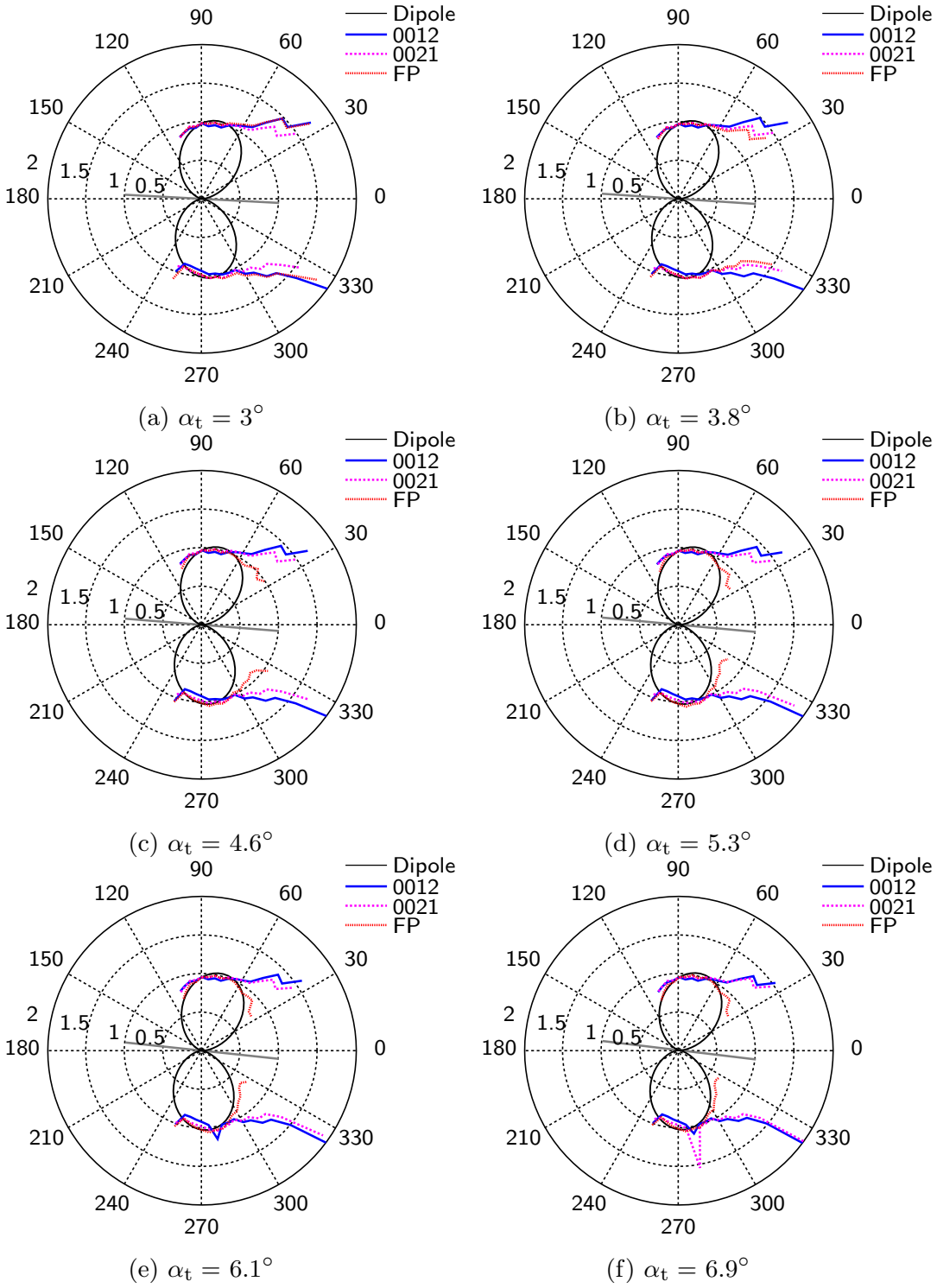

(a) $\alpha_t = 3°$ (b) $\alpha_t = 3.8°$

(c) $\alpha_t = 4.6°$ (d) $\alpha_t = 5.3°$

(e) $\alpha_t = 6.1°$ (f) $\alpha_t = 6.9°$

Figure 22: Measured directivity of a NACA 0012 airfoil, NACA 0021 airfoil, and flat plate from 280-670Hz, α_t = 3-6.9°. Airfoil chord line represented by a straight line.

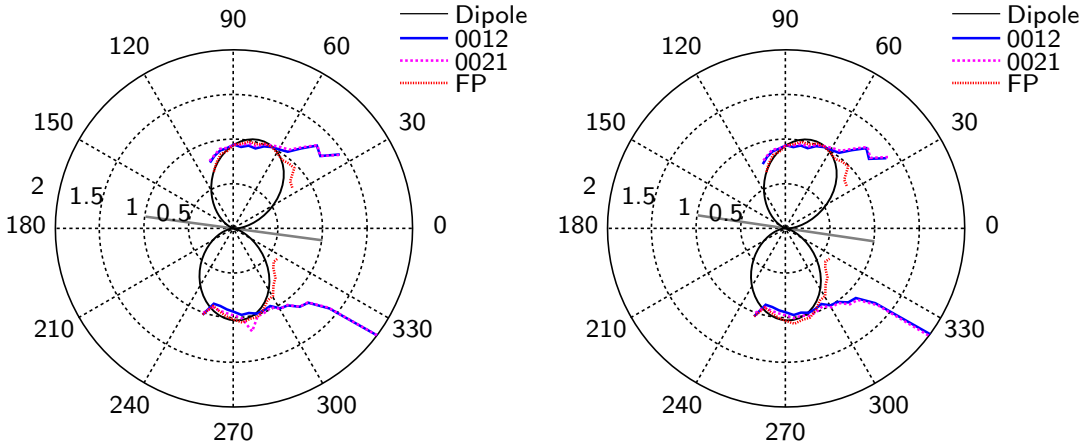

(a) $\alpha_t = 7.6°$ (b) $\alpha_t = 8.4°$

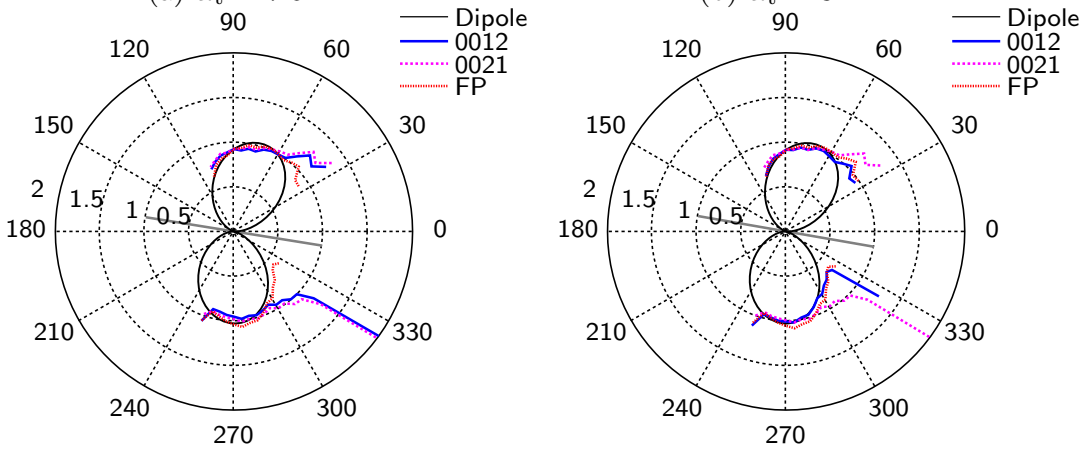

(c) $\alpha_t = 9.1°$ (d) $\alpha_t = 9.9°$

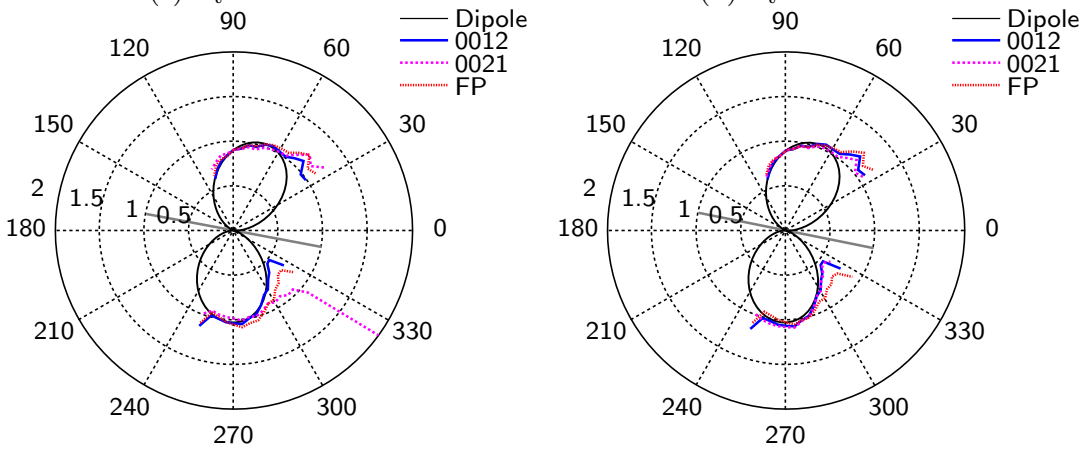

(e) $\alpha_t = 10.7°$ (f) $\alpha_t = 11.4°$

Figure 23: Measured directivity of a NACA 0012 airfoil, NACA 0021 airfoil, and flat plate from 280-670Hz, $\alpha_t = 7.6$-$11.4°$. Airfoil chord line represented by a straight line.

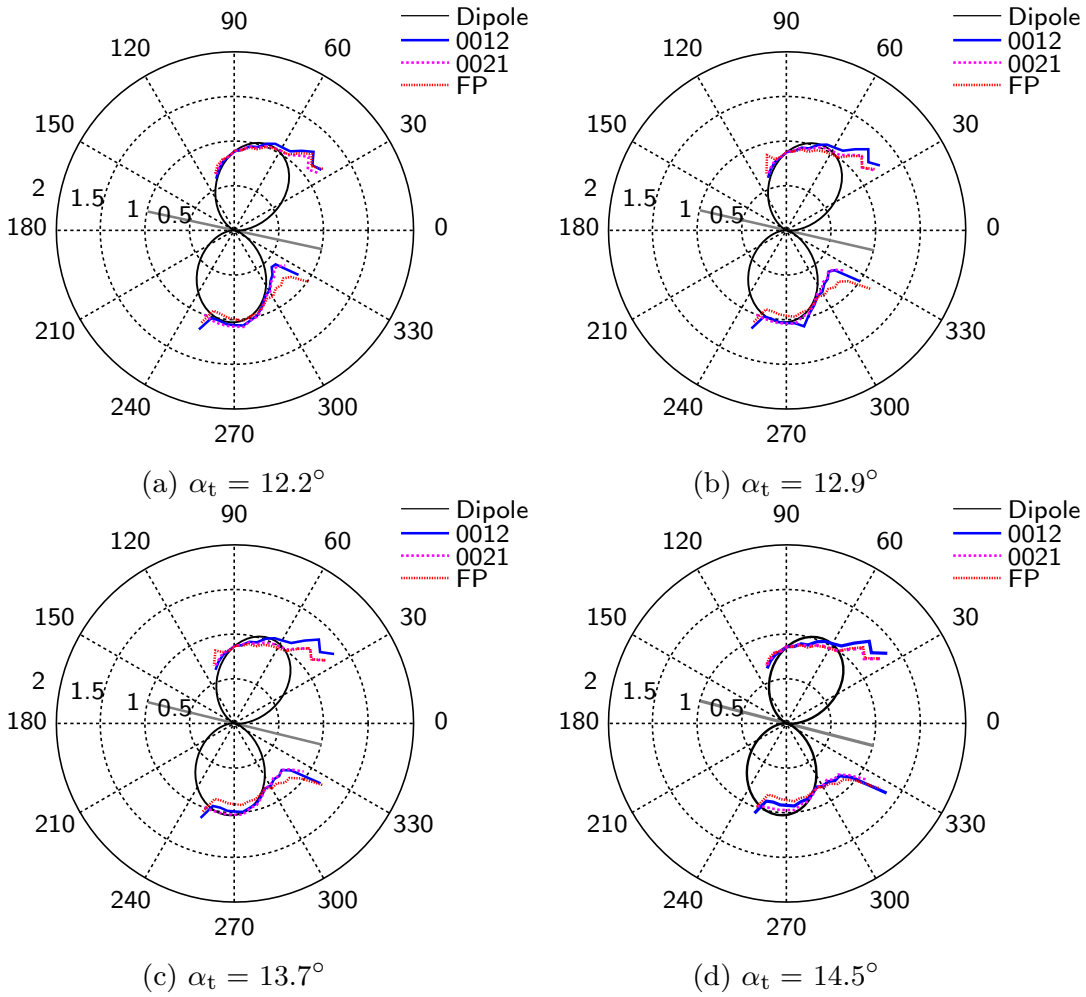

(a) $\alpha_t = 12.2°$ (b) $\alpha_t = 12.9°$

(c) $\alpha_t = 13.7°$ (d) $\alpha_t = 14.5°$

Figure 24: Measured directivity of a NACA 0012 airfoil, NACA 0021 airfoil, and flat plate from 280-670Hz, $\alpha_t = 12.2$-$14.5°$. Airfoil chord line represented by a straight line.

3.6. Repeatability

Figure 25 shows the directivity in the light stall regime for the NACA 0012 in the first experimental session for both the clockwise and anti-clockwise rotation directions. In addition to this the data from the anti-clockwise rotation direction is shown, but rotated 180 degrees. This rotation corrects for the change in observation angle with respect to the airfoil when the airfoil is rotating in the anticlockwise direction. As can be seen there is good agreement between the clockwise and anti-clockwise rotation directions apart from the influence of the jet noise at the extremities. This indicates that any asymmetry in the microphone array and wind tunnel are not significantly affecting the results.

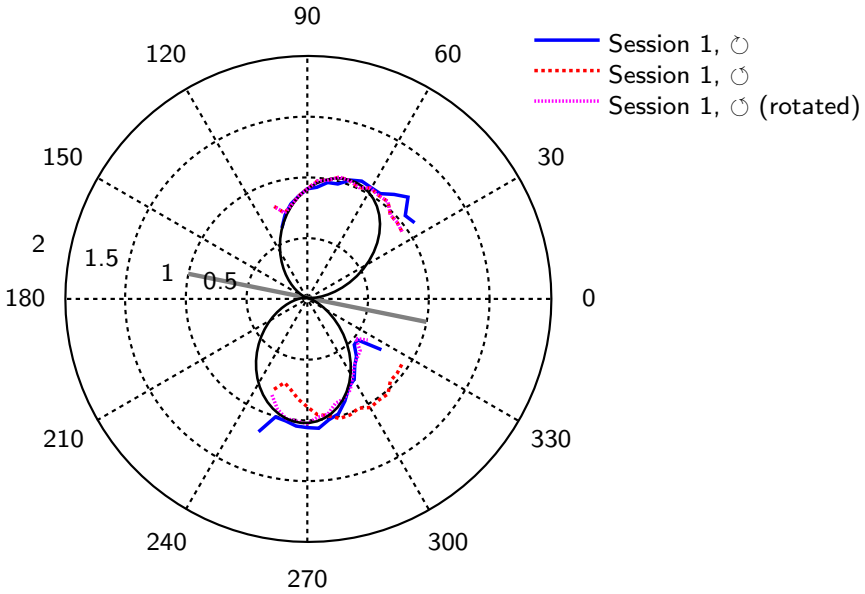

Figure 25: Directivity of NACA 0012 airfoil at $\alpha_t = 11.4°$ showing clockwise, anti-clockwise and anti-clockwise (rotated 180°) tests

Figure 26 shows that the directivity of the NACA 0012 at 15° is repeatable for both rotation directions. The figure also appears to show that while the data are mostly consistent on the suction side of the airfoil, the data from the pressure side is less uniform because the normalisation is referenced to the theoretical dipole at 90°. If the data are normalised with reference to -90° the situation is reversed.

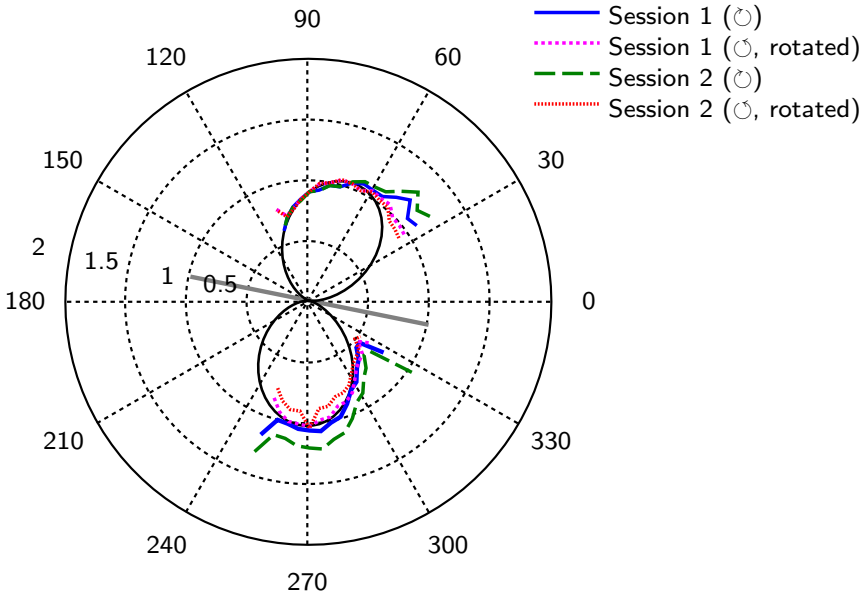

Figure 26: Directivity of NACA 0012 airfoil at 15° comparing the four sets of data

Comparisons of spectra of the airfoils during light stall are shown in Figures 27 & 28. These plots compare the data obtained at the Microphones at ±90°

in the standard tests with the data obtained at $\mp 90°$ in the tests where the direction of rotation is reversed. The data show that even for each of the four tests the slight differences in the shapes of the peaks at light stall are reproduced. The angle at which the spectra are identical between experimental sessions differs slightly due to aforementioned misalignment of the 0° datum, and it can be seen in some of the spectra (such as the anti-clockwise rotation direction spectrum of the first session in Figure 27) do not match as closely as the others. This is because the degree of misalignment is such that the data from that session was captured at angles of attack that differ enough to produce slightly different spectra but not enough to be reliably corrected.

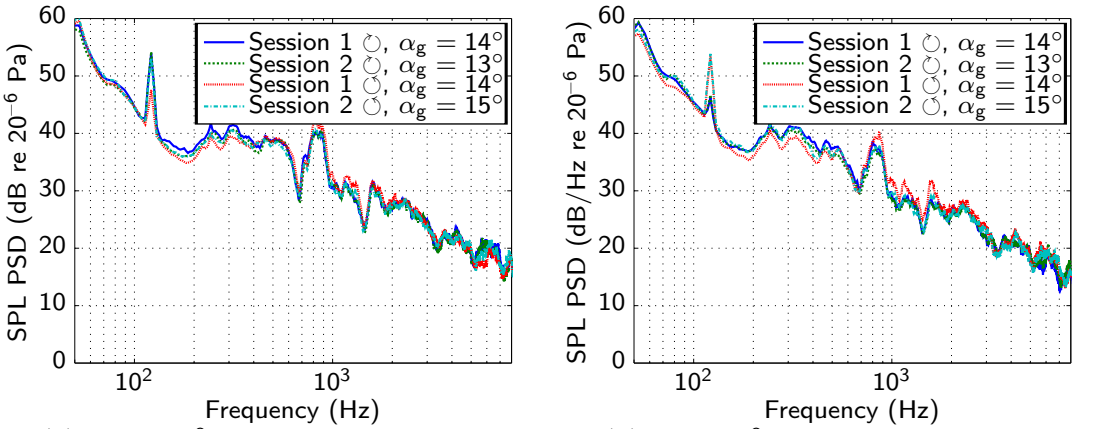

(a) $\theta = +90°$ for the clockwise rotation and $\theta = -90°$ for the anti-clockwise rotation

(b) $\theta = -90°$ for the clockwise rotation and $\theta = +90°$ for the anti-clockwise rotation

Figure 27: SPL PSD of for at uncorrected "light stall" angles for the four sets of NACA 0012 data

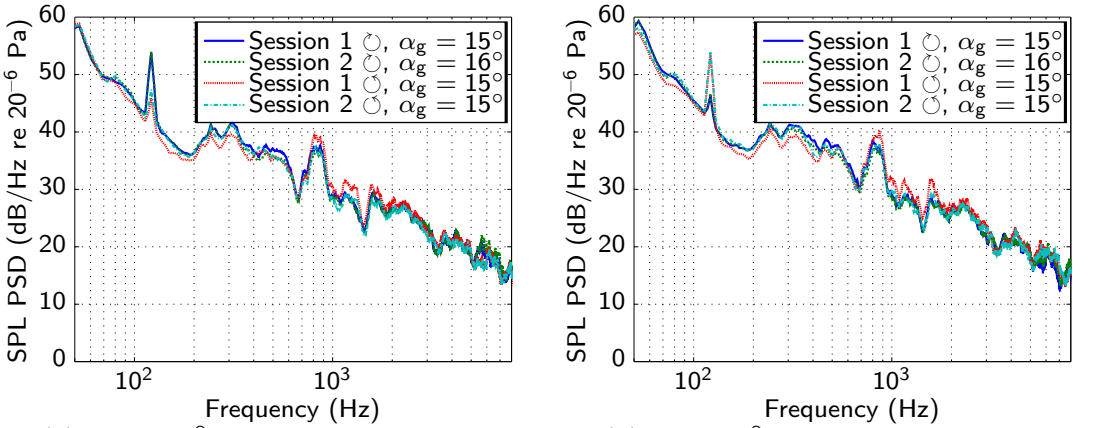

(a) $\theta = +90°$ for the clockwise rotation and $\theta = -90°$ for the anti-clockwise rotation

(b) $\theta = -90°$ for the clockwise rotation and $\theta = +90°$ for the anti-clockwise rotation

Figure 28: SPL PSD of for at uncorrected "light stall" angles for the four sets of NACA 0021 data

4. Discussion

Vorticity fields from a computational study of a flat plate by Tamai, indicate the vorticity produced by the separated shear layer peaks near 7.5° [20]. This angle corresponds to the peak value of noise in observed from the flat plate in this study, indicating that the observed noise may be caused by this vorticity interacting with the airfoil. Furthermore, a direct numerical simulation of a NACA 0012 airfoil performed by Rodriguez et al., for a Reynolds number of 50,000 at angles of attack at 5°, 8°, 9.25° and 12°, indicate a similar pattern[17] . In the study by Rodriguez et al. vorticity grows from 5° to 12° angle of attack, with strong vortex shedding starting in the 9.25° case. Again this corresponds with the angle of onset for the noise in the light stall regime for the NACA 0012 in the present study, shown further in Section 3.3. Unfortunately to the author's knowledge similar flow fields in this angle of attack range for the NACA 0021 airfoil are not available in the literature.

Wake measurements of a NACA 0012 airfoil, performed by Huang & Lin identified four vortex shedding modes that may be present as the angle of attack increases at Reynolds numbers between 20×10^3 and 100×10^3[21]. At high angles of attack the airfoil wake exhibits a supercritical vortex shedding mode where the vortices shed due to the separated turbulent boundary layer are coherent and exhibit a Strouhal number based on frontal height of $St_h = 0.1 - 0.2$. At low angles of attack and Reynolds numbers the shed vortices are dominated by instabilities in the laminar boundary layer. Between these regions there is a transitional region between subcrticial and supercritical vortex shedding mode where the vortex shedding loses coherency. Wake measurements of a NACA 0018 airfoil by Yarusevych & Boutilier showed that as the airfoil moves from the laminar to transitional regime and coherence is lost the velocity fluctuation spectral peak broadens into the shape found in the current experiment. This change in the energy spectrum found between $Re_c = 70 \times 10^3$ and $Re_c = 100 \times 10^3$ also shares similarities with a change in wake regime that was found in a previous study on a NACA 0021 airfoil indicating that both airfoils lose wake coherence under similar flow conditions[22]. Figure 29 compares the measured directivity and the theoretical dipole with two more theoretical dipoles that are not located at the centre of the array. One of these is located at the trailing edge of the airfoil, and the other is located at the exit of the end-plates. This figure shows that the discrepancy between the theoretical dipole and the measured data on the pressure side of the airfoil is lessened if the source is assumed to be at the trailing edge. It therefore stands to reason that the vortex shedding from the trailing edge is the source of the observed noise in the light-stall regime, although the vortex shedding from the leading edge likely contributes as it is also coherent with the measured sound.

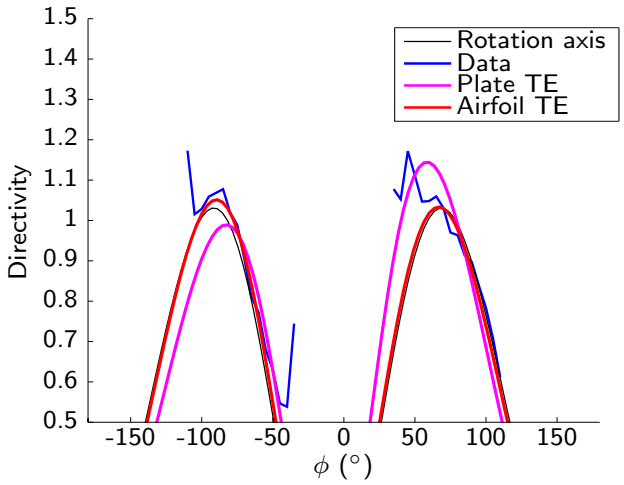

Figure 29: Measured directivity of NACA 0012 airfoil at $\alpha_t = 11.4°$ compared with theoretical directivity of convected dipoles centered on the airfoil rotation axis, airfoil trailing edge, and the trailing edge of the end-plates. Spherical spreading is assumed

From the available flow-field data for the NACA 0012 airfoil and flat plates, the rise in low-frequency noise as an airfoil enters the light stall regime, over the broadband noise produced before stall, appears to be due to vorticity produced by the separated boundary layer. This corroborates the results of this study where the formation of peaks in the sound spectrum coincided with an increase in velocity fluctuations at this frequency and the separation of the flow over the airfoil. This feature of the spectrum also exhibits a dipolar directivity, which may change the amount of low-frequency noise observed downstream during times when this feature is present. In addition for a given rate of change of the noise with angle of attack when entering a stall regime is larger, such as observed in the current results for the NACA 0021 when compared to the NACA 0012, the resulting change in noise level over time will occur over a shorter period, resulting in a more impulsive noise characteristic.

While the current results are not in the correct Reynolds number range to be directly applicable to wind turbine noise, if similar behaviour is observed at those Reynolds numbers then blades crossing into the stall regime will result in short periods where low-frequency noise levels increase upstream and downstream of the rotor. The low-frequency noise content in the “light stall” regime is strongly dipolar, which could explain previous field measurements showing that the directivity of low frequency wind turbine noise is concentrated in the upstream and downstream directions under certain conditions [23]. This is also in agreement with the findings of an extensive investigation into the “other amplitude modulation” phenomenon by RenewableUK which suggested that transient stall may be contributing to a downstream observation of amplitude-modulated noise [24]. Future research is required in order to determine whether the behaviour that has been observed at low Reynolds numbers is also present in that regime.

5. Conclusion

Self-noise from NACA 0012 and NACA 0021 airfoils at a Reynolds number of 96,000 was measured in the anechoic wind tunnel at the University of Adelaide using a polar microphone array. It was found that at the onset of stall the noise produced in the range of 200Hz-700Hz increased suddenly by approximately 5dB and this was accompanied by a change in directivity to that of a convected dipole. Furthermore, the noise generated by the NACA 0021 airfoil increased by a smaller amount than the NACA 0012 and the flat plate in the range of 400-700Hz, but transitioned to this state much more rapidly than the NACA 0012. Even after investigating this transition with an angular resolution of 0.1°, no intermediate state between the pre-stall and stall noise regimes could be detected for the NACA 0021, which is more representative of a wind turbine airfoil, compared with a smooth transition over a range of at least 2° for the NACA 0012 airfoil and 8° for the flat plate. This implies that the noise of the thicker NACA 0021 airfoils will display a more impulsive characteristic than the NACA 0012 in this Reynolds number range under a cyclic change of angle of attack. In addition to this the low-frequency noise generated as the airfoils stall displays a strong dipolar directivity, indicating that there could be further periodic changes in noise level at downstream locations. A wake study and analysis of the measured directivity indicate that vorticies shed from the trailing edge after separation are the most likely source of this noise. However more research, using similar methodology at higher Reynolds numbers, is required in order to determine how these airfoils behave under the conditions experienced by wind turbines in the field before conclusions can be drawn about impulsive wind turbine noise.

[1] Brooks, T. F., Pope, D. S., and Marcolini, M. A. *Airfoil self-noise and prediction.* National Aeronautics and Space Administration, Office of Management, Scientific and Technical Information Division, 1989.

[2] Paterson, R. W., Vogt, P. G., Fink, M. R., and Munch, C. L. Vortex noise of isolated airfoils. *Journal of Aircraft 10*, 5 (1973), 296–302.

[3] Fink, M., and Bailey, D. Airframe noise reduction studies and clean-airframe noise investigation. Tech. rep., 1980.

[4] Madsen, H. A., Bertagnolio, F., Fischer, A., and Bak, C. Correlation of amplitude modulation to inflow characteristics.

[5] Oerlemans, S. Effect of wind shear on amplitude modulation of wind turbine noise. *International Journal of Aeroacoustics 14*, 5–6 (2015), 715–728.

[6] Laratro, A., Arjomandi, M., Kelso, R., and Cazzolato, B. A discussion of wind turbine interaction and stall contributions to wind farm noise. *Journal of Wind Engineering and Industrial Aerodynamics 127* (2014), 1–10.

[7] Bianchi, S., Corsini, A., Sheard, A. G., and Tortora, C. A critical review of stall control techniques in industrial fans. *ISRN Mechanical Engineering 2013* (2013), 1–18.

[8] Oerlemans, S., and Schepers, J. Prediction of wind turbine noise and validation against experiment. *Noise Notes 9*, 2 (2010), 3–28.

[9] Moreau, S., Roger, M., and Christophe, J. Flow features and self-noise of airfoils near stall or in stall. In *15th AIAA/CEAS Aeroacoustics Conference* (2009).

[10] Ostowari, C., and Naik, D. Post-stall wind tunnel data for NACA 44XX series airfoil sections. Tech. rep., Solar Energy Research Institute, 1985.

[11] Huyer, S. A., Simms, D., and Robinson, M. C. Unsteady aerodynamics associated with a horizontal-axis wind turbine. *AIAA journal 34*, 7 (1996), 1410–1419.

[12] Timmer, W. An overview of NACA 6-digit airfoil series characteristics with reference to airfoils for large wind turbine blades. In *47th AIAA Aerospace Sciences Meeting including The New Horizons Forum and Aerospace Exhibition.*

[13] Swalwell, K., Sheridan, J., Melbourne, W., et al. The effect of turbulence intensity on stall of the NACA 0021 aerofoil. In *Proceedings of the14th Australasian Fluid Mechanics Conference* (2001), pp. 10–14.

[14] Gaunaa, M. *Unsteady aerodynamic forces on NACA 0015 airfoil in harmonic translatory motion.* PhD thesis, 2002.

[15] Howe, M. *Acoustics of fluid-structure interactions.* Cambridge University Press, 1998.

[16] Laratro, A., Arjomandi, M., Cazzolato, B., and Kelso, R. An experimental comparison of the self-noise of NACA 0012 and NACA 0021 airfoils at stall. *Submitted to International Journal of Aeroacoustics* (2017).

[17] Rodríguez, I., Lehmkuhl, O., Borrell, R., and Oliva, A. Flow past a NACA 0012 airfoil: From laminar separation bubbles to fully stalled regime. In *Direct and Large-Eddy Simulation IX* (2015).

[18] Bahr, C., and Cattafesta, L. N. Limits of coherence-based aeroacoustic analysis in the presence of distributed sources. *The Journal of the Acoustical Society of America 129*, 6 (2011), 248–253.

[19] Bertagnolio, F., Madsen, H. A., Bak, C., Troldborg, N., and Fischer, A. Aerodynamic noise characterization of a full-scale wind turbine through high-frequency surface pressure measurements. *International Journal of Aeroacoustics 14*, 5-6 (2015), 729–766.

[20] Tamai, M. Experimental investigations on biologically inspired airfoils for MAV applications. Master's thesis, Iowa State University, 2007.

[21] Huang, R. F., and Lin, C. L. Vortex shedding and shear-layer instability of wing at low-Reynolds numbers. *AIAA Journal 33*, 8 (1995), 1398–1403.

[22] Yarusevych, S., Sullivan, P. E., and Kawall, J. G. On vortex shedding from an airfoil in low-reynolds-number flows. *Journal of Fluid Mechanics 632* (2009), 245–271.

[23] Friman, M. Directivity of sound from wind turbines. Master's thesis, KTH, 2011.

[24] Renewable UK. Wind turbine amplitude modulation: research to improve understanding as to its cause and effect, 2013.

Chapter 6

Sound Scattering Due to a Vortex

6.1 Chapter overview

In this chapter an experimental investigation of the sound scattered by a decaying Rankine vortex is presented and compared with theory. This is done to determine whether a quasi-steady analysis of scattering is appropriate for a wind turbine undergoing dynamic stall, or if more-complicated methods are required in order to properly describe the propagation of sound. The focus is on the scattering of sound from vortices, as while the vortices do also generate noise it is of a quadrupolar nature and is expected to be significantly lower than the noise generated by the airfoil at subsonic Mach numbers.

It was found that existing modelling techniques, applied in a quasi-steady manner, are adequate to describe the scattering from a decaying vortex. When this is applied to a full-scale wind turbine, sound generation is strongest on the outer parts of the blades where the reduced frequency is low, and therefore the probability that dynamic stall will occur is low, and the circulation of the dynamic-stall vortex if it does occur is also low. This means that the portion of sound scattered and the sound pressure level of the incident sound field have an opposite trend with changes in spanwise location on the blade. In addition, the scattering potential decreases as the frequency of scattered sound decreases, so low-frequency noise will experience less scattering.

6.2 Discussion of the effects of dynamic stall vorticies on wind turbine noise

Statement of Authorship

Title of Paper	An experimental investigation into the effect of vortex decay on the scattering of sound
Publication Status	☐ Published ☐ Accepted for Publication ☑ Submitted for Publication ☐ Unpublished and Unsubmitted w ork w ritten in manuscript style
Publication Details	Laratro, A., Arjomandi, M., Kelso, R., and Cazzolato, B. An experimental investigation into the effect of vortex decay on the scattering of sound. Submitted to International Journal of Acoustics and Vibration (March 2017)

Principal Author

Name of Principal Author (Candidate)	Alex Laratro		
Contribution to the Paper	- Data collection, analysis, visualisation, and interpretation - Writing of the manuscript and production of original figures - Correspondence with editor and reviewers including the production of all cover letters and rejoinders		
Overall percentage (%)	80%		
Certification:	This paper reports on original research I conducted during the period of my Higher Degree by Research candidature and is not subject to any obligations or contractual agreements with a third party that would constrain its inclusion in this thesis. I am the primary author of this paper.		
Signature		Date	

Co-Author Contributions

By signing the Statement of Authorship, each author certifies that:

i. the candidate's stated contribution to the publication is accurate (as detailed above);

ii. permission is granted for the candidate to include the publication in the thesis; and

iii. the sum of all co-author contributions is equal to 100% less the candidate's stated contribution.

Name of Co-Author	Maziar Arjomandi		
Contribution to the Paper	- Supervision of the work, including the production of the manuscript - Participation in the development of the concepts and ideas presented in the manuscript - Evaluation and editing of the manuscript prior to submission		
Signature		Date	

Name of Co-Author	Benjamin Cazzolato		
Contribution to the Paper	- Supervision of the work, including the production of the manuscript - Participation in the development of the concepts and ideas presented in the manuscript - Evaluation and editing of the manuscript prior to submission		
Signature		Date	

Name of Co-Author	Richard Kelso		
Contribution to the Paper	- Supervision of the work, including the production of the manuscript - Participation in the development of the concepts and ideas presented in the manuscript - Evaluation and editing of the manuscript prior to submission		
Signature		Date	

An experimental investigation into the effect of vortex decay on the scattering of sound

Alex Laratro[a], Maziar Arjomandi[a], Benjamin Cazzolato[a], Richard Kelso[a]

[a] *School of Mechanical Engineering, The University of Adelaide, South Australia 5005, Australia*

Abstract

When a wind-turbine blade undergoes dynamic stall, large vortices are shed into the wake, and these will have an effect on the directivity of the noise emissions from the wind turbine. The problem of refraction and scattering of noise by vorticity has been well documented in the literature, but only under steady-state conditions. It is widely assumed that the large difference in time scales between the decay of a vortex and sound passing through that vortex means that the scattering problem can be treated as quasi-steady, but this has not been experimentally verified. This paper investigates the impact of transient vorticity on the scattering problem by passing sound through vortices which decay over periods 2.5×10^4 and 1.8×10^5 times larger than the time taken for the sound to pass through the vortex cores. The results suggest that a quasi-steady approach is suitable for wind turbine aeroacoustics. The effect that dynamic stall vortices may have on the temporal stability of wind turbine noise is then discussed and it is concluded that its impact is likely to be minor.

Keywords:
Vortices, Sound scattering, Wind energy, Dynamic stall

1. Introduction

In recent years there has been an interest in the generation of low-frequency noise by wind turbines and the impact that this noise has on the surrounding populations. In particular, a phenomenon known as "other amplitude modulation", which is characterised by short and unpredictable instances of periodic modulation of the low-frequency (20-200Hz) noise signal [1]. While the cause of this periodic signal is still a matter of debate, there is evidence to suggest that instances of periodic stall on the wind turbine blades may be a primary contributor [2]. Additionally, there has been research into the effects that the structure of the turbine wake and atmospheric boundary layer have on the propagation of the low-frequency noise produced under these conditions [3]. This research

Email address: alex.laratro@adelaide.edu.au (Alex Laratro)

suggests that temperature and wind-speed gradients in the atmospheric boundary layer can result in the downward refraction of sound, which subsequently reflects off of the ground as shown in Figure 1. Because less sound is radiated upwards, this creates a zone where the cylindrical spreading occurs and the sound produced by the turbine can be detected across greater distances than predicted by spherical spreading models.

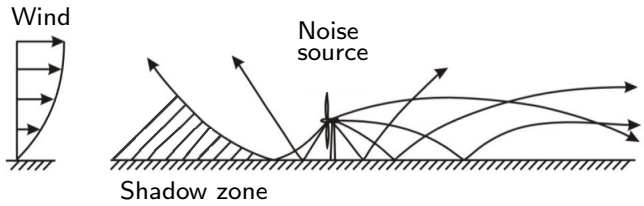

Figure 1: Atmospheric refraction of wind turbine noise in a positive velocity gradient. Adapted from Hansen et al. [3]

Another factor in the propagation of wind-turbine noise is the potential for the changing wake structure to affect the far-field noise levels over time. Studies by Peng [4] and Lee et al. [5] indicate that taking the wake into account when modelling the propagation of wind turbine noise can have a significant effect on noise predictions. These studies indicate that the presence of a turbulent wake can cause a spatial amplitude modulation pattern to form, increasing and decreasing the noise received at ground level downwind of a wind turbine. Barlas et al. [6] investigated how the unsteady wake affects noise propagation, observing that the sound is "ducted" by the wake velocity deficit and then released after wake breakdown, causing an increase in the levels of amplitude modulation observed at ground level downwind of the turbine. Barlas et al. also predicted that the maximum distance at which amplitude modulation can be observed upwind of the turbine increases with wavelength. This is because the formation of the shadow zone (see Figure 1) is also dependent on wavelength, and the distance at which the effect becomes pronounced is greatest at low frequencies.

The research presented here focuses on the phenomenon of dynamic stall, wherein an airfoil undergoes a rapid change in angle-of-attack past the stall angle, as is sometimes observed on wind turbine blades [7, 8], resulting in the shedding of a large vortex known as the dynamic stall vortex. The dynamic stall vortex moves through the wake as it dissipates, and has the potential to act as a scatterer for the low-frequency noise produced by the blades after the stall event, as shown in Figure 2. This will affect the overall directivity of the airfoil noise once the dynamic-stall event ends and the flow around the airfoil settles into a deep-stall state, and then recovering as the angle of attack is decreased and the flow reattaches to the blade. If the potential for scattering from these vortices is significant, then their introduction into the wake may result in further unsteady noise downwind.

Circulation of the fluid in the dynamic-stall vortex scales with the freestream velocity, U_∞, and the reduced frequency given by

$$\kappa = \frac{\dot{\alpha} c}{2 U_\infty}, \tag{1}$$

where $\dot{\alpha}$ is the rate of change of angle of attack, and c is the airfoil chord. The angle at which the dynamic-stall vortex is released does not vary significantly when compressibility effects are small [9]. Because of this, the time it takes for the dynamic stall vortex to form at a given reduced frequency decreases as the pitch rate, $\dot{\alpha}$, increases. When using a small airfoil chord the pitch rate must be higher for a given reduced frequency, so in small-scale tests the time scale of a dynamic stall event is reduced, so direct measurement of the sound produced during a dynamic stall event is not feasible.

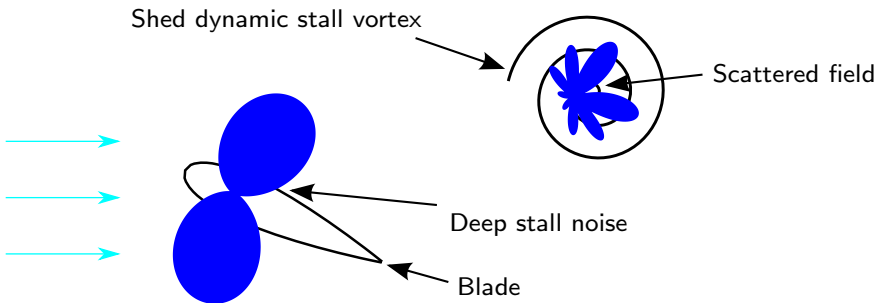

Figure 2: Scattering of sound from a shed dynamic stall vortex as it convects downstream of an airfoil that has resumed emission of deep stall noise. The lobes represent the directivity of the sound sources

A number of experiments have been conducted to investigate the effect of vorticity on the propagation of sound. Horne [10] used suction and tangential air jets to generate line vortices, and then measured how they scattered a plane wave. Labbé & Pinton [11] produced a vortex using corotating discs with blades on the outside that ejected air and then drew it in through holes in the centres of the discs. The waves produced by Labbé & Pinton were not ideal plane waves but this was not considered an issue as they were mostly concerned with the changes induced by the vortex. The vortex produced in that case underwent a noticeable precession, which affected the results. Manneville et al. [12] used an experimental setup similar to both that of Horne and Labbé & Pinton, with a set of corotating discs and a pump connected to the central holes to provide suction. In these experiments it was observed that the scattered field from the vortex reduced the overall sound pressure at negative angles from the direction of sound propagation and increased the sound pressure at positive angles from the direction of sound propagation. This indicates that the net effect of the vortex is the refraction of sound in the direction of rotation.

Several models for determining the scattering of sound from vorticity are described by Colonius et al. [13]. It was observed that the density amplitude of the scattered sound has a local minimum in the incident direction of the sound wave surrounded by two maxima at approximately $\pm 30°$. The normalised peak density amplitude of the scattered sound field, $\rho_{\text{scattered}}/(\rho_{\text{in}}\epsilon)$, was found to

collapse to values between 2 and 2.75 (increasing with observation distance), where $\rho_{\text{scattered}}$ and ρ_{in} are the root-mean-square density perturbations of the scattered and incident fields respectively. The term ϵ is the normalised circulation of the vortex,

$$\epsilon = \Gamma/(a_\infty \lambda), \tag{2}$$

where Γ is the circulation of the vortex, λ is the wavelength of the incident sound, and a_∞ is the speed of sound. As the value of $\rho_{\text{scattered}}/(\rho_{\text{in}}\epsilon)$ is approximately constant, the value of $\rho_{\text{scattered}}$ depends on the amplitude of the incident sound field, ρ_{in} and the normalised circulation parameter ϵ. As such, the peak amplitude of the scattered field increases with both the vortex circulation and the frequency of the scattered sound as these are directly proportional to the value of ϵ.

As the amplitude of the scattered sound wave is proportional to the circulation of the vortex, the ability to predict it leads to the ability to predict the scattered field. The parameter

$$\Gamma^* = \frac{\Gamma}{cU_\infty}, \tag{3}$$

is also a normalised circulation that relates the circulation to the velocity of the flow and length scale of the vortex. Typical circulations of dynamic stall vortices from large wind turbines have not been measured, but PIV measurements of the dynamic stall of a vertical-axis wind turbine by Ferreira et al. [14] indicate that at a Reynolds number of 50,000 a typical value for Γ^* is approximately 8 as the vortex forms, and then it linearly decreases with time as the vortex convects away from the surface. Another experimental investigation by Gharali & Johnson [15] measured the circulation of the dynamic stall vortex formed on the suction surface of an oscillating SD7037 airfoil. These results showed that for a Reynolds number of 4,000 the maximum circulation increased with reduced frequency, reaching a value of $\Gamma^* = 3.4$ for $\kappa = 0.12$. For comparison, measurements of wind turbine tip vortices at Reynolds numbers of 11,000 and 1,000, based on chord and the freestream velocity in the reference frame of the blade, yielded normalised circulation values of approximately 0.7-1.7 (depending on tip speed ratio) [16] and 0.4 [17] respectively.

As a step towards addressing the gaps in the literature, this study focuses on the effects of vortex decay on the problem of a sound scattering by a vortex. The directivity of a sound wave scattered by the decaying vortex is compared to both the steady-state case and the case where the vortex is not present. Then a conclusion is drawn as to whether the quasi-steady approximation is sufficient with regards to the problem of dynamic stall vortices and comments are made on the expected strength of the scattered field in wind turbine applications.

2. Method

2.1. Experimental setup

The vortex was produced between two corotating discs with diameters of 300mm, as shown in Figure 3, which could be driven at rotational speeds of 0-20rps in the negative z-direction. The discs were coated in a 25mm thick layer of acoustic foam to both produce a rough surface, thereby increasing the energy imparted to the surrounding air, as well as providing over 50% absorption of reflected acoustic energy above 750Hz. A vacuum pump was connected to 20mm holes in the centres of each disc and this extracted air to produce a low pressure region to form the vortex core. The flow was characterised using velocity measurements obtained with a TFI brand Cobra Probe, which is a 4-hole pressure probe capable of measuring the flow velocity up to a velocity of 45m/s, and pitch and yaw angles of up to $\pm 45^{\circ}$. The Cobra Probe was mounted to a 3-axis traverse (seen in Figure 3b), and aligned to the experimental coordinate system as shown in Figure 3a. The vortex velocity field was characterised by taking velocity measurements from y = -170mm to 170mm at three different heights, and the relationship between velocity and rotational speed was measured at four different locations, as shown by the dots in Figure 3c. As the probe is only able to measure incident flow with a pitch and yaw of $\pm 45^{\circ}$, it was not possible to measure the entire velocity field of the vortex without remounting the probe, so additional measurements were then taken after moving the probe to the opposite side of the vortex to check for axisymmetry.

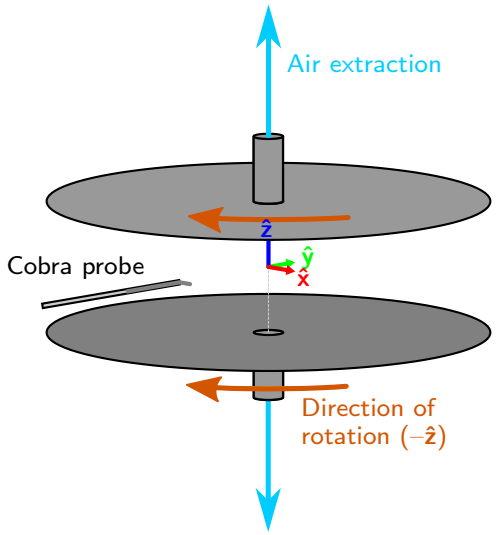

(a) Schematic of vortex generation rig

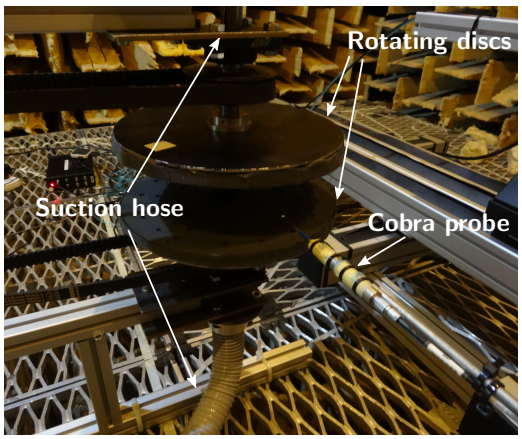

(b) Photograph of experimental setup for bulk fluid velocity measurements

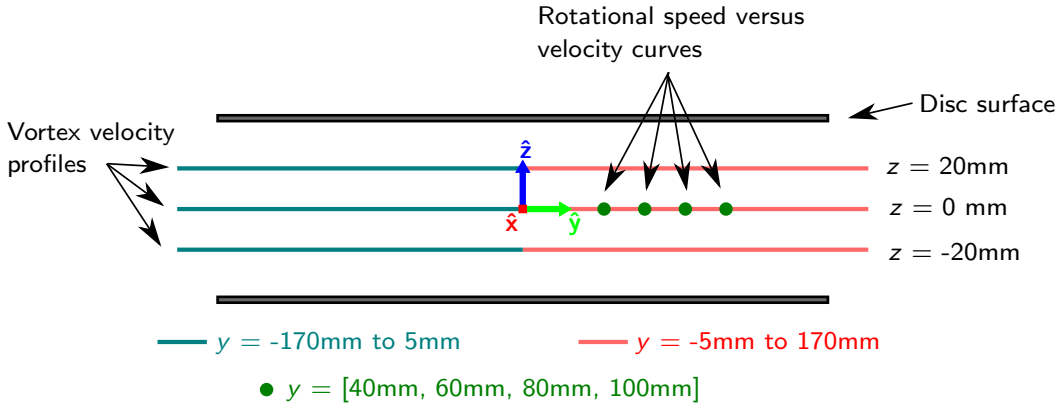

(c) Measurement locations

Figure 3: Experimental setup for bulk fluid velocity measurements

Sound measurements were performed using an existing array of 32 GRAS 40PH microphones, placed in the midplane of the vortex at a radius of 540mm and angles from -75°to 80°in 5° increments, as shown in Figure 4. Sound was generated by a 30mm diameter speaker placed at $x = 515$mm.

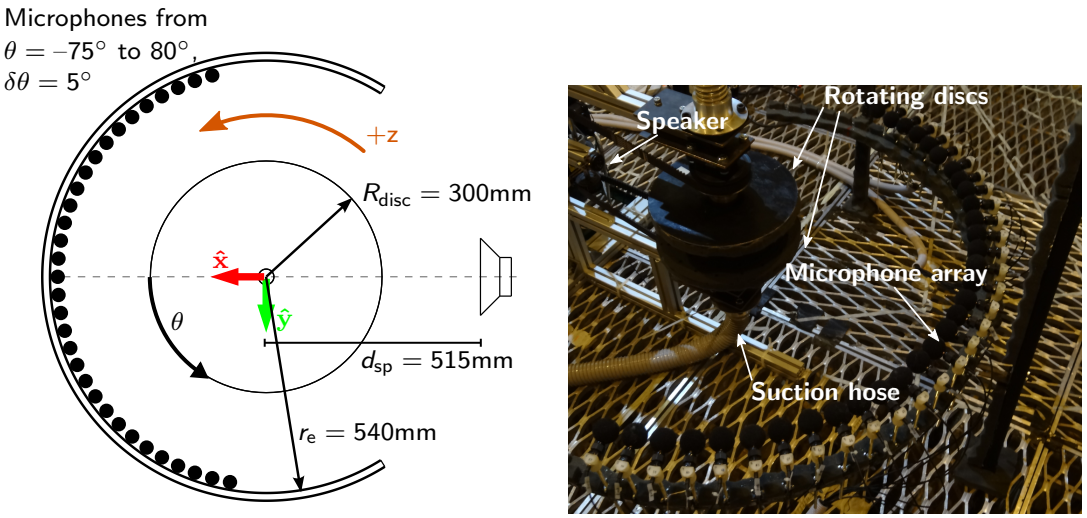

(a) Planar schematic showing microphone locations in relation to discs and speaker

(b) Photograph of experimental setup for acoustic measurements

Figure 4: Experimental setup for acoustic measurements

Steady-state acoustic and velocity measurements were taken at disc rotational speeds from 0rps to 20rps in increments of 5rps. All acoustic tests were conducted using tonal sources, providing high signal-to-noise ratios above background. The chosen frequencies were 512Hz, 1024Hz and 2048Hz, which correspond to values of r_e/λ of 0.8, 1.6 and 3.2 respectively, where r_e is the radius of the microphone array. Octave frequency shifts were chosen instead of multiples of ten to both avoid interference from any electrical noise and to bin-centre the tones regardless of spectrum bandwidth. Each frequency was generated at separate times to prevent contamination by higher-order harmonics. Transient sound and velocity measurements were also taken using a rotational speed profile that decreased linearly from 20rps to 0rps over periods of 2 and 15 seconds. The discs were held at the starting speed of 20rps for several seconds before recording started in order to ensure that it had fully developed, and then two more seconds after recording had begun to establish a baseline measurement.

All data were collected at a sampling rate of 32,768Hz. The microphones are rated to 10kHz, and as previously mentioned, the Cobra Probe is rated to 2kHz. Each steady-state velocity measurement was taken as a single 15 second buffer, and the steady-state acoustic data were collected over ten non-consecutive 15 second buffers, with a short delay as the previous buffer is saved. The acoustic data were processed using Welch's method, with a Hanning window 8192 points long and a 50% overlap, leading to a total of 1190 averages and a frequency resolution bandwidth of 4Hz. Each of the 30 transient data spectrograms were generated using a short-time Fourier transform with the same parameters, and then averaged to form a final spectrogram for each case. Using a frequency resolution bandwidth of 4Hz with a 50% overlap gives a time resolution of 0.125 seconds, and each Fourier transform is of a sample 0.25 seconds long.

The parameter of interest in the experiment is the ratio of the mean-square

sound pressure between the vortex-on and vortex-off states, $p^2_{\text{on}}/p^2_{\text{off}}$, at the frequency of interest. This value quantifies the amount of refraction through the vortex and is also equivalent to a ratio of sound intensities, $I_{\text{on}}/I_{\text{off}} = p^2_{\text{on}}/p^2_{\text{off}}$, in the far field.

3. Results

3.1. Vortex characterisation

Prior to the commencement of acoustic experiments, the vortex generator was characterised to confirm that the vortex was suitable, and to measure the relationship between circulation and rotational speed. Figure 5 shows the steady-state tangential velocity profile, $u_\theta(y)$, and resulting local circulation, $\Gamma = 2\pi r$, where $r = \sqrt{x^2 + y^2}$, for the tested rotational speeds.

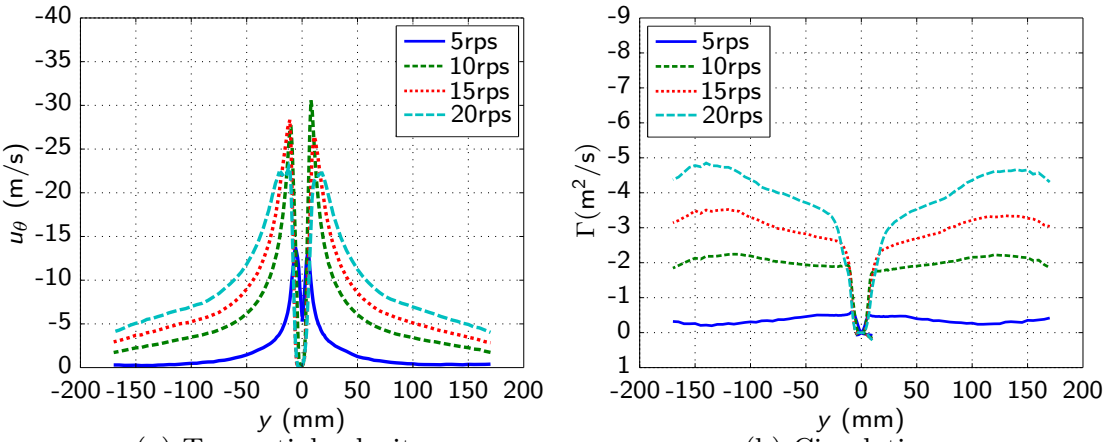

(a) Tangential velocity (b) Circulation

Figure 5: Vortex velocity profile for rotational speeds from 5rps to 20rps

In Figure 6 the variation in circulation versus rotational speeds is plotted, and shows that there is an approximately linear relationship between rotational speed and circulation above f_ω = 9rps. The term Γ_{mean} referred to in Figure 6a is the mean of the circulation between the core radius, r_{c}, and the limit of measurement, y = 170mm. Figure 6b is the result of the measurements at y = 40mm, 60mm, 80mm, and 100mm, with rotational speeds from 0rps to 20rps with a 1rps spacing. It was desired that the circulation decreases linearly over time to simulate a dynamic-stall vortex decaying [14]. There is a small non-linearity in the circulation-versus-rotational-speed characteristic of the experimental setup below 7rps, however this is not expected to have a significant effect in the run-down experiments.

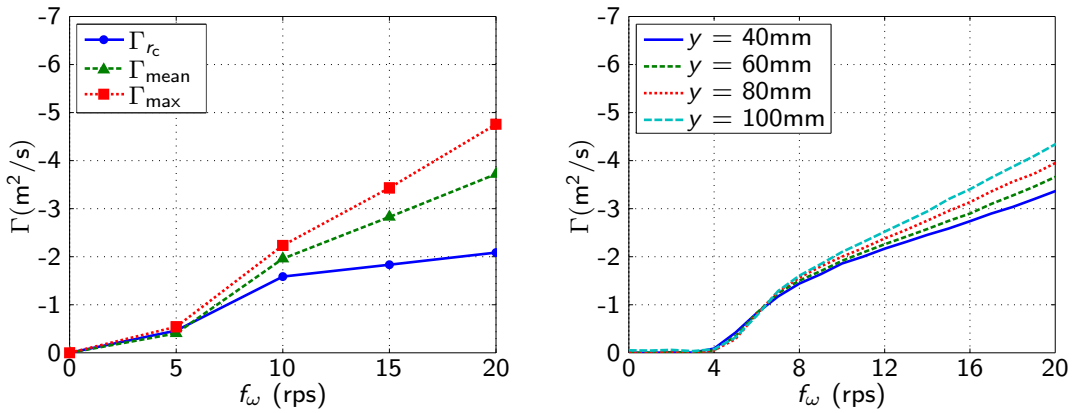

(a) Variation of core, mean, and maximum circulation in vortex velocity profiles

(b) Variation of local circulation at the locations detailed in Figure 3c

Figure 6: Variation of circulation of the vortex in the $z = 0$ plane with rotational speed of discs

Figure 7 shows the three components of velocity for the f_ω = 20rps case. Figure 7b shows that the radial flow towards the centre is greatest in the mid-plane, and that near the edges of the discs the radial flow is directed outwards. It can be seen the radial flow is strongest in the mid-plane of the vortex and centripetal, whereas closer to the discs centrifugal flow occurs due to the rotation being more dominant.

From these measurements a characteristic acoustic time-scale can be defined, $\tau_{20} = 2r_{20}/a_\infty$, where r_{20} is the core radius at a disc rotational speed of 20rps and a_∞ is the ambient speed of sound. This value can then be used to non-dimensionalise the vortex decay time, T.

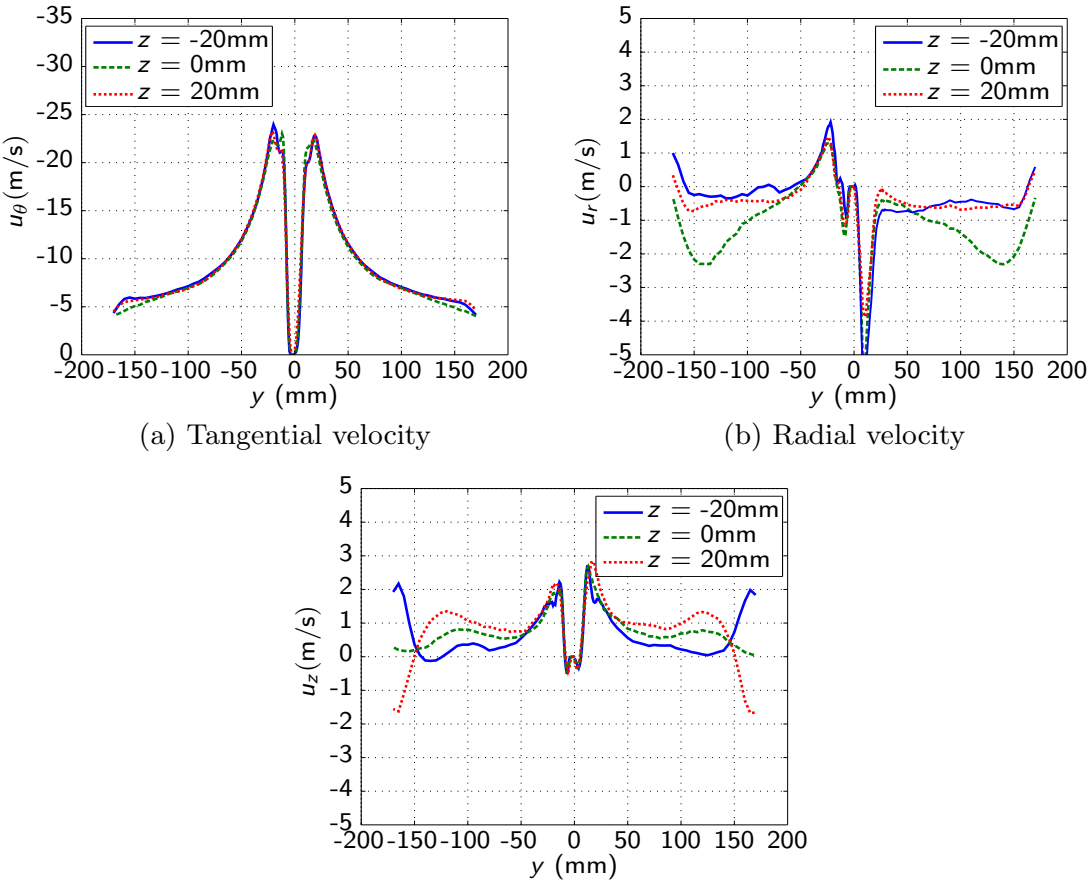

(a) Tangential velocity

(b) Radial velocity

(c) Axial velocity

Figure 7: Velocity profiles for a rotational speed of $f_\omega = 20$rps

3.2. Steady-state scattering

Figure 8 shows the ratio between the root-mean-square sound pressures measured at each microphone when the vortex is present and not present for the 2048Hz tone. At several rotational speeds the overall sound power has decreased dramatically, which upon review of the data appears to be due to an instability in the gain of the speaker.

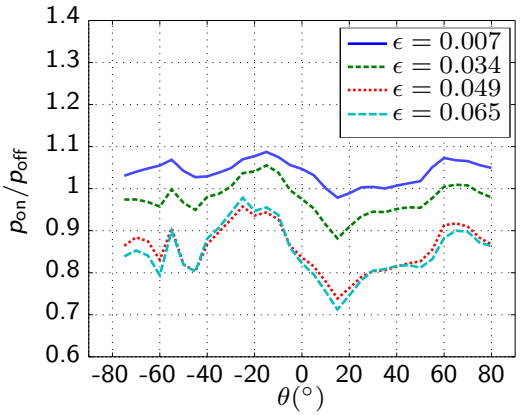

Figure 8: Ratio between steady state root-mean-square sound pressures at $f = 2048$Hz in vortex on and vortex off states for rotational speeds from 5rps ($\epsilon = 0.007$) to 25rps ($\epsilon = 0.085$)

When the results are normalised such that the mean value of p_{on}^2/p_{off}^2 is 1, that is, assuming that the captured sound power is constant, then we obtain the values displayed in Figure 9 for the 1024Hz and 2048Hz test sounds. It can then be seen that sound is directed from regions with positive angle to regions with negative angle and the changes in directivity increase with the circulation of the vortex and the frequency of incident sound, as expected. The results for the 512Hz case are not shown here because, as will be shown later, the data for that case did not produce conclusive results.

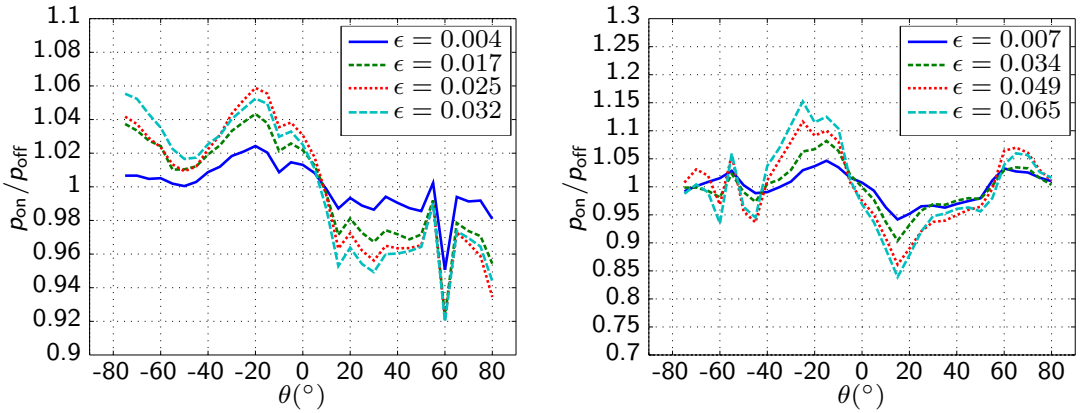

(a) $f = 1024$Hz (b) $f = 2048$Hz

Figure 9: Ratio between steady state RMS sound pressure in vortex on and vortex off states for different values of ϵ based on Γ_{mean}, normalised such that the mean value of p_{on}^2/p_{off}^2 is 1

Using the experimental parameters and the model of Colonius et al. [13], predictions for the scattered field strength can be produced as shown in Figure 10. This model decomposes the problem into an incident sound wave and a scattered sound wave, and predicts the amplitude of the sound wave scattered from the vortex, $p_{scattered}$, as a fraction of the amplitude of the incident field p_{in}. As the incident and scattered sound waves are coherent they can be added

directly, meaning that once phase, which is not included in the model of Colonius et al. [13], is accounted for, then $p_{\text{on}}/p_{\text{off}}$ is equivalent to $p_{\text{scattered}}/p_{\text{in}} + 1$.

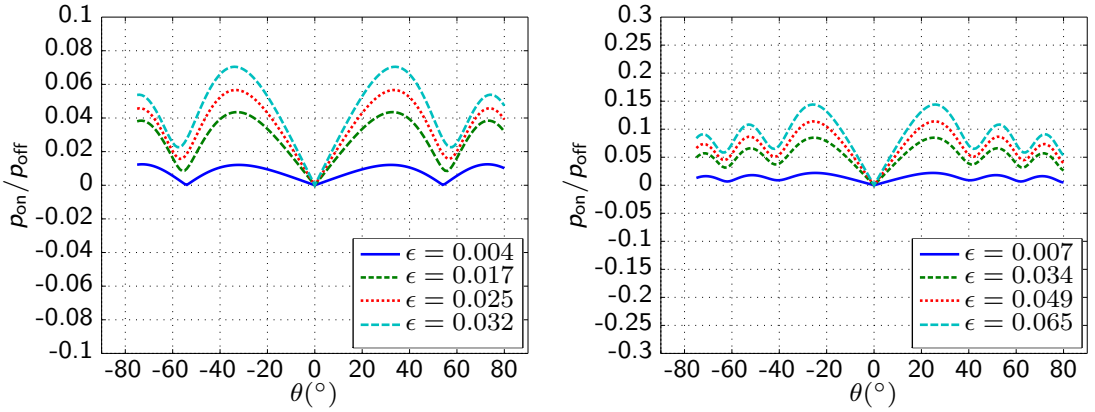

(a) $f = 1024$Hz (b) $f = 2048$Hz

Figure 10: Analytical predictions of the sound pressure amplitude of the scattered field

The analytical predictions give good agreement with the experimental results for the most part, though the results for the 1024Hz tone (Figure 10a) do not agree at higher disc rotational speeds. The predictions in Figure 10 show the amplitude of the scattered wave, but as mentioned previously do not take phase into account, which is why they do not show the destructive interference at positive angles that is evident in the experimental results. This interference pattern, where sound is refracted in the direction of vortex rotation, is also observed in the experimental work of Horne [10] which indicated that as the observation angle from the direction of vortex propagation deviated from zero, the phase difference between the incident and scattered field changes. At small angles from the incident direction this leads to a lower sound amplitude in the negative θ direction for a vortex circulating in the positive z-direction as the scattered field destructively interferes with the incident field (Figure 11). This is consistent with the observations of the current experiments, though the direction in which the sound is refracted in reversed due to the vortex having negative circulation.

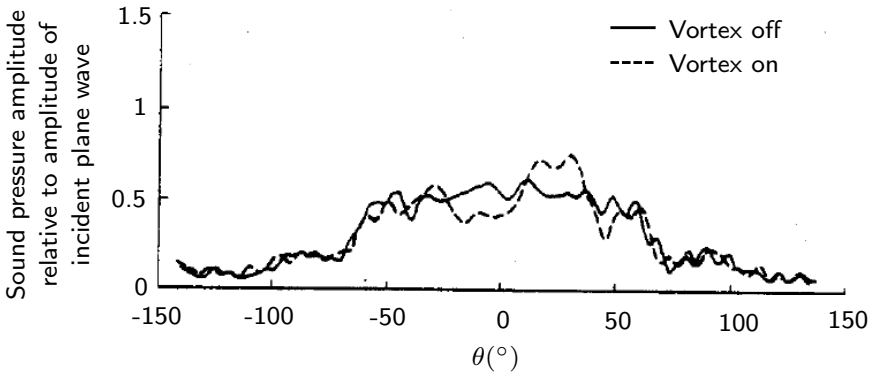

Figure 11: Comparison of sound pressure amplitudes measured within and without the presence of a scattering vortex, $\epsilon = 0.1275$, $r_e/\lambda = 5.92$. Adapted from Horne [10]

3.3. Transient scattering

Comparisons of the change in sound directivity at 2048Hz between the vortex-off and vortex-on states for the different rotational speed profiles, are shown in Figure 12. This is done by displaying the steady-state value of p_{on}/p_{off} at a given rotational speed alongside the values of p_{on}/p_{off} derived from the short-time Fourier transforms of the corresponding transient tests. The normalisation scheme used to process the steady state data is not required for the transient cases, as the sound output power from the speaker is consistent for each of these tests.

The comparison between the steady-state and transient results show that there is little difference in the change of directivity between the steady-state case and the 15-second and 2-second-long linear frequency profiles ($T/\tau_{20} = 2.5\times10^4$ and $T/\tau_{20} = 1.8\times10^5$ respectively). This information is presented in a different format in Figure 14 which shows the value of p_{on}/p_{off} at each of the time steps of the short-time Fourier transforms. Figures 13 & 15 then show the same information for the cases with the 512Hz and 2048Hz tones respectively. It can be seen that there is no notable difference in the change in directivity as the period of time over which the vortex decays decreases. Of note is the 512Hz case shown in Figure 13 which shows that there is no discernible scattering in this case. The signal-to-noise ratio was lower at this frequency, but as the coherence between the signal sent to the speaker and the signals recieved at the microphones were above 99%, this is not likely to be the cause of the observation. However, the scattered field is expected to be weaker again by a factor similar to that between 1024Hz and 2048Hz cases (i.e., about 1/3rd), making it harder to detect and this could be why no consistent scattering pattern is observed. Similarly, the scattering of the 1024Hz tone fluctuated somewhat with time, but when viewed as a whole the trend is easier to discern.

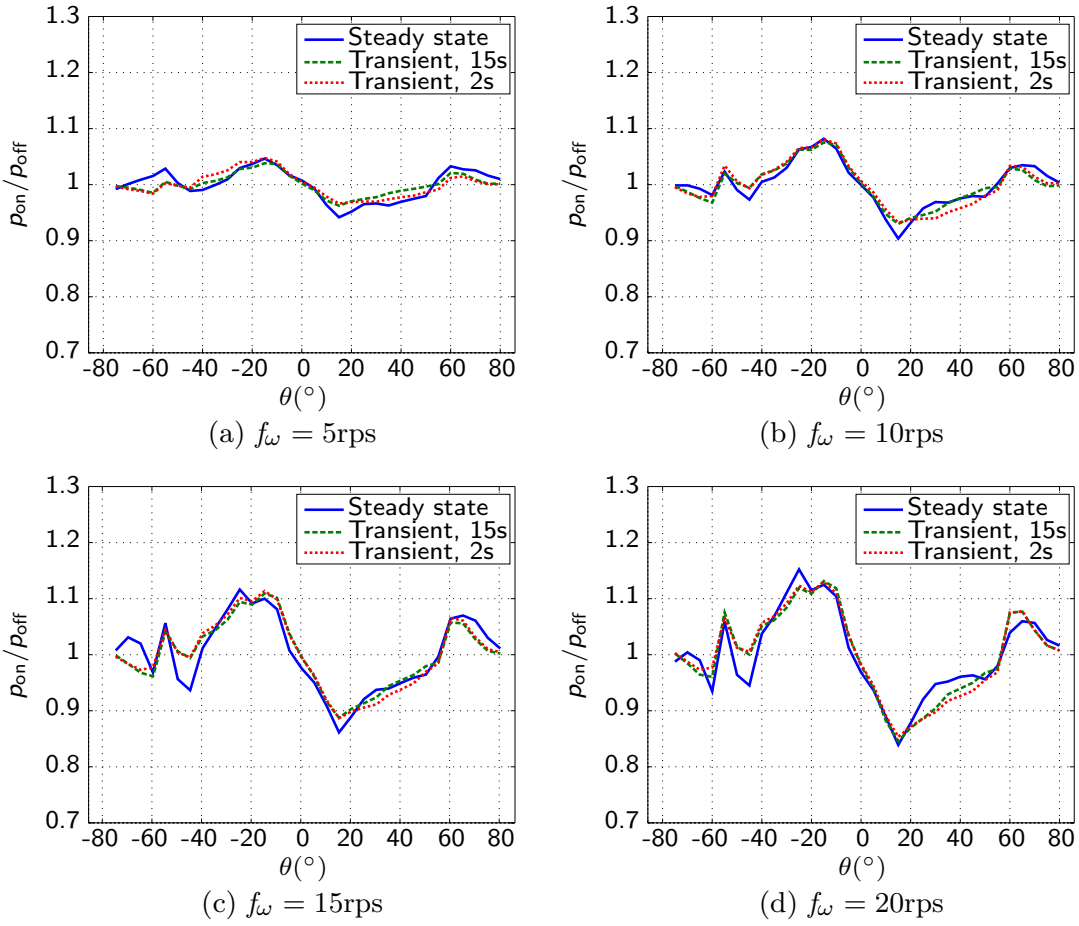

(a) $f_\omega = 5$rps (b) $f_\omega = 10$rps

(c) $f_\omega = 15$rps (d) $f_\omega = 20$rps

Figure 12: Comparison of steady-state measurements of the ratio between RMS sound pressure at $f = 2048$Hz in vortex on and vortex off states, with measurements of the ratio between RMS sound pressure at $f = 2048$Hz during vortex decay with periods of $T = 15$s and $T = 2$s and the RMS sound pressure at $f = 2048$Hz without the presence of a vortex

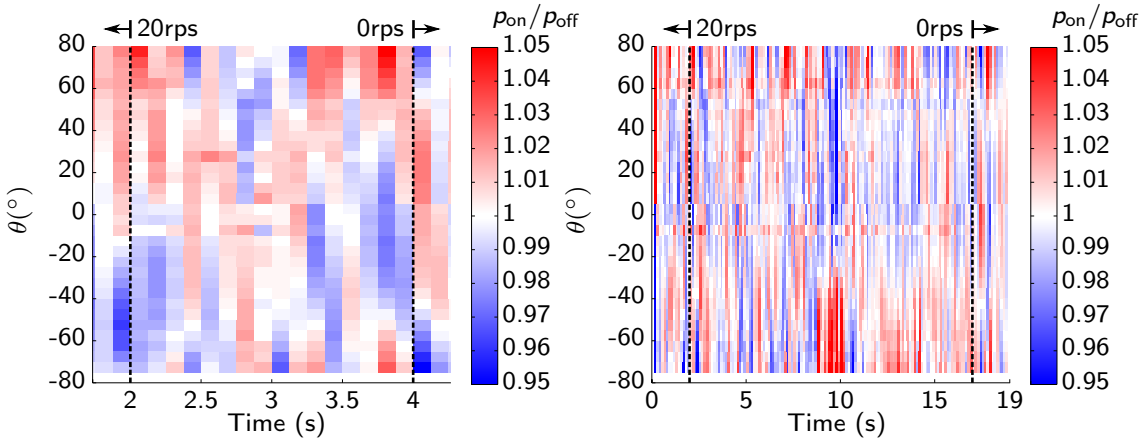

(a) $T = 2$s (b) $T = 15$s

Figure 13: Variation with time of the ratio between RMS sound pressure at $f = 512$Hz during vortex decay with periods of $T = 15$s and $T = 2$s and the RMS sound pressure at $f = 512$Hz without the presence of a vortex. Dashed lines represent the beginning and end of velocity profile

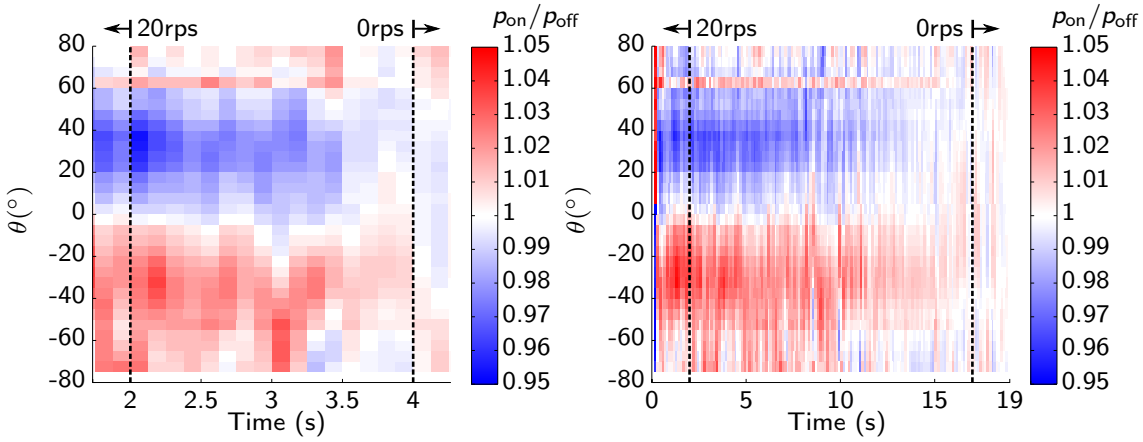

(a) $T = 2$s (b) $T = 15$s

Figure 14: Variation with time of the ratio between RMS sound pressure at $f = 1024$Hz during vortex decay with periods of $T = 15$s and $T = 2$s and the RMS sound pressure at $f = 1024$Hz without the presence of a vortex. Dashed lines represent the beginning and end of velocity profile

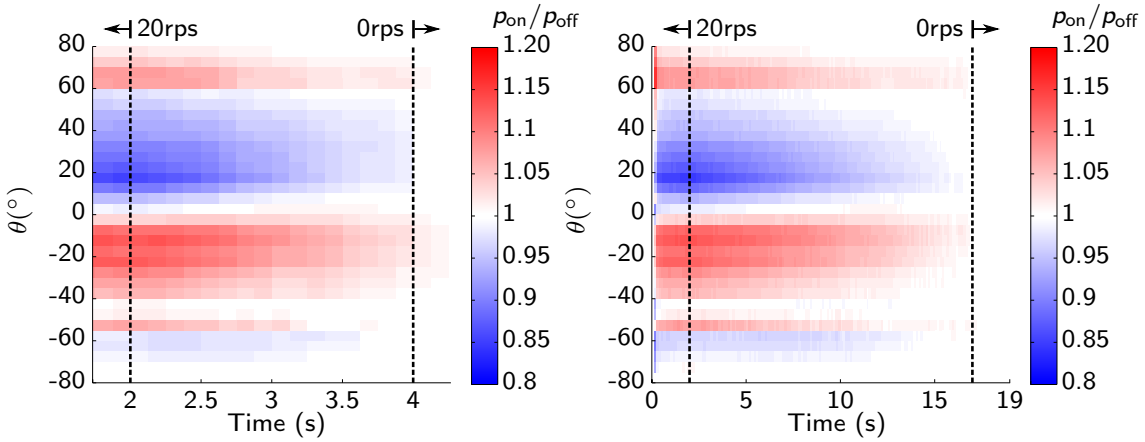

(a) $T = 2$s (b) $T = 15$s

Figure 15: Variation with time of the ratio between RMS sound pressure at $f = 2048$Hz during vortex decay with periods of $T = 15$s and $T = 2$s and the RMS sound pressure at $f = 2048$Hz without the presence of a vortex. Dashed lines represent the beginning and end of velocity profile

4. Discussion

The current results indicate that for the decay periods studied, 2.5×10^4 and 1.8×10^5 times the acoustic time scale, a quasi-steady approach to predicting scattering is sufficient. As the ratio between the time scales is much greater than unity, this result was expected as the propagation of the sound through the vortex is expected to be decoupled from the changes in the vortex velocity field. As such the modelling approach of Colonius et al. [13] can be easily implemented into transient noise models if required, such as predicting the effect that coherent vortices such as those shed in a dynamic-stall event have on airfoil noise propagation. It is not yet known if the vortices shed during dynamic stall are strong enough to cause significant enough scattering to take this effect into account when modelling wind turbine noise.

Refraction and scattering of sound from a vortex is primarily characterised by the normalised circulation parameter ϵ (see Equation 2) and as ϵ increases, more of the incident acoustic energy is scattered [13]. The normalised circulation of a dynamic stall vortex, Γ^* (see Equation 3), is in turn dependent on reduced frequency. Equations 2 & 3 can then be combined to form:

$$\epsilon = \Gamma^* \frac{fcU_\infty}{{a_\infty}^2}. \tag{4}$$

Ferreira et al. [14] observed a value of $\Gamma^* \approx 8$ for a reduced frequency of $\kappa = 0.125$ and a Reynolds number of 50,000. Subsequently Gharali & Johnson [15] observed values of $\Gamma^* = 3.4$ for a reduced frequency of $\kappa = 0.12$ and $\Gamma^* \approx 2.3$ for a reduced frequency of 0.05 at a Reynolds number of 4,000.

Large-scale wind turbines operate at much higher Reynolds numbers based on blade chord (on the order of 10^6 to 10^7), which increases the circulation of the dynamic stall vortex. Wind turbines of 2MW capacity also have blades with

large chords, ranging from approximately 1m at the tip to around 4m at the root, increasing the length scale of the dynamic stall vortex and proportionally decreasing the minimum frequency at which refraction will be significant. There are no measurements reported in the literature that describe the decay of a dynamic-stall vortex in the wake of a horizontal-axis wind turbine, however, as an example, with a core radius of $r_c = 1$m and a vortex decay time on the order of $T = 10$s, the value of T/τ is 3.4×10^3. This is an order of magnitude lower than the lowest value obtained during this experiment but still much greater than unity, and it would remain so after an order of magnitude reduction. A time-scale ratio this low was not achieveable with the current experimental setup, so it is still possible that transient effects will be observable, but as the ratio of time constants is so much greater than unity, this suggests that the steady-state modelling approach can be applied to wind turbine noise propagation.

As the reduced frequency is proportional to the chord and inversely proportional to the free-stream velocity, dynamic-stall events are less severe near the tip of the blade. Using a Siemens SWT-2.3-93 wind turbine [18] operating in 8m/s winds with a tip-speed ratio of 8 as an example, then near the blade tip, $U_\infty = 64$m/s, $c = 0.8$m, and $\kappa \approx 0.009$. This is considered quasi-steady and will not generate a strong dynamic stall vortex. For this example scenario the parameters at a location of 30% span are $U_\infty \approx 20.6$m/s, $c \approx 3.5$m, and $\kappa \approx 0.09$. The results of Gharali & Johnson [15] then suggest that the circulation of the vortex will be at least $\Gamma^* = 2.9$, and likely higher due to the higher Reynolds number. Taking this number as a lower bound for the circulation of the vortex at this reduced frequency gives

$$\epsilon \approx 2.9 \times \frac{fcU_\infty}{{a_\infty}^2} \tag{5}$$

and then for the 30% span location $\epsilon \approx 0.0018f$, which is large enough to cause significant scattering even at very low frequencies ($\epsilon = 0.09$ for $f = 50$Hz). As the sound pressure level produced by a section of the blade scales with somewhere between the fifth and sixth of power Mach number [19, 20], the interaction between sound and vortices produced at inboard locations is unlikely to have any significant effect on the overall noise emissions of a wind turbine. The competing factors that contribute to the amplitude of the scattered field are summarised in Table 1.

Table 1: Variation in parameters that affect sound scattering amplitude with spanwise location. *denotes parameters that also have an indirect effect due to their relationship with other parameters

	Increasing spanwise location	**Effect on ϵ**
c	Decreases	Decreases*
U	Increases	Increases*
Re	Increases with cU	Increases
κ	Decreases with c/U	Decreases

In addition to the potential of the dynamic stall event to scatter sound, the time it takes for the flow around the airfoil to resume the emission of low frequency noise after the dynamic stall event is important. As the vortex moves downstream it continues to decay and the distance to the sound source increases, which reduces the strength of the incident field, both of these factors weaken the scattered sound field, reducing the effect of scattering on the overall directivity of the wind turbine's noise emissions. If the scattering is weak, then not only will it have only a small impact on the wind turbine noise, but it may be dominated by other sources of turbulence, such as the helical tip vortices produced by the rotating blades.

As current knowledge of the effect of reduced frequency and Reynolds number on the circulation of dynamic stall vortices is very limited, it cannot be definitively stated under which conditions and at which locations on the blade the scattering effect will be dominant, and the lack of this parameterisation of dynamic stall vortices is the most significant impediment to further analysis.

5. Conclusion

The effect that transience has on the scattering of sound from a vortex in air was investigated from normalised circulations from $\epsilon = 0.002$ to $\epsilon = 0.085$. It was found that the ratio of the period of vortex decay to the acoustic time-scale (from $T/\tau = 2.5 \times 10^4$ to 1.8×10^5) has no discernible impact on the scattering amplitude of sound. This suggests that the ratio of decay period to time-scale is sufficiently high for a quasi-steady approach to be used when predicting how sound will be scattered by a decaying vortex, such as the one shed from the leading edge of an airfoil during dynamic stall. In the case of a wind-turbine airfoil, noise scattering by a dynamic-stall vortex is likely to be weak relative to the sound generated by the blades. This is because at the locations on the blades where airfoil noise production is strong, the scattering potential of the vortex is weak, and vice-versa.

More detailed analysis of the effect of dynamic stall on the propagation of wind turbine noise is not currently feasible without further research into several components of the phenomenon. Primarily, it is necessary to determine how the circulation of the dynamic stall vortex is affected by changes in Reynolds number and reduced frequency, as scattering is proportional to this circulation. Secondly, it is necessary to determine how the dynamic stall vortex decays in the wake of an airfoil and how long it takes the flow to settle into a deep stall state after a dynamic stall event. If these parameters are measured, then it will be possible to estimate the impact of dynamic stall vortices on the directivity of wind turbine noise without resorting to computationally modelling the wind turbine wake and the propagation of the blade noise.

[1] Doolan, C. A review of wind turbine noise perception, annoyance and low frequency emission. *Wind Engineering 37*, 1 (2013), 97–104.

[2] Renewable UK. Wind turbine amplitude modulation: research to improve understanding as to its cause and effect, (2013).

[3] Hansen, K., Hessler, G., Hansen, C., and Zajamsek, B. Prediction of infrasound and low frequency noise propagation for modern turbines. In *6th International Meeting Conference on Wind Turbine Noise* (2015).

[4] Peng, Y. Propogation (sic) of wind turbine noise through wakes and turbulent atmosphere. Master's thesis, 2014.

[5] Lee, S., Lee, D., and Honhoff, S. Prediction of far-field wind turbine noise propagation with parabolic equation. *The Journal of the Acoustical Society of America 140*, 2 (2016), 767–778.

[6] Barlas, E., Zhu, W. J., Shen, W. Z., and Andersen, S. J. Wind turbine noise propagation modelling: An unsteady approach. In *Journal of Physics: Conference Series* (2016), vol. 753, IOP Publishing.

[7] Shipley, D. E., Miller, M. S., and Robinson, M. C. Dynamic stall occurrence on a horizontal axis wind turbine blade. Tech. rep., National Renewable Energy Lab, Golden, CO, US, 1995.

[8] Choudhry, A., Arjomandi, M., and Kelso, R. Horizontal axis wind turbine dynamic stall predictions based on wind speed and direction variability. *Proceedings of the Institution of Mechanical Engineers, Part A: Journal of Power and Energy 227*, 3 (2013), 338–351.

[9] Chandrasekhara, M., and Carr, L. Flow visualization studies of the Mach number effects on dynamic stall of an oscillating airfoil. *Journal of Aircraft 27*, 6 (1990), 516–522.

[10] Horne, W. Measurements of the scattering of sound by a line vortex. In *Proceedings of the AIAA 8th Aeroacoustics Conference* (1983).

[11] Labbé, R., and Pinton, J.-F. Propagation of sound through a turbulent vortex. *Physical Review Letters 81*, 7–17 (1998), 1413–1416.

[12] Manneville, S., Roux, P., Tanter, M., Maurel, A., Fink, M., Bottausci, F., and Petitjeans, P. Scattering of sound by a vorticity filament: An experimental and numerical investigation. *Physical Review E 63*, 3 (2001).

[13] Colonius, T., Lele, S. K., and Moin, P. The scattering of sound waves by a vortex: numerical simulations and analytical solutions. *Journal of Fluid Mechanics 260* (1994), 271–298.

[14] Ferreira, C. S., van Kuik, G., van Bussel, G., and Scarano, F. Visualization by PIV of dynamic stall on a vertical axis wind turbine. *Experiments in Fluids 46*, 1 (2009), 97–108.

[15] Gharali, K., and Johnson, D. A. PIV-based load investigation in dynamic stall for different reduced frequencies. *Experiments in Fluids 55* (2014), 1–12.

[16] Sherry, M., Nemes, A., Lo Jacono, D., Blackburn, H. M., and Sheridan, J. The interaction of helical tip and root vortices in a wind turbine wake. *Physics of Fluids 25*, 11 (2013).

[17] Maalouf, B., Dobrev, I., and Massouh, F. Vortex structure in the wake of a wind turbine rotor. In *19ème Congrès Français de Mécanique* (2011).

[18] Siemens AG. *Wind Turbine SWT-2.3-93: Technical specifications*, 2015.

[19] Howe, M. A review of the theory of trailing edge noise. *Journal of Sound and Vibration 61*, 3 (1978), 437 – 465.

[20] Brooks, T. F., Pope, D. S., and Marcolini, M. A. *Airfoil self-noise and prediction.* National Aeronautics and Space Administration, Office of Management, Scientific and Technical Information Division, (1989).

Chapter 7

Conclusion

There are a number of potential sources for low-frequency or impulsive noise generated by wind turbines, and whilst there is some debate as the generation mechanisms, they can be broadly broken down into two categories: anomalous noise generation, and anomalous sound propagation. Many of these potential causes are presently under-researched, but it is thought that stall of the blades is a primary contributor to the phenomenon [1].

In this thesis, both steady-state (static) and dynamic stall were investigated as potential causes for unsteady noise generation by wind turbines. For the steady-state case, where the intermittent occurrence of periodic stall on a wind turbine blade leads to a similarly periodic change in the levels of low frequency noise, the focus is on noise generation. For the case of dynamic stall the focus is on propagation, where the release of large coherent vortices into the wake may result in a change in directivity due to sound refraction and/or scattering. It was hypothesised that the low-frequency noise is scattered by the vortices shed due to the onset of deep stall after the dynamic stall event, followed by flow reattachment via the light stall regime as the angle of attack decreases. This means that both the ability to predict the noise due to stall, and the changes in directivity due to scattering of this noise due to the vortex are required to predict the overall changes due to a dynamic stall event.

Experiments on small-scale airfoils at a Reynolds number of 96,000 showed that the three airfoil profiles tested (flat plate, NACA 0012, and NACA 0021) displayed an increase in low-frequency noise levels near stall, across the frequency band from a Strouhal numbers of 0.45 to 1.1. Of these airfoil models, the thickest profile, the NACA 0021, displayed the sharpest increase in noise level with change in angle of attack, although the total noise level was approximately 2dB lower than the NACA 0012. Directivity measurements indicate that the noise generated by all three airfoils at stall is strongly dipolar, and measurements of the wake velocity spectra indicate that this noise is coherent with vorticity shed from the airfoil at these angles of attack. These observations are consistent with previously published measurements which indicate that under light-stall conditions the airfoil flow-

field is characterised by a separation point near the leading edge and shedding of small-scale vorticity into the wake [2, 3], before transitioning to larger-scale vortex shedding as the angle of attack is increased further.

By integrating the power spectral density of the acoustic pressure across a frequency range of interest, the total sound pressure level in that range can be established. This can be applied to the case of wind turbine amplitude modulation, where the temporal variation of the spectrum is an important factor in complying with noise emission limits and the most important factor in preventing community noise complaints. If the change of blade angle of attack with time is known, then measurements of the spectrum variation with angle of attack can be used to predict how the sound pressure level changes with time. This means that the methodology established in this thesis is well suited to the modelling of transient phenomena associated with amplitude modulation of wind turbine noise.

Experiments were also conducted on the scattering of sound by a vortex with a similar decay pattern to the vortex produced during dynamic stall. After comparing the scattered sound with predictions by a quasi-steady model based on the work of Colonius et al. [4], it was confirmed that the scattering of sound from a decaying vortex can be modelled using a quasi-steady approach when the decay time of the vortex is several orders of magnitude greater than the time taken for sound to travel through the vortex. Estimates of the strength of scattering due to dynamic stall on a horizontal-axis wind turbine indicate that it will be possible for significant scattering to occur. It is worth noting that, even if the occurrence of dynamic stall produces a burst of low-frequency noise, the Mach numbers at the inboard sections of wind turbine blades, where dynamic stall is the most likely to occur, are much lower than the outboard segments where quasi-steady-state stall occurs. Because the sound pressure level of airfoil trailing-edge noise scales with the fifth-power of Mach number, the scattered sound from dynamics stall vortices shed from inboard locations will be of significantly lower sound pressure level than the noise produced from the outboard sections. It is therefore likely that stall contributions to the overall wind turbine noise will be dominated by quasi-steady-state stall on the outboard sections of the blade.

7.1 Research significance

It was previously known that when airfoils stall they begin to produce low-frequency noise. However, until the experiments detailed in this thesis were conducted, there was little information about how this noise differs between airfoils nor the influence of angle of attack in post stall regimes. This thesis presents information about how the flat plate, the NACA 0012 and the NACA 0021 profiles respond to the same flow conditions and angles of attack. In addition, a large amount of new information has been collected regarding the response of the airfoil noise spectra to small variations in angle of attack, which will enable

more accurate modelling in the future.

The results of the airfoil self-noise experiments suggest that the changes in the low-frequency noise level under stalled conditions can be correlated with changes in wake velocity spectra and the lift of the airfoil. Force and velocity measurements do not require specialised laboratory conditions like those of an anechoic test chamber. This makes these experiments easier to conduct than comprehensive simultaneous acoustic and flow measurements, especially under field conditions. This in turn means that it will be easier to predict how airfoils will perform from the perspective of the rate of change of noise level as the airfoils enter stalled conditions.

The methodology used also shows that it is feasible to determine the total sound pressure level of spectral peaks and use them to predict these changes using a dataset with a high angle-of-attack resolution. While the background noise level in the anechoic wind tunnel used in the current research is too high for the data to be directly applied in this way, other researchers using a similar approach will be able to directly simulate the low-frequency noise level of a wind turbine after producing an experimental noise map for a given airfoil. This approach gives a higher fidelity representation of how the radiated and propagated noise can be expected to change as a wind turbine blade rotates.

It has previously been expected that, due to the vast difference in time-scales, which is multiple orders of magnitude, that vortex scattering of low frequency noise can be treated in a quasi-steady manner. This has now been experimentally confirmed, and gives researchers increased confidence to use quasi-steady models of the scattering of wind turbine noise from wake vortices, such as those produced when the wind turbine blade undergoes dynamic stall. Advanced propagation models that take the structure of the wind turbine wake into account are important as it has been recently discovered that wind-turbine noise emissions can exhibit both spatial and temporal amplitude modulation.

Taken together, these results indicate that it is likely that periodic stall on horizontal-axis wind turbine blades is responsible for the production of impulsive noise and/or amplitude-modulated low-frequency noise that has been observed in the field and is sometimes the cause of noise complaints. Through either wake velocity, acoustic pressure, or surface pressure measurements, the low-frequency noise produced when the airfoil stalls can be predicted and modelled. A holistic propagation model that takes into account refraction through atmospheric velocity gradients and scattering from wake vorticity, can then be used to predict the noise observed in the far-field.

7.2 Topics for future research

In order to reach a more complete understanding of how static stall and dynamic stall affect the noise produced by full-scale wind turbines, more research is required in several

areas. The following is a series of key areas in which the present research needs to be expanded before a definite solution for noise estimation from wind-turbines is possible.

1. The present experiments on airfoil self-noise need to be replicated on wind-turbine airfoils at higher Reynolds numbers. A larger airfoil chord is preferrable for gathering this data as it allows the reduced frequency, Mach number and Reynolds number to more closely mirror the real scenarios the data will be applied to. Preferrably, the effect of higher Reynolds number and more realistic airfoil profiles would be investigated separately in order to determine the effects of changing these parameters individually. A larger chord also allows the addition of surface pressure measurements in future experiments, which in turn enables validation of the model of Moreau et al. [5] under these conditions. A larger span-to-chord ratio would also be beneficial, as it increases the sound pressure produced by the airfoil, and decreases the contribution of wall effects to the overall sound measurement.

2. More representative airfoil noise data can be collected using the methodology established in this thesis, and used to create wind-turbine noise models. By modelling the wind-turbine blades in a quasi-steady state, the effect of the increase in noise level at stall can be investigated experimentally by directly relating the instantaneous angle of attack of the blades to the sound pressure level data, as shown in Chapter 5. This approach will allow researchers to investigate how the rate of change of airfoil noise with angle of attack stands to effect the sound generation under gust conditions.

3. Direct measurement of the noise generated by the formation of a dynamic stall vortex will lead to new insights into the how the occurrence of dynamic stall may affect wind turbine noise. However, due to the proportionality between airfoil chord and the time scale of the dynamic-stall event, this noise cannot be easily measured without a large airfoil. This, in turn, creates the need for a large wind tunnel facility as well as a large high-speed servo-motor.

4. The nature of the effect of the dynamic stall vortex on existing airfoil self-noise, once it is shed into the wake, is now known. This scattering can now be considered when constructing future wind turbine noise models if the need arises. However it will require a strong dynamic-stall event to produce enough of an effect on overall directivity of the turbine, so in most cases analysis of the scattering from these vortices will not be required. Small vertical-axis turbines experience dynamic stall more regularly and across the entire span, so an investigation into how this may affect the noise produced by this turbine configuration can also be conducted.

References for Chapter 7

[1] Renewable UK. Wind turbine amplitude modulation: research to improve understanding as to its cause and effect, 2013.

[2] Huang, R. F., and Lin, C. L. Vortex shedding and shear-layer instability of wing at low-Reynolds numbers. *AIAA Journal 33*, 8 (1995), 1398–1403.

[3] Rodríguez, I., Lehmkuhl, O., Borrell, R., and Oliva, A. Direct numerical simulation of a NACA 0012 in full stall. *International Journal of Heat and Fluid Flow 43* (2013), 194–203.

[4] Colonius, T., Lele, S. K., and Moin, P. The scattering of sound waves by a vortex: numerical simulations and analytical solutions. *Journal of Fluid Mechanics 260* (1994), 271–298.

[5] Moreau, S., Roger, M., and Christophe, J. Flow features and self-noise of airfoils near stall or in stall. In *15th AIAA/CEAS Aeroacoustics Conference* (2009).

Appendix A

Preliminary Findings on the Noise Generated by Simple Airfoils Near Stall

A.1 Chapter overview

Prior to writing the manuscript presented in Chapter 4, the preliminary results of the experiment detailed in that chapter were submitted to the 3rd Symposium of Fluid-Sound-Structure Interactions and Control. A short conference paper was published as a result of this, which is presented in this chapter and can also be found at doi:10.1007/978-3-662-48868-3_3. At this stage the significances of the changes in noise level with angle of attack had not been established, and so this paper is focused on the noise spectra produced.

A.2 Self-noise spectra of NACA 0012 and NACA 0021 airfoils at stall

Statement of Authorship

Title of Paper	A comparison of NACA 0012 and NACA 0021 self-noise at low Reynolds number
Publication Status	☑ Published ☐ Accepted for Publication ☐ Submitted for Publication ☐ Unpublished and Unsubmitted w ork w ritten in manuscript style
Publication Details	Laratro A., Arjomandi M., Cazzolato B., Kelso R. (2016) A Comparison of NACA 0012 and NACA 0021 Self-noise at Low Reynolds Number. Fluid-Structure-Sound Interactions and Control. Lecture Notes in Mechanical Engineering. Springer, Berlin, Heidelberg

Principal Author

Name of Principal Author (Candidate)	Alex Laratro		
Contribution to the Paper	- Data collection, analysis, visualisation, and interpretation - Writing of the manuscript and production of original figures - Correspondence with editor and reviewers including the production of all cover letters and rejoinders		
Overall percentage (%)	80%		
Certification:	This paper reports on original research I conducted during the period of my Higher Degree by Research candidature and is not subject to any obligations or contractual agreements with a third party that would constrain its inclusion in this thesis. I am the primary author of this paper.		
Signature		Date	

Co-Author Contributions

By signing the Statement of Authorship, each author certifies that:

i. the candidate's stated contribution to the publication is accurate (as detailed above);

ii. permission is granted for the candidate to include the publication in the thesis; and

iii. the sum of all co-author contributions is equal to 100% less the candidate's stated contribution.

Name of Co-Author	Maziar Arjomandi		
Contribution to the Paper	- Supervision of the work, including the production of the manuscript - Participation in the development of the concepts and ideas presented in the manuscript - Evaluation and editing of the manuscript prior to submission		
Signature		Date	

Name of Co-Author	Benjamin Cazzolato		
Contribution to the Paper	- Supervision of the work, including the production of the manuscript - Participation in the development of the concepts and ideas presented in the manuscript - Evaluation and editing of the manuscript prior to submission		
Signature		Date	

Name of Co-Author	Richard Kelso		
Contribution to the Paper	- Supervision of the work, including the production of the manuscript - Participation in the development of the concepts and ideas presented in the manuscript - Evaluation and editing of the manuscript prior to submission		
Signature		Date	

A Comparison of NACA 0012 and NACA 0021 Self-noise at Low Reynolds Number

A. Laratro, M. Arjomandi, B. Cazzolato and R. Kelso

Abstract The self-noise of NACA 0012 and NACA 0021 airfoils are recorded at a Reynolds numbers of 96,000 in an anechoic wind tunnel at an angle-of-attack range of −5°–40°. Results suggest that the low angle-of-attack tonal noise of the airfoils behaves differently, with the NACA 0021 producing tones at much higher angles-of-attack but not near 0°. Noise generated at the onset of stall is subtlely different, with signature of the NACA 0012 forming over a larger angular range compared to the NACA 0021 where the stall signature forms suddenly.

Keywords Aeroacoustics · Stall noise · Airfoil noise

1 Introduction

At low angles-of-attack airfoils produce tonal noise as transitional boundary layer instabilities convect past the trailing edge, generating noise which further excites the boundary layer (McAlpine 1997; Arcondoulis et al. 2009). On NACA 0012 airfoils this noise typically occurs over a small range of angles-of-attack, when the separation point is near the trailing edge the tonal frequencies tend to increase or stay constant as the angle increases (McAlpine 1997; Arcondoulis et al. 2009). A study by Hansen et al. (2010) on NACA 0021 airfoils indicates that tonal noise is not present at 0°, persists to higher angles-of-attack and decreases in frequency as the angle-of-attack is increased. These differences were not discussed by Hansen et al. (2010) but suggest that the tonal noise properties of the airfoils differ. This tonal noise is also sensitive to environmental factors hindering comparisons (Hansen et al. 2010).

At high angles-of-attack airfoils act similar to bluff bodies and shed large vortex streets. This generates sound at a frontal-height based Strouhal Number of between 0.15 and 0.2 at moderate Reynolds numbers similar to a flat plate (Fage and Johansen

A. Laratro (✉) · M. Arjomandi · B. Cazzolato · R. Kelso
School of Mechanical Engineering, The University of Adelaide, Adelaide, SA, Australia
e-mail: alex.laratro@adelaide.edu.au

Y. Zhou et al. (eds.), *Fluid-Structure-Sound Interactions and Control*,
Lecture Notes in Mechanical Engineering,
DOI 10.1007/978-3-662-48868-3_3

1927; Colonius and Williams 2011). During the transition to fully separated flow airfoil noise is less well understood.

Brooks et al. (1989) conducted extensive testing of the self-noise of NACA 0012 airfoils over a range of angles-of-attack. They found that as angle-of-attack increases and the airfoil stalls the shed vortices become larger and self-noise shifts to lower frequencies. While the data of Brooks et al. uses range of angles and Reynolds numbers its detail is limited by the use of 1/3-octave spectra which makes it difficult to discern peaks due to vortex shedding. More recent work by Moreau et al. (2009) presented much higher resolution spectra and showed that there are peaks in the airfoil noise near stall that are not resolved when the data is presented in third-octave bands. At angles of attack from approximately 14–20° they reported small peaks in the spectra attributed to separation noise that decreased in amplitude as the angle-of-attack was further increased. Beyond this range the larger and sharper peaks attributed due to bluff body vortex shedding formed and moved to lower frequencies with higher angles as expected.

The objective of the current work is two-fold; Firstly to expand upon the experimental findings of Moreau et al. (2009) by recording data in the light-stall regime for both NACA 0012 and NACA 0021 airfoils and identifying if there are differences in their spectra. Secondly to use the data collected to investigate the differences between tonal noise of the NACA 0012 and NACA 0021 airfoils as seen in the data of (Hansen et al. 2010).

2 Method

In order to achieve high angles-of-attack with the available facilities the airfoils had to be mounted vertically. This resulted in a design span of 73 mm, to account for small deflections in the end plates. A servo motor mounted to the rig enabled remote control of the angle-of-attack, and did not significantly affect the background noise at high flow-speeds. The rig placed the airfoil several chord lengths from the exit of the nozzle (as shown in Fig. 1) in order to give a larger arc line-of-sight to the airfoil

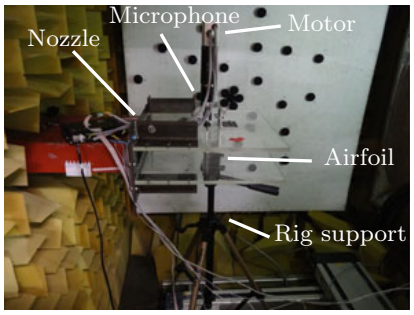

Fig. 1 Experimental setup

Table 1 Experimental parameters

Nozzle size	75mm × 275mm	
Airfoil profile	NACA 0012	NACA 0021
Chord	50mm	
Span	73mm	
Thickness	6mm	10.5mm
Aspect ratio	1.46	
Relative flow width	5.5	

for future testing, and several chord lengths before the end of the plates to allow wake development.

The microphone used was located 0.61 m from the rotation axis at polar and azimuthal angles of 91.2° and −0.4° respectively. Each spectrum was created with Welch's method with a sampling frequency of 2^{15} Hz and a window length of 2^{13} Hz with 150 averages. The experiment was conducted a speed of 30m/s, corresponding to a Reynolds numbers of 96,000. Spectra were produced for angles-of-attack from −5 to 40° at a resolution of 1° (Table 1).

3 Results

The experimental results, shown in Fig. 2, show two regimes of tonal noise at low and at high angles-of attack, as expected. The NACA 0021 airfoil does not generate tones until 2–3° which then decrease in frequency as the angle-of-attack is increased before fading at 12°. This is in some agreement with the results of Hansen et al. (2012) where tonal noise was detected as low as 1° and corroborates both the trend of tonal noise not being generated at 0° and the frequency decreasing as the angle is increased. This suggests that the tonal noise behaviour observed in the NACA 0021 is intrinsic to the airfoil at this Reynolds number and not a result of environmental

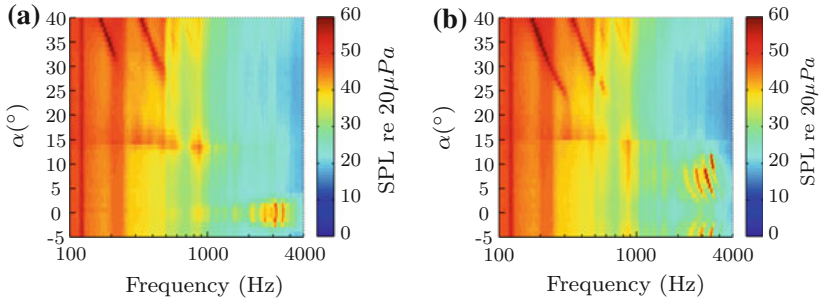

Fig. 2 Spectra of airfoils at U = 30 ms^{-1}, Re = 96,000, $\Delta\alpha = 1°$, $\Delta f = 4$ Hz

conditions. Note that the geometric angles-of-attack is presented here and the true angle-of-attack is given by $\alpha_t = 0.76\alpha$ (Brooks et al. 1989).

At post-stall angles-of-attack the airfoils display similar vortex shedding behaviour. In this regime the airfoils are acting as bluff bodies, and the change in thickness does not significantly affect vortex shedding frequency. A low frequency peak similar to that reported by Moreau et al. (2009) is seen between the tonal and bluff body noise, referred to as light stall in that study. Secondary peaks are also seen at slightly higher frequencies and will be discussed in further detail below. It is important to note that as the airfoil begins to stall there is a noticeable increase in broadband noise level below approximately 900 Hz and a decrease in noise level above. The speed at which this change occurs is noticeably different for each airfoil, with the NACA 0021 experiencing a more rapid change in noise signature. This is believed to be indicative of the NACA 0021 stalling more sharply in these conditions. The behaviour of the NACA 0012 is consistent with both lift data in literature (Marchman et al. 1998) and a direct numerical simulation by Rodríguez et al. (2013) which indicated that the onset of stall occurred over a range of angles for the NACA 0012 in this Reynolds number range. The simulation indicated that the peaks in the noise at stall occur due to instabilities in the separated shear layer near the leading edge as well as vorticity produced near the trailing edge. Similarly lift data for the NACA 0021 near the experimental Reynolds number how a sharp decrease in lift at the onset of stall corresponding to the sharp increase in low-frequency noise observed in this study (Marchman et al. 1998). Comparable simulations could not be found in the literature, however it is reasonable to assume that similar flow phenomenon are responsible for the observed noise for both airfoils.

As mentioned previously, some anomalous peaks appear in the data, with a wide peak near 950 Hz that increases in strength with angle-of-attack and then decreases as the airfoil stalls. What was initially believed to be secondary peaks at around 550 Hz may be due to a related phenomenon. These peaks at are located at frequencies that are prominent in the background noise when the end-plates are installed as shown in Fig. 3, however they rise and fall with the changes in noise at stall. Because of this it is currently believed that these peaks are a result of an aeroacoustic coupling between

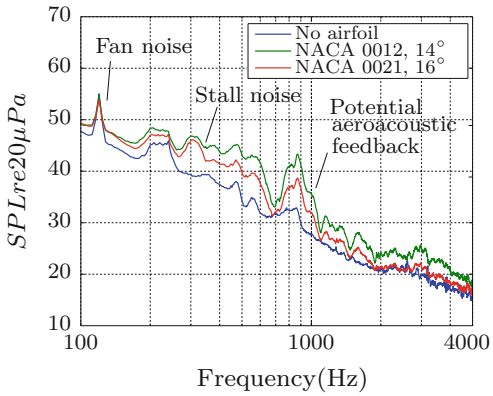

Fig. 3 Spectra of airfoils at stall for U = 30 ms^{-1}, Re = 96,000

the airfoil and the end-plates, and steps are being taken to attempt to reduce the effect. Regardless, the large difference in the behaviour of this coupling between the NACA 0012 and NACA 0021 airfoils suggests that after the coupling is suppressed that some difference in spectrum will remain.

4 Conclusion

NACA 0012 and NACA 0021 airfoils with 50 mm chord were tested in the anechoic wind tunnel at the University of Adelaide at a Reynolds number of 96,000 at various angles-of-attack. Noticeable differences were found in the characteristics of how their self-noise spectra change as the angle-of-attack is increased, including confirmation of a lack of NACA 0021 tonal noise near 0° as seen in the data of Hansen et al. (2010). The onset of bluff body behaviour occurred later for the NACA 0012 airfoil and the onset of stall took place more gradually compared to the NACA 0021. There is evidence that there are differences in the broadband behaviour of these airfoils as they approach stall, however due to a possible aeroacoustic coupling between the airfoil and the experimental rig this cannot be determined conclusively.

References

Arcondoulis E, Doolan C, Zander A (2009) Airfoil noise measurements at various angles of attack and low Reynolds number. In: Proceedings on Acoustics 2009

Brooks T, Pope D, Marcolini M (1989) Airfoil self-noise and prediction. NASA Reference Publication, Technical report 1218

Colonius T, Williams D (2011) Control of vortex shedding on two- and three-dimensional aerofoils. Phil Trans R Soc A 369(1940):1525–1539

Fage A, Johansen F (1927) On the flow of air behind an inclined flat plate of infinite span. Proc R Soc Lond Ser A 116:170–197

Hansen K, Kelso R, Doolan C (2010) Reduction of flow induced tonal noise through leading edge tubercle modifications. AIAA Paper 2010:3700

Marchman F, Gunther C, Gundlach J (1998) Semi-span testing at low reynolds number. AIAA Paper 608

McAlpine A (1997) Generation of discrete frequency tones by the flow around an aerofoil. PhD thesis, School of Mathematics, University of Bristol

Moreau S, Roger M, Christophe J (2009) Flow features and self-noise of airfoils near stall or in stall. In: 15th AIAA/CEAS Aeroacoustics conference

Rodríguez I, Lehmkuhl O, Borrell R, Oliva A (2013) Direct numerical simulation of a naca0012 in full stall. Int J Heat Fluid Flow 43:194–203

Appendix B

Computational Simulation of a Similar Experimental Setup

B.1 Chapter overview

While the experimental campaign detailed in Chapters 4 & 5 was being conducted, another researcher at The University of Adelaide conducted a computational fluid dynamics and aeroacoustics simulation using the experimental setup and experimental data as a basis, before moving onto a more advanced simulation. This provided more detailed insight into the flow around the NACA 0012 airfoil under the experimental conditions and showed the extent of separation under light-stall conditions. Because this work provides more information about the NACA 0012 flow field under similar conditions, the manuscript produced is presented in this chapter.

B.2 Computational simulation of the flow field around a NACA 0012 airfoil at stall

Statement of Authorship

Title of Paper	Aeroacoustic behaviour of a NACA 0012 airfoil
Publication Status	☐ Published ☐ Accepted for Publication ☐ Submitted for Publication ☑ Unpublished and Unsubmitted w ork w ritten in manuscript style
Publication Details	

Principal Author

Name of Principal Author	Nima Sedaghatizadeh		
Contribution to the Paper	- Production of simulation model - Data collection, analysis, visualisation, and interpretation - Writing of the manuscript and production of original figures		
Overall percentage (%)	80%		
Certification:	This paper reports on original research I conducted during the period of my Higher Degree by Research candidature and is not subject to any obligations or contractual agreements with a third party that would constrain its inclusion in this thesis. I am the primary author of this paper.		
Signature		Date	

Co-Author Contributions

By signing the Statement of Authorship, each author certifies that:

i. the candidate's stated contribution to the publication is accurate (as detailed above);

ii. permission is granted for the candidate to include the publication in the thesis; and

iii. the sum of all co-author contributions is equal to 100% less the candidate's stated contribution.

Name of Co-Author (Candidate)	Alex Laratro		
Contribution to the Paper	- Supply of preliminary experiment parameters and experimental data - Participation in the development of the concepts and ideas presented in the manuscript - Evaluation and editing of the manuscript prior to submission		
Signature		Date	

Name of Co-Author	Maziar Arjomandi		
Contribution to the Paper	- Supervision of the work, including the production of the manuscript - Participation in the development of the concepts and ideas presented in the manuscript - Evaluation and editing of the manuscript		
Signature		Date	

Name of Co-Author	Benjamin Cazzolato		
Contribution to the Paper	- Supervision of the work, including the production of the manuscript - Participation in the development of the concepts and ideas presented in the manuscript - Evaluation and editing of the manuscript		
Signature		Date	

Name of Co-Author	Richard Kelso
Contribution to the Paper	- Supervision of the work, including the production of the manuscript - Participation in the development of the concepts and ideas presented in the manuscript - Evaluation and editing of the manuscript

Aeroacoustic behaviour of a NACA 0012 airfoil

Nima Sedaghatizadeh, Alex James Laratro, Maziar Arjomandi, Benjamin Cazzolato, Richard Kelso

School of Mechanical Engineering, the University of Adelaide, Adelaide, SA, 5005

Abstract

In this study, the aeroacoustic behaviour of a NACA 0012 airfoil at different angles of attack including shallow and deep stall, is computationally investigated using ANSYS Fluent. For this purpose, an embedded LES technique is utilised to compute the flow field, pressure fluctuations and aerodynamic forces. The Ffowcs-Williams and Hawkings analogy is used to calculate the far-field noise signatures emitted from the airfoil. The results of aeroacoustic modelling show that as the angle of attack increases and the blade experiences stall, the peak frequency of the noise signal decreases due to the generation of large eddies on the suction side of the airfoil. Narrowband spectra show that the highest noise level occurs at a reduced frequency of 1.9 in light stall condition (18 degrees angle of attack), while the reduced frequency associated to the highest noise level is almost doubled (3.58) for 5 degrees of angle of attack. The directivity diagrams of total sound pressure level for both conditions form dipoles with their axis of symmetry perpendicular to the chord line. However, the directivity pattern of peak frequencies, shows strong dipole behaviour for the airfoil aligned in a direction normal to the chord line when in stall, while the results for the pre-stall condition show a stronger signature towards the leading edge, resulting in a dipole which is aligned more in the direction of the chord line. The directivity pattern at this particular frequency shows that, in addition to trailing edge noise, other noise sources are present which cannot be explained by trailing edge noise theory.

Introduction

Airfoils, are known as a source of aerodynamic noise. Investigation of the noise generation mechanisms, and and techniques to control them has been an ongoing endeavour for researchers and engineers for the last 30 years(Kim et al., 2015, Laratro et al., 2016). Airfoil noise is mainely generated by fluctuating surface forces exerted by turbulent eddies and instabilities in the flow which interact with different parts of an airfoil (Kim et al., 2014, Brooks et al., 1989). The spatial content of the aerodynamic noise from an airfoil is primarily related to the size of the eddies, with larger eddies producing lower frequencies (Moorhouse et al., 2007). Based on the source of the eddies and the part of the airfoil they interact with, the generated noise can be divided into four main categories: Unsteady turbulent-inflow; Stall noise; trailing edge noise; and laminar-boundary-layer-vortex-shedding noise (Brooks et al., 1989). Among these mechanisms, TE noise has been the focus of researchers, since it is the dominant broadband mechanism in aerodynamic and hydrodynamic applications, where the airfoil operates at low angles of attack (Sandberg, 2015, Jianu et al., 2012). However, there is an evidence that in some applications, such as wind turbines which operate in unsteady inflow conditions, the airfoil undergoes partial or dynamic stall, which results in increased noise levels and amplitude modulation (Madsen et al., 2014, Laratro et al., 2014). Figure 1 shows the mechanisms of noise generation and associated eddies on the blade of a wind turbine constructed from airfoil sections. Trailing edge noise is generated by the small eddies in the size of the turbulent boundary layer at trailing edge of the airfoil and has a dominant high frequency and is attenuated in short distance from its source. However, recent studies and reports from residents around wind farms show low frequency noise at distances far downstream of wind turbines (Pedersen and Waye, 2004). It is hypothesised that this noise is generated due to stall on the blade (Oerlemans, 2011, Moreau et al., 2009).

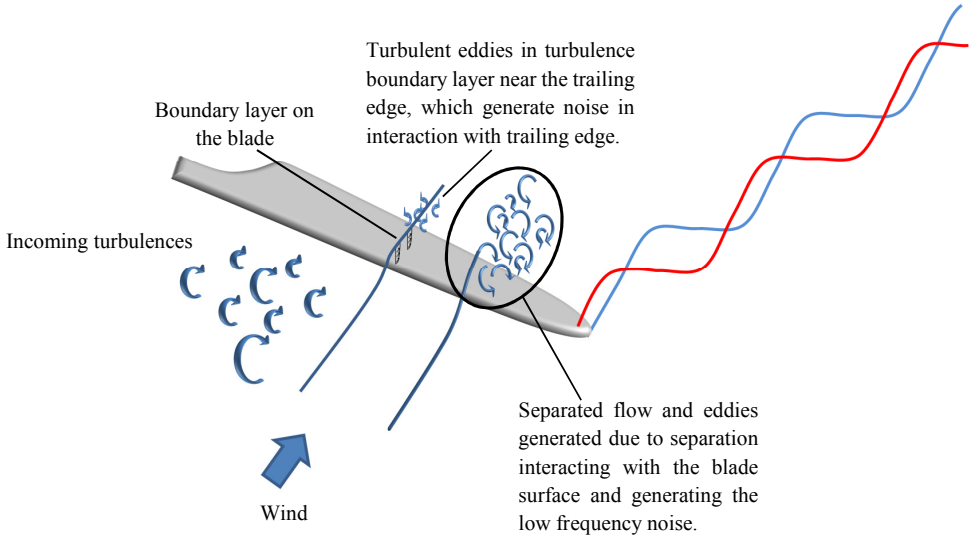

Figure 1 Incoming flow features and different noise generation mechanisms. Small eddies in the turbulent boundary layer interacting with trailing edge generate broadband trailing edge noise, large separated eddies are responsible for low frequency stall noise, and incoming turbulences in interaction with blade generate turbulent inflow noise which its frequency with larger eddies generating lower frequency noise.

Several empirical and analytical approaches have been developed to predict and investigate the noise emitted from airfoils. One of the first attempt for predicting the aerodynamically generated noise was conducted by Powell (1959). He introduced three main sources of noise from flat plate moving at zero incidence: 1) layer noise, 2) edge noise, and 3) wake noise. He reported that the main contributor to noise generation is the surface pressure fluctuation near the trailing edge. Based on his study, edge noise is dipole and its power varies with U^5 where U is the free stream velocity. The other two mechanisms have quadrupole directivity and their power depends on the eighth power of the velocity (Powell, 1959). By combining analytical models with experimental methods, several researchers have proposed semi-empirical models to predict the aeroacoustic signature of airfoils. While these semi-empirical methods have proven to be an acceptable method to predict the noise for some given cases, in some others they have given inaccurate results. Leloudas et al. (2007) used Brooks et al. (1989) model to calculate the emitted noise from a wind turbine and found a systematic problem with the prediction of blunt trailing edge noise for frequencies above 3 kHz. In the work of Moriarty

and Migliore (2003), the predictions were compared to wind tunnel test data of 20 cm chord airfoils (NACA 0012 and S822). The results for the NACA 0012 were reported not to be very accurate for relatively low Reynolds numbers. In the case of the S822 airfoil, poor agreement between predictions and experimental data was reported in general.

Faster and multi-processor computers have enabled researchers to model the flow field around an airfoil with the required accuracy determination of noise signals (Richard et al., 2008, Sandberg, 2015). However, accurate CFD methods are time consuming and computationally expensive, while simpler models are incapable of providing accurate results with a sufficient spectral content which is needed for acoustic calculations. The use of hybrid models like embedded LES models has opened the door to resolving the flow field with high resolution in desired zones, while using simpler models in other zones to reduce the computation cost (Gritskevich et al., 2012, Menter and Egorov, 2010).

This study investigates the aerodynamically generated noise by a NACA 0012, using an Embedded Large Eddy Simulation technique (ELES) for the computation of the flow field. A dynamic Smagorinsky-Lilly model with a central differencing scheme for momentum discretisation was used to capture small instabilities in the flow near the surface for the airfoil. The acoustic signature of the interaction of the airfoil and fluid flow at different angles of attack was numerically predicted to better understand the noise generation mechanism of an airfoil at stall. Three different angles of attack (AoA) were chosen to create pre-stall, light stall, and deep stall conditions and the pressure fluctuation at several receiving locations were calculated using the FW-H analogy. Moreover, the effect of change in angle of attack on flow features and their correlation with directivity of the noise is analysed and discussed.

Numerical modelling methodology

In this study to calculate the flow field, an ELES approach is used. ELES is a multi-domain approach which benefits from the accuracy of LES in the regions of interest and the lower computational demand of RANS in other regions. In this work, the computational domain was divided into two regions: a cylindrical region around the airfoil where LES is used; and the rest of the domain where Scale Adaptive Simulation (SAS) is performed. SAS was chosen because it performs similar to a standard Reynolds Average Navier-Stokes (RANS) model in steady flows, but allows the formation of broadband turbulence spectra for unstable flows. This model is able to provide sufficient spectral content for acoustic computations, while RANS models are unable due to their time-averaged nature (Menter, 2010). As shown in Figure 2, SAS can capture more details of instabilities in the flow compared to RANS models. Thus, it is possible to capture large range of frequencies of the instabilities and fluctuations in the flow.

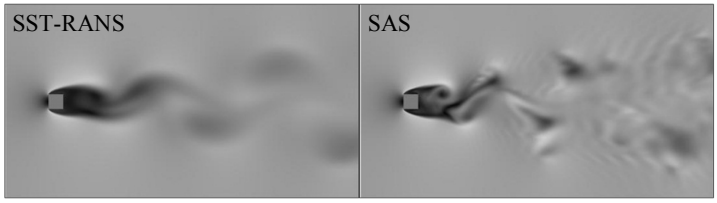

Figure 2 Comparison of instantaneous velocity field by SST-RANS (left) and SAS (right), showing more details and instabilities when SAS was applied (Maliska et al., 2012).

The difference between standard RANS and SAS models lies in the treatment of the scale-defining equation. The original SAS model (Menter and Egorov, 2010) was formulated as a two-equation model, with the variable $\varphi = \sqrt{k}L_t$ for the scale equation:

$$\frac{\partial(\rho k)}{\partial t} + \frac{\partial\left(\rho\overline{U_j}k\right)}{\partial x_j} = P_k - c_\mu^{\frac{3}{4}}\rho\frac{k}{\varphi^2} + \frac{\partial}{\partial x_j}\left(\frac{\mu_t}{\sigma_k}\frac{\partial k}{\partial x_j}\right) \tag{1}$$

$$\frac{\partial(\rho\varphi)}{\partial t} + \frac{\partial\left(\rho\overline{U_j}\varphi\right)}{\partial x_j} = \frac{\varphi}{k}P_k\left(\xi_1 - \xi_2\left(\frac{L_t}{L_{vK}}\right)^2\right) - \xi_3\rho k + \frac{\partial}{\partial x_j}\left(\frac{\mu_t}{\sigma_\varphi}\frac{\partial\varphi}{\partial x_j}\right) \tag{2}$$

$$L_{vK} = \kappa \left| \frac{\overline{U'}}{\overline{U''}} \right|; \quad \overline{U'} = S = \sqrt{2 S_{ij} S_{ij}}; \quad \overline{U''} = \sqrt{\frac{\partial^2 \overline{U_i}}{\partial x_j \partial x_j} \frac{\partial^2 \overline{U_i}}{\partial x_k \partial x_k}} \tag{3}$$

$$S_{ij} = \frac{1}{2}\left(\frac{\partial \overline{U_i}}{\partial x_j} + \frac{\partial \overline{U_j}}{\partial x_i} \right); \quad L_t = \frac{\varphi}{\sqrt{k}} \tag{4}$$

As shown in the SAS model, the main new term which appears in the transport equation (Equation 2) is the one including the von Karman length scale L_{vK}, which does not appear in a standard RANS model. The second derivative of velocity (U'') allows the model to adjust its length scale to those structures already modelled in the flow. This functionality is not present in a standard RANS model. This leads to more LES-like behaviour, which can capture more instabilities and agrees more closely with the experimental observations.

The interface between the two zones (LES and SAS zones) is treated such that the consistency between two regions is maintained. To do so, synthetic turbulence is introduced at the interface between the two regions with two different approaches. The LES part of the computations is formulated as below (Wilcox, 1998):

$$\frac{\partial \rho}{\partial t} + \frac{\partial}{\partial x_i}\left(\rho \overline{u_i} \right) = 0 \tag{5}$$

$$\frac{\partial (\rho \overline{u_i})}{\partial t} + \frac{\partial (\rho \overline{u_j}\,\overline{u_i})}{\partial x_j} = \frac{\partial \sigma_{ij}}{\partial x_j} - \frac{\partial \overline{p}}{\partial x_i} - \frac{\partial \tau_{ij}}{\partial x_j} \tag{6}$$

In above equations, $\overline{u}$ is the resolved velocity, σ is the stress tensor due to molecular viscosity, obtained from resolved velocity and τ_{ij} is the subgrid scale stress defined as $\tau_{ij} = \rho \overline{u_i u_j} - \rho \overline{u_i}\,\overline{u_j}$. To close the set of equations the Boussinsque hypothesis is used for the calculations as below (Wilcox, 1998, Menter, 2010):

$$\tau_{ij} - \frac{1}{3}\tau_{kk}\delta_{ij} = -2\mu_t \overline{S_{ij}} \tag{7}$$

where μ_t is subgrid turbulent viscosity, calculated using Smagorinsky-Lilly model as $\mu_t = \rho L_s^2 \left|\overline{S}\right|$. $\overline{S}$ is the resolved strain rate as presented in Equation (4) and L_s is the mixing length for subgrid length scale computed by:

$$\left|\overline{S}\right| \equiv \sqrt{2\overline{S_{ij}}\,\overline{S_{ij}}}, \quad L_s = \min\left(\kappa d, C_s V^{1/2}\right) \tag{8}$$

where κ is the von Karman factor, d is the closest distance to walls, C_s is the Smagorinsky factor, and V is the volume of the computational cell. The value of C_s has a significant effect on large scale fluctuations in the mean shear and transitional regimes. To address this problem Germano et al. (1991), and then subsequently Lilly (1992), proposed a method in which the Smagorinsky constant is calculated dynamically using the resolved motion data.

The noise signature used in the model presented in this paper is computed based on coupling the CFD for the aerodynamic calculations with Ffowcs-Williams and Hawkings (FW-H) model. One of the main advantages of using FW-H analogy compared to direct aeroacoustic computation is that calculating the sound signature indirectly from the CFD results, which significantly reduces the computational demand. The FW-H model is essentially an extension to Lighthill's theorem, which takes into account the noise source related to surfaces in an arbitrary motion. The FW-H equation is written as (Williams and Hawkings, 1969) :

$$\begin{aligned}\frac{1}{a_0^2}\frac{\partial^2 \acute{p}}{\partial t^2} - \nabla^2 \acute{p} = {} & \frac{\partial^2}{\partial x_i \partial x_j}\{T_{ij}H(f)\} - \frac{\partial}{\partial x_i}\{[P_{ij}n_j + \rho u_i(u_n - v_n]\delta(f)\} \\ & + \frac{\partial}{\partial t}\{[\rho_0 v_n + \rho(u_n - v_n]\delta(f)\}\end{aligned} \tag{9}$$

where u_i is the fluid velocity component in x_i direction, u_n is the fluid velocity component normal to the surface ($f = 0$), v_i is the surface velocity component in x_i direction and v_n denotes the surrafce velocity component normal to the surface. $\delta(f)$ and $H(f)$ in the FW-H equation are the Dirac delta and Heavyside functions, respectively, where $f = 0$ corresponds

to the source surface and $f > 0$ denotes the exterior flow region. $\acute{p}$ is defined as the gauge hydrodynamic pressure while a_0, P_{ij} and T_{ij} represent speed of sound, compressive stress tensor and Lighthill's stress tensor, respectively. Equation (9) is reduced to Lighthill's theorem if there is no surface (i. e., $H = 1$).

The FW-H equation can be integrated analytically assuming a free-space flow without any obstacles between the sound source and the receiver. The solution to this is given in Equation (10), broken into quadrupole, dipole and monopole terms.

$$
\begin{aligned}
&H(f)\acute{p}(x,t) = \\
&\frac{1}{4\pi}\int_V \frac{\partial^2}{\partial y_i \partial y_j}\left[\frac{1}{|1-M_r|}T_{i,j}\left(y, t-\frac{r}{a}\right)\right]\frac{dy}{r} + \qquad \text{Quadrupole} \\
&+\frac{1}{4\pi}\int_{f=0}\frac{\partial}{\partial y_i}\left[\frac{1}{|1-M_r|}F_i\left(y, t-\frac{r}{a}\right)\right]\frac{dy}{r|\nabla f|} + \qquad \text{Dipole} \\
&+\frac{1}{4\pi a_0}\int_{f=0}\frac{\partial}{\partial t}\left[\frac{1}{|1-M_r|}Q_i\left(y, t-\frac{r}{a}\right)\right]\frac{dy}{r|\nabla f|} \qquad \text{Monopole}
\end{aligned}
\tag{10}
$$

where $F_i = P_{i,j}n_j + \rho u_i(u_n - v_n)$ and Q= $\rho v_n + \rho(u_n - v_n)$. Quadrupole term which is represented by a volume integral, contributes to the unsteady stresses in the region outside the source surface, while surface integrals represented by dipole and monopole terms are respectively related to the flow interaction with moving bodies and body thickness. The quadrupole term is often negligible compared to the other two terms and becomes zero for subsonic flows. Thus the FW-H model in this study utilises the monopole and dipole terms to calculate the noise emission from the airfoil.

Computational Domain and Grid Specification

The computational domain was constructed based on the experiment conducted by Moreau et al. (2009) as shown in Figure 3. Figure 4 shows the computational domain and its dimensions.

This geometry was selected because of the availability of the data required for validation. The dimensions of the airfoil and Reynolds number for each case are similar to the ones used by Moreau et al. (2009) and are presented in Table 1.

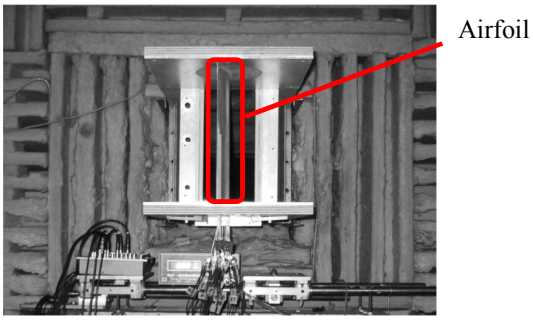

Figure 3 Experimental setup at Ecole Centrale de LyonECL (Moreau et al., 2009)

Table 1 Investigated cases in this study.

Angle of attack	Chord Reynolds number	Chord length
5°	1.3×10^5	10 cm
18°	1.3×10^5	10 cm
40°	1×10^5	5 cm

A uniform velocity field was selected for the inlet and a pressure outlet with zero gauge pressure was chosen for outlet boundary condition. The computational domain was extended compared to the experiment to eliminate the effect of reverse flow in outlets to improve the stability of the computations and accuracy of the results.

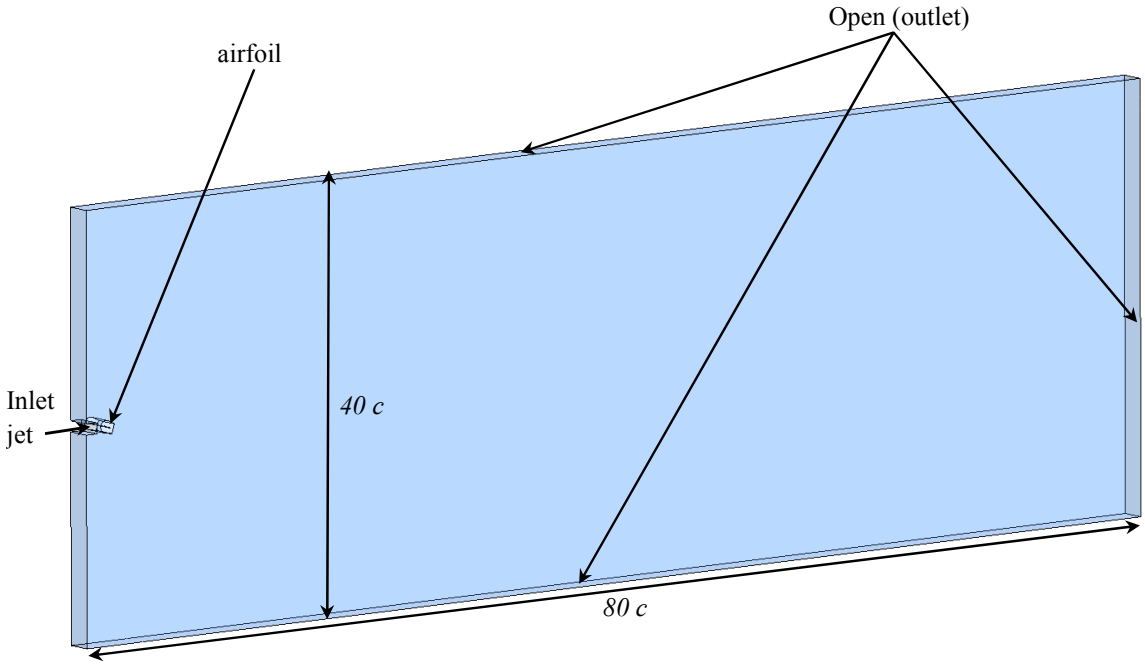

Figure 4 Computational domain used for current simulations. The domain is extended to eliminate the reverse flow at outlets.

Figure 5 shows the mesh and domain used in the simulation. The LES zone around the airfoil consists of two million cells and the total number of elements in the domain is approximately 3.5 million. Domain consists of hexahedral elements with growth rate of 1.1 in near field and 1.2 far from airfoil. The non-dimensional y^+ is set to one, in order to capture the boundary layer at the required accuracy.

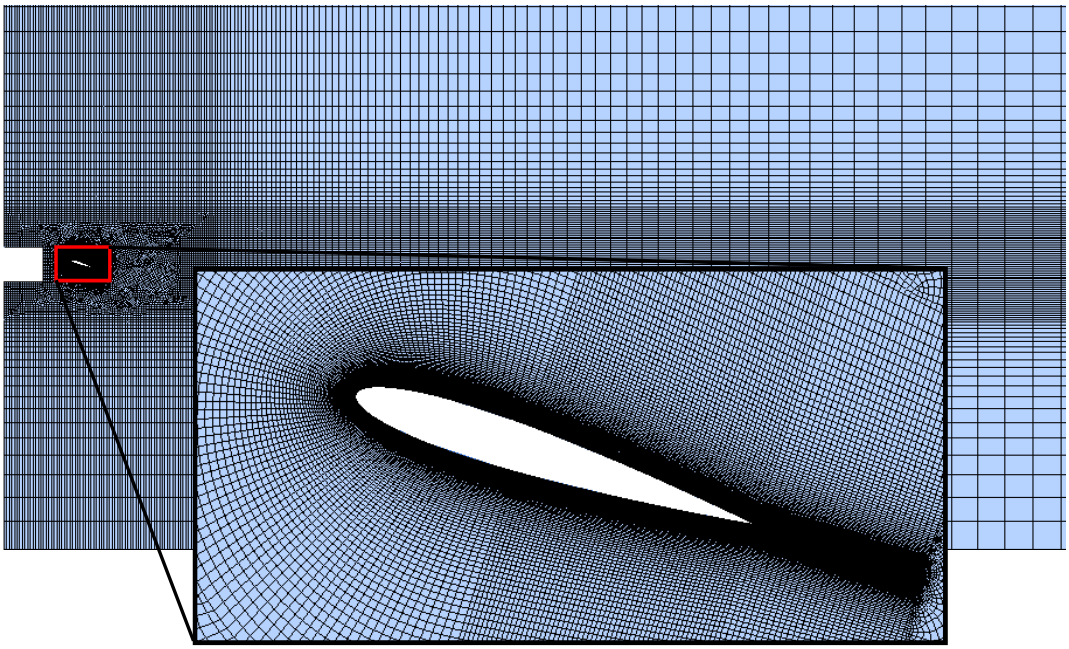

Figure 5 Generated mesh in the computational domain and zones. The airfoil area is magnified to show the grid around the airfoil.

A time step of $\Delta t = 1 \times 10^{-5}\ s$ was used to ensure that the maximum Courant–Friedrichs–Lewy (CFL) number lies in the range of unity for most of domain, especially in the wake region. To change the angle of attack for each case, the blade and associated mesh is rotated together to maintain the same mesh structure when the angle of attack changes.

Validation

For validation purposes, the model was solved at a Reynolds number of 1.34×10^5 and at an angle of attack of 18°, such that the results can be compared with the experiment carried out in the small anechoic wind tunnel at Ecole Centrale de Lyon by Moreau et al. (2009). Figure 6 shows the comparison of the pressure coefficient obtained from the CFD simulation with the ones reported by Moreau et al. (2009). The comparison shows a good agreement with a maximum deviation of 10% for the areas inside the pressure coefficient diagrams. It should also be noted that there were only 16 measurements points on the airfoil surface in the experiment which hindered the experiment. At the trailing edge and leading edge where

significant changes in surface pressure is expected, the experimental data is limited due to the practicality of the used measurement devices.

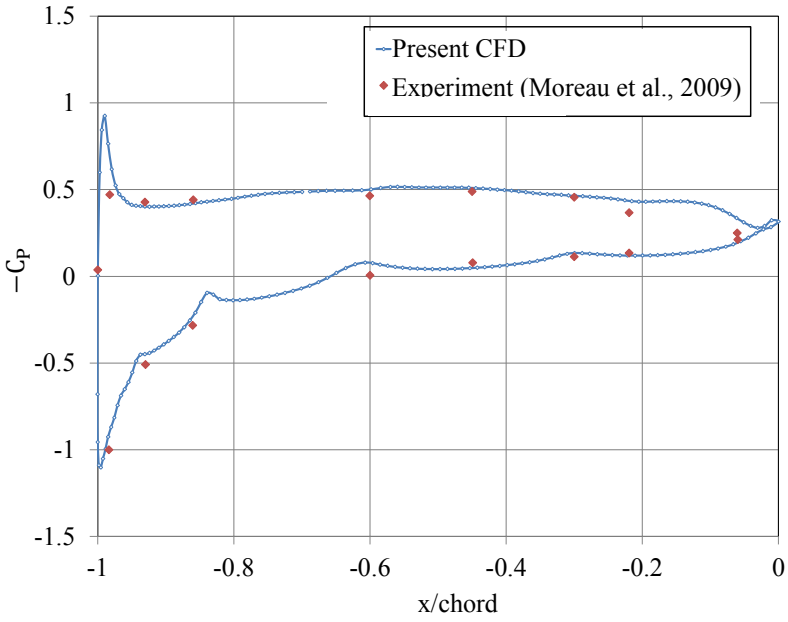

Figure 6 Comparison of computational results and experiment pressure coefficient.

To further evaluate the validity of the model, the lift coefficient has been recorded at each time-step (Figure 7). Figure 7 (b) shows the Fast-Fourier Transform of the lift coefficient to identify the frequency of the vortex shedding. The first frequency of the lift coefficient fluctuation is approximately 118Hz which corresponds to Strouhal number of St=0.59, which is close to the experimental Strouhal number of St=0.58 by Suzuki et al. (2006) and shows the ability of the model to capture the instabilities in the flow.

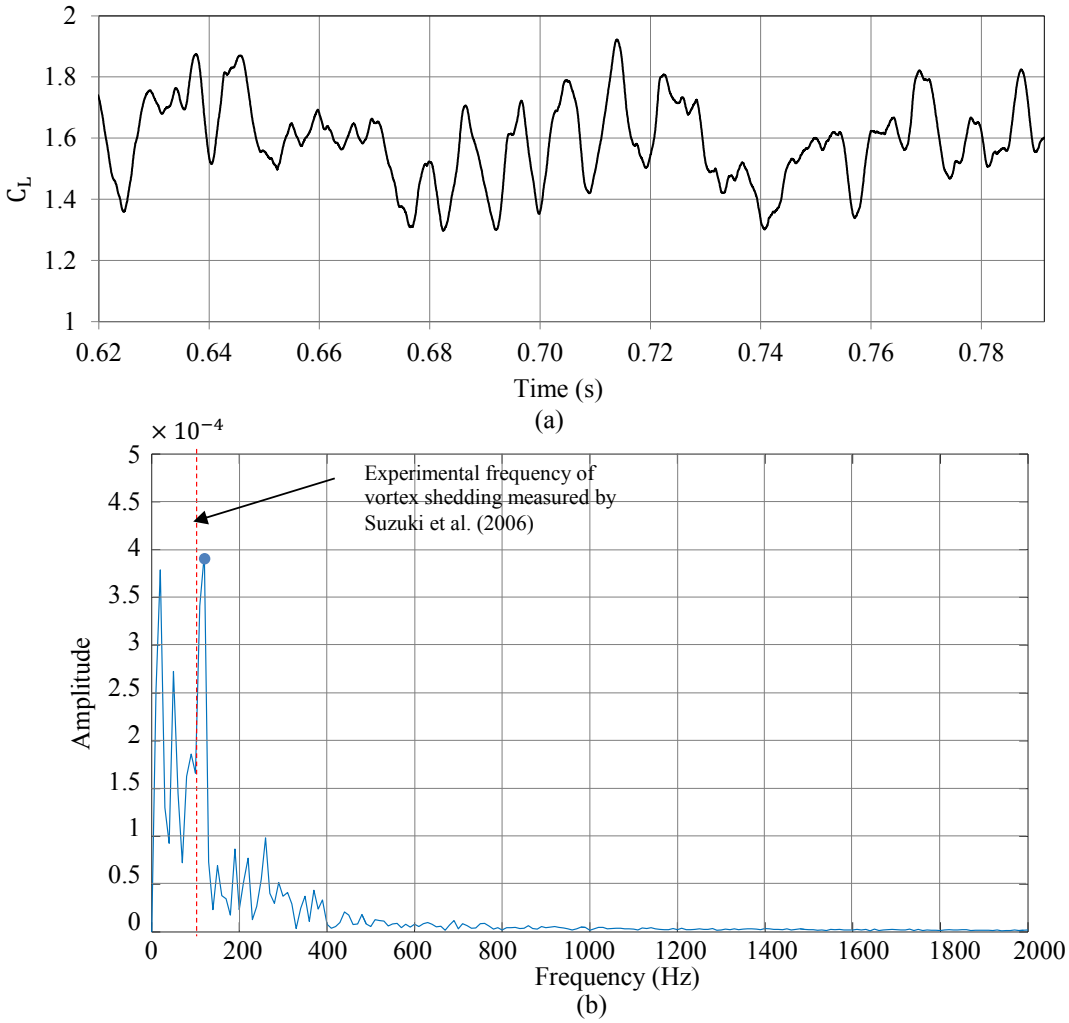

Figure 7 (a) Lift coefficient variation of the airfoil with time, used to calculate the frequency of the vortex shedding. (b) FFT of lift coefficient with first frequency around 118 Hz compared with Suzuki et al. (2006).

Results and discussion

Figure 8 shows an overview of the turbulence in the flow using the Q-criteria. It can be seen that the flow is separated from the suction surface at high angles of attack when the airfoil experienced stall. In the 40° case, the highly turbulent structures in the flow indicate that the airfoil is in the deep stall condition. Separated flow structures, with smaller eddies, can be also seen in the 18° case. The figure also shows that the size of the eddies is in direct correlation with the angle of attack, with eddies becoming larger and stronger as the angle of attack increases. This can be explained by the increase in the size of the projected area which is located

in front of the flow. It can be also seen from the turbulent eddies that the flow separates from leading edge for AoA greater than 18°. Large scale turbulence for large angles of attack interact with whole surface of the blade where it is expected to result in higher noise levels for lower frequencies compared to 5° degrees angle of attack.

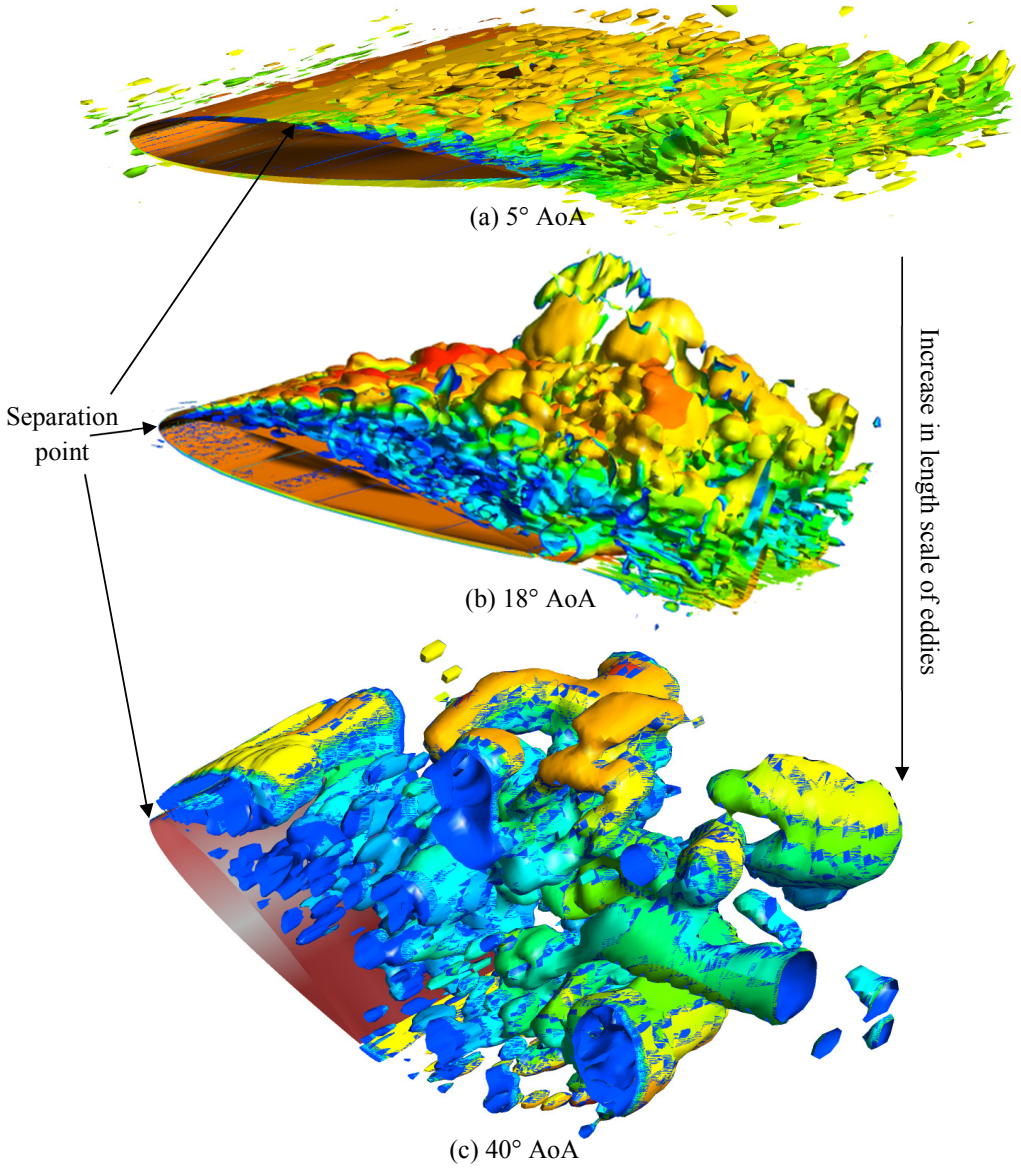

Figure 8 Velocity contour on iso-surface of Q-criterion showing the turbulent structures separated from the airfoil surface; a) AoA=5°, b) AoA=18°, c) AoA=40°.

Defining a length scale of turbulent structures in the flow is important in aeroacoustic since it has significant effect on the far-field noise spectra and noise source parameter modelling (Kamruzzaman et al., 2011). Having an estimation about this length scale can also help to identify the underlying noise generation mechanism, since the larger eddies interact with larger surface and result in higher frequency noise emission. The integral length scale is calculated

using the turbulent kinetic energy and its dissipation rate as $l = \frac{k^{3/2}}{\varepsilon}$ (Tennekes and Lumley, 1972, Wilcox, 1993). The integral length scale qualitatively shows the distance in which the fluid elements are moved by large turbulent structures. To compare the integral length scale of studied cases, its variation on the horizontal centre line (see Figure 10) is calculated and depicted in Figure 9. The integral length scale generally increases as the angle of attack increases. Integral length scale shows large structures in the wake of stalled airfoils with the size comparable with chord line. For both stall conditions, a peak exist in the diagram, which is associated to the shed vortices downstream of the airfoil. With large vortices in these cases, it is expected that the frequency of the noise signals decreases at far field.

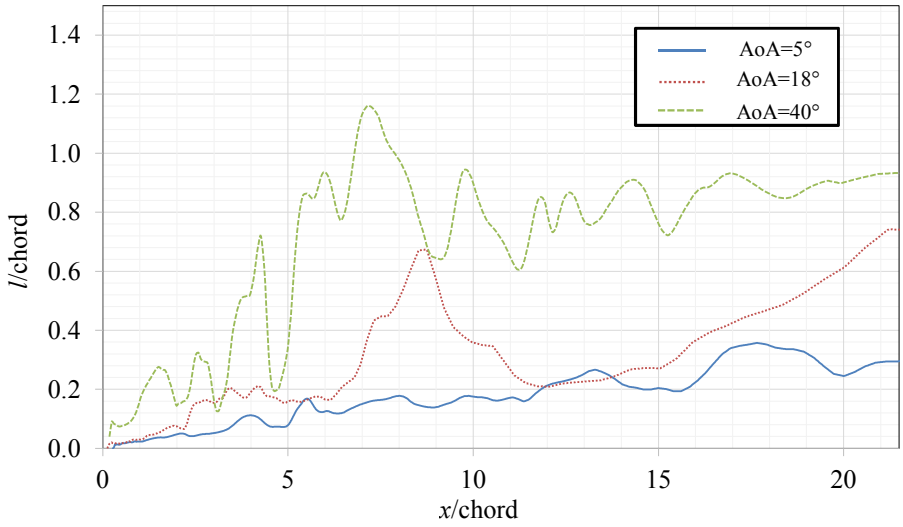

Figure 9 Integral length scale downstream of the airfoil.

Streamlines on the mid-section plane of the flow are presented in Figure 10 which show several vortical structures separating from the airfoil surface. It can be seen that the separation starts at the leading edge for 18º and 40º degrees, whereas at 5° there is laminar flow separation from the airfoil surface at the mid-chord and forms a turbulent boundary layer on trailing edge. For 5° and 18° of AoA, vortex breakdown occurs at the end of the laminar shear-layer as a consequence of the instabilities developed by the action of a Kelvin-Helmholtz mechanism.

These high frequency fluctuations in the velocity field grow in magnitude as the distance from the leading edge increases and eventually cause the shear layer to roll-up and undergo transition to turbulence (Prasad and Williamson, 1997, Rodriguez et al., 2011a). At high angles of attack the airfoil acts like a bluff body, with large separation and the formation of a Karman vortex street. As can be seen in Figure 10 (a) small eddies for low angles of attack interact with the airfoil close to the trailing edge, while for higher angles of attack whole suction surface is influenced by generated eddies. Thus, it is expected that the source of noise for low angle of attack is trailing edge area while for the high angles of attack the whole airfoil surface is the noise generation source. The size of the eddies significantly increases when angle of attack changes from 18° to 40°, whilst the number of turbulent eddies decreases. Based on the size of the eddies and surface which they interact with, it is expected that whole surface of the airfoil produces noise in these cases consequently the dominant noise frequency decreases as angle of attack increases.

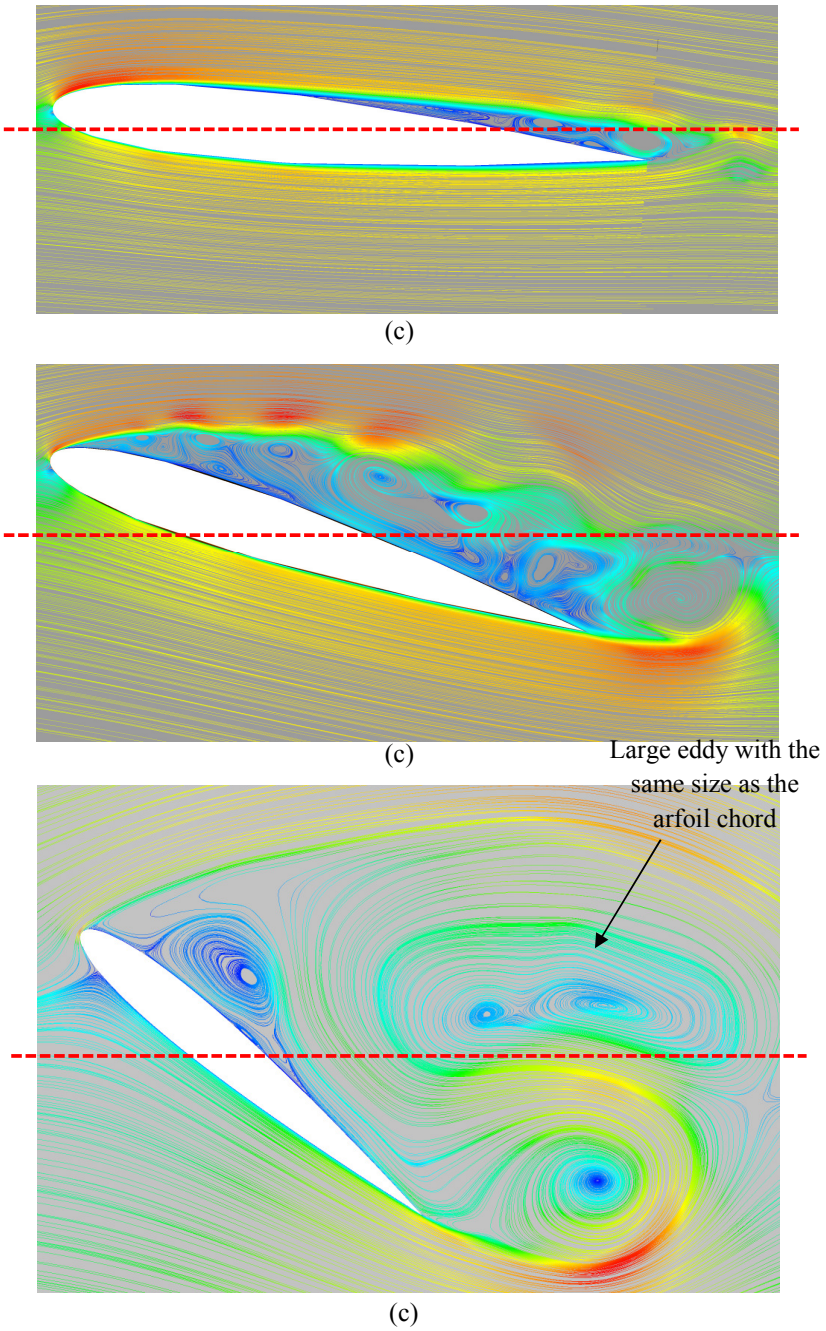

Figure 10 Instantaneous streamline for different cases in order to show the size of the vortices separated from the airfoil surface and interacting with it, (a) AoA= 5°, (b) AoA= 18°, (c) AoA= 40°. Dashed red lines shows the line on which the integral length scale is calculated.

Aeroacoustic results

As mentioned in the section of numerical method, the quadrupole term in FW-H analogy is neglected in the governing equations. Thus, the noise signatures are associated to flow-surface

interaction and vortex-vortex interactions are not considered in calculations. The instantaneous local pressure deviation fluctuations are displayed in Figure 11. As can be seen the plot shows dipole characteristics for pressure field. These pressure dipoles are aligned with the chord line for 18° and 5° angles of attack, however they are not for the 40º case. This behaviour can be explained by the large separation and bluff body behaviour of the airfoil at this angle of attack. The magnitude of the pressure fluctuations also increases significantly at this angle.

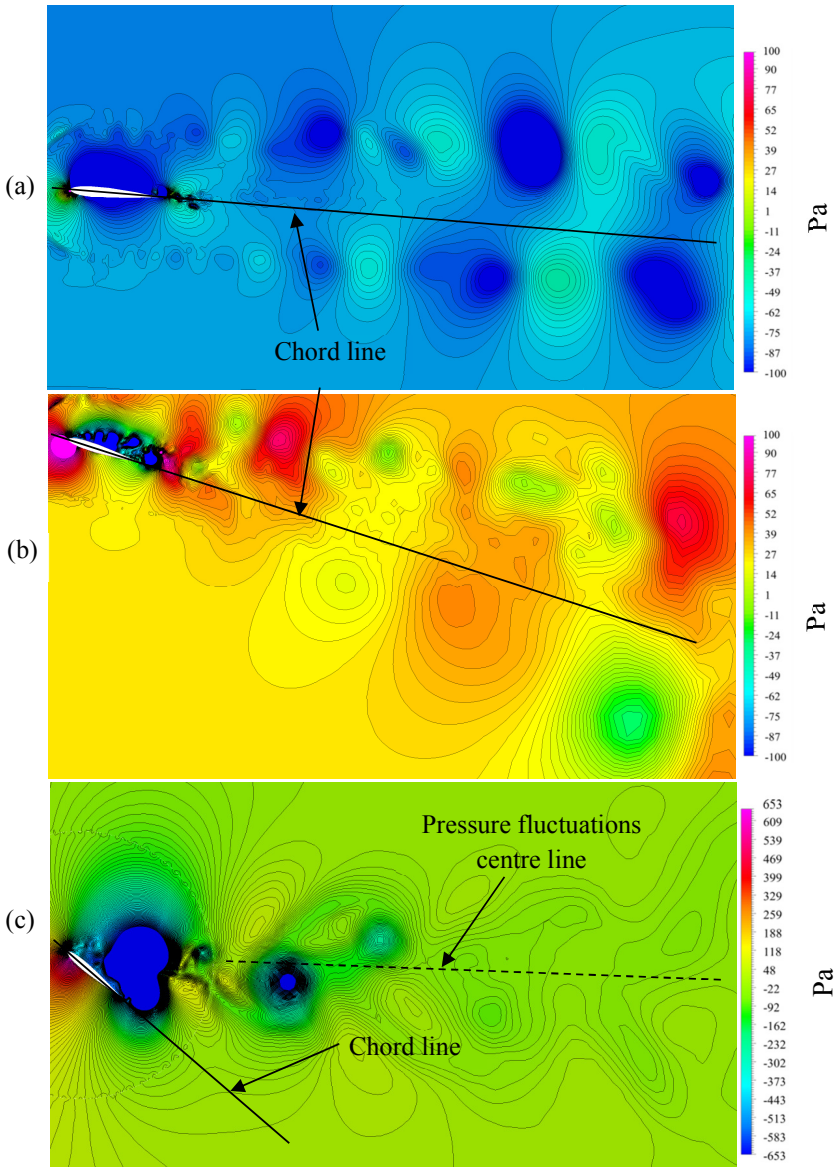

Figure 11 Deviation of the local pressure with respect to atmospheric pressure, a) AoA=5°, b) AoA=18°, and c) AoA=40°

Over 7500 samples of surface pressure on the airfoil were collected during 0.15 second time period to calculate the far field sound pressure. This setting resulted in the frequency resolution about 6 Hz. It should be noted that the vortex shedding frequency based on the Strouhal number is 117 Hz corresponding to 0.0085 s for shedding period, and current time span can provide accurate resolution for acoustic study. The receivers were located at a 70 chords away from the

airfoil centre (see Figure 12). Receivers were located symmetrically around the airfoil such that the chord line passess through a pair of receivers. Using Ffowcs-Williams and Hawkings analogy, the far-field noise signatures at receiver locations were calculated. The spectra of these noise signatures are presented in Figure 13. As can be seen in the Figure 13, the noise SPL is greatest at low frequencies for the 18º and 40º cases. The frequency of the generated noise depends on the size of the turbulent eddies; and generally $f \propto {}^{U}/_{l}$ where l is integral length scale and U is mean flow velocity. For the small angle of attack (5°) the frequency of the peak is much higher, which is due to the dominance of small vorticities at trailing edge of the airfoil. As shown in Figure 10 the size of the eddies increases as the angle of attack increases. Thus, the frequency content decreases with larger turbulent structures forming on the airfoil surface. The larger separated structure at 40º leads to a reduction in the peak frequency of the noise in far field compared to the 18º case.

The sound pressure spectra at far-field for 18° angle of attack shows different behaviour at some receivers. The sound spectra for receivers 1, 2, 3, 8, 9, 10 and 20 have a relative minimum at the reduced frequency of 6, while other receivers have their relative peaks. For the reduced frequencies higher than 40, at the high angles of attack, the trend of sound pressure level is different for different receivers, specially receivers 1 and 9 which are located along the chord line. Due to the high frequency content of the noise it can be concluded that the noise is generated by the small eddies interacting with trailing edge. Thus it is hypothesised that this behaviour is caused by the effect of large eddies on the small scale eddies in turbulent boundary layer.

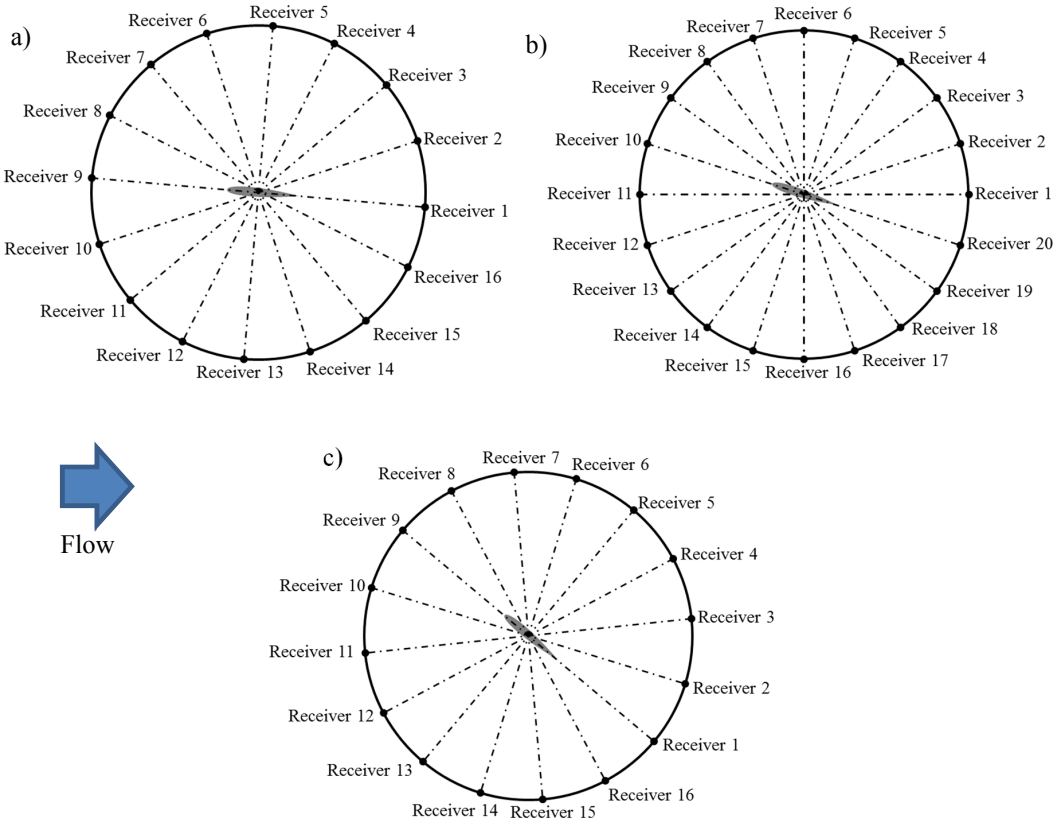

Figure 12 Relative locations of the receivers with respect to the airfoil, a) 5º AoA, b) 18º AoA, and c) 40º AoA. Twenty receivers were used for 18° AoA case to ensure covering the directions along the chord-line as well as perpendicular direction.

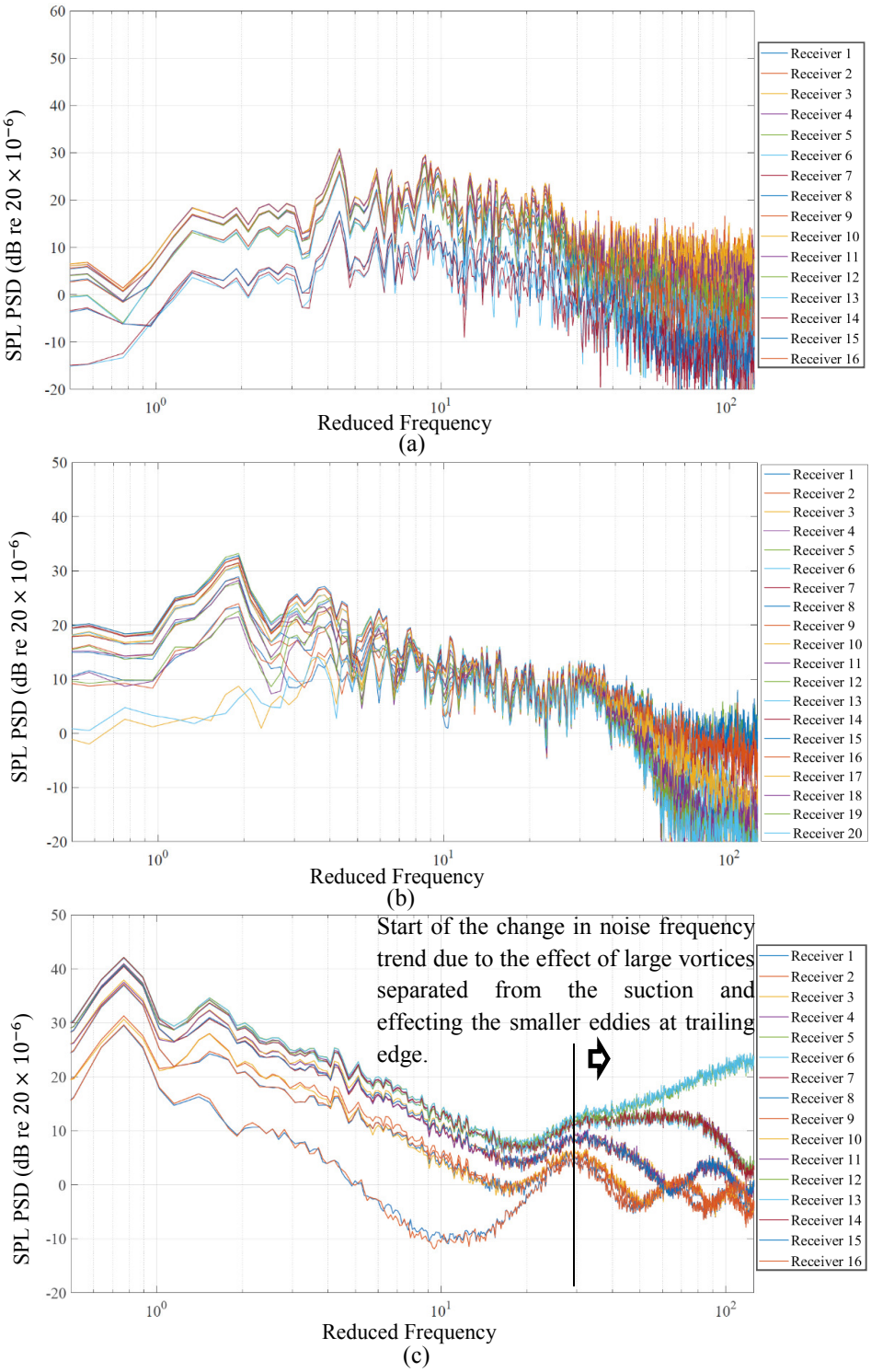

Figure 13 Sound pressure level density at 70 chords distance from airfoil, a) AoA=5°, b) AoA=18°, c) AoA=40°.

The change in narrowband spectra 70 chords downstream of the airfoil for the 3 cases is presented at in Figure 14. As can be seen the dominant frequency decreases as the AoA increases. The shift of the dominant frequency towards the lower frequency with increasing the angle of attack is caused by the increase in size of the separated vortices from airfoil surface (see Figure 9 and 10).

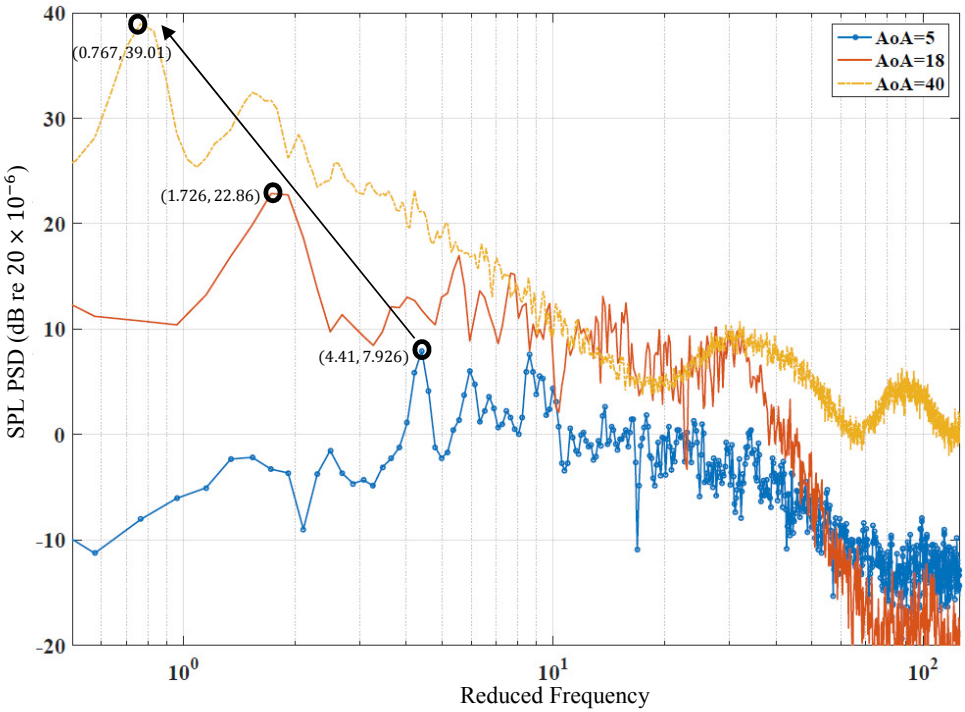

Figure 14 comparison of narrowband spectra for 3 different cases. As expected the frequency content of the noise decreases as the AoA increases and separation occurs on the blade surface.

Figure 15 shows the contours of surface acoustic power level on the airfoil surface at peak frequencies for each case. As can be seen the dominant noise source is located near trailing edge, for 5º angle-of-attack. There is no distinct source location with higher acoustic pressure level at the onset of stall for 18 degrees angle of attack. This can be due to the interaction of several eddies interacting with the whole suction surface of the airfoil. Interaction of large eddies formed in the deep stall condition at 40 degrees AoA, results in noise emission from the whole surface of the airfoil. However, the amplitude of the noise source is slightly higher at

the trailing edge which is caused by the formation of the bound vortices at the trailing edge due to pressure difference between the suction and the pressure sides of the airfoil. Comparing figures 8, 9 and 10, it can be seen that the vortex length-scale formed on the suction side of the airfoil is almost equal to the large portion of the suction surface with second highest pressure level. It can be concluded that the main mechanism of the noise generation for this case is the stall noise due to the separated large eddies.

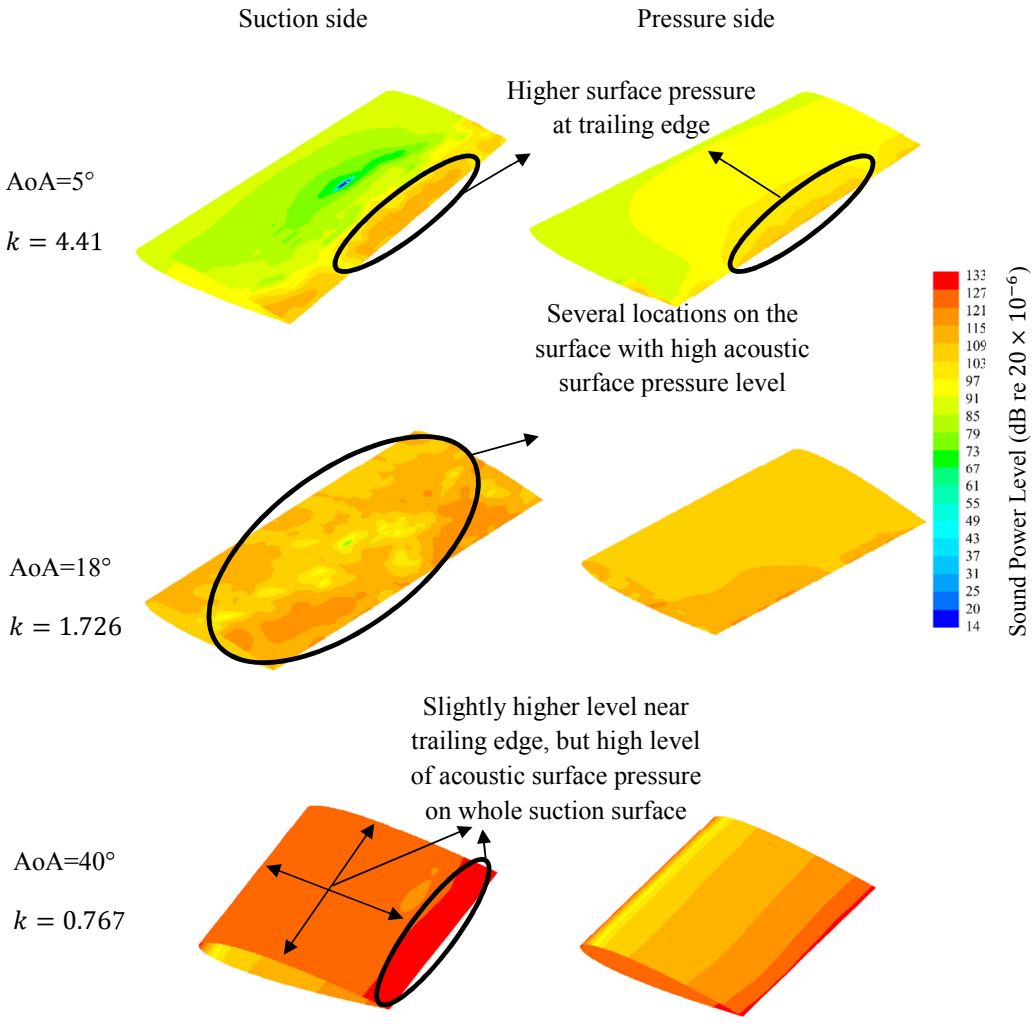

Figure 15 Acoustic surface pressure contours at peak frequencies for 3 cases

The directivity of the noise was investigated by calculating the overall sound pressure level at a distance of 70 chords away from the airfoil. It should be noted that, as the implemented FW-

H analogy in this study doesn't take into account the quadrupole sources, it is expected to only see the monopole and dipole behaviours of the noise propagation in the results. The overall sound pressure level for all cases is dipolar, normal to the chord line. However, for 18 degrees angle of attack the overall sound pressure level shows mostly monopole directivity.

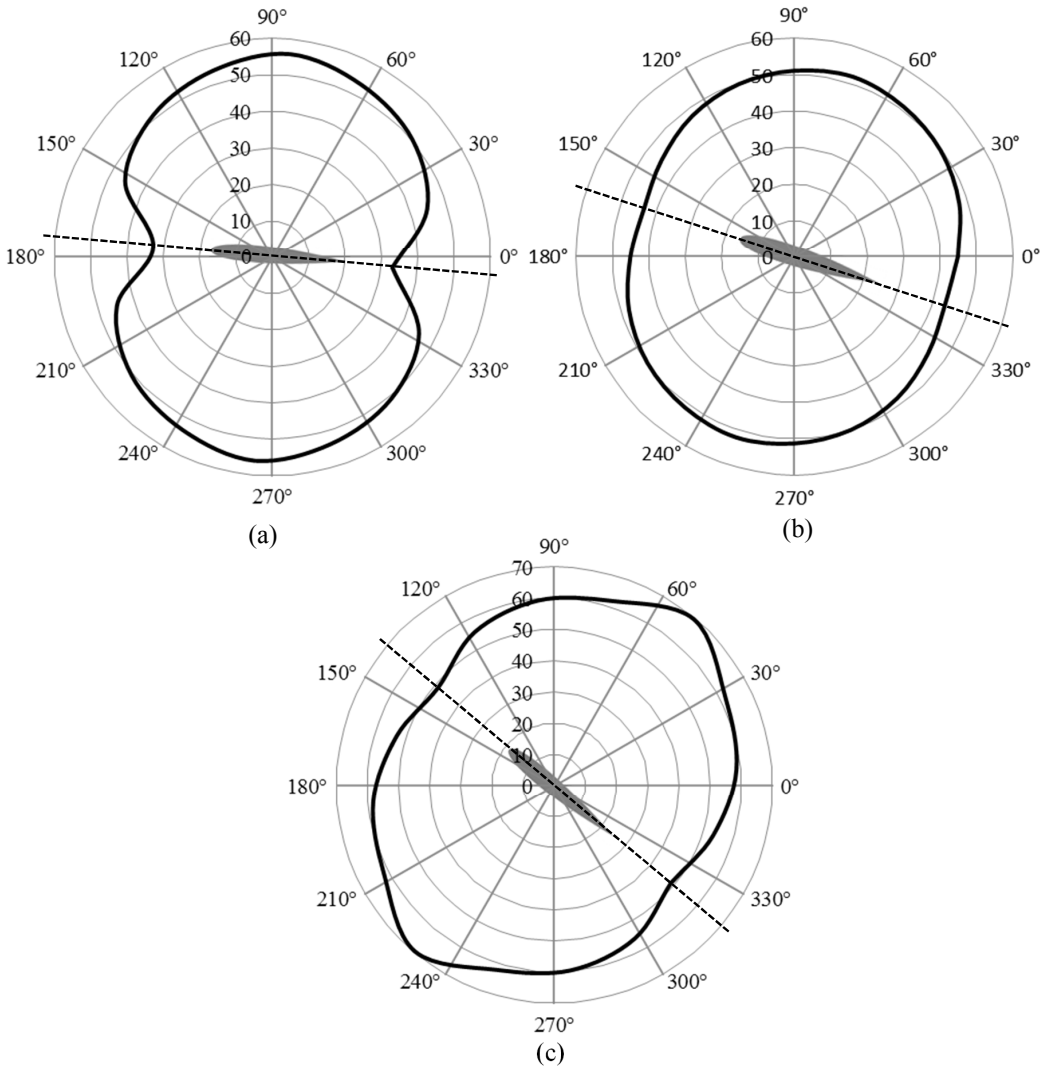

Figure 16 Directivity of the overall sound pressure level, a) AoA=5°, b) AoA=18°, c) AoA=40°.

The directivity of the noise at the peak frequencies is also shown in Figure 17. The directivity of the peak for 5 degrees angle of attack shows a dipole directivity with higher noise level toward the leading edge of the airfoil. This behaviour could be caused by the existing additional

noise sources which are not predicted by trailing edge theories. These source can result in anti-symmetric radiation of the sound in specific frequencies which has previously shown in the direct numerical simulation studies (Sandberg and Jones, 2010). More investigation should be carried out to find out the underlying mechanism for this behaviour. As can be seen for the highest noise level for stall condition, the noise is stronger perpendicular to the chord line. The dipole directivity of the stall noise can be clearly seen while airfoil is in stall condition at 18º. To better demonstrate the directivity pattern of the peak frequency, the variation of angle between chord normal and peak to peak direction (β) versus angle of attack is shown in Figure 17 (d). Diagram shows that the angle between peak directivity and chord normal is the highest when the angle of attack is small. This angle decreases as the angle of attack increases up to 40° angle of attack in which the chord normal and peak to peak line overlap. This shows that at deep stall the noise whole airfoil surface is a noise source and noise is radiated perpendicular to the airfoil chord-line.

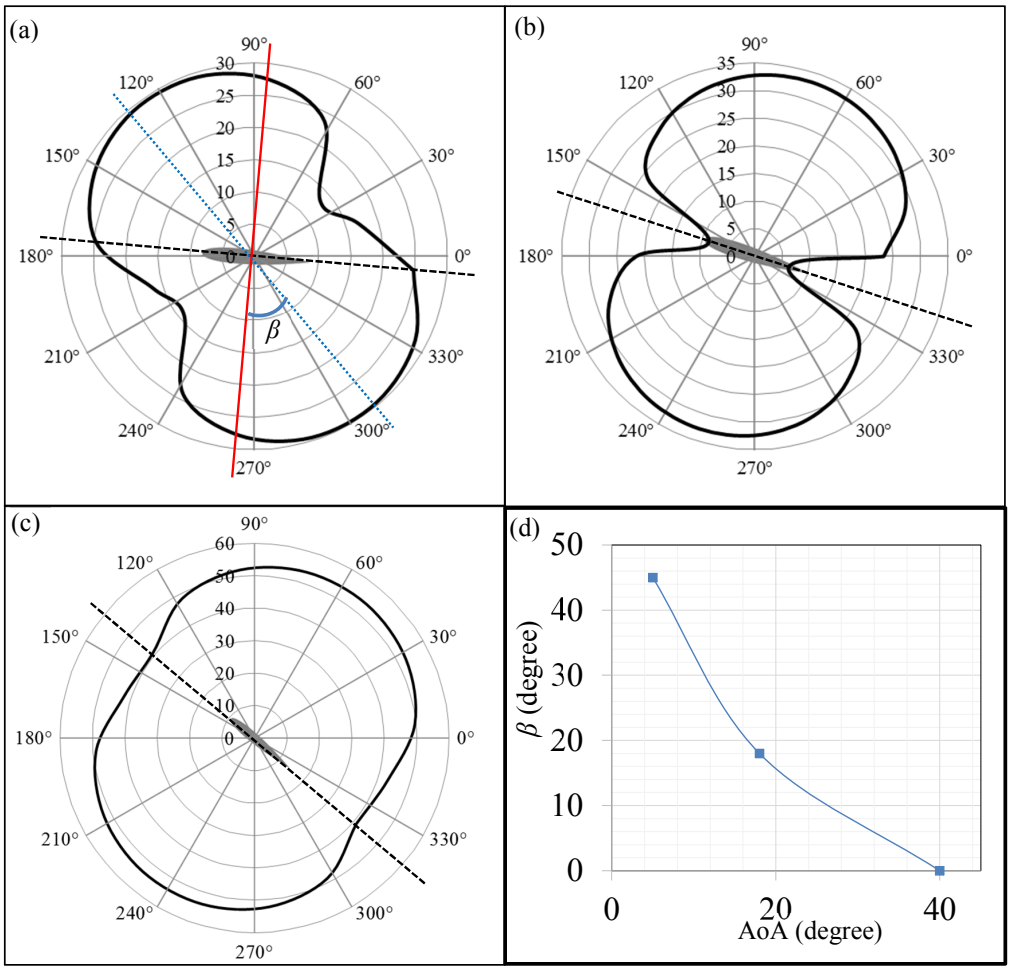

Figure 17 Directivity of the peak frequencies for 3 cases, (a) AoA=5°, Peak at k=4.41, (b) AoA=18°, Peak at k=1.726, (c) AoA=40°, Peak at k=0.767, (d) variation of β (angle between chord normal and peak direction) versus angle of attack.

Conclusion

The acoustic field generated by an airfoil at 5º, 18º and 40º of angles-of attack, corresponding pre-stall, shallow stall and deep stall conditions was investigated using computational fluid dynamics. An Embedded LES (ELES) method was used to calculate the flow field and acoustic pressure fluctuations in the domain. Results showed a good agreement between the computed and measured aerodynamic forces and vortex shedding frequency.

Results of the acoustic modelling showed higher SPL at the trailing edge of the airfoil for the small angle of attack, while the high level regions are scattered on suction side at the onset of

stall. Acoustic pressure level contours also revealed that the whole suction surface is acting as a sound source for deep stall condition. Aeroacoustic calculations showed dipole directivity for peak frequencies in all cases. These dipoles have higher magnitude in perpendicular direction to chord line for stall condition, while they shows higher noise radiating towards the leading edge at pre-stall condition. According to trailing edge noise theory, trailing edge noise which is the dominant noise source on airfoils especially for pre-stall conditions, is dipole and radiates perpendicular to chord line. However, this study showed that at some frequencies the airfoil noise radiates in other directions which is in contrast with trailing edge noise theory prediction. This contradiction has been also reported in previous literature using DNS simulation for low Reynolds Number flow over NACA 0012 airfoil. This behaviour shows that at some frequencies there are other noise sources which can't be explained by trailing edge noise theory. The physical cause of this behaviour should be more investigated using experimental studies or direct aeroacoustic computations using accurate turbulence models.

References

Brooks, T. F., Pope, D. S. & Marcolini, M. A. 1989. Airfoil self-noise and prediction. NASA.

Doolan, C. J., Moreau, D. J. & Brooks, L. A. 2012. Wind turbine noise mechanisms and some concepts for its control. *Acoustics Australia,* **40,** 7-13.

Germano, M., Piomelli, U., Moin, P. & Cabot, W. H. 1991. A dynamic subgrid-scale eddy viscosity model. *Physics of Fluids A* **3,** 1760-1765.

Gritskevich, M., Garbaruk, A., Schütze, J. & Menter, F. 2012. Development of ddes and iddes formulations for the k-ω shear stress transport model. *Flow, Turbulence and Combustion,* **88,** 431-449.

Herr, M. & Dobrzynski, W. 2005. Experimental investigations in low-noise trailing edge design. *AIAA Journal,* **43,** 1167-1175.

Jianu, O., Rosen, M. A. & Naterer, G. 2012. Noise pollution prevention in wind turbines: Status and recent advances. *Sustainability,* **4,** 1104-1117.

Katz, J. & Plotkin, A. (eds.) 2001. *Low-speed aerodynamics*: Cambridge University Press.

Kim, D., Lee, G.-S. & Cheong, C. 2015. Inflow broadband noise from an isolated symmetric airfoil interacting with incident turbulence. *Journal of Fluids and Structures,* **55,** 428-450.

Kim, T., Jeon, M., Lee, S. & Shin, H. 2014. Numerical simulation of flatback airfoil aerodynamic noise. *Renewable Energy,* **65,** 192-201.

Laratro, A., Arjomandi, M., Cazzolato, B. & Kelso, R. 2016. A comparison of naca 0012 and naca 0021 self-noise at low reynolds number. *In:* ZHOU, Y., LUCEY, A. D., LIU, Y. & HUANG, L. (eds.) *Fluid-structure-sound interactions and control: Proceedings of the 3rd symposium on fluid-structure-sound interactions and control.* Berlin, Heidelberg: Springer Berlin Heidelberg.

Laratro, A., Arjomandi, M., Kelso, R. & Cazzolato, B. 2014. A discussion of wind turbine interaction and stall contributions to wind farm noise. *Journal of Wind Engineering and Industrial Aerodynamics,* **127,** 1-10.

Leloudas, G., Zhu, W. J., Sørensen, J. N., Shen, W. Z. & Hjort, S. 2007. Prediction and reduction of noise from a 2.3 mw wind turbine. *The Science of Making Torque from Wind, IOP Publishing, Journal of Physics, Conference Series,* **75**.

Lilly, D. K. 1992. A proposed modification of the germano subgrid-scale closure method. *Physics of Fluids A,* **4,** 633-635.

Madsen, H. A., Bertagnolio, F., Fischer, A. & Bak, C. 2014. Correlation of amplitude modulation to inflow characteristics. *Proceedings of 43rd International Congress on Noise Control Engineering.* The Australian Acoustical Society.

Menter, F. R. & Egorov, Y. 2010. The scale-adaptive simulation method for unsteady turbulent flow predictions. Part 1: Theory and model description. *Flow, Turbulence and Combustion,* **85,** 113-138.

Moorhouse, A., Hayes, M., Sabine von Hünerbein, Piper, B. & Adams, M. 2007. Research into aerodynamic modulation of wind turbine noise: Final report.

Moreau, S., Roger, M. & Christophe, J. 2009. Flow features and self-noise of airfoils near stall or in stall. *15th AIAA/CEAS Aeroacoustics Conference (30th AIAA Aeroacoustics Conference).* Miami, Florida.

Moriarty, P. & Migliore, P. 2003. Semi-empirical aeroacoustic noise prediction code for wind turbines National Renewable Energy Laboratory

Nobbs, B., Doolan, C. J. & Moreau, D. J. Characterisation of noise in homes affected by wind turbine noise. Acoustics 2012 - Fremantle, 21-23 November 2012 Fremantle, Australia.

Oerlemans, S. 2011. An explanation for enhanced amplitude modulation of wind turbine noise. National Aerospace Laboratory NLR.

Pedersen, E. & Waye, K. P. 2004. Perception and annoyance due to wind turbine noise—a dose–response relationship. *Journal of the Acoustical Society of America,* **116,** 3460-3470.

Richard, S., Lloyd, J. & Neil, S. 2008. Direct numerical simulations of noise generated by turbulent flow over airfoils. *14th aiaa/ceas aeroacoustics conference (29th aiaa aeroacoustics conference).* American Institute of Aeronautics and Astronautics.

Sandberg, R. D. 2015. Compressible-flow dns with application to airfoil noise. *Flow, Turbulence and Combustion,* **95,** 211-229.

Santana, L. D., Schram, C. & Desmet, W. 2016. Low-frequency extension of amiet′s theory for compact airfoil noise predictions. *Journal of Sound and Vibration*.

Stephane, M., Michel, R. & Julien, C. 2009. Flow features and self-noise of airfoils near stall or in stall. *15th aiaa/ceas aeroacoustics conference (30th aiaa aeroacoustics conference).* American Institute of Aeronautics and Astronautics.

Suzuki, Y., Miyazawa, M., Kato, C. & Fujita, H. 2007. Analysis of aerodynamic sound sources in a flow around a two-dimensional airfoil under stalled conditions. *INTERNOISE 2006.* Honolulu, Hawaii.